**Abstract**

# Continuous Optical Production of Ultracold Vibronic Ground State Polar Molecules

Colin David Bruzewicz

2014

We present recent results on the formation of ultracold polar molecules via photoassociation. Beginning with pre-cooled samples of Rb and Cs atoms, we produce electronically-excited molecules that inherit the ultracold temperature of their atomic precursors. In order to create large samples of ultracold molecules in their vibrational and rotational $X^1\Sigma^+(v{=}J{=}0)$ ground state, we study two different photoassociative regimes. In the first, molecules are created in a particular highly vibrationally-excited molecular state and decay strongly to a weakly-bound vibrational level in the ground $a^3\Sigma^+$ state. To study a possible population transfer scheme from this state to the $X^1\Sigma^+(v{=}J{=}0)$ ground state, we present high-resolution depletion spectroscopy of the $a^3\Sigma^+ \rightarrow c^3\Sigma^+$ transition for use in the first stage of a proposed Stimulated Raman Adiabatic Passage (STIRAP) transfer. In the second photoassociative regime, molecules are created in deeply-bound, electronically-excited vibrational levels that decay directly to the $X^1\Sigma^+(v{=}0)$ state, obviating the need for population transfer. Through theoretical analysis and subsequent experimental verification, we demonstrate continuous formation of $X^1\Sigma^+(v{=}0)$ RbCs molecules at rates in excess of $10^3$/s. We then conclude with detailed calculations of a method to purify the molecular sample of unwanted excited molecular states, based on inelastic scattering with ultracold Cs atoms.

# Continuous Optical Production of Ultracold Vibronic Ground State Polar Molecules

A Dissertation
Presented to the Faculty of the Graduate School
of
Yale University
in Candidacy for the Degree of
Doctor of Philosophy

by
Colin David Bruzewicz

Dissertation Director: David DeMille

May 2014

UMI Number: 3580643

All rights reserved

INFORMATION TO ALL USERS
The quality of this reproduction is dependent upon the quality of the copy submitted.

In the unlikely event that the author did not send a complete manuscript
and there are missing pages, these will be noted. Also, if material had to be removed,
a note will indicate the deletion.

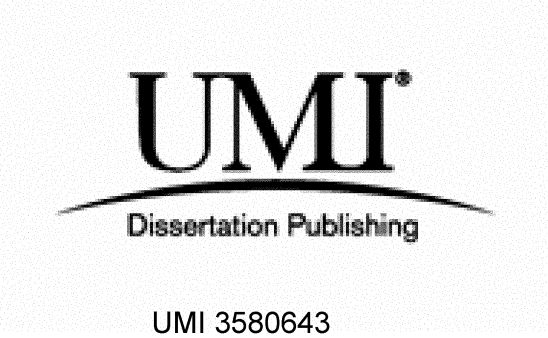


UMI 3580643
Published by ProQuest LLC 2014. Copyright in the Dissertation held by the Author.
Microform Edition © ProQuest LLC.
All rights reserved. This work is protected against
unauthorized copying under Title 17, United States Code.

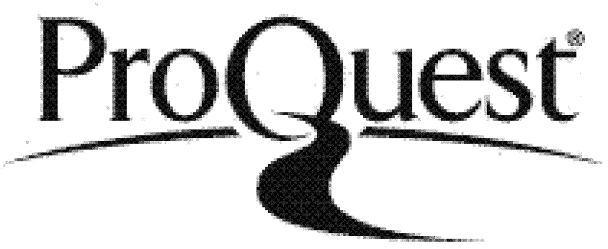


ProQuest LLC
789 East Eisenhower Parkway
P.O. Box 1346
Ann Arbor, MI 48106-1346

Copyright © 2014 by Colin David Bruzewicz

All rights reserved.

# Acknowledgments

This work is the product of years of tireless (and often tired) effort from all of the members of Team RbCs at Yale. Your diligence, vision, creativity, and unshakable confidence that we could do it made all of this possible. Thank you.

# Contents

**Acknowledgments** i

**1 Introduction** 1

1.1 Ultracold Physics: Atoms and Molecules . . . . . 1

1.1.1 Dipolar Physics . . . . . 2

1.1.2 Ultracold Chemical Reactions . . . . . 3

1.2 Requirements for Making Ultracold Molecules . . . . . 3

1.2.1 Trapping and Inelastic Scattering . . . . . 4

1.2.2 Direct Cooling . . . . . 6

1.2.3 Indirect Cooling: Engineering Molecules from Pre-Cooled Atoms . . 7

1.3 Outline of Thesis . . . . . 10

**2 Physics of Optical Cooling and Trapping** 11

2.1 Introduction . . . . . 11

2.2 Atomic Cooling in Magneto-Optical Traps . . . . . 12

2.2.1 Doppler Cooling . . . . . 12

2.2.2 Spatial Confinement . . . . . 13

2.2.3 Implementation in Alkali Atoms . . . . . 13

2.2.4 The Forced Dark SPOT MOT . . . . . 14

2.2.5 MOT Laser Systems . . . . . 15

2.2.6 MOT Diagnostics, Improvements . . . . . 18

2.2.7 Experimental Chamber . . . . . 21
2.3 Trapping in a Conservative Dipole Trap . . . . . 24
2.3.1 Dipole Force Calculation . . . . . 25
2.3.2 Laser Astigmatism . . . . . 27
2.3.3 $CO_2$ Beam Imaging . . . . . 28
2.3.4 Two-Frequency Acousto-Optical Modulator Driver . . . . . 29
2.3.5 Trap Geometry . . . . . 33
2.3.6 Trap Loading . . . . . 34
2.4 Summary . . . . . 35

**3 The Atomic and Molecular Theory of Photoassociation 38**

3.1 Introduction . . . . . 38
3.2 Molecular State Labeling . . . . . 39
3.2.1 Axial Symmetry and Projection onto the Internuclear Axis . . . . . 39
3.2.2 Hund's Cases and Selection Rules . . . . . 39
3.3 Reading Potential Energy Curves . . . . . 45
3.4 Spectroscopic Data to Potential Curves to Molecular Wavefunction . . . . . 48
3.4.1 Inversion of Spectroscopy to get Potentials to get Wavefunctions . . 48
3.5 Creating Molecules Out of Atoms . . . . . 50
3.5.1 PA Excitation Rate . . . . . 51
3.5.2 PA as Inelastic Scattering . . . . . 51
3.6 Calculating Rotational Line Strengths in Photoassociation . . . . . 53
3.6.1 Atomic Scattering State . . . . . 56
3.6.2 Excited Molecular State . . . . . 57
3.6.3 Calculating Matrix Elements . . . . . 60
3.6.4 Accounting for Unresolved Hyperfine Structure in the Excited State 61
3.7 Summary . . . . . 63

**4 Weakly-Bound Photoassociation** **65**

4.1 Introduction . . . . . 65

4.1.1 Long-Range PA to the $\Omega = 0^-$ State at 897 nm . . . . . 66

4.1.2 Radiative Stabilization to $a^3\Sigma^+$ ($v$=36) . . . . . 67

4.1.3 Stimulated Emission Pumping to $X^1\Sigma^+$ ($v$=0) . . . . . 67

4.2 Proposed Stimulated Raman Adiabatic Passage (STIRAP) to $X^1\Sigma^+$ ($v$=0) 71

4.2.1 Dressed State Theory . . . . . 71

4.2.2 Requirements . . . . . 74

4.3 Narrowband Spectroscopy . . . . . 79

4.3.1 Molecular Detection . . . . . 79

4.3.2 Depletion Spectroscopy . . . . . 81

4.3.3 Theoretical Treatment . . . . . 82

4.3.4 Results . . . . . 88

4.4 Attempts to Simplify the Spectroscopy . . . . . 97

4.4.1 PA in the Optical Trap . . . . . 97

4.4.2 Bright State PA . . . . . 100

4.4.3 Limitations . . . . . 101

4.5 Summary . . . . . 103

**5 Deeply-Bound Photoassociation** **104**

5.1 Introduction . . . . . 104

5.2 Photoassociation at 11824 $cm^{-1}$ . . . . . 105

5.2.1 REMPI Spectroscopy of the $X^1\Sigma^+ \rightarrow (4)^1\Sigma^+$ Transition . . . . . 107

5.2.2 Cross-Correlation Method . . . . . 107

5.2.3 REMPI Spectroscopy of the $X^1\Sigma^+ \rightarrow (2)^1\Pi$ Transition . . . . . 111

5.3 Photoassociation to the $(2)^3\Pi_{0^+}$ State . . . . . 115

5.3.1 Franck-Condon Factor Analysis . . . . . 115

5.3.2 Rotational PA Spectroscopy . . . . . 115

5.3.3 REMPI Analysis of Populations of Decay from $(2)^3\Pi_{0^+}$ ($v'$=10) . . . 117
5.3.4 Saturation of Photoassociation Rate . . . 121
5.3.5 Molecular $X^1\Sigma^+(v=0)$ Production Rate . . . 122
5.3.6 Nature of the Photoassociation State at 11824 $cm^{-1}$ . . . 124
5.3.7 Verifying Assignments . . . 126
5.4 Summary . . . 128

**6 Future Directions** **129**
6.1 Introduction . . . 129
6.2 Depletion Spectroscopy of the $X^1\Sigma^+(v=0)$ State . . . 129
6.3 Molecular Trapping and Sample Purification . . . 131
6.3.1 Photoassociation in the Optical Trap . . . 131
6.3.2 Steady-State Molecular Accumulation . . . 133
6.3.3 Simple Population Models . . . 133
6.3.4 Simulated Scrubbing . . . 134
6.4 Further Cooling . . . 136
6.4.1 Hyperfine Cooling in the Rovibronic Ground State . . . 136
6.4.2 Sympathetic Cooling with Cs Atoms . . . 137
6.4.3 Evaporative Molecular Cooling . . . 137
6.4.4 Temperature Measurement . . . 138
6.5 Conclusion . . . 139

**Microchannel Plate Readout** **142**

**Spin-Orbit Mixing** **143**

**Extensions of Line Strength Calculation** **145**

# List of Figures


1.1 Schematic representation of scattering between vibrationally-excited molecules and ground state molecules . . . . . 5

2.1 Doppler cooling of an atom . . . . . 13

2.2 Cycling transition in $^{85}$Rb . . . . . 14

2.3 Schematic of beam-splitting optics for 6-beam Rb MOT . . . . . 17

2.4 Schematic of beam-expanding optics for 6-beam Rb MOT . . . . . 18

2.5 Screenshot of absorption imaging . . . . . 20

2.6 Experimental chamber . . . . . 22

2.7 Magnetic field coils . . . . . 24

2.8 High resolution $CO_2$ laser beam profile . . . . . 30

2.9 Circuit diagram for the two-frequency AOM driver . . . . . 31

2.10 Optical paths of the two-frequency $CO_2$ laser AOM system . . . . . 33

2.11 Optical trap geometry . . . . . 34

2.12 Absorption images of atoms trapped in an optical dipole trap . . . . . 36

2.13 Atomic Cs temperature . . . . . 37

3.1 Angular momentum coupling in Hund's case (a) molecules . . . . . 41

3.2 Angular momentum coupling in Hund's case (b) molecules . . . . . 42

3.3 Angular momentum coupling in Hund's case (c) molecules . . . . . 43

3.4 The Franck-Condon principle . . . . . 47

3.5 Schematic representation of the use of the RKR1 and LEVEL 8.0 programs 49

3.6 Schematic representation of PA as inelastic scattering . . . . . 52
3.7 Dependence of the PA rate coefficient, $K_{PA}$, on the laser intensity . . . . . 54
3.8 Angular momentum coupling for two colliding alkali atoms . . . . . 56

4.1 Potentials involved in weakly-bound PA and depletion spectroscopy . . . . 68
4.2 Schematic representation of population transfer in a $\Lambda$-system . . . . . 72
4.3 Evolution of the probabilities to be in states $|1\rangle$ and $|3\rangle$ during STIRAP . . 74
4.4 Geometrical interpretation of adiabatic rotation of instantaneous eigenvector during STIRAP . . . . . 75
4.5 Schematic of optical layout for delayed self-heterodyne measurement . . . . 78
4.6 Delayed self-heterodyne measurement results . . . . . 78
4.7 Time of flight $RbCs^+$ ion signal during depletion . . . . . 82
4.8 Angular momentum recoupling in the $a^3\Sigma^+$ state of RbCs . . . . . 86
4.9 Hyperfine splittings of the $a^3\Sigma^+$ state in RbCs . . . . . 90
4.10 Depletion spectroscopy of the $a^3\Sigma^+(v{=}36) \rightarrow c^3\Sigma^+_{0^-}(v{=}34)$ transition . . . . 93
4.11 Depletion spectroscopy $a^3\Sigma^+(v{=}36) \rightarrow c^3\Sigma^+_{0^-}(v{=}34, 36)$ transitions . . . . . 95
4.12 Simulated depletion spectrum of the $a^3\Sigma^+ \rightarrow c^3\Sigma^+_{0^-}$ transition . . . . . 96
4.13 Depletion spectroscopy of the $a^3\Sigma^+(v{=}36) \rightarrow c^3\Sigma^+_1(v{=}34)$ transition . . . . 98
4.14 Molecular yield for varying PA time . . . . . 100
4.15 Simulated population dynamics for PA in an optical trap . . . . . 101
4.16 Splitting of the Rb $5s_{1/2}$ + Cs $6s_{1/2}$ atomic asymptote by the hyperfine interaction . . . . . 102

5.1 Calculated wavefunctions for free-to-bound photoassociation and bound-to-bound $(2)^3\Pi_{0^+}(v'{=}10) \rightarrow X^1\Sigma^+(v{=}0)$ spontaneous decay . . . . . 106
5.2 Relevant potential energies for deeply-bound PA near 11824 $cm^{-1}$ and REMPI spectroscopy of the $X^1\Sigma^+ \rightarrow (4)^1\Sigma^+$ transition . . . . . 108
5.3 Ion signal, simulated spectrum, and cross-correlation of transitions from the $X^1\Sigma^+(v{=}1)$ level to vibrational levels in the $(4)^1\Sigma^+$ state . . . . . 110

5.4 REMPI spectroscopy of the PA line at 11824 $cm^{-1}$ using the $X^1\Sigma^+ \rightarrow (2)^1\Pi$ transition . . . 112
5.5 Cross-correlation of the PA line at 11824 $cm^{-1}$ to the $X^1\Sigma^+(v=1)$ state . . 113
5.6 Ion signal and simulated spectrum from low-lying vibrational levels in the $X^1\Sigma^+$ state to vibrational levels in the $(2)^1\Pi$ state . . . 114
5.7 Calculated Franck-Condon factors and $X^1\Sigma^+(v=0)$ ion signals . . . 116
5.8 PA spectrum showing rotational structure of the $(2)^3\Pi_{0^+}(v'=10)$ level . . . 118
5.9 Relevant potential energy curves for RbCs for PA to the $(2)^3\Pi_{0^+}$ state . . . 119
5.10 REMPI scan of vibrational progression of the $X^1\Sigma^+(v_x) \rightarrow (2)^1\Pi$ $(v'_\Pi)$ transitions . . . 120
5.11 Onset of saturation in molecular production from the $(2)^3\Pi_{0^+}(v'=10)$ level 122
5.12 Saturation behavior of the $(2)^3\Pi_{0^-}$ state (single-pass) . . . 125
5.13 Saturation behavior of the $(2)^3\Pi_{0^-}$ state (retroreflected) . . . 126

6.1 Depletion of $X^1\Sigma^+(v=0)$ molecules . . . 130
6.2 Schematic of trap purification through atomic scrubbing . . . 132
6.3 Simulated molecular density evolution in the presence of inelastic scattering 135
6.4 Schematic representation of depletion temperature measurement . . . 140

A.1 MCP readout circuit . . . 142

C.1 $J=1/J=3$ signal ratio for different values of the $\Pi$ state amplitude, $b_\Pi$, in $\Omega'=0^-$ states . . . 149
C.2 Centrifugal barrier heights for $\ell$=1-3 partial waves in RbCs . . . 150

# List of Tables


1.1 Energy scales for two molecular states of interest in $^{85}$RbCs . . . . . 5

2.1 Table of control voltages and corresponding optical powers in the primary and secondary diffracted orders of the two-frequency AOM system. . . . . 32

3.1 Calculated partial wave contributions, $\tilde{W}(J', \ell)$, from all $M_{F(\mathrm{Rb})}, M_{F(\mathrm{Cs})}$ combinations to purely Hund's case (a) $^3\Pi_0(|\Lambda'|=1,\ S'=1)$ state, deeply-bound PA levels . . . . . 63

4.1 Summary of transition dipoles, Rabi frequencies, and expected powers for proposed STIRAP transfer . . . . . 76

4.2 Laser dyes and solvents . . . . . 80

4.3 Hyperfine energies of the $a^3\Sigma^+$ state . . . . . 89

4.4 Available quantum numbers and rotational energies for molecular states throughout the photoassociation, spontaneous decay, and depletion processes 91

5.1 Relative $X^1\Sigma^+(v_x)$ vibrational level populations, $p_{v_x}/p_{v_0}$, following spontaneous decay from the PA line at 11824 cm$^{-1}$, extracted from REMPI spectroscopy data. . . . . 112

5.2 Resonance frequencies for PA to different vibrational levels in the $(2)^3\Pi_{0^+}$ state . . . . . 117

5.3 Relative $X^1\Sigma^+(v_x)$ vibrational level populations, $p_{v_x}/p_{v_0}$, following spontaneous decay from $(2)^3\Pi_{0^+}(v'=10)$, extracted from REMPI spectroscopy data . . . . . 118

5.4 Calculated partial wave contributions, $\tilde{W}(J',\ell)$, from all $M_{F(\mathrm{Rb})}, M_{F(\mathrm{Cs})}$ combinations to purely Hund's case (a) $^3\Pi_0(|\Lambda'|=1,\ S'=1)$ state, deeply-bound PA levels . . . . . 128

C.1 Calculated partial wave contributions, $\tilde{W}(J',\ell)$, from all $M_{F(\mathrm{Rb})}, M_{F(\mathrm{Cs})}$ combinations to purely long-range PA levels correlated to the $6p_{1/2}$ and $6p_{3/2}$ atomic Cs asymptotes . . . . . 148

# Chapter 1

# Introduction

## 1.1 Ultracold Physics: Atoms and Molecules

The advent of atomic laser cooling nearly 30 years ago has heralded a sustained period of growth in physics that has culminated in no fewer than 3 Nobel Prizes [1, 2, 3, 4, 5]. The level of control over the quantum state, from the single-particle to many-body regime, has permitted detailed study of subfields as seemingly disparate as precision metrology [6], quantum information [7], trace element detection [8], and possible time variation of the fundamental physical constants [9]. This rapid development has been aided by the relative ease with which an ultracold atomic physics experiment can now be built, which has greatly lowered the barrier to entry into the field. In fact, the associated techniques have become robust enough to realistically permit study of Bose-Einstein condensates in the International Space Station using commercially available, standalone devices [10].

Although the generation of ultracold atoms has become routine, the simple level structure that is required for efficient atomic laser cooling also necessarily limits the species that can be studied. Extensions to numerous atoms beyond the alkalis that were first studied are now possible (including the alkaline-earths, many metastable noble gases as well as Cr, Dy, Er, Yb, and Tm), but the vast majority of species have yet to be cooled, due to their complex level structure. This becomes even more challenging when considering molecular

systems. Due to the additional degrees of freedom associated with rotation and vibration, molecules have a much richer internal energy structure than their constituent atoms. These added levels complicate the repeated cycle of light absorption and spontaneous emission that permits laser cooling. Nevertheless, the promise of novel physics available in ultracold molecular systems has stimulated very rapid progress over the past 10 years [11, 12]. Using the paradigm of the successes of ultracold atomic physics, groups across the world have tried to replicate the conditions of atomic systems in molecular experiments. With comparable densities and interactions times, polar molecular systems are predicted to push many of the frontiers explored in atomic systems as well as open entirely new fields of research that have no atomic analogues.

### 1.1.1 Dipolar Physics

Although homonuclear molecules have features that make them amenable to numerous studies, such as possible time variation in the proton-to-electron mass ratio [13], the full potential of ultracold molecular physics is in many ways captured best in heteronuclear polar molecules. The electric dipole moment in heteronuclear molecules gives rise to an entirely different mediating interaction between particles. The van der Waals force seen in atoms, although responsible for a host of physical phenomena, is much simpler than the electric dipole-dipole interaction that exists between polar molecules.[1] The governing molecular Hamiltonian is given in [11] by

$$V_{\mathrm{dd}} = \frac{\vec{d}_1 \cdot \vec{d}_2 - 3(\vec{d}_1 \cdot \hat{r})(\vec{d}_2 \cdot \hat{r})}{r^3} \tag{1.1}$$

where $\vec{d}_i$ is the dipole moment of the $i$th molecule, $\vec{r}$ is the vector between the molecules' centers-of-mass, and $\hat{r}$ is the unit vector of $\vec{r}$. This interaction is both anisotropic and long-range, compared to the isotropic and very short-range ($1/r^6$) van der Waals interac-

[1] There is an analogous magnetic dipole-dipole interaction between magnetic atoms, but the interatomic force is generally much weaker. Nevertheless, atomic dipolar effects have been observed in Bose-Einstein condensates of chromium [14] and dysprosium [15].

tion. When coupled with the tailored potentials made possible with optical lattices, this qualitatively different interaction is predicted in [16] to give rise to states with topological order. Such a system could be used as the basis of a molecule-based quantum computer, first proposed in a different form in [17].

### 1.1.2 Ultracold Chemical Reactions

Molecules are also amenable to study through their chemical reactions. These reactions can be understood as a type of inelastic scattering where the reactants, defined by their quantum numbers, constitute an entrance channel and the products, with generically different quantum numbers, make up the exit channel. Further, due to the ultracold temperatures possible in select systems, the scattering occurs over a very limited number of partial waves due to the centrifugal barrier, which quickly becomes larger than the thermal collision energy. The reaction process can then be tuned with the exquisite control made possible through modern experimental techniques. As discussed in [12], if this controlled chemistry can be coupled with state-selective detection of the products, such as Resonance-Enhanced Multiphoton Ionization, the resulting population distribution can potentially be studied in great detail.

## 1.2 Requirements for Making Ultracold Molecules

In order to study the physics associated with molecular systems, it is desirable to replicate as many of the experimental conditions associated with atomic systems as possible. In this context, there are three related aspects that are most important. First, the sample must be large and dense enough that interactions among the molecules are frequent and observable. Second, many experiments address quantum state-sensitive processes. Hence, the molecules generally must be limited to a very small subset of the available states. Third, the sample must be long-lived so as to allow for sophisticated experiments that typically take place on the order of seconds.

Roughly speaking, these requirements are most easily satisfied in very cold systems. First, molecules with very low thermal energy ($\sim$1 mK$\cdot k_B$) can be optically trapped. This confinement can give rise to large, dense samples if the trap is loaded from a suitable source. Second, many molecular energy scales are between ultracold and room-temperature thermal energies. Hence, thermal occupation at $T \leq 1$ mK naturally limits the available quantum states. Third, the molecular state that is most amenable to robust optical trapping is the absolute ground state, the level favored by thermal occupation at ultracold temperatures. Traditionally, the relevant figure of merit of ultracold systems is the phase space density, $\rho$, given in [18] by $\rho = n\lambda_{\mathrm{dB}}^3$, where $n$ is the density and $\lambda_{\mathrm{dB}}$ is the de Broglie wavelength. The de Broglie wavelength is given by $\lambda_{\mathrm{dB}} = h/\sqrt{3mk_BT}$, where $m$ is the mass, $k_B$ is Boltzmann's constant, $h$ is Planck's constant, and $T$ is the temperature. Hence, experiments of this type consistently strive for the densest samples and the lowest temperatures.

### 1.2.1 Trapping and Inelastic Scattering

Assuming ultracold molecular temperatures can be achieved, robust trapping becomes of primary importance. Molecules can be translationally very cold while still possessing a great deal of internal energy in the form of vibration and rotation. Although the associated splittings vary for different molecular species and states, the energy difference between adjacent vibrational or rotational levels is almost always much greater than the depth of any optical trap ($U_{\mathrm{trap}} \leq 1$ mK$=7\times10^{-4}$ cm$^{-1}$), as seen in Table 1.1. Hence, any inelastic (state-changing) collision that reduces the internal energy will liberate enough energy to quickly eject the molecule from the trap. In order to achieve long trapping lifetimes, it is therefore necessary to either create the molecules in or transfer them to their absolute ground state. In the ground state, the molecules can no longer convert internal energy into kinetic energy. This is shown schematically in Figure 1.1. Then, if the thermal translational energy is less than difference to the lowest excited state, all collisions will be purely elastic. In the absence of additional loss mechanisms, such as chemical reactions, the sample is collisionally stable.

| | $X^1\Sigma^+(v=0)$ | $a^3\Sigma^+(v=36)$ |
|---|---|---|
| Vibration | 50 | 1 |
| Rotation | 0.03 | 0.004 |

Table 1.1: Energy scales for two molecular states of interest in $^{85}$RbCs. Vibrational energy is the separation from the next vibrational level. Rotational energy is the splitting between the $J$=0 and $J$=1 levels. Energies come from values in [19]. All energies are in cm$^{-1}$. 1 mK=$7\times10^{-4}$ cm$^{-1}$

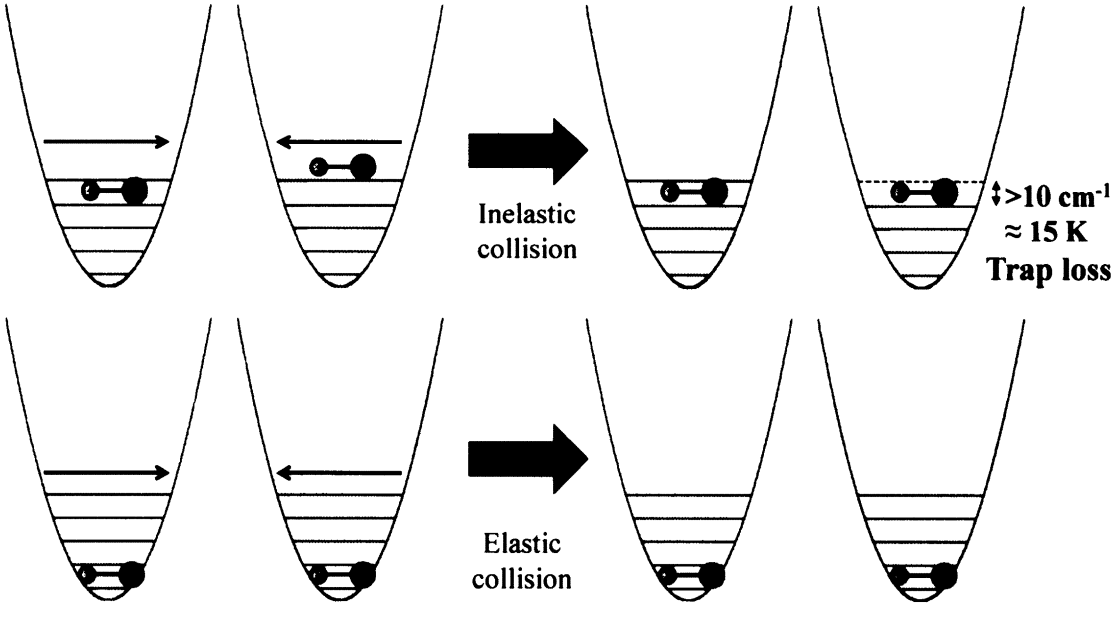


Figure 1.1: Schematic representation of scattering between vibrationally-excited molecules and ground state molecules. When vibrationally-excited molecules inelastically scatter, enough energy is liberated to eject both collision partners from an optical trap. Ground state molecules have no lower energy state to occupy, and, if ultracold in their translational motion, do not have sufficient energy to excite internal motions in the collision. Hence, their collisions are purely elastic, and the molecules remain in the trap following the collision.

#### Difficulties

Reaching the temperatures that have become routine in atomic systems is the fundamental challenge of ultracold molecular physics. The main techniques associated with molecular cooling can be broadly divided into two categories. First, there are direct methods that begin with a sample of molecules and subsequently cool that sample. Second, and of greatest importance to the work presented here, are indirect methods that create molecules out of pre-cooled atomic precursors. To date, the indirect and direct cooling methods have addressed very different physical regimes due to the different experimental conditions available to each.

### 1.2.2 Direct Cooling

Direct cooling processes are in some sense the most intuitive. Beginning with some sample of molecules, one only needs some mechanism that can cool them. These techniques generally benefit from the large molecular densities and numbers associated with macroscopic sources of the species under study. These larger numbers come, however, at the cost of higher ultimate temperatures, typically >1 mK. Many of the techniques of direct cooling are applicable to a large number of molecules, including biological compounds that are of great interest across many fields.

#### Buffer Gas Cooling

By placing a molecular vapor in contact with a reservoir gas, the molecular temperature can quickly be brought to that of the reservoir ($\approx$4 K for He) through thermalizing collisions. The clearest benefit of this scheme is the wide applicability to many different molecules. High brightness molecular beams based on this process have been pioneered in the Doyle group at Harvard [20, 21] and subsequently replicated elsewhere. These cryogenically-cooled beams have been used to study a wide variety of molecules and have probed phenomena such as Zeeman relaxation [22] and, very recently, to measure the electric dipole

moment of the electron [23].

#### Stark Deceleration

The Stark deceleration technique, although technically not cooling, has successfully created trapped samples of numerous molecular species. Through the repeated application of strong, spatially-inhomogeneous, time-dependent electric fields, a subset of the Maxwell-Boltzmann distribution of a molecular beam can be made to climb many potential hills due to the Stark effect [24]. This results in a significant reduction in the forward velocity for the chosen subset of the beam, which can subsequently loaded into a magnetic, electrostatic, or magnetoelectrostatic trap [25, 26, 27]. Recently, this scheme has been used in the first demonstration of evaporative molecular cooling, possibly leading to much higher phase space densities in the future [28].

#### Laser Cooling of Molecules

For many years, the direct laser cooling of molecules was thought to be impossible, due to the absence of closed optical cycling transitions. Recently, however, approximately closed transitions for experimentally feasible conditions have been demonstrated in cryogenic beams of SrF [29], YO [30], and CaF [31]. The very rapid progress achieved in these experiments appears to be leading up to molecular magneto-optical trapping in the very near future, but trapping of laser cooled molecules has yet to be demonstrated. Although this technique cannot be generalized to all molecules, it is predicted to be useful in cooling other species as well.

### 1.2.3 Indirect Cooling: Engineering Molecules from Pre-Cooled Atoms

The indirect molecular cooling methods take full advantage of the robust techniques of atomic laser cooling. Atomic temperatures of $\sim$100 $\mu$K and densities of $10^{11}$ cm$^{-3}$ are easily achieved using magneto-optical traps [32]. The phase density can be further increased by taking advantage of techniques, such as evaporative cooling, associated with Bose-Einstein

condensation. By creating molecules from these pre-cooled samples, the molecules inherit the ultracold translational temperature of the constituent atoms. Generally, this comes at the cost of an increase in the internal energy associated with the vibrational structure of the molecule. In order to prevent rapid trap loss due to inelastic scattering, the molecules must be transferred to or created in their absolute ground state. Further, the constituent atoms of the molecule must be amenable to laser cooling. This greatly limits the molecular species that can be studied, as only a relatively small subset of the elements can be efficiently laser-cooled.

### Feshbach Association

The most successful ultracold polar molecule experiment to date is based on the Feshbach association of $^{40}K^{87}Rb$ at the Joint Institute for Laboratory Astrophysics in Boulder [33]. Beginning with nearly degenerate samples of K and Rb, a magnetic field sweep brings the atomic scattering state through resonance with the highest-lying bound level of the $a^3\Sigma^+$ molecular state via the Zeeman effect. This process coherently transforms the atoms into molecules with very high efficiency. These so-called Feshbach molecules are exceedingly weakly-bound but are quickly transferred to their absolute ground state via a coherent two-photon Raman transition [34]. This scheme has since been used to study many molecular processes, such as dipolar chemical reactions and stereodynamics [35, 36]. The successes of this experiment have stimulated numerous groups to develop similar systems that use different bialkali molecules [37, 38, 39].

### Photoassociation

This thesis describes molecular production using a simpler process called photoassociation. By shining an intense laser on two overlapped magneto-optical traps, colliding atoms are resonantly excited to a bound molecular state [40]. These electronically-excited molecules quickly spontaneously decay to numerous rotational and vibrational levels of the electronic ground states. Through a judicious choice of the excited molecular bound state used to

create the molecules, one can, to some extent, control the ground state molecular levels that are populated. In this thesis, we examine two very different photoassociative regimes: one that creates weakly-bound molecules that need to be transferred to the absolute ground state and another where the molecules are created in deeply-bound states that directly decay to the ground state, obviating the need for state transfer.

### Why RbCs?

The $^{85}Rb^{133}Cs$ molecule studied here has two advantageous features for a photoassociation experiment. First, the constituent alkali atoms are very easy to laser cool. The necessary wavelengths ($\lambda_{Rb}$=780 nm, $\lambda_{Cs}$=852 nm) can be reached trivially with widely-available semiconductor diode lasers. Second, the chemical energetics of RbCs suggest that a pure ground state sample should be collisionally stable to two-body collisions [41]. The relevant chemical reactions are given by

$$\mathrm{RbCs} + \mathrm{RbCs} \rightarrow \mathrm{Rb_2} + \mathrm{Cs_2}\ (29\ \mathrm{cm^{-1}}) \tag{1.2}$$

$$\mathrm{RbCs} + \mathrm{Cs} \rightarrow \mathrm{Rb} + \mathrm{Cs_2}\ (187\ \mathrm{cm^{-1}}) \tag{1.3}$$

$$\mathrm{RbCs} + \mathrm{Rb} \rightarrow \mathrm{Rb_2} + \mathrm{Cs}\ (-157\ \mathrm{cm^{-1}}) \tag{1.4}$$

Because the RbCs + RbCs replacement reaction is endothermic at an energy orders of magnitude above the ultracold scale (<1 mK·$k_B$), this reaction does not proceed under our conditions. In KRb, the analogous reaction is exothermic (≈-9 $\mathrm{cm^{-1}}$) and barrierless, leading to rapid, destructive chemical reactions for a gas of molecules moving freely in three dimensions [41].[2] The collisional stability of RbCs, along with its relatively large electric dipole moment in the ground state of 1.3 D [42], has inspired other groups [37, 39] to study this molecule as well, albeit generally using the $^{87}Rb$ isotope.

RbCs molecules using either Rb isotope are predicted to be chemically non-reactive in

[2]Electric fields have been used to frustrate the barrierless, exothermic KRb + KRb → $K_2$ + $Rb_2$ chemical reaction by confining the molecules to a quasi-2D geometry and taking advantage of the purely repulsive nature of the dipole-dipole interaction in this geometry [36].

the ground state, but due to its favorable $s$-wave scattering length, $^{87}$Rb is more amenable to evaporative cooling than $^{85}$Rb [43]. Hence, lower temperatures and higher phase-space densities can be reached in $^{87}$Rb, which is especially important for experiments using Feshbach association. $^{85}$Rb, however, benefits from a greater natural isotopic abundance (~2.6:1) [44] as well as more detailed spectroscopy in the literature, especially in the context of photoassociation, as in [45].

## 1.3 Outline of Thesis

We begin with a brief discussion of the experimental techniques of atomic laser cooling and trapping that are used to create the requisite samples of ultracold precursor Rb and Cs atoms. Given the wide availability of numerous works devoted exclusively to this subject, we focus on the features of our setup that are most unique. Next, we describe the photoassociation process that turns these atoms into diatomic RbCs molecules. Additionally, we develop a formalism that bridges the divide between the atomic and molecular basis state wavefunctions. This affords a much deeper understanding of the quantum states populated through all stages of our experiments.

The remainder of the thesis is devoted to the experimental results and analysis of work done in two very different photoassociative regimes. Initially, we detail attempts to extend work done previously in this group on the creation of weakly-bound, highly vibrationally-excited molecules. We present high-resolution depletion spectroscopy of the $a^3\Sigma^+ \rightarrow c^3\Sigma^+$ transition for proposed Stimulated Raman Adiabatic Passage (STIRAP) transfer to the rovibronic $X^1\Sigma^+(v{=}J{=}0)$ ground state. Next, we demonstrate numerous pathways to the rovibronic ground state via photoassociation to deeply-bound molecular states. Through detailed theoretical analysis and subsequent experimental verification, we show continuous formation of $X^1\Sigma^+(v{=}0)$ RbCs molecules at rates in excess of $10^3$/s. The thesis then concludes with a discussion of future directions for this technique, including optical trapping and subsequent sample purification.

# Chapter 2

# Physics of Optical Cooling and Trapping

## 2.1 Introduction

In order to create large samples of ultracold molecules via photoassociation, we require large, dense samples of the atomic precursors. The atoms that are introduced into our chamber are initially at temperatures of several hundreds of Kelvin. Hence, we require some technique to remove large quantities of thermal energy from a sample of fast-moving, randomly-directed atoms. Fortunately, this particular problem has been very successfully addressed with the now very mature techniques of laser cooling and magneto-optical trapping. The creation of atomic samples with temperatures of hundreds of $\mu$K (or much less) has become routine, and detailed discussions of the associated theory can be found in textbooks, such as [18]. We present a brief discussion of the relevant mechanisms here, focusing especially on the constraints imposed on the states populated. Additionally, we present recent improvements to our system that is capable of trapping ultracold molecules as well as atoms. Throughout this discussion, we detail the relevant features of the experimental apparatus.

## 2.2 Atomic Cooling in Magneto-Optical Traps

The magneto-optical trap (MOT) has become the standard tool for generating samples of ultracold atoms [32]. Through the repeated velocity and spatially-dependent scattering of laser photons, atomic systems with very high entropy are organized into dense samples of slow-moving atoms. The fundamental physical mechanism that makes this possible is the optical cycling transition. In this process, an atom undergoes many ($\sim 10^7$/s) excitations and spontaneous decays from a carefully tuned and properly polarized laser.

### 2.2.1 Doppler Cooling

To see how this can be used to slow an atom, we consider the following quasi-1D process. An atom moving in a given direction absorbs a photon moving in the anti-parallel direction, as shown in Figure 2.1. By momentum conservation, the atom necessarily slows down by $\Delta v = \hbar k/m$ ($\approx$ 4 mm/s for Cs), where $k$ is the photon's wavevector and $m$ is the atomic mass. Very quickly ($\tau$ <100 ns), the atom spontaneously decays, emitting a photon in a random direction. Again, by momentum conservation, the atom recoils, but over many cycles, the effect of this process is to preferentially reduce the velocity in the initial direction while the net recoil averages to zero.

If we add a second laser that propagates anti-parallel to the first, we can slow atomic motion for both directions, provided we can guarantee that the atom absorbs photons from the correct beam for a given direction of motion. This is done by red-detuning the laser frequency relative to the atomic transition frequency at rest. Then the Doppler shift of the moving atom relative to laser propagation brings the atom into resonance with the correct beam until the atomic velocity is comparable to the recoil velocity from a single photon. We can then extend this to 3 dimensions by including two more pairs of counter-propagating beams that span $x$-$y$-$z$ space.

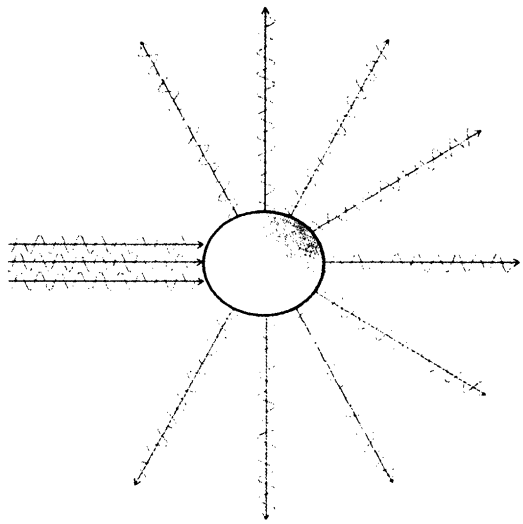

Figure 2.1: Doppler cooling of an atom. In this schematic, the atom, which is moving to the left, absorbs photons from a laser propagating to the right and emits photons isotropically. The net effect is to dramatically reduce the velocity in the leftward direction without a significant increase in any other direction.

### 2.2.2 Spatial Confinement

In order to achieve the necessary trapping of the atoms, we must also generate a spatial restoring force towards the center of our trap. With the inclusion of a magnetic field gradient from a pair of anti-Helmholtz coils, the Zeeman effect shifts atoms closer to resonance as they move farther from the center of the trap, resulting in an increased photon scattering rate and correspondingly increased restoring force. We guarantee that atoms absorb photons from the correct laser beam so as to be pushed into, rather than out of, the trap through a judicious choice of laser polarization.

### 2.2.3 Implementation in Alkali Atoms

As an example of the alkali atoms of interest here, the lowest energy levels of $^{85}$Rb are shown in Figure 2.2. Electric dipole selection rules dictate that spontaneous decay from the $|F' = 4, M'_F = 4\rangle$ state will always populate the $|F = 3, M_F = 3\rangle$ state. With the appropriate choice of laser polarization, the $|F = 3, M_F = 3\rangle \rightarrow |F' = 4, M'_F = 4\rangle$ transi-

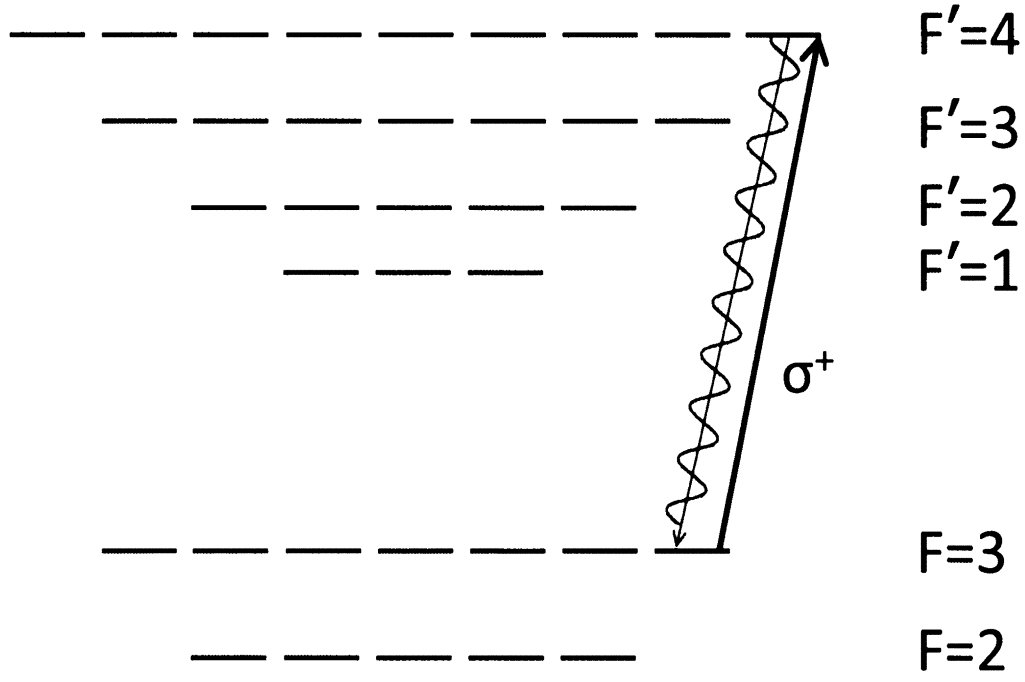


Figure 2.2: Cycling transition in $^{85}$Rb. Not shown are occasional off-resonant absorption events of the counter-propagating $\sigma^-$ beam that drive transitions to the $|F' = 3, M_F = 2, 3\rangle$ sublevels. The repumping laser (not shown) drives the $|F = 2\rangle \rightarrow |F' = 3\rangle$ transition.

tion then constitutes a closed, cycling transition. Imperfect polarization and off-resonant excitation sometimes excites a $|F = 3, M_F = 3\rangle \rightarrow |F'' = 3, M''_F = 2, 3\rangle$ transition. This state can decay to the $|F = 2\rangle$ manifold of states, which are no longer resonant with the cooling laser. To combat this, we include an additional repumping laser tuned to the $|F = 2\rangle \rightarrow |F' = 3\rangle$ transition that pumps atoms back into the cooling cycle. In the case of Cs, the $|F = 4, M_F = 4\rangle \rightarrow |F' = 5, M'_F = 5\rangle$ transition provides the closed cycle, and repumping drives $|F = 3\rangle \rightarrow |F' = 4\rangle$.

### 2.2.4 The Forced Dark SPOT MOT

Higher densities can be achieved in MOTs by shelving sufficiently cold atoms in the center of the trap in the lower hyperfine ground state, called the dark state here. In this dark state, the atoms are no longer constantly undergoing the optical cycling transition, reducing

a number of density-limiting mechanisms detailed in [18]. This technique was first used in a spontaneous optical force (SPOT) trap in Na in Ref. [46], where a small mask on the repumping beam imaged a hole in the center of the trap. This allowed the atoms to naturally decay to the dark state after several photon scatters from the trapping beam. In our implementation, we accelerate the accumulation in the dark state with the inclusion of a weak depumping beam that drives the non-cycling $|F = 3\rangle_{\mathrm{Rb}} \rightarrow |F' = 3\rangle_{\mathrm{Rb}}$ ($|F = 4\rangle_{\mathrm{Cs}} \rightarrow |F' = 4\rangle_{\mathrm{Cs}}$ ) transition in the masked hole of the repumping beam, as in [47]. These so-called forced dark SPOT traps routinely yield MOTs with peak densities, $n$, and atom numbers, $N$, in excess of $n$=$10^{11}$ cm$^{-3}$ and $N$=$10^{7}$.

From the nature of the dark SPOT MOT, the vast majority of atoms are in their lower hyperfine ground state ($F_{\mathrm{Rb}} = 3, F_{\mathrm{Cs}} = 4$). Due to the magnetic field gradient and the laser polarizations from the 3-D beams in the MOT, the atoms sample all available projections of their angular momentum, $M_F$. Later in this thesis, when we calculate photoassociation rates for different rotational levels, this will be an important consideration.

### 2.2.5 MOT Laser Systems

For the particular atoms used in this experiment, the MOT lasers can easily be generated using robust tunable semiconductor diode laser systems. We use a combination of commercial and homemade systems.

#### Extended Cavity Diode Lasers

Early work of this thesis was devoted to developing low-cost alternatives to commercially-available extended cavity diode laser (ECDL) systems for use in atomic physics experiments. By building laser systems from their component subsystems, the cost can easily be cut in half.

The first laser design we used was based on a Littman-Metcalf geometry [48] successfully implemented at the University of Colorado at Boulder/JILA [49]. Here, a small portion of the light output from the diode is diffracted, reflected, and fed back into the laser cavity.

The laser frequency can then be tuned by changing the length of the extended cavity using either a coarse turning screw or a fine piezoelectric transducer (PZT) attached to the reflecting mirror. This design is generally thought to afford a longer mode-hop free tuning range compared to the Littrow design. Further, because the diffraction grating is fixed in space, tuning the laser frequency does not translate the laser beam in space.

For the Littman-Metcalf lasers used here, we constructed sophisticated injection current and temperature controllers, also based on designs from UC Boulder/JILA. At the time of construction, commercially-available control electronics were not widely used due to uncertainty in performance. Over the course of this thesis, however, numerous companies developed laser diode control systems that satisfied our performance requirements and have subsequently been integrated into our system. Specifically, we use the Thorlabs LDC 240C and TED 350 units for injection current and temperature control.

An alternative design based on the Littrow laser geometry is also used in this experiment. Here, the laser frequency is tuned by tilting the diffraction grating relative to the laser diode. In order to compensate for the translation of the beam pointing during tuning, an additional mirror is attached to a plane parallel to the grating face, as in [50]. This cancels the motion to first order, which is generally sufficient for our purposes. The Littrow laser geometry has the additional benefit of slightly larger laser output power, compared to the Littman-Metcalf design. Electronics from Stanford Research Systems (Model LDC501) control both the current and temperature for the Littrow laser used here.

For the relatively modest laser intensities required for the repumping lasers, a single ECDL generally produces enough power. For the MOT trapping beams, however, power requirements are such that a single diode is generally not sufficient. To increase the output power, we use tapered amplifier (TA) systems that can produce single-mode laser powers up to 2 W for input powers of 10-20 mW.[1]

[1]TAs for 735 and 780 nm were purchased from Eagleyard Photonics. The Cs trapping laser uses an integrated 852 nm TA from Toptica Photonics (TA 100). An additional TA for 1020 nm was purchased from m2k-Laser.

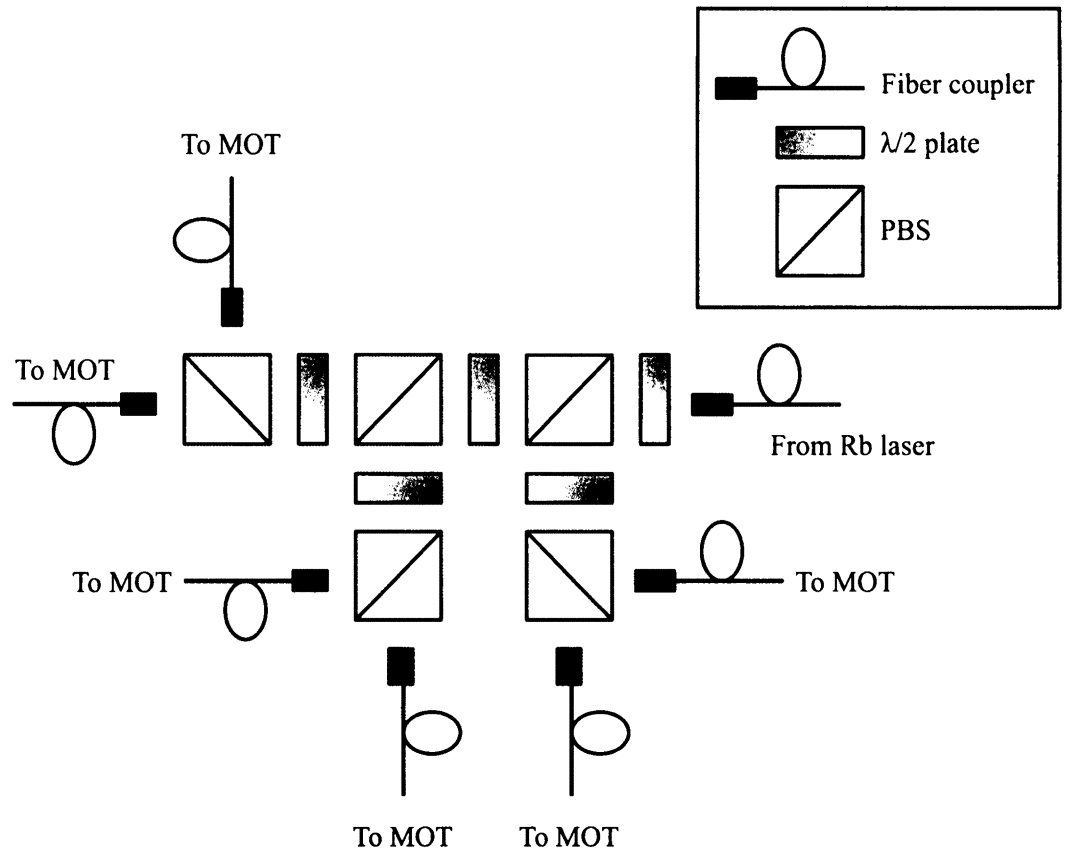


Figure 2.3: Schematic of beam-splitting optics for 6-beam Rb MOT. Shaded rectangles are zero-order half-wave plates that can be rotated to change the amount of light that is reflected and transmitted by the polarizing beamsplitter (PBS).

### 6-Beam Rb MOT

To generate the 6 trapping beams for the Rb MOT, we proceed as follows. From a single polarization-maintaining optical fiber, the beam is split into six components using the half-wave plates and polarizing beam splitters shown in Figure 2.3. The power balance, and corresponding restoring forces, of the counter-propagating beam pairs can then be adjusted trivially by rotating the appropriate wave plate. The atomic sample can then be moved in space. This greatly simplifies the procedure of overlapping the two MOTs, which historically has been one of the most time-consuming tasks in this experiment.

Following the division into six parts, each beam is coupled into its own polarization-maintaining fiber to be sent to the experimental chamber. The fiber output is then ex-

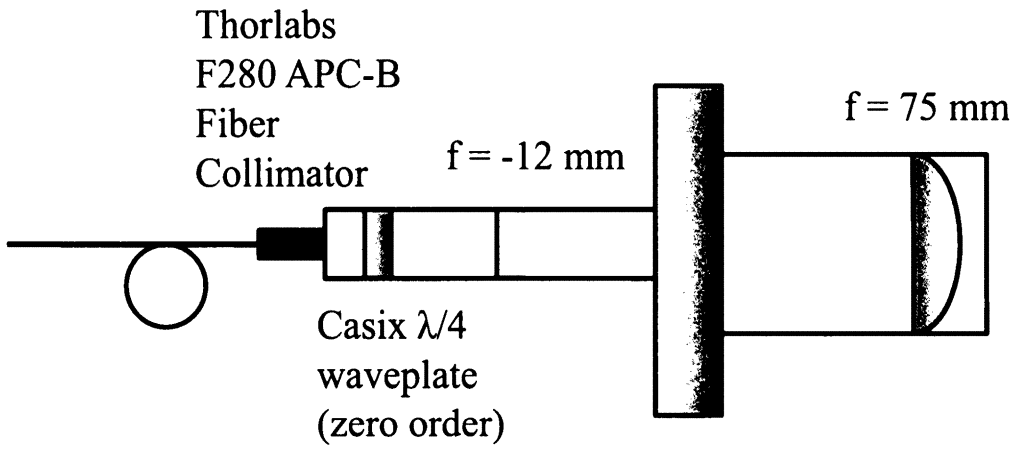


Figure 2.4: Schematic of beam-expanding optics for 6-beam Rb MOT. The shaded rectangle between the telescope lenses is an aluminum piece that mates 1" and 2" lens tubes. This piece was also designed to fit in 2" kinematic mirror mounts.

panded and properly polarized using the design shown in Figure 2.4. The location and pointing of each beam can then be adjusted independently via a kinematic mirror mount. The Cs MOT setup uses the same 3-beam geometry used in [51].

### 2.2.6 MOT Diagnostics, Improvements

To determine the location, size, density, and atom numbers in our MOTs, we rely on atomic absorption imaging. This is another technique that takes advantage of optical cycling transitions. A weak beam of resonant light ($P < 300$ $\mu$W) is shone through the atomic clouds and imaged onto a CCD camera. The absorption and subsequent scattering of photons by the atoms casts a shadow on the image. From the absorption depth, the size, atom number, and density of the clouds can be calculated. This technique is incredibly powerful and serves as the primary readout signal for the majority of ultracold atomic physics experiments.

We have benefited greatly from the sophisticated software developed to analyze absorption images in real-time. We have used a particular program from the atomic physics groups

at the Institute for Quantum Optics and Quantum Information in Innsbruck, Austria [52]. This has been fully integrated into the main timing software, based on the open-source Cicero Word Generator software [53]. These programs allow for measurements of MOT parameters in real time, greatly reducing the amount of time required to optimize and characterize the atomic samples. A screenshot from the absorption imaging program is shown in Figure 2.5.

In a typical absorption imaging measurement, the MOT is loaded for 3-5 s until the steady-state density is achieved. Then, the MOT lasers are blocked and the magnetic field is switched off, allowing the atomic cloud to expand ballistically due to its thermal energy and to fall under the influence of gravity. After a variable free expansion time on the order of 1-20 ms, the repumping and and fill-in[2] beams are turned on and unblocked for 100 $\mu$s to pump all of the atoms into the upper hyperfine state. Next, the resonant imaging beam is switched on while the repumping and fill-in beams remain on. During this imaging pulse, which lasts 149 $\mu$s, the atoms absorb the imaging beam and cast a shadow on the CCD camera, which is recorded by a LabView program. 140 ms later, after the atoms have completely fallen out of the detection region, the imaging, repumping, and fill-in beams are pulsed on as before to measure the background signal in the absence of atoms.

The imaging analysis software normalizes the signal in the presence of atoms by the background signal to generate the 2D atomic absorption signal. The vertical and horizontal dimensions are then fit to Gaussian curves. The transmitted intensity, $I$, at resonance can then be related to the atomic density, as in [54], by

$$\frac{I}{I_0} = e^{-\tilde{n}\sigma_0} \tag{2.1}$$

where $I_0$ is the unattenuated laser intensity, $\sigma_0$ is the known absorption cross-section, and $\tilde{n}$ is the column density, given by the density integrated over the propagation length through the atom cloud. This expression can then be inverted to yield the peak density, $n$, and

[2]The fill-in beam is tuned to the repumping transition and fills in the dark volume of the dark SPOT MOT.

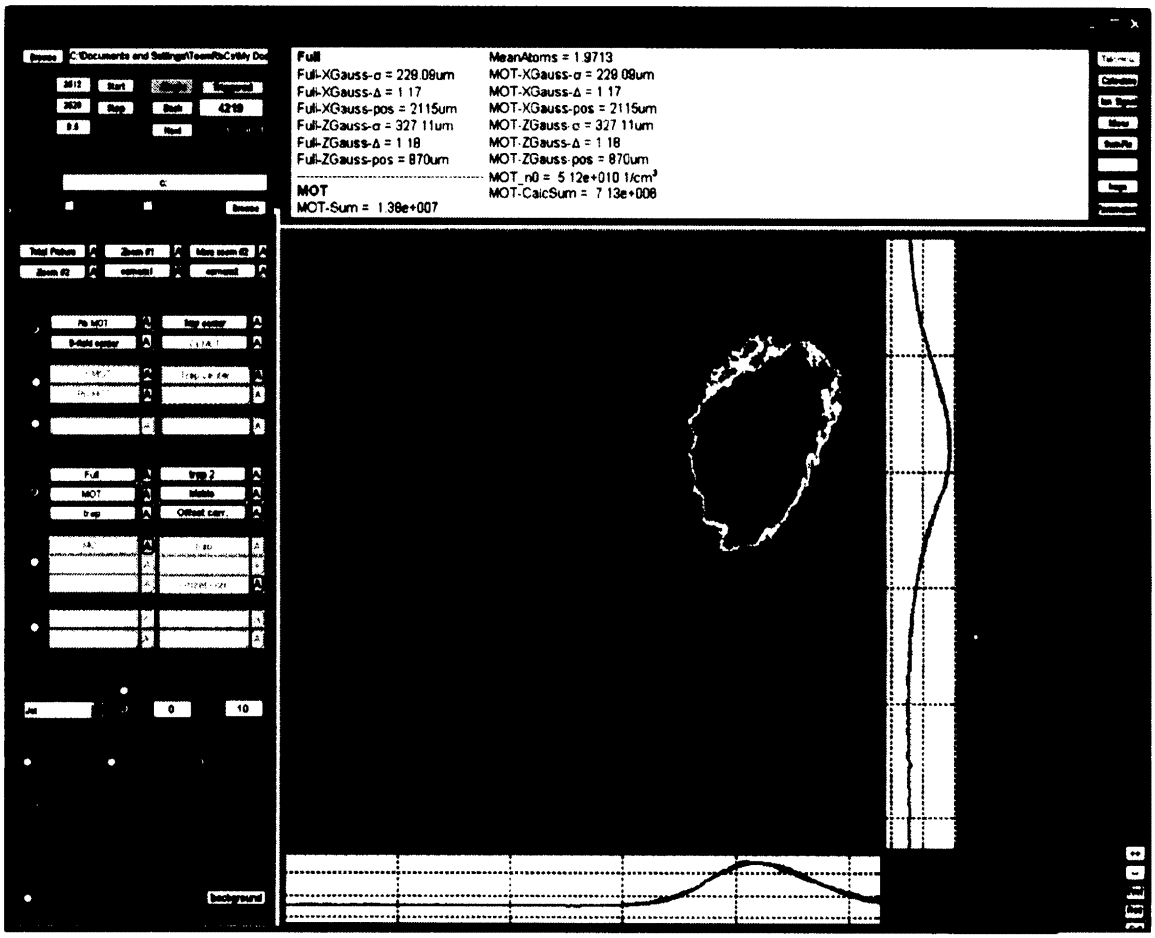


Figure 2.5: Screenshot of absorption imaging program. The integrated program from Innsbruck gives relevant MOT characteristics (size, density, location) in real-time. Images of the absorption beam are taken in both the presence and absence of the atoms to normalize the signal.

atom number, $N$. Further, the temperature of the sample can be determined by measuring the cloud density for different free expansion times. For expansion times longer than the inverse MOT trap frequency, the time-dependent density profile for thermal clouds is given in [54] by

$$n_{tof}(r,t) \propto \exp\left(\frac{-mr^2}{2t^2}/k_B T\right) \tag{2.2}$$

where $m$ is the atomic mass, $r$ is the distance from the cloud's center, $k_B$ is Boltzmann's constant, $t$ is the expansion time, and $T$ is the temperature. All of the relevant calculations for the desired MOT parameters are done automatically by the imaging analysis software.

### 2.2.7 Experimental Chamber

The experiment takes place in an stainless steel, ultra-high vacuum (UHV) chamber (Kimball Physics Expanded Spherical Octagon) equipped with Conflat viewports and electrical feedthroughs. In order to achieve the necessary low pressures ($\sim 10^{-10}$ Torr), we take great care to keep the interior of the chamber free of outgassing materials and contaminants. This was done by confining ourselves to vacuum-safe materials, such as stainless steel, oxygen-free high conductivity copper, and Macor. Remaining unique pieces, such as the ion detectors, are specifically designed to operate at very low pressure. The chamber is also continuously pumped by an ion pump and is equipped with a titanium sublimation pump to further reduce the pressure.

#### Atomic Sources

We controllably introduce alkali vapor into chamber through the use of heated getters from SAES and Alvatec.[3] Running an electrical current of 4-6 A through a chromate salt of Rb or Cs (SAES) or a suitable alloy, such as $Bi_2Cs$ (Alvatec), releases neutral atoms (as well as other species) towards the center of our chamber. The trapping beams are able to cool and trap a small fraction of the resulting Boltzmann distribution of atoms to load the MOTs.

The getters have multiple advantages and disadvantages compared to other MOT loading schemes. First, they are very easy to mount into the chamber and operate. Zeeman slowers and 2D-MOTs require additional lasers in order to pre-cool atoms while coldfingers attached to macroscopic ampules often require cooling systems to control the alkali vapor density. Getters only require electrical vacuum chamber feedthroughs and controllable current supplies. Second, the available alkali vapor pressure can be adjusted by changing the current through the getters. Thermal vapors typically take many hours to equilibrate

[3] At the very beginning of this generation of the experiment, the MOTs were loaded from thermal background vapor from macroscopic ampules of alkali. The resulting background atomic vapor density was much too high to permit efficient optical trapping and also destroyed a pair of ZnSe optical viewports used for 10.6 $\mu$m light.

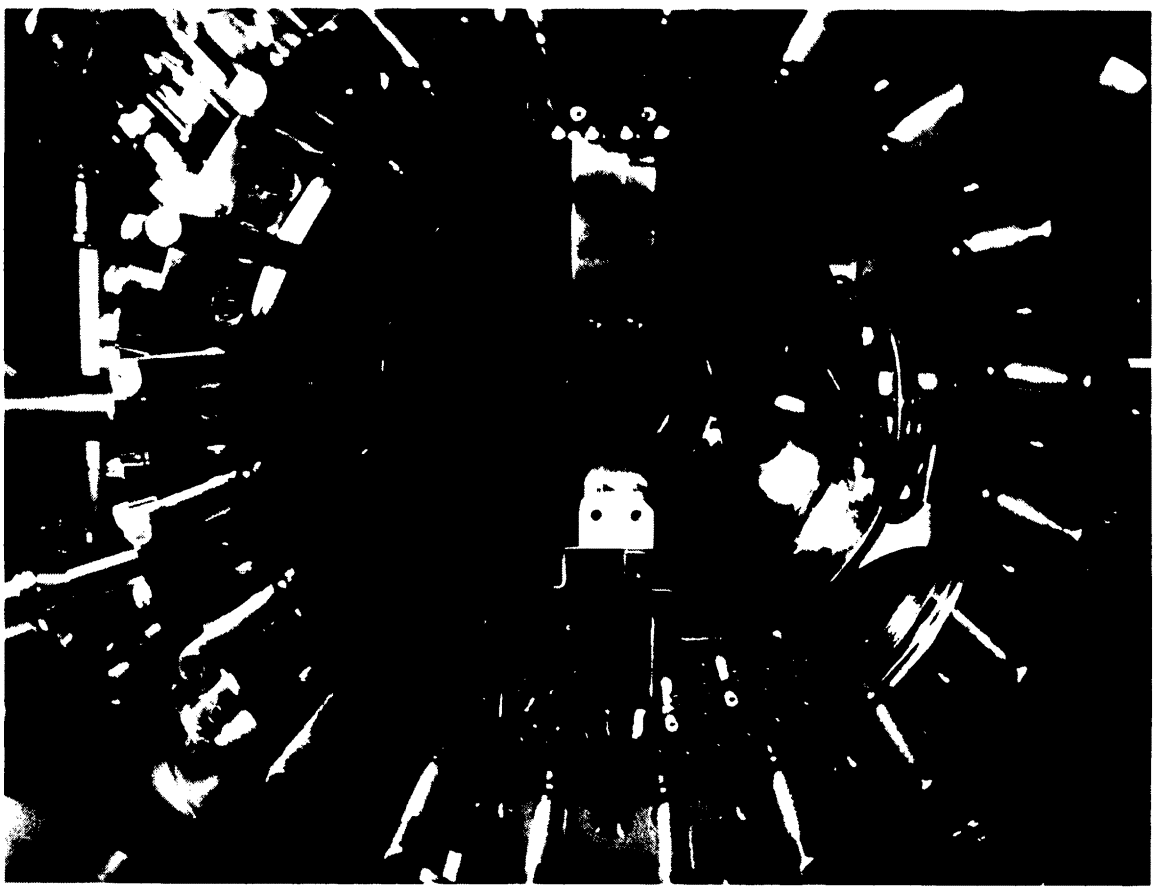

Figure 2.6: Experimental chamber. The chamber itself is a stainless steel, expanded spherical octagon from Kimball Physics. Beryllium-copper barrel connectors hold the atomic getter sources that are controlled via electric feedthroughs. To the right is a microchannel plate ion detector that also serves as an opposing electrode for time-of-flight detection. To the left is the monolithic Channeltron detector that was used for most of the work here. High-voltage electrodes extend from above and below but were not used here. MOT trapping lasers propagate along the diagonals as well as into and out of the page.

following changes in the coldfinger temperature.

The greatest weakness of the getter based system is the finite supply of alkali vapor. The getters eventually deplete over the course of the experiment and must be replaced. This requires breaking vacuum and subsequent rebaking of the chamber, which takes the experiment offline for several weeks. Further, for the longer term goals of this experiment, the background pressure caused by the getters will likely be too large to permit long optical trapping lifetimes. Design and construction of a Zeeman slower system for Rb and Cs that will greatly reduce the vacuum pressure is already well underway.

### Magnetic Field Coils

We generate the necessary magnetic field gradient with a pair of self-built anti-Helmholtz coils. Two large aluminum bobbins ($d > 8$") hold two parallel sets of 25 windings of copper wire each, shown in Figure 2.7. The wire is coated with Kapton prevent shorting between windings and to the bobbin. Additionally, this wire (0.032×0.365 HAPT-200C MWS Wire Industries) has a large aspect ratio to allow for many windings with relatively low resistance. To remove the dissipated heat, we machined a narrow channel into each bobbin into which we tightly fit copper refrigerator tubing covered in Arctic Silver thermal contacting compound. Water continuously runs through the tubing, resulting in coils that are only slightly warm to the touch at full power (~37 A, ~9 V). During the coil winding procedure, potting epoxy was used to ensure good thermal contact of all the windings to the aluminum bobbin. Lastly, the aluminum bobbins were cut to frustrate eddy currents and subsequent unintended magnetic fields after the magnetic field gradient for the MOTs was quickly switched off. Based on the geometry of the chamber and coils, we calculate that we can create a magnetic field gradient of ≈10 G/cm [55].

Figure 2.7: Magnetic field coils used to generate field gradient necessary for MOTs. The flat ribbon wire allows for dense packing of coil windings with relatively low electrical resistance. The bobbin is mounted directly onto the 8" Conflat viewport of the chamber.

## 2.3 Trapping in a Conservative Dipole Trap

Although MOTs are integral to our experiment, these atomic workhorses have not yet been fully extended to molecular systems. Due to the numerous additional degrees of freedom in molecules, such as vibration and rotation, optical cycling transitions are generally unavailable, as molecules quickly decay to non-resonant levels that are no longer addressed by the trapping lasers.[4] Hence, in order to optically trap molecules, we require a technique that does not involve the scattering of photons.

Even before the development of laser cooling, groups began developing optical traps that rely on the dipole force exerted by a laser's electric field on polarizable particles, such as latex beads [56]. Later, this scheme was extended to address laser cooled atoms [57]. This trapping mechanism can be understood in a number of functionally equivalent ways. For a largely classical treatment based on treating the atom as an oscillating dipole, we

[4]Recent results in select molecules have demonstrated optical cycling and cooling of molecular beams, but robust trapping using this technique has not yet been achieved [29].

recommend Ref. [58], which we follow closely here. Here we use a semi-classical treatment based on time-dependent perturbation theory. We treat the atom as a quantum system interacting with a classical electric field. As we will show, a focused laser beam creates a spatially-dependent Stark shift that generates a conservative restoring potential that can be used to confine atoms as well as molecules.

### 2.3.1 Dipole Force Calculation

We begin with the perturbative result for the dipole potential of a two-level quantum system subject to an oscillating electric field of the form $\vec{\mathcal{E}} = \mathcal{E}_0 \sin(\omega t)\hat{z}$ from [58]

$$U_{dip} = -\frac{3\pi c^2}{2\omega_0^3}\left(\frac{\Gamma}{\omega_0 - \omega} + \frac{\Gamma}{\omega_0 + \omega}\right) I(\mathbf{r}) \tag{2.3}$$

where $c$ is the speed of light, $\omega_0$ is the unperturbed transition frequency, $\omega$ is the oscillation frequency of the electric field, $\Gamma$ is the natural linewidth of the transition, and $I(\mathbf{r})$ is the spatially-dependent intensity of the laser.

In the limit where the detuning from resonance ($\Delta = \omega_0 - \omega$) is much smaller than the driving and resonant frequencies, the second term in the parentheses is ignored in the rotating-wave approximation, and we find

$$U_{dip} = -\frac{3\pi c^2}{2\omega_0^3}\left(\frac{\Gamma}{\Delta} I(\mathbf{r})\right) \tag{2.4}$$

From an analogous calculation of the photon scattering rate, [58] shows that $\Gamma_{sc} \sim I/\Delta^2$. Hence, for a given desired potential, one can reduce the scattering rate by increasing the detuning and intensity. To this end, we employ a very far-detuned, very high power $CO_2$ laser so as to minimize the photon scattering rate, as demonstrated in [59].

The particular trapping laser that we use operates at 10.6 $\mu$m and is so far-detuned that the rotating-wave approximation breaks down. In this so-called quasi-electrostatic trap limit, where the rotating and counter-rotating components of the laser field contribute

to the potential at comparable levels, the calculation is slightly more subtle. Returning to the perturbative dipole potential, we have

$$U_{dip} = -\frac{3\pi c^2 \Gamma}{2\omega_0^4}\left(\frac{1}{1-\frac{\omega}{\omega_0}} + \frac{1}{1+\frac{\omega}{\omega_0}}\right) I(\mathbf{r}) \tag{2.5}$$

Taylor expanding the two denominators yields

$$U_{dip} \simeq -\frac{3\pi c^2 \Gamma}{2\omega_0^4}\left(1 + \frac{\omega}{\omega_0} + 1 - \frac{\omega}{\omega_0}\right) I(\mathbf{r}) = -\frac{3\pi c^2 \Gamma}{\omega_0^4} I(\mathbf{r}) \tag{2.6}$$

The next task is to examine the spatial dependence of the laser beam from which we can derive the oscillation frequencies about the potential minimum. We begin with the expression for the intensity distribution of a Gaussian beam of power $P$ focused by a spherical lens at $z = 0$

$$I(r,z) = \frac{2P}{\pi w^2(z)} \exp\left(\frac{-2r^2}{w^2(z)}\right) \tag{2.7}$$

where $w$ is the radial extent of the laser. The relation between the radial and axial extents of the focused beam are given by

$$w(z) = w_0 \sqrt{1 + \left(\frac{z}{z_R}\right)^2} \tag{2.8}$$

where $w_0$ is the beam waist and the Rayleigh range, $z_R$, is given by $z_R = \pi w_0^2/\lambda$. Taylor expanding the coordinates under the assumption that the axial and radial extents of the atoms are much smaller than the Rayleigh range and beam waist, respectively, we have

$$I(r,z) \simeq \frac{2P}{\pi w^2(z)}\left(1-\frac{2r^2}{w^2(z)}\right) \tag{2.9}$$

$$\simeq \frac{2P}{\pi w_0^2}\left(1+\left(\frac{z}{z_R}\right)^2\right)\left(1-\frac{2r^2}{w_0^2(1+(\frac{z}{z_R})^2)}\right) \tag{2.10}$$

$$\simeq \frac{2P}{\pi w_0^2}\left(1-\left(\frac{z}{z_R}\right)^2\right)\left(1-\frac{2r^2(1-(\frac{z}{z_R})^2)}{w_0^2}\right) \tag{2.11}$$

$$\simeq \frac{2P}{\pi w_0^2}\left(1-2\left(\frac{r}{w_0}\right)^2-\left(\frac{z}{z_R}\right)^2\right) \tag{2.12}$$

To further compensate against gravity, we retroreflect the beam to create a vertical standing wave trap, which alters the $I(\mathbf{r})$ term. The relevant changes are that the electric field is doubled due to the retroreflection, which quadruples the intensity, and that the intensity is now modulated as $\cos^2(kz)$ where $k$ is the wavevector associated with the laser wavelength. Putting all of this together yields

$$U_{OL} = U_0\cos^2(kz)\left(1-2\left(\frac{r}{w_0}\right)^2-\left(\frac{z}{z_R}\right)^2\right) \tag{2.13}$$

where $U_0$ is the trapping potential at $z$=$r$=0. Taylor expanding the $\cos^2(kz)$ term and retaining terms that are only quadratic in any coordinate, we have for small $r$ and $z$,

$$U_{OL} = U_0\left(1-2\left(\frac{r}{w_0}\right)^2-(kz)^2\right) \tag{2.14}$$

For our particular geometry, we expect trap depths on the order of $U_0 \approx k_B{\cdot}200$ $\mu$K with $w_0 \approx 200$ $\mu$m. Using the crude parametrization of [58], we find that the axial restoring force, $F_z \sim U_0 k \sim k_B{\cdot}120$ mK/mm, is much greater than the gravitational force, $mg = k_B \cdot 260$ $\mu$K/mm for RbCs, as desired.

### 2.3.2 Laser Astigmatism

In this derivation, we have assumed that the beam is initially a well-collimated, symmetric Gaussian beam. The beam coming from the $CO_2$ laser (Coherent GEM Select 100) is,

however, significantly astigmatic with respect to its vertical and horizontal axes. As a result, if the beam propagates through a spherical lens, the focal points of the vertical and horizontal axes occur at different locations, potentially massively reducing the optical trap depth.

To correct this astigmatism, we send the 100 W $CO_2$ laser beam through two independent, cylindrical Galilean telescopes.[5] The telescopes are designed to collimate the orthogonal axes of the laser independently. With the proper focal lengths, one could also try to match the beam waists in the vertical and horizontal directions. Unfortunately, cylindrical lenses for $CO_2$ lasers are very difficult to purchase, due to very low customer demand.[6] Hence, we collimated the axes as well as possible and accepted a non-circular beam. The oval shape mostly only changes the shape of the trapping volume without significant reduction of the trap depth. In order to more accurately characterize the beam parameters and minimize the astigmatism, we developed a novel $CO_2$ laser beam imaging system.

### 2.3.3 $CO_2$ Beam Imaging

Characterizing the $CO_2$ beam is fairly difficult, given the high optical power. In the earlier generation of this experiment, two razor blades were mounted in front of a 10 W optical power meter to measure slices of the two-dimensional power distribution [60]. This entire assembly was mounted to a manual translation stage to sample the entire beam. This technique was done at full laser power, so small slices of the beam spot ($\sim$30 mm$\times$1 mm) routinely contained more than 10 W of power. The data was then fit to determine the beam waist in each dimension. This technique is slow, labor-intensive, and relatively dangerous. Given the importance of understanding the beam size and divergence of the beam for the purposes of laser trapping, we developed a more robust method. In particular, by rastering a small detector over the entire beam spot, we are able to extract high-resolution

[5] We use Galilean, rather than Keplerian, telescopes to avoid focusing the very high power laser outside of the vacuum chamber.

[6] We have used II-VI and Design Research Optics almost exclusively for our $CO_2$ optics.

2D information of the beam profile. We can gain further information on the vertical and horizontal divergences of the beam by installing a flip mirror that changes the effective propagation distance of the laser before reaching the detector.

#### Pyroelectric Detector

The far-infrared detector is a Boston Electronics/VIGO pyroelectric detector (VIGO PVM-10.6 detector, VIGO VPDC-5H pre-amplifier). The high optical power associated with the $CO_2$ laser would instantly destroy the detector if it were exposed to full power. To overcome this problem, we installed a 99.5/0.5% beamsplitter (Design Research Optics) and sampled the much weaker portion of the beam. The remaining power was directed to an absorptive beam dump.

#### Two-Dimensional Translation Stage

The active area of the pyroelectric detector ($\sim$1 mm$^2$) is only a small fraction of the entire beam size, so in order to measure the entire beam, it is necessary to mount the detector on a movable stage. Two perpendicular translation stages attached to stepper motors (Zaber T-NA08A25) provide the necessary sampling range ($\sim$1 in$^2$). A LabView program rasters the translation stages over the beam spot while recording the intensity at each location. From this 2D intensity profile, we can fit vertical and horizontal Gaussian waists to the result. This is done automatically by the LabView program, which has greatly simplified the waist measurement process. For the highest-resolution scans, as in Figure 2.8, rastering over the beam spot takes $\sim$30 minutes.

### 2.3.4 Two-Frequency Acousto-Optical Modulator Driver

When using an optical trap, it is very useful to be able to switch the system on and off in a fast and controlled manner with digital control. Direct switching of our Coherent GEM Select 100 laser is not possible, but by passing the laser through an acousto-optical modulator (IntraAction AGM-406B1), one can instead switch the RF power applied to the

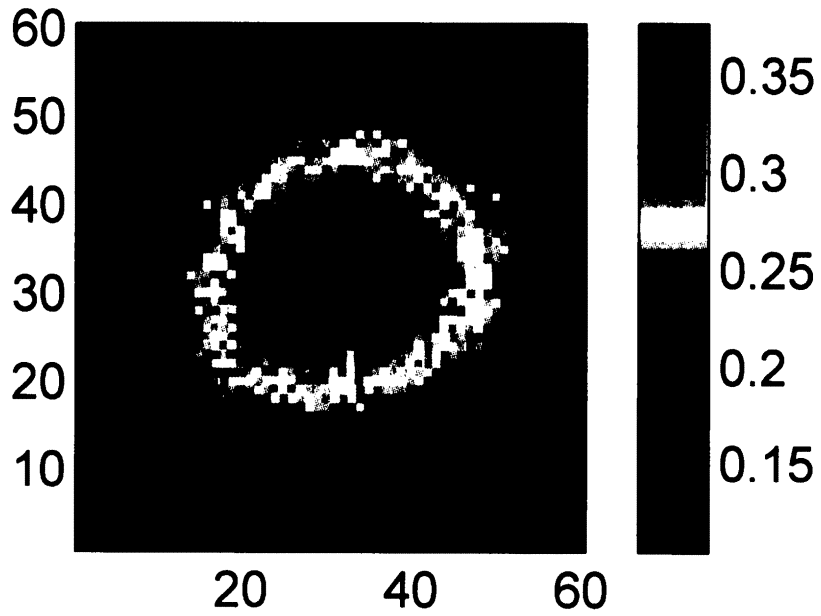


Figure 2.8: High resolution $CO_2$ laser beam profile. Axes refer to step number. This beam spot corresponds $1/e^2$ power beam radius of $\sim$5 mm.

AOM to create an optical switch. This process is complicated by the high powers associated with the $CO_2$ laser. Specifically, 40 W of RF power are required to efficiently diffract the $CO_2$ beam, and switching this large power load results in significant temperature fluctuation within the AOM crystal. This leads to pointing errors that sweep the position of the high power laser beam over several millimeters of travel.

Ref. [61] describes an AOM driver system that utilizes two separate modulation frequencies. As the RF power at one frequency is ramped down, lowering the optical power in the diffracted order at that frequency, the RF power at the other modulation frequency is increased to keep the total RF power in the AOM crystal constant. Under this constant RF power, pointing errors due to temperature fluctuations are greatly reduced.

### Design and Construction

The design for our two-frequency driver is two independent voltage controlled oscillators (VCO) whose powers can be controlled by analog voltages sent from our computer. These

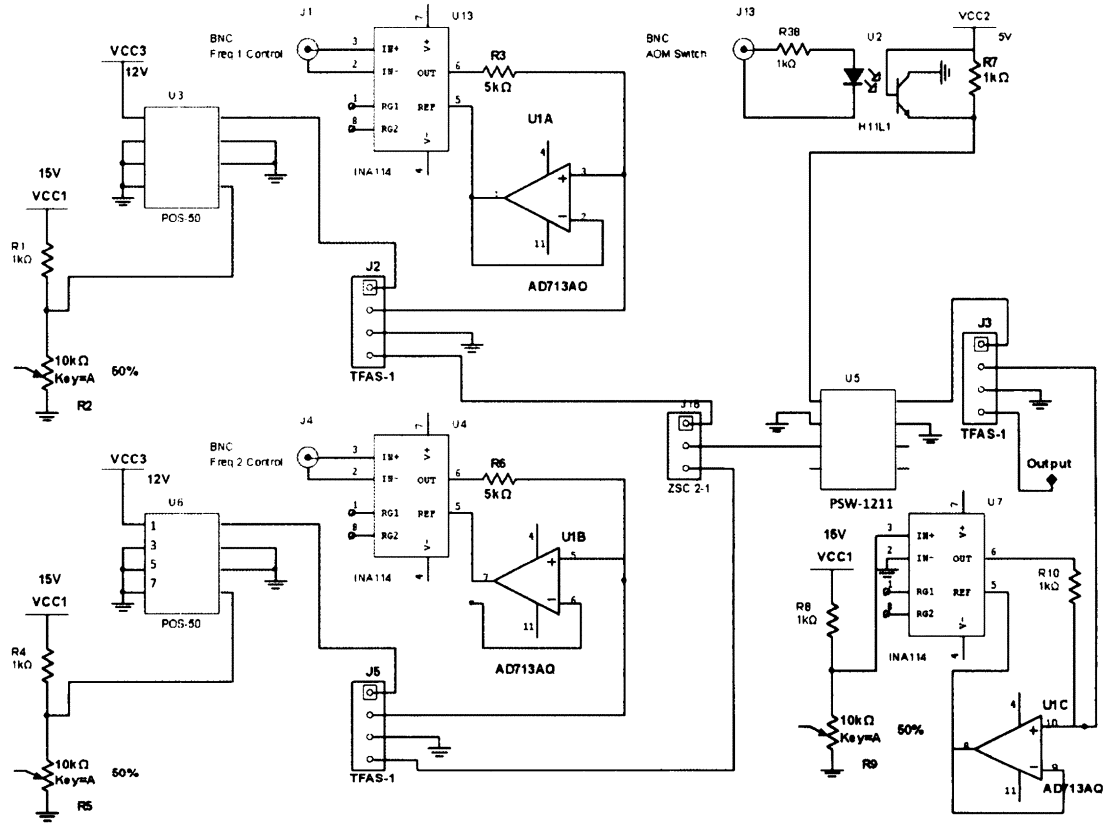


Figure 2.9: Circuit diagram for the two-frequency AOM driver. Two independent voltage-controlled oscillators are combined to give a two-frequency signal that is amplified and sent to the AOM.

two RF signals are then combined, and the two-frequency sum can be switched by a TTL pulse from the control computer. The circuit is shown in Figure 2.9. This signal is then sent to the high-power amplifier found inside a commercial AOM driver (IntraAction GE AOM Driver).

Characterization of the high-power amplifier was done by dumping the ~40 W output into a high-power 40 dB RF attenuator (RF-Lambda) and measuring the output with a spectrum analyzer. We also measured the bandwidth of the AOM by measuring the reflected power as a function of driving frequency with a directional coupler. With this information, we were able to find driving frequencies that are spaced enough to provide adequate separation of the primary and compensating beams and that do not reflect large amounts of power.

| 30 MHz VCO Voltage (V) | 30 MHz Power (dBm) | 45 MHz VCO Voltage (V) | 45 MHz Power (dBm) | $CO_2$ Laser Power (W) |
|---|---|---|---|---|
| 2.2 | -1.92 | 0.2 | -14.83 | 62.1 |
| 2.0 | -3.00 | 0.58 | -7.50 | 54.7 |
| 1.8 | -3.87 | 0.77 | -5.70 | 48.1 |
| 1.6 | -4.75 | 0.9 | -4.68 | 41.9 |
| 1.4 | -5.66 | 1.0 | -3.91 | 35.1 |
| 1.2 | -6.68 | 1.07 | -3.37 | 28.3 |
| 1.0 | -7.95 | 1.15 | -2.87 | 21.1 |
| 0.8 | -9.54 | 1.20 | -2.49 | 15.4 |
| 0.6 | -11.49 | 1.235 | -2.17 | 10 |
| 0.4 | -14.39 | 1.26 | -1.94 | 5.16 |
| 0.2 | -19.35 | 1.264 | -1.77 | 1.64 |

Table 2.1: Table of control voltages and corresponding optical powers in the primary and secondary diffracted orders of the two-frequency AOM system.

Although we expect that the high-power amplifier is at least approximately linear for driving frequencies within its bandwidth, we have no reason to assume that the amplifier gain is constant over this band. Thus providing constant power to the AOM is not as simple as providing a constant sum of control voltages to the two voltage controlled oscillators. Instead we generated an empirical table of constant RF driving power for a variety of primary driving frequency powers. This method assumes that the high-power RF attenuator yields constant attenuation over the relevant frequencies, but this assumption should be valid.

### Performance

When changing the amount of RF power supplied at the primary driving frequency, we expect that the optical power in that diffracted order will change accordingly while the optical power in the compensating beam changes inversely. For our chosen driving frequencies we found the expected behavior in the primary beam, but the optical power in the compensating beam never went above 10 W. This was attributed to the failure of

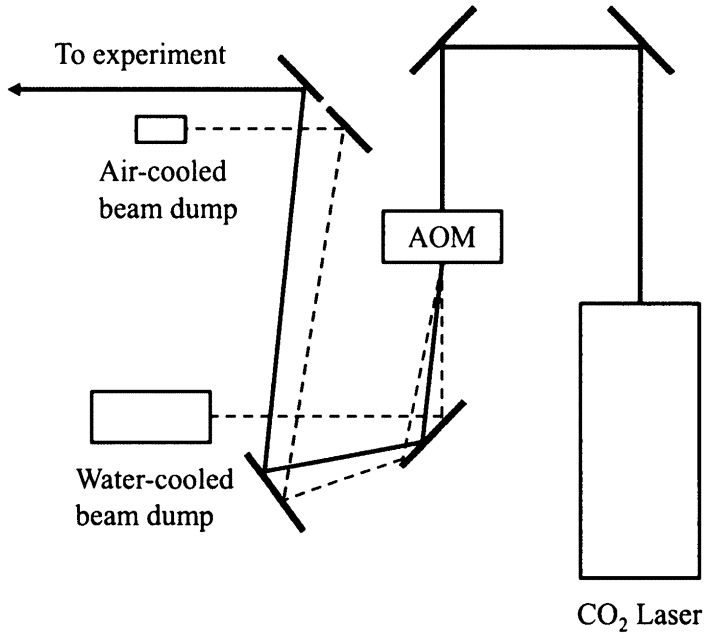


Figure 2.10: Beam paths for the strongest diffracted orders of the two-frequency $CO_2$ laser AOM system. The undiffracted light from the AOM as well as the diffracted order from the compensating RF frequency are directed to absorptive beam dumps.

the AOM system to satisfy the Bragg condition for both of the driving frequencies. As a result, the optical power that we expected to go into the compensating beam went into the undiffracted (zeroth order) beam. This beam is already sent into an absorptive dump. Hence, additional optical power presents no problem. The relevant beam paths are shown in Figure 2.10.

### 2.3.5 Trap Geometry

To achieve the greatest confinement against gravity, we orient the optical trap vertically. The $CO_2$ laser beam has horizontal and vertical $1/e^2$ intensity waists near the lens location of $w_x$=4.2 mm and $w_y$=5.0 mm, and is sent through a 1" ($f$=10") ZnSe lens before entering the chamber. Upon exiting the chamber, the beam propagates through an identical lens, is retroreflected, and travels through the second lens again before re-entering the chamber. This setup is shown schematically in Figure 2.11.

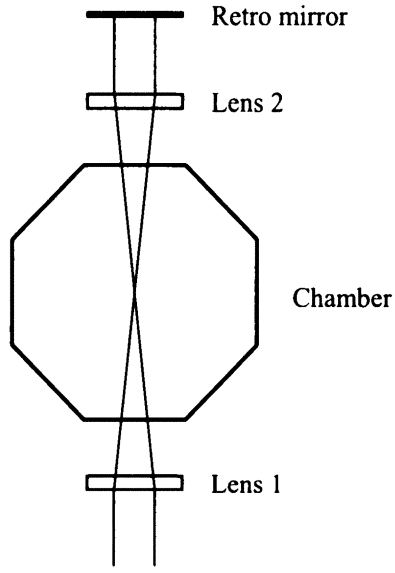


Figure 2.11: Schematic geometry of optical trap. $CO_2$ laser beam propagates vertically on first pass before retroreflection. Lenses are separated by twice the focal length.

In order to more accurately model the optical trap depth for our particular lens geometry, we have simulated the beam path using the ABCD matrix formalism, as in [62]. For a given entrance beam size and divergence, the locations and Gaussian waists of the various focal points can be calculated. This allows for calculation of the laser intensity and trap depth along the optical path. For the relatively long focal length lattice lenses ($f$=10") used here and a 50 W single-pass laser power, we find that the trap depth at the center of the chamber is on the order of ≈200-250 $\mu$K, where the maximum trap depth is given approximately by $U_{OL} \approx 4\alpha I$ where $I$ is the single-pass laser intensity and $\alpha$ is the static polarizability approximated by the atomic Cs value ($\alpha_{Cs} \approx 0.02$ MHz/(kW/cm$^2$)), given in atomic units in [63].

### 2.3.6 Trap Loading

Following the work presented in Gilfoy [51], we load atoms into the optical trap using a 10 ms optical molasses phase. During this process, the magnetic field gradient is shut off, and the trapping lasers are further red-detuned on the order of several linewidths to Doppler

cool the atoms. Approximately 10-20% of atoms initially in the MOT are loaded into the trap at temperatures of 10 $\mu$K. Figure 2.12 shows absorption imaging of $\approx 5 \times 10^5$ optically trapped atoms. When imaged, the trap is turned off, and the atoms are allowed to freely expand before the imaging pulse begins. By varying the expansion time (2-15 ms) and measuring the cloud size, we can measure the atomic temperature. as seen in Figure 2.13. Based on the temperature of the thermalized atoms in the trap ($\approx$ 10 $\mu$K), we can put a lower experimental bound on the optical trap depth of 100 $\mu$K for Cs atoms, using the approximate scaling laws in [64]. This is consistent with a calculated value of $\approx$200 $\mu$K based on our geometry.

## 2.4 Summary

Here we have described the relevant details of the two independent magneto-optical traps that provide the dense samples of ultracold atoms used in our photoassociation experiments. Using forced dark SPOT MOTs, we generate samples of $^{85}$Rb and $^{133}$Cs with densities in excess of $10^{11}$ cm$^{-3}$ at temperatures $\approx$100 $\mu$K. Following a 10 ms optical molasses phase, we can optically trap in excess of $5 \times 10^5$ atoms of each species in a quasi-electrostatic trap made with a high-power $CO_2$ laser. These samples, either in the optical trap or directly out of the MOTs, provide the necessary conditions to efficiently create ultracold diatomic molecules via photoassociation, which is described in the next chapter.

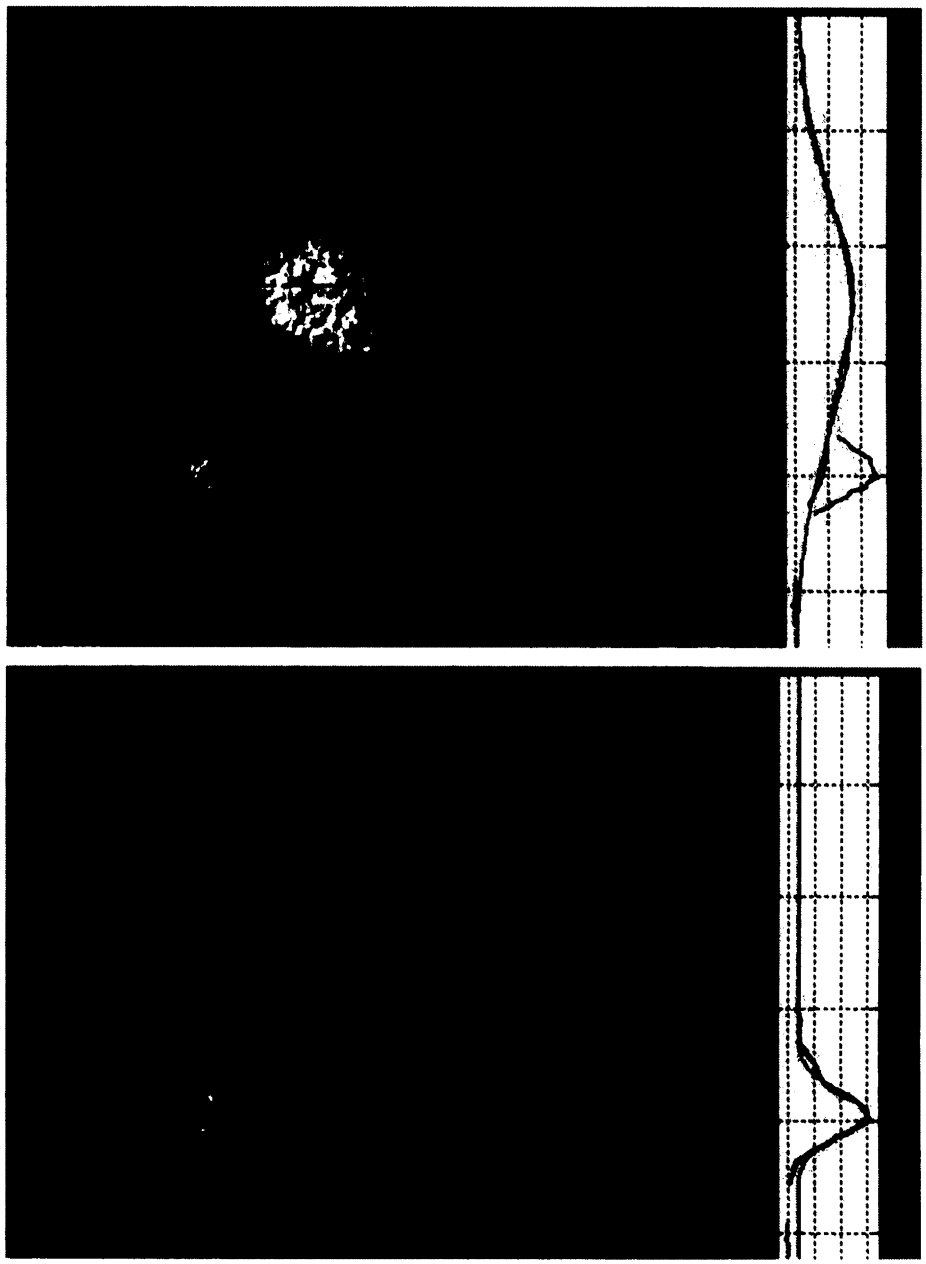

Figure 2.12: Absorption images of atoms trapped in the optical dipole trap. Trapped atom clouds are allowed to expand for approximately 2 ms before the imaging pulse begins. The large diffuse cloud consists of expanding atoms that are not loaded into the trap. Upper image shows atomic clouds 17 ms after trap loading. Lower image shows atoms trapped for 50 ms.

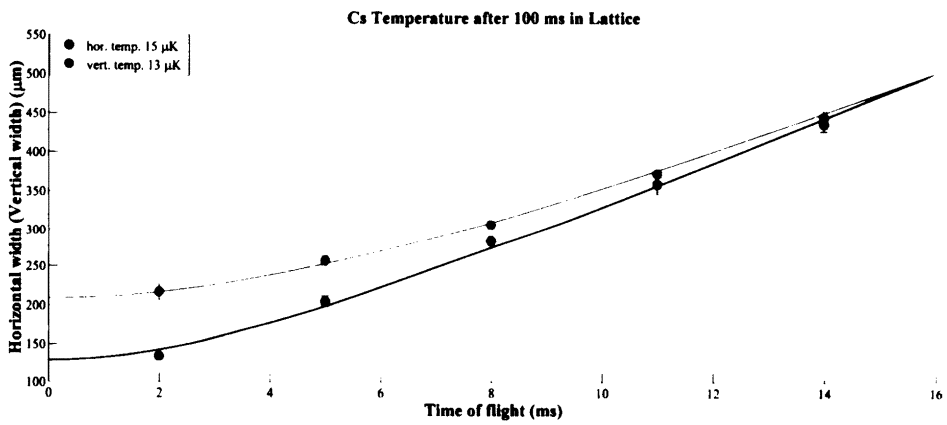


Figure 2.13: Measurement of Cs atom temperature after 100 ms in optical trap. The horizontal (blue) and vertical (red) widths are measured for different free expansion times. Fit lines model ballistic expansion and are used to extract the sample temperature.

# Chapter 3

# The Atomic and Molecular Theory of Photoassociation

## 3.1 Introduction

Here we lay out the formalism necessary to understand much of the notation used to describe the molecular states we study. Our method is to try to retain as much as intuition as possible from more familiar atomic systems, while keeping in mind that certain aspects of molecular physics have no atomic analogue. With this strategy, we can follow the evolution of the precursor atoms as they become diatomic molecules. First, we describe the systems used to label different molecular states based on the interactions of their constituent angular momenta. In this description, we detail the most salient features of different classes of molecular states as they relate to this work. Second, we relate these labels to the potential energy curves that show the numerous levels associated with the RbCs molecule. Third, we discuss the translation of potential energy curves into molecular state energies and wavefunctions. Finally, we bridge the gap between atomic and molecular systems with a calculation of the photoassociation (PA) rate and its dependence on the rotational level of the PA state.

## 3.2 Molecular State Labeling

The molecular states that we study are described by a number of different constituent angular momenta. In particular, we have the electronic orbital angular momentum ($L$), the electronic spin ($S$), the rotation of the nuclei (known in the literature as $R$, here as $\ell$), and the nuclear spins ($I_{\mathrm{Rb}}$, $I_{\mathrm{Cs}}$). A great deal of molecular spectroscopy is devoted to determining how these constituent angular momenta couple together, and numerous textbooks have been devoted to the subject [65, 66, 67]. Detailing all possible couplings is well beyond the scope of this work, and often textbooks apply a general approach that includes many special cases. In the hopes of simplifying understanding, we focus our attention on couplings that are of particular interest here.

### 3.2.1 Axial Symmetry and Projection onto the Internuclear Axis

Although molecules inherit their angular momenta from their atomic precursors, the spherical symmetry seen in atomic systems is broken by the internuclear axis, $\hat{n}$. Instead, a cylindrical symmetry about this axis emerges. In the case of the orbital angular momentum, $L$, only its projection on the internuclear axis, $\Lambda$, remains a good quantum number. The magnitude of this projection often dominates the molecular energetics, and as a result, we must consider projections of other angular momenta in order to fully assign the spectra. These additional labels tend to complicate molecular systems compared to atomic systems but are necessary to understand the observed behavior.

### 3.2.2 Hund's Cases and Selection Rules

Most of the molecular spectrum is determined by various ways in which the various angular momenta combine. The order in which angular momenta couple are described in a number of limiting cases known as Hund's cases [65, 67, 68]. Analytical forms of the basis states from the Hund's cases can then be used to construct the true energy eigenstates of the system. Based on the relative strengths of different interactions, such as electrostatic forces,

spin-orbit coupling, and rotation, the basis states of the appropriate case can often be used as good approximations for the molecular energy eigenstates.

One of the great difficulties of molecular physics is that the Hund's case (and corresponding set of basis states) that simply describes one particular state is often much less appropriate for another state in the same molecule. Thus when calculating matrix elements between two such states, it is necessary to choose a basis that is not optimal for at least one of the states. This is an unfortunate reality of molecular calculations, but with judiciously chosen bases, one can try to minimize the computational complexity.

Here we detail the most important features of the states used in our experiments. Initially we omit discussion of the complications due to hyperfine structure. Once the coupling schemes for electronic angular momenta are established, we briefly describe possible couplings of the nuclear spins.

### Hund's Case (a) $X^1\Sigma^+$

In Hund's case (a) states, shown in Figure 3.1, the electrostatic forces strongly couple $L$ and $S$ to the internuclear axis to yield the projections, $\Lambda$ and $\Sigma$, that add to give $\Omega$. We then add $\Omega$ to $\ell$ to form the total angular momentum, $J$. The rotational energy in a particular vibrational level is given by $B_e J(J+1)$, where $B_e$ is the rotational constant. As a general rule for RbCs, Hund's case (a) is most appropriate for deeply-bound levels where interatomic forces dominate.

Case (a) states are labeled as ${}^{2S+1}\Lambda_\Omega$. For $\Sigma$ states ($\Lambda = 0$), there is an additional symmetry denoted by a superscript $\pm$. This describes whether or not the electronic wavefunction changes sign following reflection through a plane containing the internuclear axis.[1] The basis states associated with this case are given as $|\eta, \Lambda, S, \Sigma, \Omega, J, M\rangle$, where $M$ is the projection of $J$ and $\eta$ represents all other quantum numbers. Much of the literature, especially [67], uses this basis for calculating matrix elements. We follow suit for most of our

[1] For the states of interest to this experiment, we need only consider $\Sigma^+$; $\Sigma^-$ states are only observed in higher-lying electronic states not accessed in this experiment.

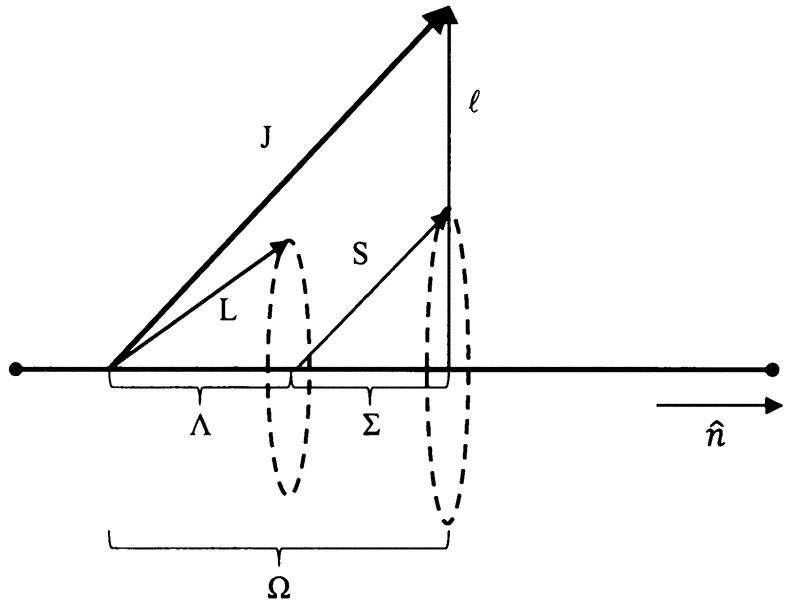


Figure 3.1: Angular momentum coupling in Hund's case (a) molecules.

calculations here and show the appropriate basis transformations as they become necessary.

### Hund's case (b) $a^3\Sigma^+$

For the Hund's case (b) states of interest here, shown in Figure 3.2, the total spin ($S$) couples to the rotation of the nuclei ($\ell$).[2] The rotational energy is given by $B_e\ell(\ell+1)$, and the parity is given by $(-1)^\ell$ for $\Lambda = 0$ states. States are labeled as $^{2S+1}\Lambda$ with the additional $\pm$ symmetry for $\Sigma$ states. In this case, $\Omega$ is not well-defined, but it is limited to the available values of $\Lambda + \Sigma$. For the Hund's case (b) states of interest in the very shallow $a^3\Sigma^+$ potential, $\Lambda = 0$ and $S = 1$; hence, $\Omega = 0, 1$. Given that $\Lambda = 0$, there is no first-order spin-orbit coupling to separate components with different values of $\Omega$.

The transformation to the Hund's case (a) basis is given in [69], and for our particular

[2]Technically, for Hund's case (b) $\Sigma$ states, $N = L + \ell$, where the projection of $L$ onto the internuclear axis, $\Lambda = 0$. $N$ then couples to $S$ to form $J$. For the very weakly-bound $a^3\Sigma^+$ state of interest here, the approximation $N = \ell$ is valid. The more rigorous relationship between $L, \Lambda, \ell$, and $N$ for the $a^3\Sigma^+$ state is analogous to that of $J_a, \Omega, \ell$, and $J$ in an $\Omega = 0$ Hund's case (c) state.

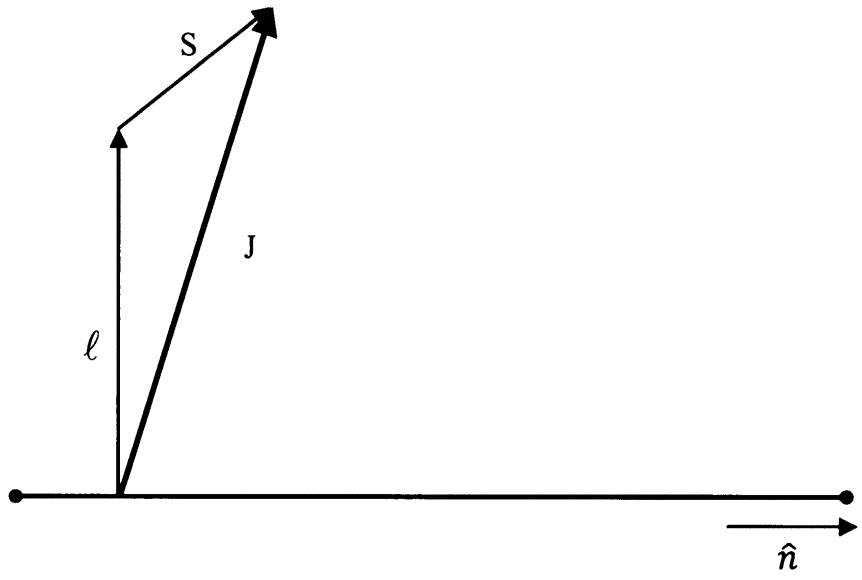


Figure 3.2: Angular momentum coupling in Hund's case (b) molecules.

$^3\Sigma^+$ state, where $\Lambda = 0$ and $N \approx \ell$, we have

$$|S, \ell, J\rangle = \sum_{\Sigma\Omega} |S, \Sigma, \Omega, J\rangle \sqrt{2\ell + 1}(-1)^{J+\Omega} \begin{pmatrix} S & \ell & J \\ \Sigma & 0 & -\Omega \end{pmatrix} \tag{3.1}$$

where we include positive and negative values for the projections $\Sigma$ and $\Omega$.

### Hund's case (c)

In Hund's case (c) states, shown in Figure 3.3, the spin-orbit interaction dominates, causing $L$ and $S$ to couple to form an intermediate $J_a$ that projects onto the internuclear axis to form $\Omega$, but without forming well-defined $\Lambda$ and $\Sigma$. States are labeled by their $\Omega$ values. For $\Omega = 0$ states, the parity of the state in the absence of rotation is written as a superscript in the molecular label.[3] The total angular momentum is given by $J = J_a + \ell$, and the rotational energy is given by $B_e J(J + 1)$. This coupling case describes the long-range PA states used in the early part of this work where interatomic forces are not particularly

[3]In the hopes of clearing up a common source of confusion, we make the following statement: $^3\Sigma^+$ potentials have $\Omega = 0^-$ symmetry.

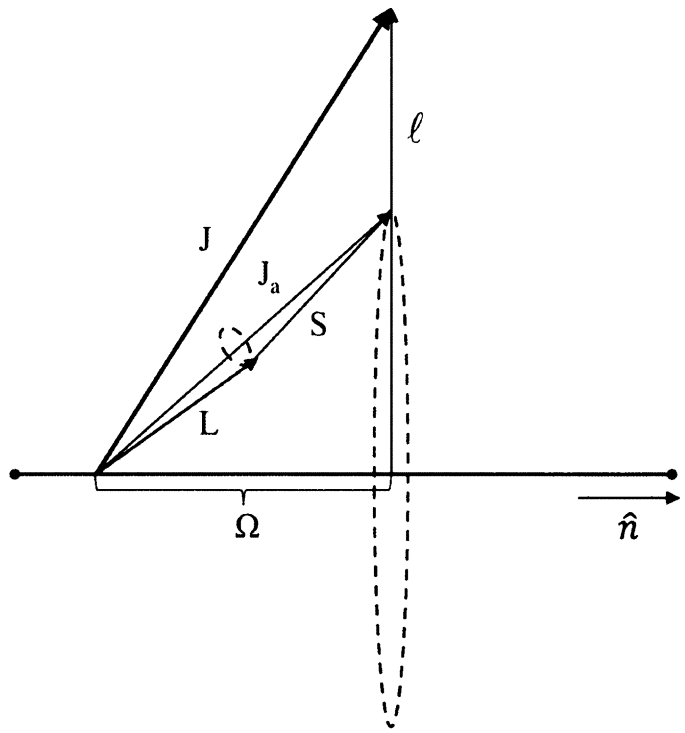


Figure 3.3: Angular momentum coupling in Hund's case (c) molecules.

strong compared to atomic spin-orbit splittings.

Unfortunately, there is no closed form transformation from Hund's case (c) to Hund's case (a). We can, however, often determine which Hund's case (a) basis states contribute to a given Hund's case (c) state with a few well-justified assumptions. We discuss this procedure later in detail in the context of calculating rotational line strengths in PA.

### Selection Rules

Just as in the case of atoms, there exist selection rules that preclude certain single-photon electric dipole transitions based on molecular symmetries. For all Hund's case bases, the following selection rules apply:

$$\Delta S = 0, \;\; \Delta J = 0, \pm 1 \;\; (J = 0 \nrightarrow J' = 0) \tag{3.2}$$

For Hund's case (a), we gain

$$\Delta\Omega = 0, \pm 1, \;\; \Delta\Lambda = 0, \pm 1, \;\; \Delta\Sigma = 0 \tag{3.3}$$

For Hund's case (c), we have

$$\Delta\Omega = 0, \pm 1, \;\; \Omega = 0^+ \rightarrow \Omega' = 0^+, \;\; \Omega = 0^- \rightarrow \Omega' = 0^-, \;\; \Omega = 0^+ \nleftrightarrow \Omega' = 0^- \tag{3.4}$$

In the course of discussing selection rules for observed transitions, we must often switch between different Hund's cases. States of a given case can be expressed as linear combinations of components from another Hund's case, and we apply the selection rules to the various components. Generally, this makes the selection rules less restrictive, as there can be numerous components available to satisfy the various conditions.

Just as in atomic systems, the selection rules that we have discussed are rarely absolute. For the purposes of this work, we are most interested in the nominally forbidden spin-flip transitions, where $\Delta S = \pm 1$. In the electric dipole approximation, transitions affect only the orbital angular momentum. Thus transitions between spin eigenstates with different values of $S$ are forbidden. However, the spin-orbit interaction, for example, mixes the spin eigenstates, resulting in non-zero transition probabilities. We show the exact form of this interaction and its effects on relevant molecular states later in the next chapter of this thesis.

### Hyperfine Structure and Ω-doubling

This description has so far neglected any possible coupling with the atomic nuclear spins. For many of the states studied here, $\Omega = 0$; such states have no first-order magnetic hyperfine structure, and we can assume that the nuclear spin is decoupled from all other angular momenta, in the limit of small electric quadrupole hyperfine structure. For many of the purposes of this work, we assume that there is an unresolved manifold of many

nuclear spin states associated with any observed feature.

For states with $\Omega \neq 0$, spectroscopy becomes much more complicated. Due to the relatively large values of $I_{Cs}$ and $I_{Rb}$ as well as the strong atomic hyperfine interactions, there are a large number of additional spectroscopic features that are well-resolved by CW laser spectroscopy. Additionally, each value of $|\Omega| \neq 0$ has two closely-spaced components of opposite parity that form a so-called $\Omega$-doublet. This has two primary effects for the work presented here. First, rotational levels are no longer parity eigenstates. Second, electric fields can mix and repel the components of the parity-doublet, potentially complicating spectroscopy. These two features are discussed later in the context of CW depletion spectroscopy.

## 3.3 Reading Potential Energy Curves

The primary goals of our molecular spectroscopy are to determine which levels can be reached from a given state via electric dipole transitions and to assign approximate relative strengths for those transitions. Given the very large number of levels available in a diatomic molecule, it is obviously impossible to efficiently display this information in any tabular form. Instead, the relevant states can be shown graphically as potential energy curves where the internal molecular energy is shown as a function of internuclear separation. With the application of a few well-justified approximations, we can then extract a great deal of information about the relative transition strengths between different molecular states.

Efficient use of potential energy curves usually relies on the use of two very useful approximations. The first, known as the Born-Oppenheimer approximation, allows us to factor the entire molecular electric dipole matrix element into electronic and nuclear components [70]. This can be justified semi-classically by considering the much faster rate at which the electronic wavefunction can change compared to that of the much more massive nuclei. In other words, the electric dipole transition takes place before the nuclear wavefunction can change appreciably.

The electric dipole matrix element between two molecular states can then be factored as

$$\langle \Psi_f | \vec{d} \cdot \vec{E} | \Psi_i \rangle = \langle \psi_f | \vec{d} \cdot \vec{E} | \psi_i \rangle \langle \chi_f(R) | \chi_i(R) \rangle \tag{3.5}$$

where $\vec{d}$ is the electric dipole operator, $\vec{E}$ is applied electric field, $|\Psi\rangle$ is the total wavefunction, $|\psi\rangle$ is the electronic wavefunction, $|\chi\rangle$ is the nuclear wavefunction, and $R$ is the internuclear separation. The first term is the electronic portion of the matrix element. This term is very similar to the transition matrix element in atomic physics. It captures information such as selection rules and angular factors involved in the transition matrix element. Typically for a fully-allowed electronic transition, we expect this to be of the order $ea_0$, where $e$ is the electron charge and $a_0$ is the Bohr radius.

The second term is an overlap integral of the two nuclear wavefunctions. The square of this term is typically quoted as the Franck-Condon factor (FCF). Assuming that selection rules are satisfied, the FCF largely determines the transition strength between two molecular states. Further, the FCF can vary by several orders of magnitude for different nominally-allowed transitions. Fortunately, the Franck-Condon principle can be used to readily extract qualitative information on the relative transition strengths from a graph of the potential energy curves.

The Franck-Condon principle, which is detailed in [65] and illustrated in Figure 3.4, states that transitions are strongest between states whose classical turning points occur at the same internuclear separation. This can be understood by approximating the nuclear wavefunction as that of a harmonic oscillator. Thus, for vibrationally-excited molecules, the wavefunction amplitude will be greatest at the classical turning points of the molecular potential. Then by drawing two vertical lines from the classical turning points of the initial molecular state, we can immediately see which states will have the greatest FCFs by looking for intersections with the various potential curves. Provided dipole transition selection rules are satisfied, these levels with the greatest FCFs will have the strongest transitions.

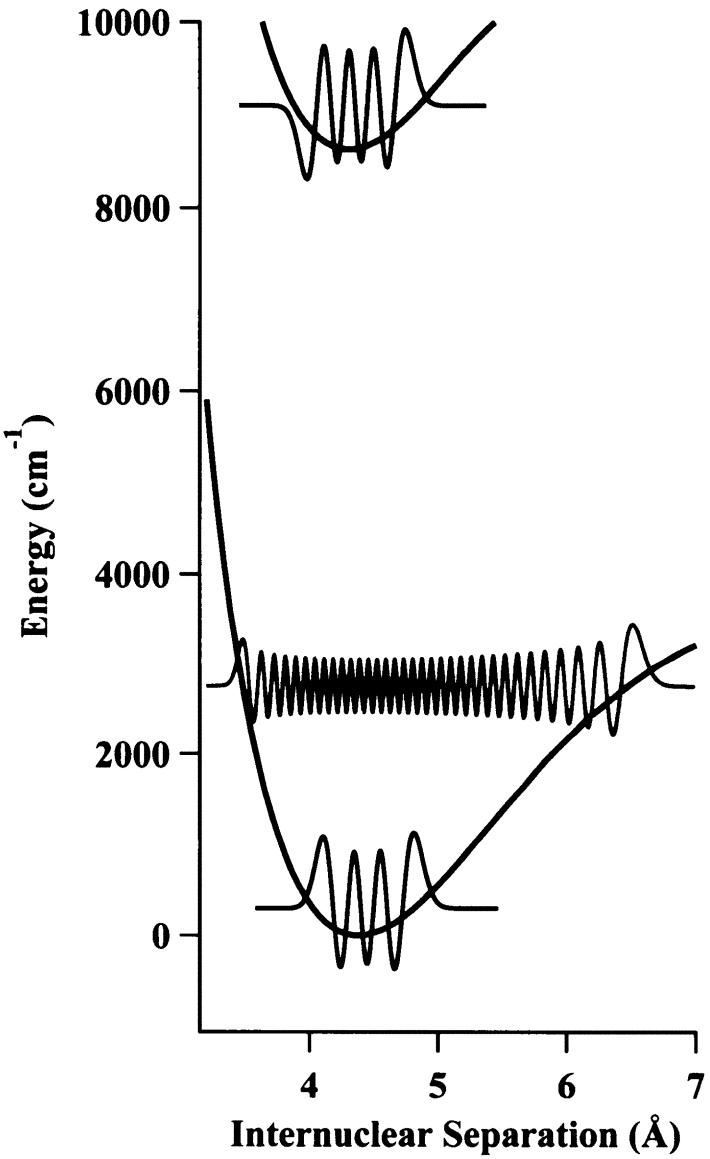


Figure 3.4: The Franck-Condon principle dictates that transitions from the upper state are favored to the lower state in blue, where the wavefunction overlap is large. The fast oscillations of the lower state in red yield a very small overlap integral and correspondingly small transition probability.

## 3.4 Spectroscopic Data to Potential Curves to Molecular Wavefunction

Given the very large number of levels available in molecular systems, it is generally not tenable to measure every possible transition. Instead, it is often much more practical to measure some relatively small subset of the possible transitions and then calculate a potential energy curve that reproduces the observed behavior. This potential energy curve can then be used to predict level locations that were not directly observed. With knowledge of the energy level locations and the molecular potential, one can solve for the nuclear wavefunction, $|\chi(R)\rangle$, which can then be used to calculate the FCF (and approximate transition strength) with any other known level.

### 3.4.1 Inversion of Spectroscopy to get Potentials to get Wavefunctions

Reconstruction of a potential from spectroscopic measurements is a familiar problem in molecular physics that has been addressed in numerous ways of varying accuracy and complexity [71, 72, 73]. For a number of molecular potentials, the collected spectroscopy is so detailed that a very accurate functional form has been written. In the case of RbCs, groups have parametrized the $X^1\Sigma^+$, $a^3\Sigma^+$, and other potentials [19, 74, 75]. For the potentials that have not yet been characterized, we can still extract a great deal of information about the shape of the potential using the Rydberg-Klein-Rees (RKR) method described in [67].

We primarily use the RKR1 implementation written by R. Le Roy [76]. With the input of level locations and the corresponding rotational constants, molecular potentials are inferred through a semi-classical calculation based on the Wentzel-Kramers-Brillouin (WKB) approximation. The potential can then be described pointwise over the desired range of internuclear spacings. The program written by Le Roy is very robust and yields highly accurate potentials.

With a known potential, finding the eigenvalues and eigenvectors of the Hamiltonian amounts to solving a second-order linear differential equation. For much of the work done

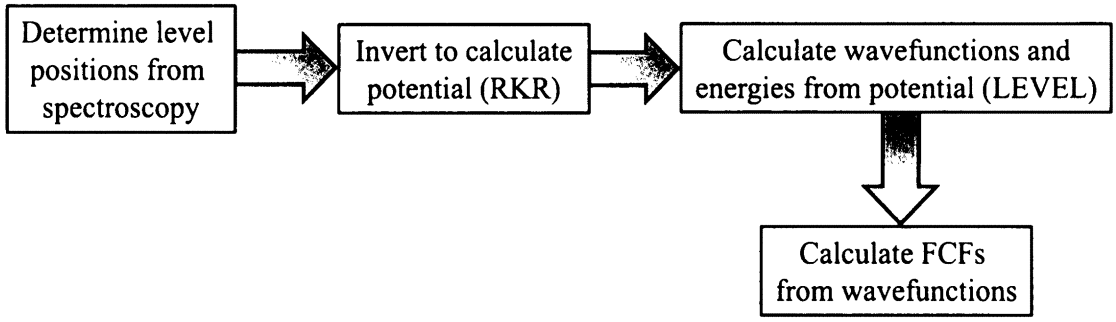


Figure 3.5: Schematic representation of the use of the RKR1 and LEVEL 8.0 programs to extract relevant molecular parameters from existing spectroscopy.

here, we have used the LEVEL 8.0 program developed by R. Le Roy [77]. This sophisticated program numerically solves the Schrödinger equation to find the bound state energies and wavefunctions for diatomic molecules. This technique has been refined over many years and has become a standard tool in molecular spectroscopy. The relationship between these programs, existing spectroscopy, and the desired wavefunctions and FCFs is shown schematically in Figure 3.5.

In the context of photoassociation, this procedure is complicated slightly for the initial scattering state that describes the precursor atoms. This state is part of a continuum and therefore cannot be unit-normalized over all space. Instead, we use so-called energy-normalized wavefunctions, $\psi_E$, as in [78]. The most salient feature of these being

$$\int \psi^*_{E'}(x)\psi_{E''}(x)dx = \delta(E' - E''). \tag{3.6}$$

To construct these states, we consider numerical solutions to the time-independent Schrödinger equation (TISE) in the presence of the shallow $a^3\Sigma^+$ potential. Given that the TISE is a second-order linear differential equation, we can integrate twice to find our solution and then invoke boundary conditions with an assumed initial scattering energy to determine the values of the integration constants. First, at very short-range, we know that there is a very steep, repulsive wall. Thus, the wavefunction amplitude must be vanishingly small

at $R$=0, which eliminates one integration constant. The second constant determines the amplitude of the wavefunction. This can be determined by calculating the long-range part of the wavefunction using the WKB approximation, as in [40], and is given by

$$|\chi(R)\rangle = \sqrt{\frac{k}{\pi E}}\sin(kR + \phi) \tag{3.7}$$

where $k$ is the de Broglie wavevector, $E$ is the collision energy, and $\phi$ is a phase factor that does not affect normalization. The numerical solution to the TISE is then scaled such that the long-range amplitude matches that of the approximate WKB wavefunction.

To calculate the free-to-bound Franck-Condon factors between two wavefunctions that are defined pointwise, we take the square of the Riemann sum of the wavefunction product, given by

$$\text{FCF} = |\sum_{n}\langle\chi_1(x_n)|\chi_2(x_n)\rangle\Delta x|^2 \tag{3.8}$$

where $\Delta x$ is a sufficiently narrow partition width ($\Delta x$=0.001 Å here). The appropriately normalized free-to-bound FCF can then be given in the atomic energy units of $E_h^{-1}$, the inverse Hartree energy.

## 3.5 Creating Molecules Out of Atoms

In our discussion of the formation of ground state molecules from atomic samples, we consider two separate steps. First, two colliding atoms absorb a resonant photon and are promoted to an electronically-excited molecular state. This step alone is technically photoassociation. The second step is the rapid spontaneous decay ($\tau \sim 10 - 100$ ns). This decay process determines which molecular levels are populated. Unsurprisingly, the ground states with the greatest transition strengths (and FCFs) in decay will be most heavily populated.

### 3.5.1 PA Excitation Rate

We can use Fermi's Golden Rule, as in [40], to formally write the PA rate as

$$\hbar\Gamma_{\mathrm{PA}} = 2\pi|\langle\Psi_{\mathrm{PA}}|\vec{d}\cdot\vec{E}|\chi(R)\rangle|^2, \tag{3.9}$$

$$\hbar\Gamma_{\mathrm{PA}} \approx \frac{\pi I}{c\epsilon_0}|\langle d\rangle|^2\, F, \tag{3.10}$$

where $|\Psi_{\mathrm{PA}}\rangle$ is the PA state wavefunction, $|\chi(R)\rangle$ is the scattering state wavefunction, $\Gamma_{\mathrm{PA}}$ is the PA excitation rate, $c$ is the speed of light, $\epsilon_0$ is the permittivity of free space, $I$ is the laser intensity, $F$ is the FCF, and $d$ is the dipole matrix element.[4]

### 3.5.2 PA as Inelastic Scattering

In this model, we have implicitly assumed a two-level system in a weak-coupling limit. In order to understand decay to electronic ground states as well as saturation behavior, we can describe PA in the language of inelastic scattering, as in [80]. The initial scattering state, termed the entrance channel, describes two colliding atoms in the presence of a resonant photon. The electric dipole transition couples the scattering state to an intermediate excited molecular state that quickly spontaneously decays into another state, distinct from the scattering state, generally termed the exit channel, as shown in Figure 3.6. We then want to calculate the rate at which flux is transferred from the entrance to exit channel.

The relevant parameter is the PA rate coefficient, $K_{\mathrm{PA}}$, which is related to the inelastic scattering cross-section, $\sigma_{\mathrm{in}}$, by

$$K_{\mathrm{PA}} = \langle v_{\mathrm{rel}}\sigma_{\mathrm{in}}\rangle, \tag{3.11}$$

where $v_{\mathrm{rel}}$ is the relative velocity of the colliding atoms and the brackets denote a thermal average. The dependence of $K_{\mathrm{PA}}$ on the excitation and decay rates has been worked out

[4] In order to write the electric field, $E$, in terms of the more experimentally practical laser intensity, $I$, we note that for $I = \frac{1}{2}\epsilon_0 c|E_0|^2$, the corresponding electric field is $E_0\cos(\omega t)$. In the rotating wave approximation, however, only half of the electric field contributes to the coupling. Hence, the squared dipole matrix element is proportional to $|E_0|^2/4$, rather than $|E_0|^2$. This can also be seen by treating the laser as part of a quantized electromagnetic field, as in [79].

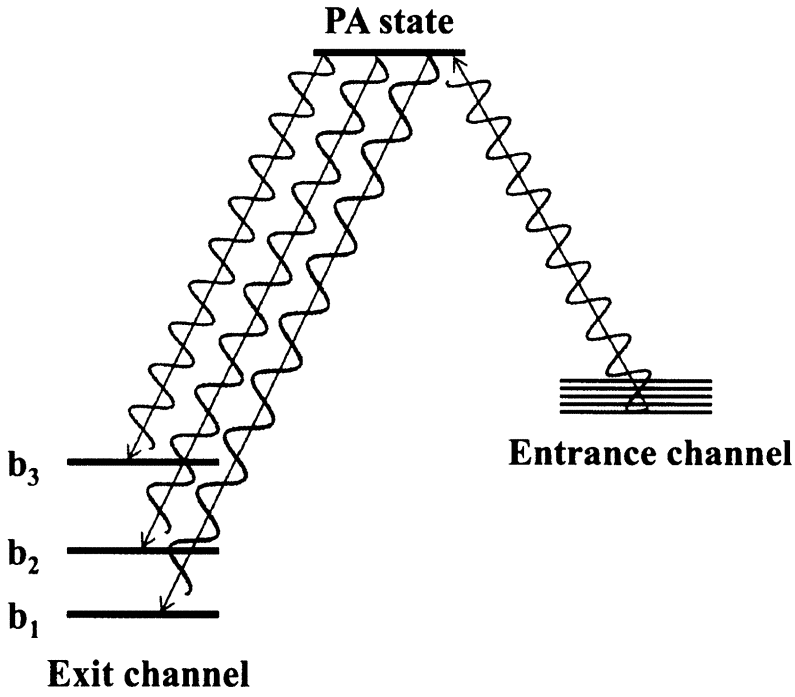


Figure 3.6: Schematic representation of PA as inelastic scattering. Colliding atoms, spread over a continuum of scattering states, constitute the entrance channel. A resonant photon couples a colliding pair into the electronically-excited PA state. The excited state quickly decays into one of many possible final states that constitute the exit channel. The relative decay strengths to different levels in the exit channel are given by the respective branching ratios, $b$.

in numerous works [80, 81] and is given by

$$K_{\mathrm{PA}} = \left\langle v_{\mathrm{rel}} \frac{\pi}{k^2} \sum_{\ell} (2\ell + 1) \frac{4\Gamma_{\mathrm{PA}}\gamma_{\mathrm{nat}}}{(\Gamma_{\mathrm{PA}} + \gamma_{\mathrm{nat}})^2} \right\rangle, \tag{3.12}$$

where $k$ is the de Broglie wavevector, $\gamma_{\mathrm{nat}}$ is the PA state linewidth, and the sum is taken over partial waves, $\ell$. At our temperatures, we expect only $v_{\mathrm{rel}}$ and $k$ to vary significantly over the thermal average; $\Gamma_{\mathrm{PA}}$ is taken to be constant, as the scattering state wavefunction, $|\chi(R)\rangle$, should only vary slowly over the relevant energies. Calculation of the thermal average is given in numerous references [40]. This allows for the conversion of an ensemble temperature, usually measured by time-of-flight expansion, into a properly weighted energy

distribution.

Retaining only the intensity dependence for $K_{\mathrm{PA}}$, we have

$$K_{\mathrm{PA}} \propto \frac{I_{\mathrm{PA}}}{(I_{\mathrm{PA}} + I_{\mathrm{sat}})^2}, \tag{3.13}$$

which is shown in Figure 3.7. The high-intensity limit of PA is remarkably different from the two-level system, in that the ground state molecular formation rate goes to zero, rather than monotonically approaching a saturated value. This is because the scattering state is part of a continuum, rather than a discrete state. Rabi flopping during the stimulated emission process couples flux out of the excited molecular state to very many continuum states before the excited molecule can spontaneously decay, which is equivalent to no photoassociation at all [82].

With the value of the PA rate constant, we can now write the total PA rate, $R_{\mathrm{PA}}$, by multiplying by the product of the atomic densities and integrating over the volume illuminated by the PA laser

$$R_{\mathrm{PA}} = K_{\mathrm{PA}} \int n_{\mathrm{Rb}} n_{\mathrm{Cs}} dV \tag{3.14}$$

To calculate the formation rate of molecules into a particular level in the electronic ground states, we multiply by the corresponding branching ratio for spontaneous decay, $b$. Later, in our discussion of deeply-bound PA, we will discuss methods of calculating these branching ratios for different vibrational levels.

## 3.6 Calculating Rotational Line Strengths in Photoassociation

We conclude this chapter with a particular calculation that models the evolution of atomic samples to photoassociated molecules while keeping very detailed account of the constituent angular momenta throughout the process. Analogous calculations have been made for homonuclear molecules such as $Na_2$ and $Cs_2$ [83, 84]. Using the results of this calculation,

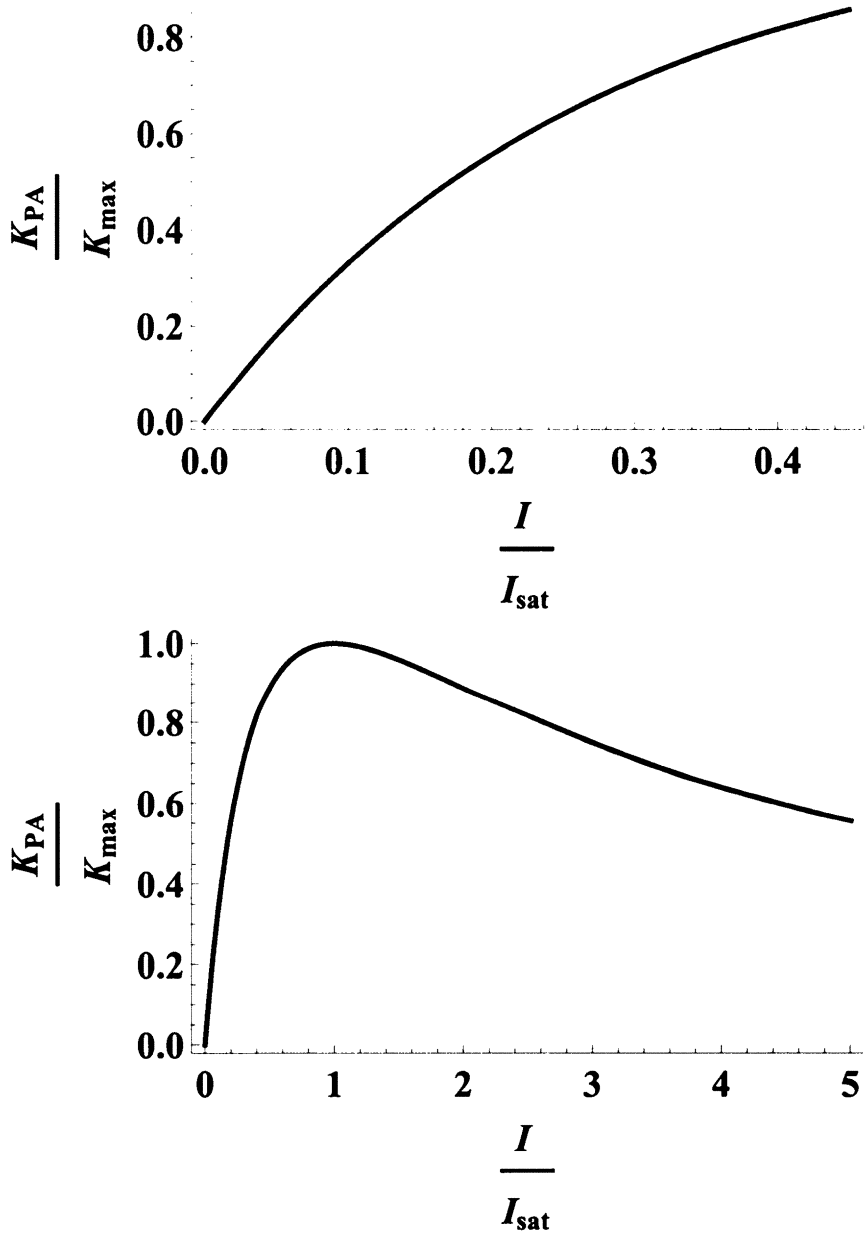


Figure 3.7: Dependence of the PA rate coefficient, $K_{\mathrm{PA}}$, on the incident laser intensity, $I$, in the low intensity (upper trace) and high intensity (lower trace) regimes. The rate coefficient is maximized when the PA excitation rate, $\Gamma_{\mathrm{PA}}$ is equal to the spontaneous decay rate, $\gamma_{\mathrm{nat}}$. When $I_{\mathrm{PA}} = I_{\mathrm{sat}}$, the inelastic cross-section reaches the unitarity limit for inelastic scattering given by $\sigma_{\mathrm{in}} = \pi/k^2$.

we are able to determine the relative line strengths for different rotational levels populated in PA to a particular $(2)^3\Pi_0$ molecular state of great experimental interest. From this analysis, we are able draw powerful conclusions about both the initial atomic scattering and final molecular states.

In order to calculate the necessary electric dipole matrix elements, we must transform the atomic scattering and bound PA states into the same basis. In the colliding atoms, the hyperfine interaction couples the electronic and nuclear spins in each ground state atom to form the total angular momentum, $F$. Thus the scattering state, shown in Figure 3.8, is described most naturally in the $|F_{\mathrm{Rb}}, M_{F(\mathrm{Rb})}\rangle\,|F_{\mathrm{Cs}}, M_{F(\mathrm{Cs})}\rangle\,|\ell, m_\ell\rangle$ basis, where $F$ is the total angular momentum of each atom, $M_F$ is its projection on the space-fixed axis, $\ell$ is the partial wave of the collision, and $m_\ell$ is its projection. The excited molecular $^3\Pi_0$ electronic eigenstates correspond to the $|\Omega, \Lambda, S, \Sigma\rangle_{\mathrm{BF}}\,|J, M\rangle\,|I_{\mathrm{Rb}}, M_{I(\mathrm{Rb})}, I_{\mathrm{Cs}}, M_{I(\mathrm{Cs})}\rangle$ basis, where the BF subscripts denote the body-fixed frame (and we omit subscripts for kets written in the default space-fixed frame). Here the rotational/electronic part of the wavefunction is written in the Hund's case (a) basis, where the total electronic spin, $S$, projects onto the internuclear axis to form $\Sigma$, which is added to the projection of the orbital angular momentum, $\Lambda$, to form $\Omega$. This total projection of the electronic angular momentum, $\Omega$, is then added to the mechanical rotational angular momentum, $\ell$, to yield the total angular momentum $J$ and its projection $M$. For the $\Omega$=0 states considered initially here, the nuclear spins $I_{\mathrm{Rb}}$, $I_{\mathrm{Cs}}$ and their projections $M_{I(\mathrm{Rb})}, M_{I(\mathrm{Cs})}$ are decoupled from the electronic angular momentum and hence may be quantized in space-fixed coordinates.

Calculating the necessary electric dipole matrix elements between these states requires several steps. First, we write both the atomic scattering and the molecular bound state in a basis of space-fixed angular momentum components, in the form: $|L, M_L, S, M_S\rangle$ $|I_{\mathrm{Rb}}, M_{I(\mathrm{Rb})}, I_{\mathrm{Cs}}, M_{I(\mathrm{Cs})}\rangle\,|\ell, m_\ell\rangle$, where $L$ is the total electronic orbital angular momentum, $S$ is the total electronic spin, $I_{\mathrm{Rb}}$ ($I_{\mathrm{Cs}}$) is the nuclear spin of Rb (Cs), and $\ell$ is the mechanical rotational angular momentum with all of their respective projections on the space-fixed axis. In this basis, it is straightforward to calculate the relative size of electric dipole

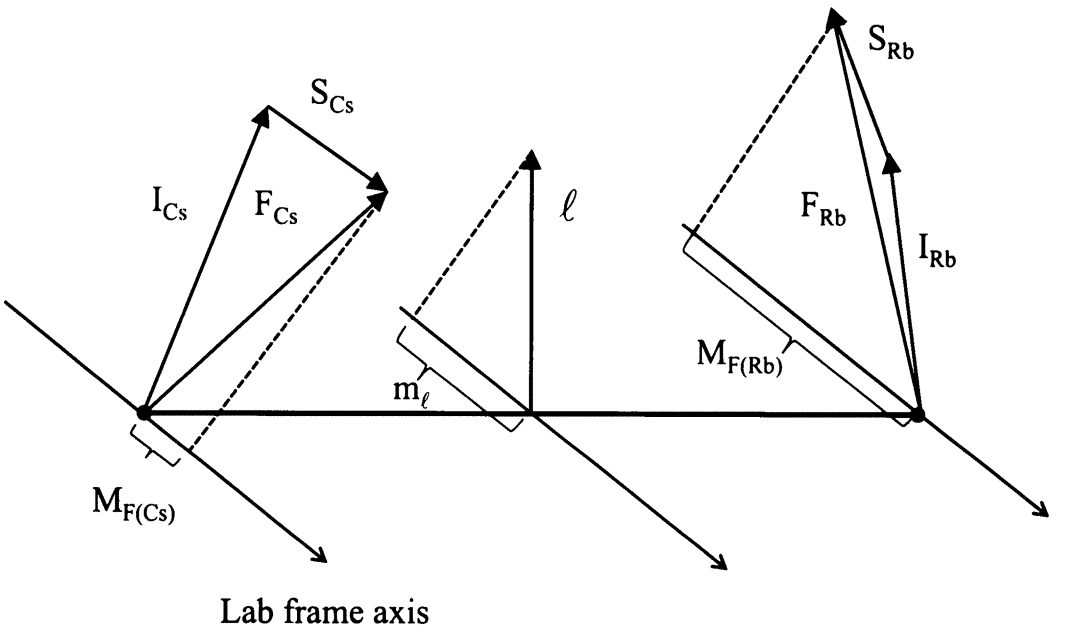


Figure 3.8: Angular momentum coupling for two colliding alkali atoms.

transition matrix elements. We then describe the correct procedure to account for both the distribution of hyperfine sublevels in the initial atomic scattering states and the final, unresolved hyperfine states in the molecular bound state.

### 3.6.1 Atomic Scattering State

Given that we operate out of dark SPOT MOTs, both atoms are in their lower hyperfine ground states. Hence we can write any colliding pair of $^{85}$Rb and Cs atoms, shown in Figure 3.8, in the $|F_{\mathrm{Rb}}, M_{F(\mathrm{Rb})}\rangle\,|F_{\mathrm{Cs}}, M_{F(\mathrm{Cs})}\rangle$ basis as $|2, M_{F(\mathrm{Rb})}\rangle\,|3, M_{F(\mathrm{Cs})}\rangle$, where $F$ is the total angular momentum for the subscript atom and $M_F$ is its projection on the space-fixed axis. The projections of the total angular momentum are spread incoherently over all possible $M_{F(\mathrm{Rb})}$ and $M_{F(\mathrm{Cs})}$ values due to the magnetic field gradient necessary for the operation of the MOTs, and thus we must consider all possible combinations. Finally, atoms in the MOT will have a distribution of $\ell$ values determined by the temperature; for any given $\ell$, there is an incoherent mixture of all $(2\ell+1)$ possible values of $m_\ell$.

We transform to the $|L, M_L, S, M_S\rangle|I_{\rm Rb}, M_{I({\rm Rb})}, I_{\rm Cs}, M_{I({\rm Cs})}\rangle|\ell, m_\ell\rangle$ basis in two steps. First, for a given $|2, M_{F({\rm Rb})}\rangle|3, M_{F({\rm Cs})}\rangle$ state, we transform to the spin-decoupled $|S_{\rm Rb}, M_{S({\rm Rb})}, I_{\rm Rb}, M_{I({\rm Rb})}\rangle\ |S_{\rm Cs}, M_{S({\rm Cs})}, I_{\rm Cs}, M_{I({\rm Cs})}\rangle$ basis. Note that $L_{\rm Cs}{=}L_{\rm Rb}{=}0$ here, as the colliding atoms are both in their $s_{1/2}$ ground states. Here $S_{\rm Rb}{=}S_{\rm Cs}{=}\frac{1}{2}$, $I_{\rm Rb}{=}\frac{5}{2}$ (for $^{85}$Rb), and $I_{\rm Cs}{=}\frac{7}{2}$. Each atomic state consists of two combinations of electronic and nuclear spin projections $(M_S, M_I)$ for a given total angular momentum projection $(M_F)$, with the relative amplitudes given by the appropriate Clebsch-Gordan coefficients.

Second, we recouple the electronic spins of these four combinations to complete the transformation to the $|L, M_L, S, M_S\rangle\,|I_{\rm Rb}, M_{I({\rm Rb})}, I_{\rm Cs}, M_{I({\rm Cs})}\rangle$ basis. This yields

$$
\begin{aligned}
&|2, M_{F({\rm Rb})}\rangle\,|3, M_{F({\rm Cs})}\rangle = \qquad (3.15)\\
&\sum_{SM_S}\sum_{\substack{M_{I({\rm Rb})}\\ M_{I({\rm Cs})}}}\sum_{\substack{M_{S({\rm Rb})}\\ M_{S({\rm Cs})}}}\langle\tfrac{1}{2}, M_{S({\rm Rb})}, \tfrac{5}{2}, M_{I({\rm Rb})}|2, M_{F({\rm Rb})}\rangle\langle\tfrac{1}{2}, M_{S({\rm Cs})}, \tfrac{7}{2}, M_{I({\rm Cs})}|3, M_{F({\rm Cs})}\rangle\\
&\langle\tfrac{1}{2}, M_{S({\rm Rb})}, \tfrac{1}{2}, M_{S({\rm Cs})}|S, M_S\rangle\,|L{=}0, M_L{=}0, S, M_S\rangle\,|I_{\rm Rb}, M_{I({\rm Rb})}, I_{\rm Cs}, M_{I({\rm Cs})}\rangle\,.
\end{aligned}
$$

Thus any colliding pair of atoms can be written as

$$
\begin{aligned}
&|g(M_{F({\rm Rb})}, M_{F({\rm Cs})}, \ell, m_\ell)\rangle = \qquad (3.16)\\
&|2, M_{F({\rm Rb})}\rangle\,|3, M_{F({\rm Cs})}\rangle\,|\ell, m_\ell\rangle =\\
&\sum_{\substack{SM_S\\ M_{I({\rm Rb})}\\ M_{I({\rm Cs})}}} A(S, M_S, M_{I({\rm Rb})}, M_{I({\rm Cs})})\,|0, 0, S, M_S\rangle\,|I_{\rm Rb}, M_{I({\rm Rb})}I_{\rm Cs}, M_{I({\rm Cs})}\rangle\,|\ell, m_\ell\rangle\,,
\end{aligned}
$$

where $A(S, M_S, M_{I({\rm Rb})}, M_{I({\rm Cs})})$ is the product of three Clebsch-Gordan coefficients as described above.

### 3.6.2 Excited Molecular State

For any $\Omega'{=}0$ state (primes are used to denote the excited state) where the electric quadrupole hyperfine structure is small compared to the state's natural linewidth, the

nuclear spin is decoupled from the electronic angular momentum. This allows us to write the nuclear spin projection values for Rb and Cs as a combination of all the unresolved $M'_{I(\mathrm{Rb})}, M'_{I(\mathrm{Cs})}$ sublevels. The wavefunction for a single hyperfine sublevel is then given by [67]

$$|e(\Omega', \Lambda', S', \Sigma', J', M', I'_{\mathrm{Rb}}, M'_{I(\mathrm{Rb})}, I'_{\mathrm{Cs}}, M'_{I(\mathrm{Cs})})\rangle = \tag{3.17}$$
$$= \sqrt{\frac{2J'+1}{4\pi}} D^{*J'}_{M'\Omega'} \, |\Lambda', S', \Sigma', \Omega'=0\rangle_{\mathrm{BF}} \, |I'_{\mathrm{Rb}}, M'_{I(\mathrm{Rb})}, I'_{\mathrm{Cs}}, M'_{I(\mathrm{Cs})}\rangle \,,$$

where $D^{*J'}_{M'\Omega'}$ is a Wigner rotation matrix that describes the transformation between the BF and space-fixed frames, taking into account their internal (spin $S'$ + orbital $L'$) angular momenta that couple to form $\Omega'$=0, as well as the mechanical rotation angular momentum ($\ell'$).

**Electronic Wavefunction in the Body-Fixed Frame**

For the simple excited molecular state we use, we can relate the wavefunction in the body-fixed Hund's case (a) basis to the relevant part of the atomic basis by noting a few selection rules. First, electric dipole transition selection rules require $L'$=1 in the excited state for transitions from the $L$=0 ground state; hence we ignore contributions to the $(2)^3\Pi_0$ states from any other atomic angular momentum states. Second, since $S'$=1 in the triplet excited state, the $\Delta S$=0 selection rule requires that only the $S$=1 part of the ground state can contribute to the transition matrix element. Third, the only permissible combinations of the projections of $L', S'$ ($\Lambda', \Sigma'$, respectively) are those such that $\Omega' = \Lambda' + \Sigma' = 0$. Last, we choose the combinations of $|L', \Lambda', S', \Sigma', \Omega'\rangle$ that have the appropriate molecular symmetries [67]. This yields

$$|^3\Pi_{\Omega'=0^+}\rangle_{\mathrm{BF}} = \frac{1}{\sqrt{2}}\big(|1,-1,1,1,0\rangle_{\mathrm{BF}} - |1,1,1,-1,0\rangle_{\mathrm{BF}}\big), \tag{3.18}$$
$$|^3\Pi_{\Omega'=0^-}\rangle_{\mathrm{BF}} = \frac{1}{\sqrt{2}}\big(|1,-1,1,1,0\rangle_{\mathrm{BF}} + |1,1,1,-1,0\rangle_{\mathrm{BF}}\big). \tag{3.19}$$

### Electronic Wavefunction in the Space-Fixed Frame

We next transform from the body-fixed frame associated with the molecule to the space-fixed frame that we have used to describe the atomic scattering state. From Zare [85], we have

$$\sqrt{\frac{2J'+1}{4\pi}} D^{*J'}_{M'\Omega'} |L',\Lambda',S',\Sigma',\Omega'\rangle_{\mathrm{BF}} = \sum_{\ell' m_{\ell'}} \sqrt{(2J'+1)(2\ell'+1)}(-1)^{m'_\ell}$$
$$\sum_{M'_L M'_S} \sum_{j' m'_j} (2j'+1) \begin{pmatrix} L' & S' & j' \\ M'_L & M'_S & -m'_j \end{pmatrix} \begin{pmatrix} L' & S' & j' \\ \Lambda' & \Sigma' & -\Omega' \end{pmatrix}$$
$$\begin{pmatrix} J' & j' & \ell' \\ M' & -m'_j & -m'_\ell \end{pmatrix} \begin{pmatrix} J' & j' & \ell' \\ \Omega' & -\Omega' & 0 \end{pmatrix} |L',M'_L,S',M'_S\rangle\, |\ell',m'_\ell\rangle\,. \quad (3.20)$$

Here $j'$ is a dummy index that runs over the possible values of $L'+S'$, and as usual $m'_j$ takes values from $-j$ to $+j$. With this expression in hand, it is useful to look for selection rules and patterns based on the 3-$j$ symbols. For $L'=S'=1$, the dummy index only takes the values $j'=0,1,2$. We also note that for $^3\Pi$ states of interest here, $\Lambda'=\pm 1$. Based on the antisymmetry of the linear combination of the $\Lambda'=\pm 1$ components of the $^3\Pi_{0^+}$ state and the properties of 3-$j$ symbols, we can conclude that only $j'=1$ terms survive in the excited state wavefunction in this case; similarly, only the $j'=0,2$ components survive for the $^3\Pi_{0^-}$ state.

The excited molecular state wavefunction for a single hyperfine sublevel can then be written as

$$|e(J',M',M'_{I(\mathrm{Rb})},M'_{I(\mathrm{Cs})}\rangle = \quad (3.21)$$
$$|\Omega'=0,J',M',M'_{I(\mathrm{Rb})},M'_{I(\mathrm{Cs})}\rangle =$$
$$\sum_{\substack{\ell' m'_\ell \\ M'_S M'_L}} B(J',M',M'_L,M'_S,\ell',m'_\ell)\, |L',M'_L,S',M'_S\rangle\, |I'_{\mathrm{Rb}},M'_{I(\mathrm{Rb})}\rangle\, |I'_{\mathrm{Cs}},M'_{I(\mathrm{Cs})}\rangle\, |\ell',m'_\ell\rangle\,,$$

where $B(J', M', M'_S, M'_L, \ell', m'_\ell)$ is the sum of the expression before the kets on the right-hand side of Equation 3.6.2, arising from both components of the relevant body-fixed $\Omega'$=0 state from Eq. 3.19.

### 3.6.3 Calculating Matrix Elements

With these expressions for the atomic scattering and excited molecular states, we are ready to calculate the desired transition matrix elements. Electric dipole transitions only affect $|L, M_L\rangle_{SF}$, with the selection rules $\Delta L$=1, $\Delta M_L$=0,±1; all other quantum numbers must remain unchanged. Thus we require matrix elements of the form $\langle 1 M'_L | d_\sigma | 00 \rangle$, where $\sigma$ denotes the polarization of the PA laser in the space-fixed frame. For convenience we can define the direction of the linear laser polarization as the quantization axis, and then calculate only $\langle 1 M'_L | d_z | 00 \rangle$ transition matrix elements. This picks out only the $M'_L$=0 components of the excited state, which implies $m'_j$=$M'_S$. Hence, we can write the components of an $\Omega'$=0 state that can be linked to the scattering state, denoted by the tilde, as

$$\sqrt{\frac{2J'+1}{4\pi}} D^{*J'}_{M'\Omega'} |\widetilde{\Omega'=0}\rangle_{BF} = \sum_{\substack{\ell' m'_\ell \\ M'_S}} B(J', M', 0, M'_S, \ell', m'_\ell) \, |1, 0, 1, M'_S\rangle \, |\ell', m'_\ell\rangle \,, \qquad (3.22)$$

where we have substituted the specific values of $L'$, $M'_L$, and $S'$.

As an example, we can write the matrix element between an initial scattering state and a single hyperfine sublevel in an $\Omega'$=$0^+$ state as

$$\langle e(\Omega'=0^+,J',M',M'_{I(\mathrm{Rb})},M'_{I(\mathrm{Cs})})|d_z|g(M_{F(\mathrm{Rb})},M_{F(\mathrm{Cs})},\ell,m_\ell)\rangle =$$

$$3\sqrt{2}\sum_{\ell' m'_\ell}\sqrt{(2J'+1)(2\ell'+1)}(-1)^{m'_\ell}\sum_{M'_S}\begin{pmatrix}1 & 1 & 1\\ 0 & M'_S & -M'_S\end{pmatrix}\begin{pmatrix}1 & 1 & 1\\ 1 & -1 & 0\end{pmatrix}$$

$$\begin{pmatrix}J' & 1 & \ell'\\ M' & -M'_S & -m'_\ell\end{pmatrix}\begin{pmatrix}J' & 1 & \ell'\\ 0 & 0 & 0\end{pmatrix}\sum_{\substack{SM_S\\ M_{I(\mathrm{Rb})}\\ M_{I(\mathrm{Cs})}}}A(S,M_S,M_{I(\mathrm{Rb})},M_{I(\mathrm{Cs})})\langle 10|d_z|00\rangle$$

$$\delta_{1S}\delta_{M'_S M_S}\delta_{\ell'\ell}\delta_{m'_\ell m_\ell}\delta_{M'_{I(\mathrm{Rb})}M_{I(\mathrm{Rb})}}\delta_{M'_{I(\mathrm{Cs})}M_{I(\mathrm{Cs})}}, \quad (3.23)$$

where $A(S,M_S,M_{I(\mathrm{Rb})},M_{I(\mathrm{Cs})})$ is defined as above and $\delta$ denotes a Kronecker delta. The atomic electronic matrix element $\langle 10|d_z|00\rangle$ is common to all matrix elements of interest here, and all remaining factors are standard angular momentum coupling coefficients that can be easily calculated.

### 3.6.4 Accounting for Unresolved Hyperfine Structure in the Excited State

When calculating the relative populations in each excited rotational level, $J'$, we must exercise some caution in correctly accounting for the unresolved hyperfine structure in the excited state. We first consider a toy system of transitions from a well-defined initial scattering state, $|0\rangle$, to two degenerate excited levels $|1\rangle, |2\rangle$. It is easy to show that transitions will be allowed to a particular normalized, linear superposition of the two degenerate levels, the so-called bright state. Conversely, there will be no transitions to the orthogonal, normalized, linear superposition of the two levels, the dark state.

To calculate the matrix element to the bright state, consider the dipole matrix elements to each of the degenerate levels denoted as $a_n=\langle 0|d_z|n\rangle$. Then we can construct an un-normalized dark state $|D\rangle \propto \frac{1}{a_1}|1\rangle - \frac{1}{a_2}|2\rangle$, such that $\langle 0|d_z|D\rangle = 0$, as well as the

orthogonal, normalized bright state, $|B\rangle$, where

$$|B\rangle = \frac{a_1}{\sqrt{a_1^2 + a_2^2}} |1\rangle + \frac{a_2}{\sqrt{a_1^2 + a_2^2}} |2\rangle . \tag{3.24}$$

From this we conclude that the dipole matrix element, $a_B = \langle 0|d_z|B\rangle$, to the bright state $|B\rangle$ is given by

$$a_B = \frac{a_1^2}{\sqrt{a_1^2 + a_2^2}} + \frac{a_2^2}{\sqrt{a_1^2 + a_2^2}} = \sqrt{a_1^2 + a_2^2}. \tag{3.25}$$

This result can easily be generalized to account for $N$ degenerate levels; we find that the matrix element to the single bright state in this case is the quadrature sum of the $N$ values of $a_n$: $a_B = \sqrt{\sum_n a_n^2}$.[5]

Thus to find the transition strength from an initial scattering state $|M_{F(\mathrm{Rb})}, M_{F(\mathrm{Cs})}, \ell, m_\ell\rangle$ to all of the unresolved sublevels within a particular rotational level, $J'$, we square the quadrature sum of the matrix elements to the unresolved sublevels in the excited state to find the total squared matrix element, $|\langle d\rangle|^2$, given by

$$|\langle d(M_{F(\mathrm{Rb})}, M_{F(\mathrm{Cs})}, \ell, m_\ell, J')\rangle|^2 = \tag{3.26}$$
$$\sum_{\substack{M' \\ M'_{I(\mathrm{Rb})} \\ M'_{I(\mathrm{Cs})}}} |\langle \Omega' = 0, J', M', M'_{I(\mathrm{Rb})}, M'_{I(\mathrm{Cs})}|d_z|M_{F(\mathrm{Rb})}, M_{F(\mathrm{Cs})}, \ell, m_\ell\rangle|^2.$$

We sum this result over $M_{F(\mathrm{Rb})}$, $M_{F(\mathrm{Cs})}$, and $m_\ell$ to calculate the contribution of a particular partial wave to the signal for a particular rotational level, $W(J', \ell)$, given by

$$W(J', \ell) = \sum_{\substack{m_\ell \\ M_{F(\mathrm{Rb})} \\ M_{F(\mathrm{Cs})}}} |\langle d(M_{F(\mathrm{Rb})}, M_{F(\mathrm{Cs})}, \ell, m_\ell, J')\rangle|^2. \tag{3.27}$$

To more clearly identify the relative sizes of the partial wave contributions, we normalize the calculated values for $W(J', \ell)$ in a given electronic state by the same value to yield

[5]This construction of properly normalized states is essentially just a form of Gram-Schmidt orthonormalization applied to the particular case of quantum mechanical state coupling [86].

| $^3\Pi_{0^+}$ | $J'$=0 | $J'$=1 | $J'$=2 | $J'$=3 | $J'$=4 | $J'$=5 |
|---|---|---|---|---|---|---|
| $\ell$=0 | 0 | 1 | 0 | 0 | 0 | 0 |
| $\ell$=1 | 1 | 0 | 2 | 0 | 0 | 0 |
| $\ell$=2 | 0 | 2 | 0 | 3 | 0 | 0 |
| $\ell$=3 | 0 | 0 | 3 | 0 | 4 | 0 |
| $^3\Pi_{0^-}$ | $J'$=0 | $J'$=1 | $J'$=2 | $J'$=3 | $J'$=4 | $J'$=5 |
| $\ell$=0 | 1.1 | 0 | 0.56 | 0 | 0 | 0 |
| $\ell$=1 | 0 | 4 | 0 | 1 | 0 | 0 |
| $\ell$=2 | 0.56 | 0 | 6.3 | 0 | 1.4 | 0 |
| $\ell$=3 | 0 | 1 | 0 | 8.8 | 0 | 1.9 |

Table 3.1: Calculated partial wave contributions, $\tilde{W}(J',\ell)$, from all $M_{F(\mathrm{Rb})}, M_{F(\mathrm{Cs})}$ combinations to purely Hund's case (a) $^3\Pi_0(|\Lambda'|=1,\ S'=1)$ state, deeply-bound PA levels. Tilde denotes that all calculated values of $W(J',\ell)$ within a given electronic state were normalized by the same value. $\tilde{W}(J',\ell)$ implies forbidden transitions. Calculated values are identical for $^{85}$RbCs ($F_{\mathrm{Rb}}$=2, $F_{\mathrm{Cs}}$=3) and ($F_{\mathrm{Rb}}$=3, $F_{\mathrm{Cs}}$=4) as well as $^{39}$K$^{85}$Rb ($F_{\mathrm{Rb}}$=2, $F_{\mathrm{K}}$=1).

$\tilde{W}(J',\ell)$. Values for $\tilde{W}(J',\ell)$ for low-lying rotational levels and partial waves, $\ell$, for both $\Omega'=0^+, 0^-$ states, are given in Table 3.1. Although our calculations initially focused on the particular case of $^{85}$RbCs with both atoms in their lower hyperfine states ($F_{\mathrm{Rb}}$=2, $F_{\mathrm{Cs}}$=3, $I_{\mathrm{Rb}}$=5/2, $I_{\mathrm{Cs}}$=7/2), we have calculated $W(J',\ell)$ for other cases as well. Specifically, we find that for $^{39}$K$^{85}$Rb in the lower hyperfine state ($F_{\mathrm{Rb}}$=2, $F_{\mathrm{K}}$=1, $I_{\mathrm{Rb}}$=5/2, $I_{\mathrm{K}}$=3/2) as well as $^{85}$RbCs with both atoms in their upper hyperfine states ($F_{\mathrm{Rb}}$=3, $F_{\mathrm{Cs}}$=4) the values of $\tilde{W}(J',\ell)$ are the same as those in Table 3.1. Later, in our discussion of deeply-bound PA, we detail the conversion of $\tilde{W}(J',\ell)$ into signal sizes for different rotational levels and atomic temperatures.

## 3.7 Summary

Here we have detailed the photoassociation process that transforms colliding ultracold atoms into excited diatomic molecules. Following the established theoretical treatment, the photoassociation rate can be calculated as a function of the PA laser intensity and elec-

tric dipole transition matrix element between the atomic scattering and molecular bound states. This matrix element is then factored under the Born-Oppenheimer approximation, and the RKR technique is applied to calculate the relevant Franck-Condon factor that governs the nuclear portion the transition. To calculate the remaining electronic component of the matrix element, we have developed a formalism that compares the rotational line strengths in PA as a function of rotational level and scattering partial wave for two particular molecular symmetries. Putting all of this together yields analysis that predicts the PA rates for many different rovibrational levels.

In the next two chapters, we discuss two very different photoassociative regimes. First, we show results from PA at very large internuclear separation and the weakly-bound ground state molecules that are formed as a result. Second, we analyze PA at very short-range and the subsequent formation of deeply-bound molecules.

# Chapter 4

# Weakly-Bound Photoassociation

## 4.1 Introduction

The initial thrust of this work was to extend the successful formation of weakly-bound molecules via long-range PA and subsequent population transfer to the vibronic ground state achieved in the work of Sage *et al.* [87]. In these experiments, PA was observed to many weakly-bound excited states in $^{85}$RbCs [45]. It was then determined that many vibrational states in the electronic ground $a^3\Sigma^+$ state were populated following radiative stabilization. One particular vibrational level was found to be heavily populated after spontaneous decay from an $\Omega = 0^-$ state near 897 nm [88]. Using Stimulated Emission Pumping (SEP), molecules from this particular vibrational level ($v$=36) were transferred to the vibrational ground state of the $X^1\Sigma^+$ state, demonstrating the first creation of a sample of ultracold vibronic ground state polar molecules.

This thesis initially sought to improve the transfer efficiency by implementing a more sophisticated process known as Stimulated Raman Adiabatic Passage (STIRAP). This involved the technological development of numerous laser systems as well as narrowband spectroscopy of the relevant molecular levels involved in the transfer process. Further, we refined the use of an optical trap first integrated into the experiment in the thesis work of Nathan Gilfoy [89]. Although this particular scheme for creating ground state polar

molecules was ultimately abandoned, many of the techniques developed during this stage of the experiment are directly applicable to the future work of this experiment.

### 4.1.1 Long-Range PA to the $\Omega = 0^-$ State at 897 nm

Photoassociation to weakly-bound, electronically-excited levels takes advantage of the potentially large Franck-Condon factors that can exist between the atomic scattering and molecular PA states. It is easy to show that the scattering state amplitude is maximized at large internuclear separation through a straightforward implementation of the WKB approximation [40]. In order to achieve the high PA rates made possible by large free-to-bound FCFs, the Franck-Condon principle requires that the PA state also have a large wavefunction amplitude at long-range. A second application to the Franck-Condon principle then dictates that spontaneous decay will favor population of electronic ground states with similarly large internuclear separation.

Beyond the large free-to-bound Franck-Condon factors and correspondingly high PA rates, the molecular structure of an $\Omega = 0$ state greatly simplifies interpretation of the spectra. Specifically, $\Omega = 0$ states have no first-order magnetic hyperfine structure, as the atomic nuclear spins have no projection of the electronic angular momentum to which they can couple. Thus, as long as the electric quadrupole hyperfine structure is too small to be resolved, the PA spectrum is a simple rotational progression with rotational energy $B_e J(J+1)$, where $B_e$ is the PA state rotational constant and $J$ is the PA state rotational level. Further, we can take advantage of the relevant electric dipole selection rules to determine which levels will be populated following spontaneous decay. From the electronic symmetry of the $\Omega = 0^-$ state at 897 nm, the $X^1\Sigma^+(\Omega = 0^+)$ electronic ground state will not be populated by single photon decay due to the $\Omega = 0^- \nrightarrow \Omega = 0^+$ selection rule. The $a^3\Sigma^+$ state, which has $\Omega = 0^-, 1$ components, however, will be populated.

### 4.1.2 Radiative Stabilization to $a^3\Sigma^+$ ($v$=36)

There are, however, no explicit selection rules constraining which vibrational levels can be populated in the electronic ground states. Instead, the population fractions are given by the branching ratios, which are largely set by the bound-to-bound Franck-Condon factors. Thus numerous vibrational levels are populated following spontaneous decay. One particular PA state was found to have very strong decay to a particular vibrational level of the $a^3\Sigma^+$ state ($v$=36) with $\sim$ 5% branching [82]. This significant population in a single vibrational level presented a very promising state from which molecules could be transferred to the vibrational ground state of the $X^1\Sigma^+$ state.

### 4.1.3 Stimulated Emission Pumping to $X^1\Sigma^+$ ($v$=0)

In order to reach the ground state, Sage *et al.* [87] used a stimulated two-photon process, known as Stimulated Emission Pumping [90]. Two photons were necessary for two reasons. First, the bound-to-bound FCF between the $a^3\Sigma^+(v=36)$ and $X^1\Sigma^+(v=0)$ is negligibly small. Hence, the transition matrix strength between the two states is essentially zero. Second, direct transitions between the triplet $a^3\Sigma^+$ and singlet $X^1\Sigma^+$ states are nominally spin-forbidden. These seeming prohibitions can be overcome by using a two-step process through an intermediate state where the individual transition strengths are sufficiently large.

The requirements of the intermediate state are detailed in [91]. First, the simultaneously large FCFs with both the $a^3\Sigma^+(v=36)$ and $X^1\Sigma^+(v=0)$ states determine the intermediate state's inner and outer turning points. Specifically, the Franck-Condon principle requires that the intermediate state's inner turning point overlap the bottom of the $X^1\Sigma^+$ potential while its outer turning point overlap the inner turning point of the $a^3\Sigma^+(v=36)$ state. Second, the intermediate state must possess sufficient mixing of singlet and triplet potentials. For heavy alkali atoms like Rb and Cs, the spin-orbit interaction often provides the requisite mixing.

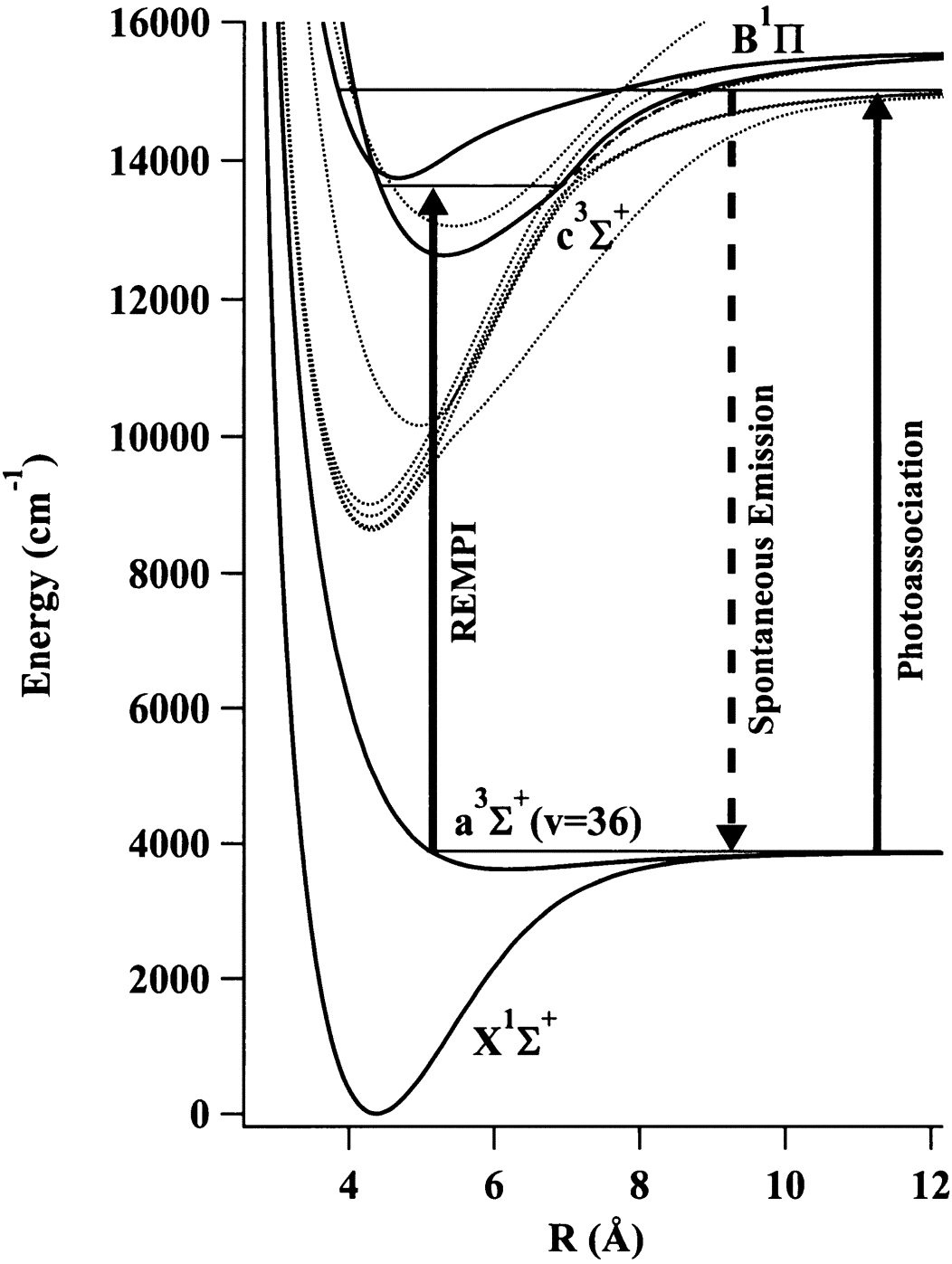


Figure 4.1: Potentials involved in weakly-bound PA and depletion spectroscopy. Molecules are photoassociated at long-range to a weakly-bound molecular state. The molecules quickly spontaneously decay and heavily populate the $a^3\Sigma^+(v{=}36)$ state. The molecules are then detected through resonant photoionization through the excited $c^3\Sigma^+$ state.

### Spin-Orbit Coupling of Singlet and Triplet Potentials

To understand the nature of the spin-orbit operator as it pertains to molecules, we follow the treatment of [67] very carefully. The relevant term in the Hamiltonian can be approximated as:

$$H_{so}^{(e)} = \sum_i a_i(R) T^1(\mathbf{l}_i) \cdot T^1(\mathbf{s}_i) \tag{4.1}$$

where $a_i(R)$ is an internuclear separation-dependent function, $\mathbf{l_i}$ ($\mathbf{s_i}$) is the orbital (spin) angular momentum of the $i$th electron, and $T^1$ denotes a rank-1 tensor. All wavefunction mixing comes from matrix elements of the form:

$$\begin{aligned} &\langle \eta, \Lambda; S, \Sigma | \, H_{so}^{(e)} \, | \eta', \Lambda'; S', \Sigma' \rangle = \\ &\sum_q (-1)^q \sum_i \langle \eta, \Lambda | \, a_i T^1_{-q}(\mathbf{l}_i) \, | \eta', \Lambda' \rangle \, \langle S, \Sigma | \, T^1_q(\mathbf{s}_i) \, | S', \Sigma' \rangle \end{aligned} \tag{4.2}$$

Using the Wigner-Eckart theorem on the $S$, $\Sigma$ portion yields

$$\langle S, \Sigma | \, T^1_q(\mathbf{s}_i) \, | S', \Sigma' \rangle = (-1)^{S-\Sigma} \begin{pmatrix} S & 1 & S' \\ -\Sigma & q & \Sigma' \end{pmatrix} \langle S | \, | T^1(\mathbf{s}_i) | \, | S' \rangle \tag{4.3}$$

where the double bars denote a reduced matrix element. Putting this all together yields

$$\begin{aligned} &\langle \eta, \Lambda; S, \Sigma | \, H_{so}^{(e)} \, | \eta', \Lambda'; S', \Sigma' \rangle = \\ &\sum_q (-1)^q (-1)^{S-\Sigma} \begin{pmatrix} S & 1 & S' \\ -\Sigma & q & \Sigma' \end{pmatrix} \sum_i \langle \eta, \Lambda | \, a_i T^1_{-q}(\ell_i) \, | \eta', \Lambda' \rangle \, \langle S | \, | T^1(\mathbf{s}_i) | \, | S' \rangle \end{aligned} \tag{4.4}$$

From this expression, it is possible to extract the relevant selection rules. Specifically, we have $\Delta S = 0, \pm 1$, $\Delta\Lambda = 0, \pm 1$, $\Delta\Sigma = 0, \mp 1$. This means that it is possible to have mixing between singlet and triplet states that have the same value of $\Omega = \Lambda + \Sigma$. The potential used for the intermediate transfer state is the $c^3\Sigma^+$ state, mixed with the nearby $B^1\Pi$ state. There is an additional potential ($b^3\Pi_1$), but this triplet state does not couple to the absolute ground state, so we will ignore it. Now we recall the Hund's case (a)

spectroscopic notation, $^{2S+1}\Lambda$, from which we infer that the $c^3\Sigma^+$ ($\Lambda$=0, $S$=1, $\Sigma$=0,1) has $\Omega = 0^-$,1 components, while the $B^1\Pi$ ($\Lambda$=1, $S$=$\Sigma$=0) state has only $\Omega = 1$. Thus in order to reach the absolute ground state, which has $\Omega = 0^+$ symmetry, it is necessary to use the $\Omega = 1$ component of the intermediate state potential, which is separated from the $\Omega = 0^-$ component by $\approx 8$ cm$^{-1}$. This complicates the necessary spectroscopy, as the large nuclear spins of RbCs can couple to a non-zero value of $\Omega$, giving rise to hyperfine structure. Further, each rotational level for the $\Omega$=1 component is actually an $\Omega$-doublet, consisting of two closely spaced levels of opposite parity. Both phenomena introduce many more spectroscopic features that are nontrivial to assign.[1]

### Successes, Limitations, and Drawbacks

Using two pulsed dye lasers, Sage *et al.* were able to transfer population from the $a^3\Sigma^+$ ($v$=36) state to the $X^1\Sigma^+$ ($v$=0) level, resulting in a vibronic ground state molecular formation rate of ~500 molecules/s [87]. This was the first realization of a sample of ultracold vibronic ground state polar molecules and was a major achievement in the now rapidly developing field of ultracold molecular physics.

There are, however, two primary limitations to the work done using Stimulated Emission Pumping. First, the pulsed lasers used to transfer population from the heavily populated $v$=36 level in the $a^3\Sigma^+$ state are spectrally broad (~0.3 cm$^{-1}$). This means that molecular structure on scales smaller than this, such as hyperfine and rotational splitting, is not resolved. Second, the molecules that were transferred to the vibrational ground state were not trapped. The MOTs that hold the atomic samples do not trap molecules, and the molecules subsequently fall away from the detection region. Thus in order to study the molecules on time scales longer than ~10 ms, it is necessary to trap the molecules.

The second problem was partially addressed in the thesis of Nathan Gilfoy at Yale [51]. In this work, a powerful $CO_2$ laser was used to create an optical trap that held weakly-

[1]There is another candidate pair of potentials mixed by the spin-orbit interaction, $b^3\Pi_{0+}/A^1\Sigma^+$ ($\Omega = 0^+$). This pair benefits from the simpler spectroscopy associated with an $\Omega = 0$ state, but the necessary laser frequency for the first transfer step is difficult to reach with a pulsed dye laser.

bound molecules in the $a^3\Sigma^+$ state as they were created by PA. He and collaborators went on to measure inelastic scattering rates for collisions between these vibrationally-excited molecules and atoms for a number of different vibrational levels [89].

## 4.2 Proposed Stimulated Raman Adiabatic Passage (STIRAP) to $X^1\Sigma^+$ ($v$=0)

In order to address the problem of poor rotational selectivity in population transfer, a more sophisticated process was proposed in Sage [82]. The process, known as Stimulated Raman Adiabatic Passage (STIRAP), replaces the pulsed lasers used in SEP with two narrowband CW lasers employed in a so-called counterintuitive pulse sequence [92]. This more complicated system of population transfer has numerous advantages over the technologically and spectroscopically simpler SEP method. First, the narrow spectral linewidth of CW diode lasers ($\sim$1 MHz) trivially resolves features like rotational and hyperfine structure in many of our relevant states. Second, the theoretical maximum transfer efficiency of STIRAP approaches 100%, whereas that in SEP is limited to 25% due to the incoherent excitation provided by our pulsed dye laser system. Third, given the coherent nature of STIRAP, the transfer process is reversible and does not add any additional entropy into the system. For these reasons, STIRAP has become a very common transfer scheme in ultracold molecular physics. STIRAP transfer of weakly-bound ultracold molecules was first demonstrated in homonuclear $Rb_2$ in [93]. It was later used in heteronuclear KRb formed via Feshbach association in [33] as well as PA in [94].

### 4.2.1 Dressed State Theory

The theoretical treatment of STIRAP has been carefully detailed in [92], and we will follow it closely here to show the method's most salient features. We begin with a three-level system with eigenstates, in the absence of lasers, $|1\rangle$, $|2\rangle$, and $|3\rangle$, shown in Figure 4.2. Here, we will consider transfer from the initial state, $|1\rangle$, to the final state, $|3\rangle$, through the

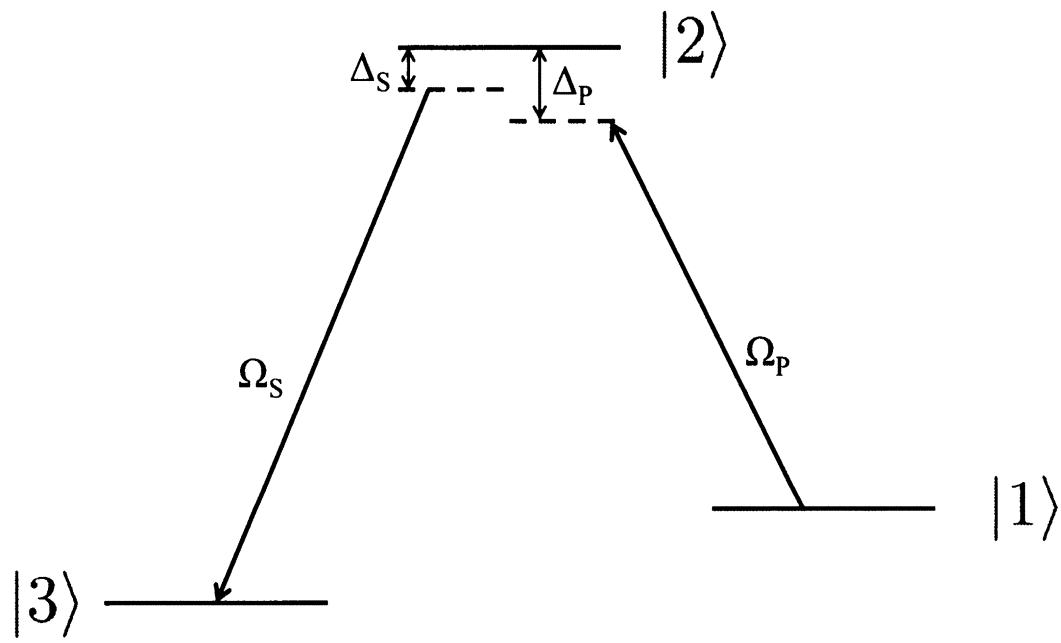


Figure 4.2: Schematic representation of population transfer from initial state, $|1\rangle$, to final state, $|3\rangle$. The $|1\rangle \rightarrow |2\rangle$ transition is generally termed the pump transition, and the $|2\rangle \rightarrow |3\rangle$ transitions is termed the Stokes transition.

potentially lossy intermediate state, $|2\rangle$.

In the case of SEP, a very high instantaneous-power laser pulse incoherently drives many Rabi oscillations throughout the pulse duration, resulting in equal probability to be in state $|1\rangle$ and $|2\rangle$. A second high power laser pulse arrives shortly after (much before the excited state lifetime of $|2\rangle$) and drives many Rabi oscillations incoherently over the sample between states $|2\rangle$ and $|3\rangle$. Hence, probability amplitude is transferred from the initial state, $|1\rangle$, to the final state, $|3\rangle$.

Understanding STIRAP, however, requires a more detailed understanding of the effect of the transfer laser beams on the instantaneous eigenstates of the system. In the dressed state formalism, the time-dependent energy eigenstates are no longer the bare states $|1\rangle$, $|2\rangle$, and $|3\rangle$, but rather linear combinations of these states with amplitudes set by the time-dependent intensities of the transfer lasers. We can write the relevant Hamiltonian in

the interaction picture as:

$$H(t) = \frac{\hbar}{2}\begin{pmatrix} 0 & \Omega_P(t) & 0 \\ \Omega_P(t) & 2\Delta_P & \Omega_S(t) \\ 0 & \Omega_S(t) & 2(\Delta_P - \Delta_S) \end{pmatrix} \tag{4.5}$$

where $\Omega_P(t)$ ($\Omega_S(t)$) is the time-dependent Rabi frequency coupling states $|1\rangle$ and $|2\rangle$ ($|2\rangle$ and $|3\rangle$) and $\Delta_P$ ($\Delta_S$) is the laser detuning from the $|1\rangle \rightarrow |2\rangle$ ($|2\rangle \rightarrow |3\rangle$) transition frequencies.[2]

This can be diagonalized to give the following time-dependent eigenstates $|\alpha\rangle, |\beta\rangle, |\gamma\rangle$:

$$|\alpha\rangle = \sin\Theta \sin\Phi |1\rangle + \cos\Phi |2\rangle + \cos\Theta \sin\Phi |3\rangle \tag{4.6}$$

$$|\beta\rangle = \cos\Theta |1\rangle - \sin\Theta |3\rangle \tag{4.7}$$

$$|\gamma\rangle = \sin\Theta \cos\Phi |1\rangle - \sin\Phi |2\rangle + \cos\Theta \cos\Phi |3\rangle \tag{4.8}$$

where $\tan\Theta = \Omega_P(t)/\Omega_S(t)$ and $\Phi$ is a known function. Figure 4.3 shows the time evolution of the instantaneous eigenvector, $|\beta\rangle$, subjected to Gaussian pulses of equal peak Rabi frequency, $\Omega_0$, with half-width, $T$, in the so-called counterintuitive pulse sequence given by

$$\Omega_P(t) = \Omega_{0(P)} e^{-\left(\frac{t-T/2}{T}\right)^2} \tag{4.9}$$

$$\Omega_S(t) = \Omega_{0(S)} e^{-\left(\frac{t+T/2}{T}\right)^2} \tag{4.10}$$

The transfer process can then be interpreted geometrically, as in Figure 4.4. The state vector, $|\psi\rangle$ begins at time $t$=0 aligned with the bare state vector $|1\rangle$. With the inclusion of the transfer lasers, $|\psi\rangle$ tightly precesses about the new instantaneous eigenstate $|\beta\rangle$. Then as the transfer laser intensities are changed, $|\beta\rangle$ rotates about $|2\rangle$ until $|\beta\rangle$ is aligned with $|3\rangle$. At this point, the probability amplitude of $|\psi\rangle$ is entirely in the final state $|3\rangle$.

Naively, this geometric interpretation appears to have rendered the intermediate state,

[2]In this discussion, the subscript $P$ stands for pump while $S$ stands for Stokes.

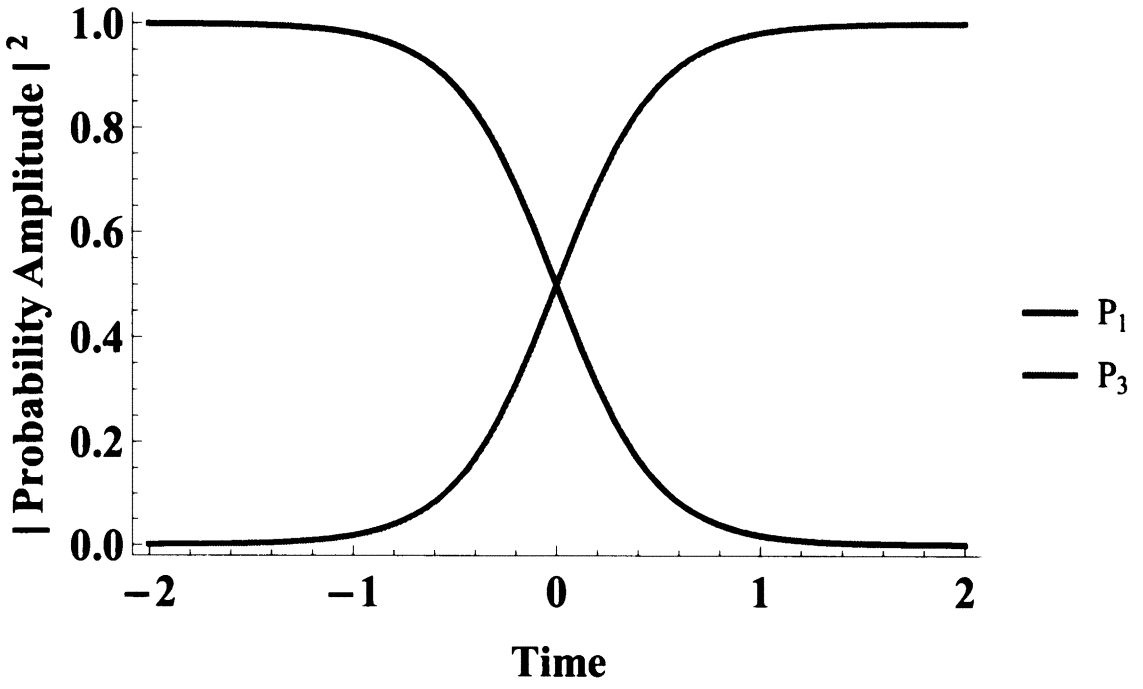


Figure 4.3: Evolution of the probabilities to be in states $|1\rangle$ and $|3\rangle$ during adiabatic evolution using the counterintuitive pulse sequence, where the Stokes laser precedes the pump laser. Stokes and pump Rabi frequencies are modeled with Gaussian time dependence.

$|2\rangle$, completely unnecessary. Its importance can be seen, however, in the time-dependent amplitudes of $|\beta\rangle$. These amplitudes are related to the electric dipole couplings between the bare states. Often, the bare states, $|1\rangle$ and $|3\rangle$, have a vanishingly small transition strength due, in our case, to a negligible Franck-Condon factor as well as a nominally spin-forbidden triplet/singlet transition. By choosing an appropriate intermediate state, however, the couplings between $|1\rangle, |2\rangle$ and $|2\rangle, |3\rangle$, which are largely set $\Omega_S$, $\Omega_P$, can yield Rabi frequencies of tens of MHz for experimentally feasible laser powers.

### 4.2.2 Requirements

Although the theoretical treatment of STIRAP shows the physical mechanism behind the transfer, we must also determine whether the conditions necessary, such as laser power and coherence, are experimentally feasible. In the context of the theoretical treatment presented here, we are interested in determining under what conditions the transfer is adi-

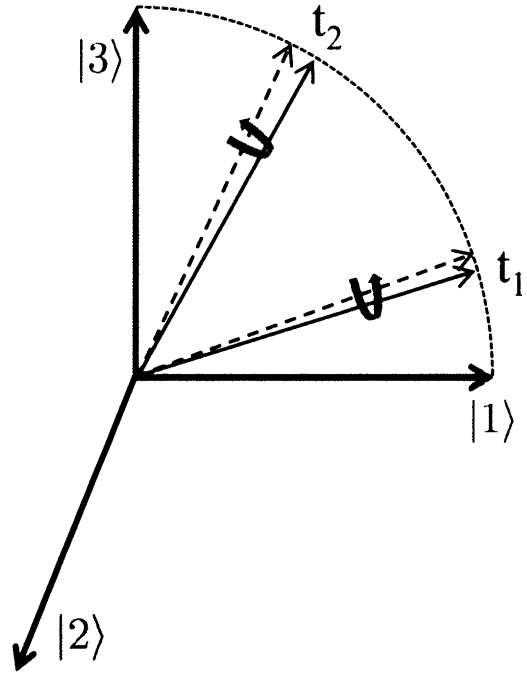


Figure 4.4: Geometrical interpretation of adiabatic rotation of instantaneous eigenvector during the STIRAP process. Molecular state vector, $|\psi\rangle$ (solid arrow), rapidly precesses about instantaneous eigenvector, $|\beta\rangle$ (dashed arrow). $|\beta\rangle$ is adiabatically rotated about the axis defined by the lossy intermediate state, $|2\rangle$, from being aligned with $|1\rangle$ to being aligned with $|3\rangle$. Separation between $|\beta\rangle$ and $|\psi\rangle$ is greatly exaggerated for clarity. $t_1$ is shortly after the transfer has begun, while $t_2$ is closer to the end of the transfer process.

abatic, that is, how closely does the state vector, $|\psi\rangle$, follow the instantaneous eigenvector, $|\beta\rangle$. Returning to the geometric interpretation of STIRAP, violation of the adiabaticity requirement leads to reduced transfer efficiency through the projection of $|\psi\rangle$ on to instantaneous eigenstates other than $|\beta\rangle$.

### High Power CW Laser Requirements

In evaluating the adiabaticity criterion, we first consider the rate of precession of $|\psi\rangle$ about the instantaneous eigenvector $|\beta\rangle$. Crudely, this rate is given by the quadrature sum of the Rabi frequencies $\Omega_P, \Omega_S$ during the transfer process. Thus, this rate must be much larger than the rate at which $|\beta\rangle$ is rotated from $|1\rangle$ to $|3\rangle$. Empirically, the requirement is that

| Transfer Laser | Wavelength (nm) | Transition Dipole ($ea_0$) | $\Omega/\sqrt{I}$ ($\sqrt{\text{s/kg}}$) | Laser Power (mW) |
|---|---|---|---|---|
| Pump | 1018.9 | 0.02 | 22000 | 80 |
| Stokes | 734.2 | 0.07 | 77000 | 7 |

Table 4.1: Summary of transition dipoles, Rabi frequencies, and expected powers for proposed STIRAP transfer. All calculations take into account the rotating-wave approximation. Hence, laser power refers to the value measured by a power meter. Powers are such that an average Rabi frequency of $2\pi \cdot 25$ MHz is reached over a 100 $\mu$m radius.

$\Omega_0 T \gg 10$, where $\Omega_0$ is the peak Rabi frequency and $2T$ is the transfer time [92].

From the RbCs spectroscopy and analysis presented in [95], we can calculate approximate Rabi frequencies per unit square root laser intensity for the pump and Stokes steps of the transfer in the standard way. Using the singlet/triplet mixing fractions and calculated Franck-Condon factors for the candidate intermediate states in [95], previous calculations have estimated the transition dipoles to be $d_P \approx 0.02\ ea_0$ and $d_S \approx 0.07\ ea_0$ between $a^3\Sigma^+(v{=}36)$ and $c^3\Sigma_1^+(v{=}34)$ [96]. The corresponding Rabi frequencies and necessary laser powers for samples confined to a 100 $\mu$m radius trap for both steps are summarized in Table 4.1.

State-of-the-art semiconductor diode lasers are often not capable of delivering sufficient power to the chamber without additional amplification. There are, however, increasingly robust tapered amplifier (TA) modules that are capable of producing tunable single-mode laser powers up to 1-2W at select wavelengths with seed powers of ~10-25 mW. TA systems capable of delivering 100 mW for both the Stokes and pump lasers based on the design in [97] were built for this purpose.

### Frequency Requirements

Given that the adiabaticity criterion requires that the effective Rabi frequency set by pump and Stokes Rabi frequencies be much greater than the inverse STIRAP transfer time, one can, in principle, simply increase the transfer time to the desired value. The limiting time scale in this problem comes from possible dephasing between the transfer lasers [98].

Dephasing results in the projection of $|\psi\rangle$ on to the lossy state $|2\rangle$, reducing overall transfer efficiency. The overall transfer efficiency for Gaussian pulses with equal half-widths and pulse separation, $T$, is given in [98] as

$$\text{Transfer Efficiency} = \frac{1}{3} + \frac{2}{3}e^{-3\gamma T/4} \tag{4.11}$$

where $\gamma$ is the dephasing rate. For $\gamma$=100 kHz and $T$=1 $\mu$s. this yields a transfer efficiency of 95%.

For our system, we can conservatively estimate the dephasing rate between the two lasers by their spectral linewidths. To determine the linewidths of our CW lasers, we built a delayed self-heterodyne system similar to that in [99]. In this scheme, the laser is divided into two paths where one beam is frequency-shifted relative to the other and sent through a long (~5 km) optical fiber. The two beams, which for an optical fiber longer than the laser's coherence length should no longer be correlated, are then recombined on a beam splitter and measured on a fast photodiode with a spectrum analyzer. A schematic diagram of the optical setup is shown in Figure 4.5. The beat note is essentially a convolution of the laser spectrum with itself centered at the frequency difference between the two beam paths [100]. If we model the spectrum as a Lorentzian, the spectral width of the laser is half that of the beat note signal. The results for both a homebuilt diode laser and a Toptica DL100 are in Figure 4.6. Although the width of the DL100 is broader than 100 kHz, it can, in principle, be narrowed with a fast frequency lock based on the Pound-Drever-Hall method [101].

In order to prevent longer term relative frequency drifts, the transfer lasers should be locked to a common reference. This is traditionally done in one of two ways. If available as in [33], a frequency comb can be used to generate an absolute frequency reference. Such frequency comb systems are, however, very expensive and sophisticated, precluding their use in many experiments. Alternatively, one can construct a fixed frequency Fabry-Perot cavity using ultra-low expansion (ULE) glass, as in [94].

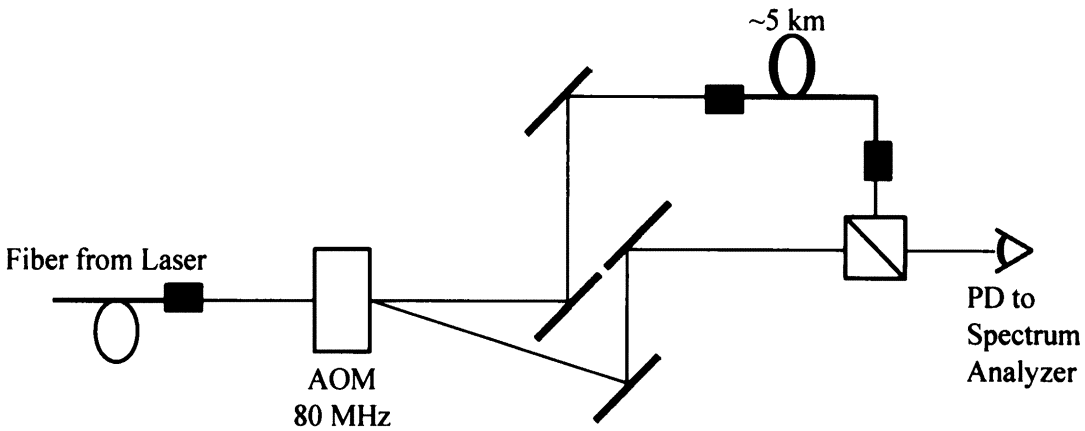


Figure 4.5: Schematic of optical layout for delayed self-heterodyne measurement. The laser beam to be tested is split into two parts separated in frequency by the AOM frequency. One path travels ~5 km to remove correlations between the two beams before they are recombined on a 50/50 beamsplitter and sent to a fast photodiode. The resulting beat note signal, centered at the AOM frequency, is twice as broad as the laser's spectral width.

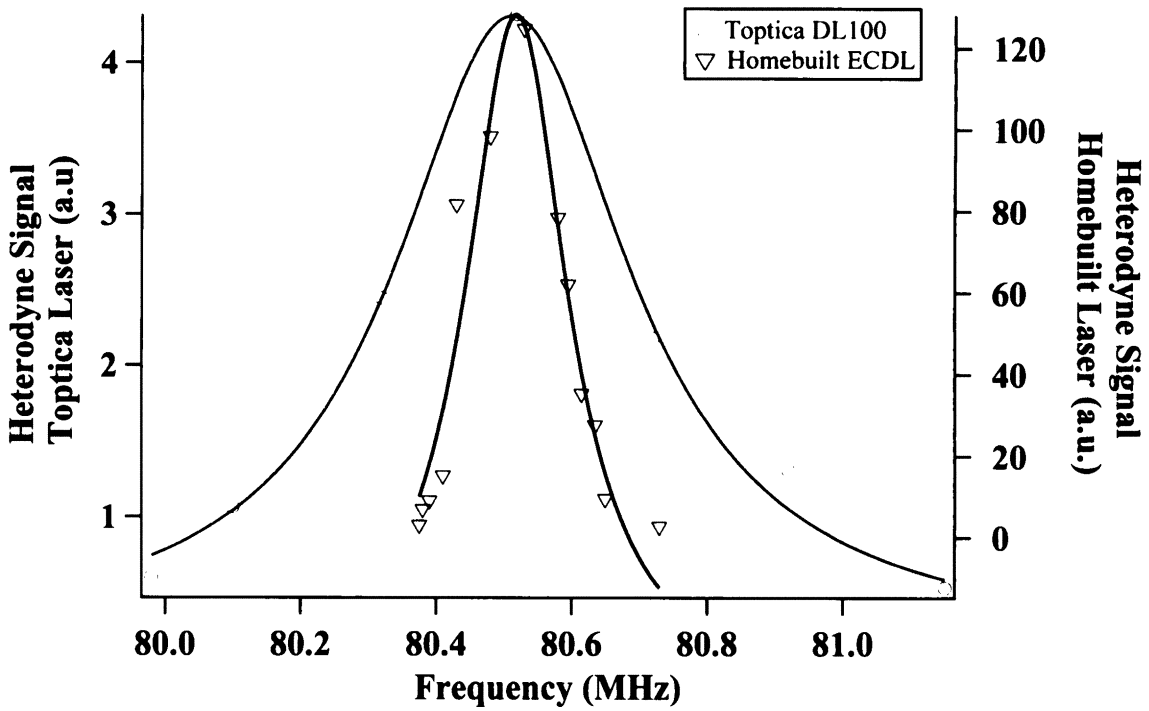


Figure 4.6: Heterodyne beat note curves of homemade ECDL and Toptica DL100. Fits correspond to laser linewidths, $\delta f_{\mathrm{DL100}} \approx 200$ kHz and $\delta f_{\mathrm{ECDL}} \approx 100$ kHz.

## 4.3 Narrowband Spectroscopy

Beyond the technological requirements for efficient state transfer, we have also assumed that we have detailed knowledge of the energies of our initial, intermediate, and final states. At the beginning of this experiment, however, the structure of many of the relevant molecular states was only approximately known. Much of the spectroscopy for our states of interest had been carried out in our group using the spectrally broad pulsed dye laser system [82]. Thus, in order to determine the locations of candidate intermediate states that have adequate transition strengths for both the pump and Stokes transfer steps, we did a great deal of narrowband spectroscopy of the $a^3\Sigma^+ \rightarrow c^3\Sigma^+$ transition near 1020 nm.

### 4.3.1 Molecular Detection

The molecules are photoassociated using widely-tunable light from a Titanium:Sapphire laser (Coherent 899, pumped by a 10 W Verdi laser). We can deliver 300-400 mW of light with a $1/e^2$ power radius of 100-200 $\mu$m to the atoms. We state-selectively detect RbCs molecules using resonance-enhanced multiphoton ionization (REMPI). In our particular 1+1 implementation, a single resonant photon from a pulsed dye laser (energy$\approx$100-300 $\mu$J, $d \approx$4 mm) promotes molecules to an electronically-excited molecular state. Approximately 10 ns later, a non-resonant 532 nm photon from an intense laser pulse (energy$\approx$1 mJ, $d \approx$4 mm) photoionizes the molecule. A strong electric field bias (2 kV) then accelerates the ion to an ion detector. The signal is analyzed by time-of-flight mass spectroscopy to differentiate molecular $RbCs^+$ ions from other atomic and molecular species. The molecular ion signal is calculated by integrating the time-of-flight trace over the appropriate narrow time window corresponding to the arrival of $RbCs^+$. By scanning the frequency of the resonant dye pulse, we can determine which ground states are populated. The laser dyes used to reach different frequency ranges are summarized in Table 4.2.

In the initial phases of this work, we detected the molecular ions using a two-stage chevron microchannel plate (Photonis APD 3025MA). This device generates a current sig-

| Laser dye | Solvent | Dye Concentration ($mg/\ell$) | Stokes Order | Frequency Range ($cm^{-1}$) |
|---|---|---|---|---|
| DCM | DMSO | 0.30 | None | 14600→15870 |
| Pyrromethene 597 | Ethanol | 0.16 | None | 16670→17450 |
| Pyrromethene 580 | Ethanol | 0.20 | 2nd | 9451→9970 |

Table 4.2: Laser dyes and solvents used in this work. To reach IR dye laser frequencies, we use a Raman converter cell (Light Age Model 101 PAL-RC) that can efficiently shift pulsed laser light up or down in frequency by integer multiples of the ground state hydrogen molecule vibrational frequency (4155.25 $cm^{-1}$). The dye laser is pumped by ~200 mJ of 532 nm light from a Quanta Ray PRO YAG laser.

nal through electron multiplication. Specifically, the accelerated molecular ion hits the detector, which releases secondary electrons upon impact. These electrons are accelerated by an internal bias field in the detector, which leads to the release of additional electrons following subsequent collisions with the internal detector walls. The charge is collected at an anode at the end of the detector to yield the signal current. The plate has multiple open channels that allow for electron multiplication of several incident ions over the detector's active area. We capacitively couple the signal from the detector using the high-voltage circuit in Appendix 1, following the design in [102]. Over time, the signal from the microchannel plate degraded and eventually became insufficient for our needs. We believe this may be due to depletion of the amplification region due to reflections from the intense ionizing laser.

In place of the degraded microchannel plate, we used a monolithic Channeltron detector (Detech 2300) coupled with a transimpedance amplifier (Ortec 9301), as had been used in previous generations of this experiment. The Channeltron has only a single electron multiplication region, as opposed to the many channels of the MCP, which generally reduces its linearity when many ions are incident at the same time. This detection method is, however, sufficient for our current spectroscopic needs.

### 4.3.2 Depletion Spectroscopy

The Sirah pulsed dye laser that generates the resonant REMPI photon has a spectral width of approximately 0.3 $cm^{-1}$. As a result, many narrow molecular features are unresolved. Efficient STIRAP transfer, however, requires much more detailed knowledge of the level structure. We stumbled upon the narrowband spectroscopic technique used here quite by accident. Initially, we had intended to use a high power CW tapered amplifier at 1020 nm to replace the resonant pulsed dye laser. The 1020 nm laser frequency was scanned over a known resonance peak, but we failed to measure any $RbCs^+$ production. We continually verified that our MOT and PA lasers were on resonance by occasionally unblocking the pulsed dye laser and seeing $RbCs^+$ ions. On one particular iteration, we neglected to block the 1020 nm laser when unblocking the pulsed dye laser. No molecular ion production was seen, as shown in Figure 4.7. After eliminating other possible causes, we blocked the 1020 nm laser beam and saw the molecular ion signal return.

This technique, often known as depletion spectroscopy, has been used successfully in a number of other cold molecule experiments [103, 104]. In this scheme, the pulsed dye laser frequency for our REMPI detection is fixed to resonantly excite a particular vibrational level in the ground state to another vibrational level in the target excited state, driving transitions from many different hyperfine and rotational levels. This yields the baseline ion signal. The narrowband CW diode laser frequency is then scanned as the ion signal is monitored. When the CW laser is resonant with a transition from the vibrational level addressed by the resonant dye laser pulse, molecules are excited and subsequently spontaneously decay before they can be ionized by the 532 nm laser pulse. Generally, the states populated following this decay are no longer resonant with the pulsed dye laser. Thus, they can no longer contribute to the ion signal when the dye laser pulse arrives, reducing the signal relative to the baseline. In order to simplify the interpretation of our data, we switch between measuring the ion signal with the depletion laser blocked and

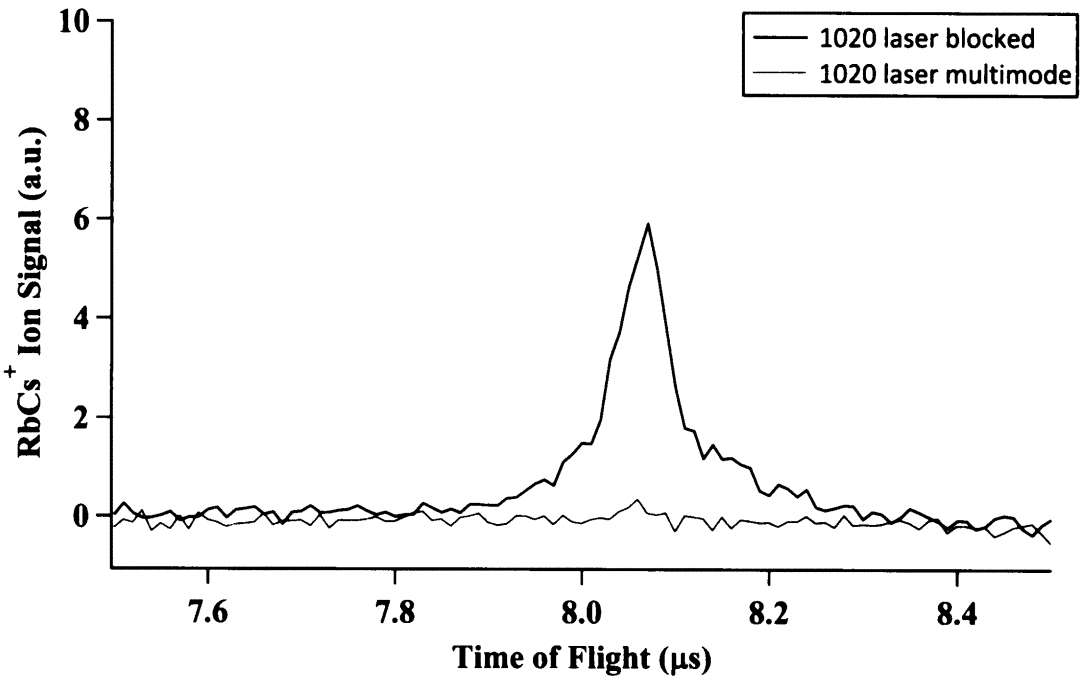


Figure 4.7: Time of flight $RbCs^+$ ion signal during depletion. With the 1020 nm laser blocked, molecules are created and detected. When unblocked, the multimode 1020 nm laser pumps all RbCs molecules present in the $a^3\Sigma^+(v=36)$ state to states that are non-resonant with the REMPI laser. Molecules are then neither ionized nor detected, resulting in no $RbCs^+$ ion signal.

unblocked with every shot and divide the results.[3]

### 4.3.3 Theoretical Treatment

There are a few subtleties worth noting with this method. First, the frequency of the depletion laser need not be within the spectral width of the pulsed dye laser. Rather, any transition that begins with molecules that would otherwise be addressed by the dye laser can be measured. Second, the total amount of signal depletion as a function of depletion laser frequency is in no way a conserved quantity for different experimental parameters, such as laser intensity.

To see how the depletion signal changes as a function of laser intensity, we consider an open two-level model where the excited state spontaneously decays out of the system with

[3]This is essentially a form of lock-in detection.

unit probability. The evolution of the ground state population is given by

$$\dot{n}_{GS} = \gamma_{\mathrm{PA}} - \Gamma_{\mathrm{loss}} n_{GS} - \Gamma_{\mathrm{dep}} n_{GS} \tag{4.12}$$

where $n_{GS}$ is the ground state molecular density, $\gamma_{\mathrm{PA}}$ is the molecular formation rate by photoassociation, $\Gamma_{\mathrm{loss}}$ is the loss rate due to molecules leaving the detection region, and $\Gamma_{\mathrm{dep}}$ is the excitation rate by the depletion laser. At steady-state ($\dot{n}_{GS} = 0$), we find

$$n_{GS} = \frac{\gamma_{\mathrm{PA}}}{\Gamma_{\mathrm{loss}} + \Gamma_{\mathrm{dep}}} \tag{4.13}$$

We then define the remaining fraction, $\mathrm{F_{rem}}$, which is given by the ratio of the depleted molecular density to the molecular density in the absence of depletion (where $\Gamma_{\mathrm{dep}}$ =0), denoted as $\bar{n}_{GS}$. This yields

$$\mathrm{F_{rem}} = \frac{n_{GS}}{\bar{n}_{GS}} = \frac{\gamma_{\mathrm{PA}}}{\Gamma_{\mathrm{loss}} + \Gamma_{\mathrm{dep}}} \frac{\Gamma_{\mathrm{loss}}}{\gamma_{\mathrm{PA}}} = \frac{\Gamma_{\mathrm{loss}}}{\Gamma_{\mathrm{loss}} + \Gamma_{\mathrm{dep}}} \tag{4.14}$$

which yields the intuitive result that in order to see significant depletion, the depletion rate must be much larger than that from other loss mechanisms. If we now assume that $\Gamma_{\mathrm{dep}} \gg \Gamma_{\mathrm{loss}}$, the ground state molecular density evolves as

$$\dot{n}_{GS} = \gamma_{\mathrm{PA}} - \Gamma_{\mathrm{dep}} n_{GS} \tag{4.15}$$

This differential equation can be solved exactly, subject to the initial condition that $n_{GS}(t{=}0){=}\bar{n}_{GS}$ to find

$$n_{GS}(t) = \gamma_{\mathrm{PA}} \left( \frac{1}{\Gamma_{\mathrm{loss}}} - \frac{1}{\Gamma_{\mathrm{dep}}} \right) e^{-\Gamma_{\mathrm{dep}} t} + \frac{\gamma_{\mathrm{PA}}}{\Gamma_{\mathrm{dep}}} \tag{4.16}$$

Scaling this result by the undepleted molecular density, $\bar{n}_{GS}$, we calculate the time-dependent

remaining fraction, $F_{rem}(t)$, which is given by

$$F_{rem}(t) = \frac{n_{GS}(t)}{\bar{n}_{GS}} = \left(\frac{\Gamma_{dep} - \Gamma_{loss}}{\Gamma_{dep}}\right) e^{-\Gamma_{dep} t} + \frac{\Gamma_{loss}}{\Gamma_{dep}} \tag{4.17}$$

Hence for $\Gamma_{dep} \gg \Gamma_{loss}$, the fraction of ground state molecular population remaining after time, $\tau$, is then given by $e^{-\Gamma_{dep}\tau}$. The excitation rate is related to the Rabi frequency, $\Omega$, by [105]

$$\Gamma_{dep} = \frac{\Omega^2}{\gamma} \tag{4.18}$$

where $\gamma$ is the natural linewidth of the transition. Hence we can define an effective saturation condition where only 5% of the ground state population remains when $\Omega^2\tau/\gamma = 3$.

From this expression, we can see for even modest laser powers, the depletion probability quickly goes to unity, due to the very long interaction time (~10 ms). It is important to note, however, that this refers only to one particular transition that may involve only a fraction of the molecules addressed by the pulsed dye laser. Thus, the depletion fraction saturates to the fraction of the baseline molecular population addressed by the depletion laser. As the power of the depletion laser becomes very high, however, the wings of the depletion laser spectrum can become important, as molecules need to scatter only one photon to be pumped away.

To examine the intensity dependence of the feature width, we note that the depletion rate is proportional to the absorption cross-section and thus has the same frequency-dependence [106]. Specifically, the frequency-dependent excitation rate becomes

$$\Gamma_{dep}(\Delta) = \frac{\Omega_R^2}{\gamma} \frac{(\frac{\gamma}{2})^2}{(\frac{\gamma}{2})^2 + \Delta^2} \tag{4.19}$$

where $\Omega_R$ is the resonant Rabi frequency and $\Delta$ is the detuning. In the limit where the feature is broadened much more than the natural linewidth, we have

$$\Gamma_{dep}(\Delta) \simeq \frac{\Omega_R^2 \gamma}{4\Delta^2} \tag{4.20}$$

We expect significant depletion for all frequencies such that $\Gamma_{\rm dep}\tau \geq 1$. Hence, we solve $\Gamma_{\rm dep}\tau = 1$ for $2\Delta$ to find a depletion feature full-width, $\Delta_{\rm dep}$. This yields

$$2\Delta = \Delta_{\rm dep} = \Omega_{\rm R}\sqrt{\gamma\tau} \tag{4.21}$$

For molecular spectra, especially in the presence of hyperfine structure, spectroscopic features are often separated by frequencies on the order of $\Delta_{\rm dep}$ for even modest $\Omega_{\rm R}$. Thus, in order to resolve very fine structure, it is often necessary to carefully control the amount of laser power in the depletion beam. For well isolated features, the depletion width can be used to extract information about the transition matrix element by extracting a measured Rabi frequency for known interaction time, laser intensity, and natural lifetime.

### Population and Structure of the $a^3\Sigma^+$ State

Photoassociation to the weakly-bound $\Omega = 0^-$ state populates numerous vibrational, hyperfine, and rotational levels in the $a^3\Sigma^+$ state. The vibrational splitting of this state ($\sim$1 $cm^{-1}$ near the $v$=36 level) is greater than the spectral width of our pulsed dye laser, and thus we are able to interrogate one single vibrational transition at a time. Hyperfine and rotational structure in the $a^3\Sigma^+$ state were, however, not well understood at the time we took our data. Fortunately, much of the structure of this state has since been beautifully elucidated in [19]. Using high-resolution Fourier transform spectroscopy, the entire electronic potential has now been thoroughly characterized, giving detailed information of the vibrational structure of the $a^3\Sigma^+$ state.

Although it was well known that the $a^3\Sigma^+$ was Hund's case (b), the relative coupling strengths among the electronic spin, atomic nuclear spins, and molecular rotation were not completely understood. It was found that the nuclear spin of Cs, $I_{\rm Cs} = \frac{7}{2}$, couples with the total electronic spin ($S = 1$ for $^3\Sigma^+$) to form a triplet of the intermediate $F_1$. $F_1$ then couples with the nuclear spin of Rb ($I_{\rm Rb} = \frac{5}{2}$) to form an additional sextet of $f$ states. Each $f$ level then has its own rotational structure given by $B_a\ell(\ell+1)$ to give the total

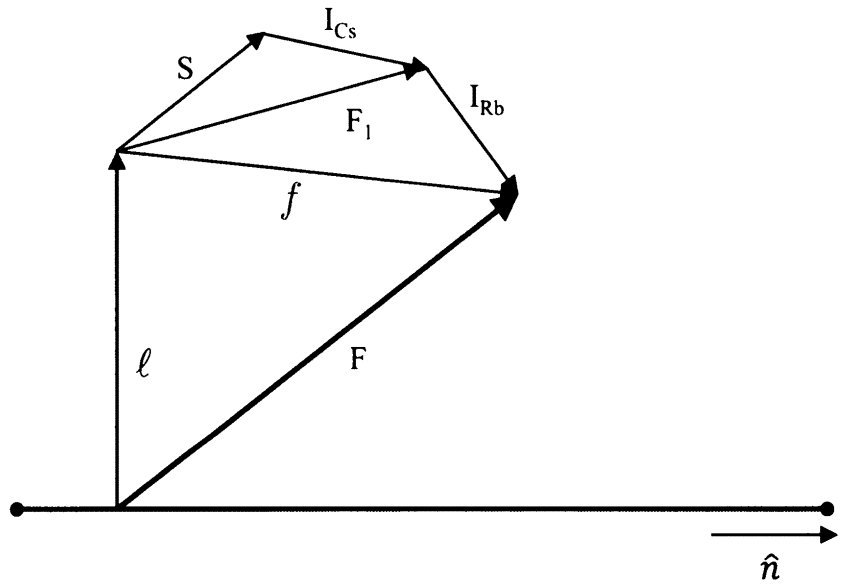


Figure 4.8: Angular momentum recoupling in the $a^3\Sigma^+$ state of RbCs. The atomic hyperfine interaction dominates the energetics of the system for these weakly-bound molecules.

angular momentum $F = f + \ell$. This coupling scheme is shown in Figure 4.8.

To calculate the approximate splittings of the hyperfine components, we can evaluate the diagonal matrix elements of the two dominant terms in the Hamiltonian. Off-diagonal matrix elements and neglected terms in the Hamiltonian will perturb the energy levels, but we expect their effects to be small. From [19], the relevant terms in the Hamiltonian are given by

$$H_{\mathrm{HFS}} = a_{\mathrm{Cs}}(S_{\mathrm{Cs}} \cdot I_{\mathrm{Cs}}) + a_{\mathrm{Rb}}(S_{\mathrm{Rb}} \cdot I_{\mathrm{Rb}}) \tag{4.22}$$

where the atomic ground state hyperfine coupling constants, $a_{\mathrm{Cs}} = 2298.16$ MHz and $a_{\mathrm{Rb}} = 1011.91$ MHz, are given in [107]. This approximate Hamiltonian comes from the fact that the atomic ground state hyperfine structure is much larger than the rotational energy. We can calculate these matrix elements using results from [67] using a careful change of angular momentum labels. If we consider the following coupling scheme

$$S_{\mathrm{Rb}} + S_{\mathrm{Cs}} = S = 1 \tag{4.23}$$

$$S + I_{\mathrm{Cs}} = F_1 \tag{4.24}$$

$$F_1 + I_{\mathrm{Rb}} = f \tag{4.25}$$

then we can use Equations 11.64 and 11.67 from [67] to calculate the desired matrix elements.[4] In particular,

$$\begin{aligned}
&\langle S_{\mathrm{Rb}}, S_{\mathrm{Cs}}, S, I_{\mathrm{Rb}}, I_{\mathrm{Cs}}, F_1, f | a_{\mathrm{Cs}}(S_{\mathrm{Cs}} \cdot I_{\mathrm{Cs}}) | S_{\mathrm{Rb}}, S_{\mathrm{Cs}}, S, I_{\mathrm{Rb}}, I_{\mathrm{Cs}}, F_1, f \rangle = \\
&a_{\mathrm{Cs}}(-1)^{S+F_1+I_{\mathrm{Cs}}+S+S_{\mathrm{Rb}}+S_{\mathrm{Cs}}+1}(2S+1)\sqrt{S_{\mathrm{Rb}}(S_{\mathrm{Rb}}+1)(2S_{\mathrm{Rb}}+1)} \\
&\sqrt{I_{\mathrm{Cs}}(I_{\mathrm{Cs}}+1)(2I_{\mathrm{Cs}}+1)} \begin{Bmatrix} I_{\mathrm{Cs}} & S & F_1 \\ S & I_{\mathrm{Cs}} & 1 \end{Bmatrix} \begin{Bmatrix} S & S_{\mathrm{Rb}} & S_{\mathrm{Cs}} \\ S_{\mathrm{Rb}} & S & 1 \end{Bmatrix}
\end{aligned} \tag{4.26}$$

$$\begin{aligned}
&\langle S_{\mathrm{Rb}}, S_{\mathrm{Cs}}, S, I_{\mathrm{Rb}}, I_{\mathrm{Cs}}, F_1, f | a_{\mathrm{Rb}}(S_{\mathrm{Rb}} \cdot I_{\mathrm{Rb}}) | S_{\mathrm{Rb}}, S_{\mathrm{Cs}}, S, I_{\mathrm{Rb}}, I_{\mathrm{Cs}}, F_1, f \rangle = \\
&a_{\mathrm{Rb}}(-1)^{2F_1+2S+f+S_{\mathrm{Rb}}+S_{\mathrm{Cs}}+I_{\mathrm{Rb}}+I_{\mathrm{Cs}}}(2S+1)(2F_1+1) \\
&\sqrt{S_{\mathrm{Rb}}(S_{\mathrm{Rb}}+1)(2S_{\mathrm{Rb}}+1)}\sqrt{I_{\mathrm{Rb}}(I_{\mathrm{Rb}}+1)(2I_{\mathrm{Rb}}+1)} \\
&\begin{Bmatrix} S & S_{\mathrm{Rb}} & S_{\mathrm{Cs}} \\ S_{\mathrm{Rb}} & S & 1 \end{Bmatrix} \begin{Bmatrix} I_{\mathrm{Rb}} & F_1 & f \\ F_1 & I_{\mathrm{Rb}} & 1 \end{Bmatrix} \begin{Bmatrix} F_1 & S & I_{\mathrm{Cs}} \\ S & F_1 & 1 \end{Bmatrix}
\end{aligned} \tag{4.27}$$

Here the terms in the curly brackets are Wigner $6j$-symbols. The resulting hyperfine energies are summarized in Table 4.3.

Lastly, there is the rotational energy. The large internuclear separations of these vibrationally-excited molecules result in small rotational constants ($B_a \approx 0.003$ cm$^{-1}$) and small rotational energies, calculated using the $a^3\Sigma^+$ potential in [19]. From our detailed knowledge of the quantum numbers of the PA and $a^3\Sigma^+$ states, we can predict the rota-

[4] In Equation 11.64 of [67], we make the following substitutions: $S \to S_{\mathrm{Cs}}, I_H \to S_{\mathrm{Rb}}, G_1 \to S, I_D \to I_{\mathrm{Cs}}, G_2 \to F_1, N \to I_{\mathrm{Rb}}, F \to f$. In Equation 11.67 of [67], we exchange $S \to S_{\mathrm{Rb}}, I_H \to S_{\mathrm{Cs}}, G_1 \to S, I_D \to I_{\mathrm{Cs}}, G_2 \to F_1, N \to I_{\mathrm{Rb}}, F \to f$.

tional levels that will be populated. These results are summarized in Table 4.4. Based on this analysis and in the absence of additional coupling between rotation and the electronic and nuclear angular momenta, we can model the level structure of a vibrational level in the $a^3\Sigma^+$ state. In particular, we would expect a well-resolved triplet (from the coupling of $I_{Cs}$ to $S$) of states whose components are each further split into a sextet by coupling to $I_{Rb}$, where the splittings between the different hyperfine components are given in Table 4.3. Finally, there would be a very-closely spaced rotational progression with energies $B_a\ell(\ell+1)$ associated with each hyperfine component.

#### Structure of the $c^3\Sigma^+$ state

The excited state has two very different components that can be addressed separately in our detection scheme. The $\Omega = 0^-$ component has no first-order magnetic hyperfine structure, and the associated levels follow a simple rotational progression given by $E_{\Omega=0^-} = B_c J_c(J_c+1)$, where $J_c$ is the $c^3\Sigma^+$ state rotational level and $B_c$ is $c^3\Sigma^+$ state rotational constant ($\sim$0.01 cm$^{-1}$) [95].

In the $\Omega = 1$ component, numerous complications arise. Because this state is correlated to the Rb $5s_{1/2}$ + Cs $6p_{1/2}$ asymptote, we expect the Rb hyperfine structure to be comparable to the ground state atomic value ($\sim$3 GHz). The rotational splitting and hyperfine structure due to Cs are expected to be smaller but of similar size with each other, greatly complicating assignment. Further, each rotational level is comprised of a closely-spaced doublet of opposite parity states. This $\Omega$-doublet is also subject to significant Stark shifts from our applied electric fields.

### 4.3.4 Results

We lock the pulsed-dye laser frequency to a transition from the $a^3\Sigma^+(v{=}36)$ state and tune our depletion laser to numerous transitions to different $\Omega = 0^-, 1$ components associated with different vibrational levels of the $c^3\Sigma^+$ state. The dye laser frequency was generally locked to excite the same vibrational transition that was being depleted, although this is

| $F_1$ | $f$ | Energy | Energy (MHz) |
|---|---|---|---|
| $\frac{9}{2}$ | 7 | $\frac{7}{4}a_{\mathrm{Cs}} + \frac{5}{4}a_{\mathrm{Rb}}$ | 5287 |
| | 6 | $\frac{7}{4}a_{\mathrm{Cs}} + \frac{17}{36}a_{\mathrm{Rb}}$ | 4500 |
| | 5 | $\frac{7}{4}a_{\mathrm{Cs}} - \frac{7}{36}a_{\mathrm{Rb}}$ | 3825 |
| | 4 | $\frac{7}{4}a_{\mathrm{Cs}} - \frac{3}{4}a_{\mathrm{Rb}}$ | 3263 |
| | 3 | $\frac{7}{4}a_{\mathrm{Cs}} - \frac{43}{36}a_{\mathrm{Rb}}$ | 2813 |
| | 2 | $\frac{7}{4}a_{\mathrm{Cs}} - \frac{55}{36}a_{\mathrm{Rb}}$ | 2476 |
| $\frac{7}{2}$ | 6 | $-\frac{1}{2}a_{\mathrm{Cs}} + \frac{5}{18}a_{\mathrm{Rb}}$ | -868 |
| | 5 | $-\frac{1}{2}a_{\mathrm{Cs}} + \frac{11}{126}a_{\mathrm{Rb}}$ | -1061 |
| | 4 | $-\frac{1}{2}a_{\mathrm{Cs}} - \frac{1}{14}a_{\mathrm{Rb}}$ | -1221 |
| | 3 | $-\frac{1}{2}a_{\mathrm{Cs}} - \frac{25}{126}a_{\mathrm{Rb}}$ | -1350 |
| | 2 | $-\frac{1}{2}a_{\mathrm{Cs}} - \frac{37}{126}a_{\mathrm{Rb}}$ | -1446 |
| | 1 | $-\frac{1}{2}a_{\mathrm{Cs}} - \frac{5}{14}a_{\mathrm{Rb}}$ | -1510 |
| $\frac{5}{2}$ | 5 | $-\frac{9}{4}a_{\mathrm{Cs}} - \frac{25}{28}a_{\mathrm{Rb}}$ | -6074 |
| | 4 | $-\frac{9}{4}a_{\mathrm{Cs}} - \frac{5}{28}a_{\mathrm{Rb}}$ | -5352 |
| | 3 | $-\frac{9}{4}a_{\mathrm{Cs}} + \frac{11}{28}a_{\mathrm{Rb}}$ | -4773 |
| | 2 | $-\frac{9}{4}a_{\mathrm{Cs}} + \frac{23}{28}a_{\mathrm{Rb}}$ | -4340 |
| | 1 | $-\frac{9}{4}a_{\mathrm{Cs}} + \frac{31}{28}a_{\mathrm{Rb}}$ | -4051 |
| | 0 | $-\frac{9}{4}a_{\mathrm{Cs}} + \frac{5}{4}a_{\mathrm{Rb}}$ | -3906 |

Table 4.3: Hyperfine energies of the $a^3\Sigma^+$ state. For the $F_1 = \frac{9}{2}, \frac{5}{2}$ levels, the hyperfine manifold extends over a frequency range similar to the ground state hyperfine splitting in atomic Rb (2-3 GHz). The $F_1 = \frac{7}{2}$ manifold spans a much narrower range (750 MHz).

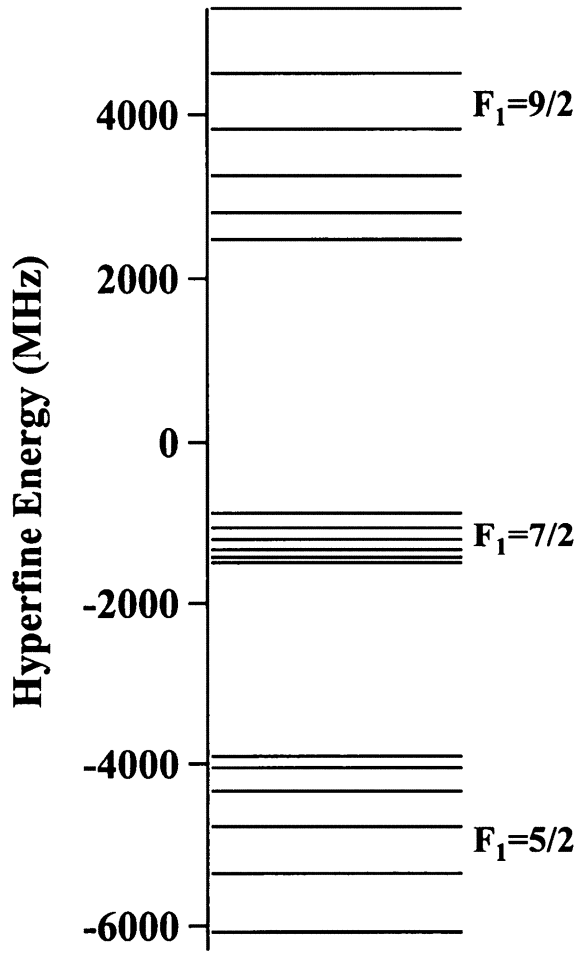


Figure 4.9: Hyperfine splittings of the $a^3\Sigma^+$ state in RbCs. Numerical values for the level locations are reproduced in Table 4.3.

| Electronic State | $\Omega$ | $J$ | $\ell$ | Parity | Rotational Energy |
|---|---|---|---|---|---|
| PA | $0^-$ | 0 | 0,2 | - | $B_{\rm PA}J_{\rm PA}(J_{\rm PA}+1)$ |
| $a^3\Sigma^+$ | $0^-$,1 | 1 | 0 | + | $B_a\ell_a(\ell_a+1)$ |
| $a^3\Sigma^+$ | $0^-$,1 | 1 | 2 | + | $B_a\ell_a(\ell_a+1)$ |
| $c^3\Sigma^+$ | $0^-$ | 0 | 0,2 | - | $B_cJ_c(J_c+1)$ |
| $c^3\Sigma^+$ | $0^-$ | 2 | 0,2 | - | $B_cJ_c(J_c+1)$ |
| | | | | | |
| PA | $0^-$ | 1 | 1,3 | + | $B_{\rm PA}J_{\rm PA}(J_{\rm PA}+1)$ |
| $a^3\Sigma^+$ | $0^-$ | 0 | 1 | - | $B_a\ell_a(\ell_a+1)$ |
| $a^3\Sigma^+$ | $0^-$,1 | 1 | 1 | - | $B_a\ell_a(\ell_a+1)$ |
| $a^3\Sigma^+$ | $0^-$,1 | 2 | 1 | - | $B_a\ell_a(\ell_a+1)$ |
| $a^3\Sigma^+$ | $0^-$,1 | 2 | 3 | - | $B_a\ell_a(\ell_a+1)$ |
| $c^3\Sigma^+$ | $0^-$ | 1 | 1,3 | + | $B_cJ_c(J_c+1)$ |
| $c^3\Sigma^+$ | $0^-$ | 3 | 1,3,5 | + | $B_cJ_c(J_c+1)$ |

Table 4.4: Available quantum numbers and rotational energies for molecular states throughout the photoassociation, spontaneous decay, and depletion processes. Molecules are photoassociated to either $J = 0$ or 1 of the $\Omega = 0^-$ state and then decay to different rotational levels in the $a^3\Sigma^+$ state. The depletion laser then drives transitions to rotational levels of the $c^3\Sigma^+$ state. Multiple values in a single box denote that the corresponding quantum number is not good for that particular molecular state. For the Hund's case (c) PA and $c^3\Sigma^+$ states, $J = L + S + \ell$, with $\Omega = 0$. For the Hund's case (b) $a^3\Sigma^+$ state, $J = N + S \approx \ell + S$.

not necessary. We used less than 5 mW CW laser light ($1/e^2$ power radius $\sim$200 $\mu$m) to deplete the molecular population. The frequency of the depletion laser was simultaneously monitored by a Burleigh wavemeter (WA-1500) and a Fabry-Perot cavity. To normalize the signal, the pulsed dye laser shots were alternately recorded with the depletion laser blocked and unblocked. The two different settings were averaged separately for 100 shots each and then divided to give a normalized ion signal.

### Depletion Spectroscopy on the $a^3\Sigma^+ \rightarrow c^3\Sigma^+_{0^-}$ Transition

Depletion spectroscopy convolves the structure of the initial and target states into a single signal, often resulting in very complicated spectra. By examining the $\Omega = 0^-$ component of the target state, we can greatly simplify the interpretation. The accessible $c^3\Sigma^+$ rotational

levels, $J_c$, for each PA state rotational level, $J_{\rm PA}$, are given in Table 4.4. The transition energies between a rotational progression in the $c^3\Sigma^+$ state and a corresponding rotational progression associated with a particular hyperfine component of the $a^3\Sigma^+$ state are given by

$$E = B_c J_c(J_c+1) - B_a \ell_a(\ell_a+1) + E_0 \tag{4.28}$$

where $E_0$ is a frequency difference that is the same for each transition. From the potentials in [19] and [95], we can crudely approximate the rotational constants, $B_a \approx 0.0028$ cm$^{-1}$ and $B_c \approx 0.01$ cm$^{-1}$.

The Hönl-London factors, which determine the relative populations of the different rotational levels in the $a^3\Sigma^+$ state, $\ell_a$, following spontaneous decay, are not known for this particular long-range PA state. Here we consider two limiting cases. In the first, we assume that only one $a^3\Sigma^+$ state rotational level ($\ell_a = J_{\rm PA}$) is populated. Under this approximation, the splittings between the rotational transitions for different PA rotational states are given by

$$\begin{aligned} \Delta E_{(J_{\rm PA}=0)} &= B_c(2(3)) - B_c(0(1)) = 6B_c \\ \Delta E_{(J_{\rm PA}=1)} &= B_c(3(4)) - B_c(1(2)) = 10B_c \end{aligned} \tag{4.29}$$

Then, based on the analysis of the hyperfine structure, we would expect for a given value of $J_{\rm PA}$, pairs of rotational transitions, separated by the appropriate value in Equation 4.29, associated with each hyperfine component. In the second limiting case, the populations of the two available $a^3\Sigma^+$ state rotational levels for a given $J_{\rm PA}$ are equal, and the transition energies are given by Eq. 4.28, where we include both possible values of $\ell_a$.

From typical $\Omega = 0^-$ depletion spectra, as shown in Figure 4.10, we see two particularly interesting features. First, two very large peaks separated by the correct multiples of the $c^3\Sigma^+$ state rotational constant dominate ($\Delta E_{(J_{\rm PA}=0)}$=0.061 cm$^{-1}$ and $\Delta E_{(J_{\rm PA}=1)}$=0.100 cm$^{-1}$). These frequency splittings have the expected ratio of 6/10 and yield a measured

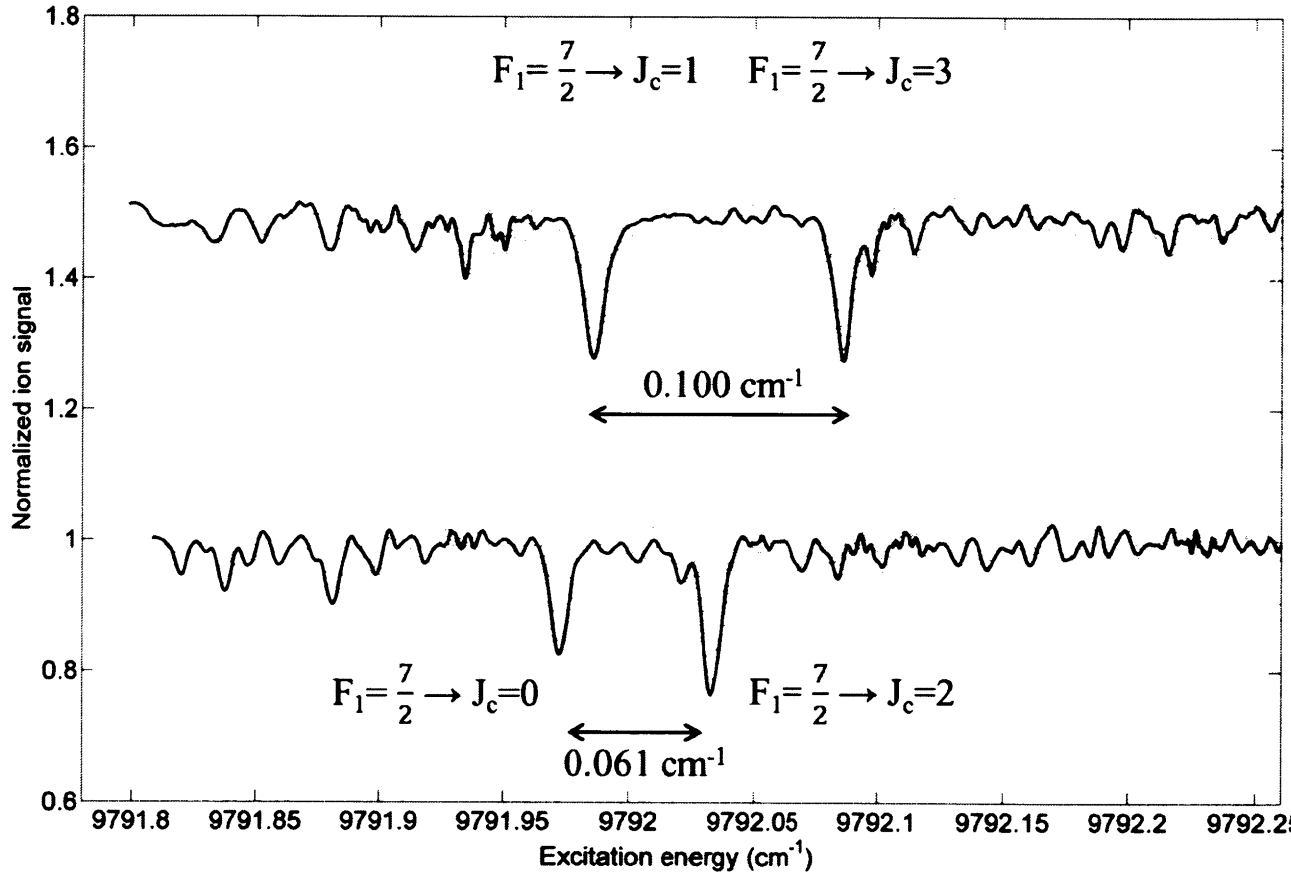


Figure 4.10: Depletion spectroscopy of the $a^3\Sigma^+(v=36) \rightarrow c^3\Sigma^+_{0^-}(v=34)$ transition. Gray dots are normalized depletion data averaged 100 shots per point. Curves are splines smoothed over 70 data points. Lower (upper) trace comes from photoassociation to $J_{PA}=0(1)$. Upper trace is offset vertically for clarity. The large features come from transitions involving the closely spaced $F_1=7/2$ hyperfine components of the $a^3\Sigma^+$ state to well-resolved rotational levels in the $c^3\Sigma^+$ state.

$c^3\Sigma^+$ state rotational constant, $B_c$=0.010 $cm^{-1}$. Second, there are additional smaller features that are also separated by the amount consistent with rotational transitions. Both of these observations are consistent with our analysis of the $a^3\Sigma^+$ hyperfine structure where only the lowest available $a^3\Sigma^+$ rotational level is significantly populated. The large central features are rotational transitions from the relatively densely-packed (and largely unresolved) $f$ states associated with $F_1 = \frac{7}{2}$ to the well-resolved rotational levels of the $c^3\Sigma^+_{0^-}$ state. The remaining smaller features are transitions from well-resolved hyperfine components associated with $F_1 = \frac{9}{2}, \frac{5}{2}$ states.

These main features are reproduced in depletion to different vibrational levels of the $c^3\Sigma^+_{0^-}$ state. As seen in Figure 4.11, the measured rotational splittings are the same to within measurement precision for the $v$=34, 36 levels of the $c^3\Sigma^+_{0^-}$ state. Additional features associated the hyperfine structure of the $a^3\Sigma^+$ state are also reproduced. This gives us high confidence in our understanding of both states.

The depletion spectra to the $\Omega = 0^-$ component of the $c^3\Sigma^+$ state has allowed us to characterize the $a^3\Sigma^+$ state while also giving a measurement of the $c^3\Sigma^+$ rotational structure ($B_c$=0.010 $cm^{-1}$). Using a simple model of equal population in all hyperfine levels of the $a^3\Sigma^+$ state, we can simulate the depletion spectra to the $c^3\Sigma^+_{0^-}$ state, shown in Figure 4.12. The simulation where only the lowest available $a^3\Sigma^+$ rotational level is significantly populated reproduces the qualitative behavior and can be refined further by calculating the expected branching ratios to the $a^3\Sigma^+$ hyperfine levels to more precisely model the initial population distribution.

### Depletion Spectroscopy on the $a^3\Sigma^+ \rightarrow c^3\Sigma^+_1$ Transition

Although the $\Omega = 0^-$ component yields simpler spectra and important spectroscopic information, this state is ultimately not useful for transfer to the $X^1\Sigma^+$ state, as the spin-orbit interaction which gives the requisite singlet/triplet mixing only affects the $\Omega$=1 component of the $c^3\Sigma^+$ state. This greatly complicates the level structure, as the nuclear spins can couple to this angular momentum, giving rise to many spectroscopically-resolved hyperfine

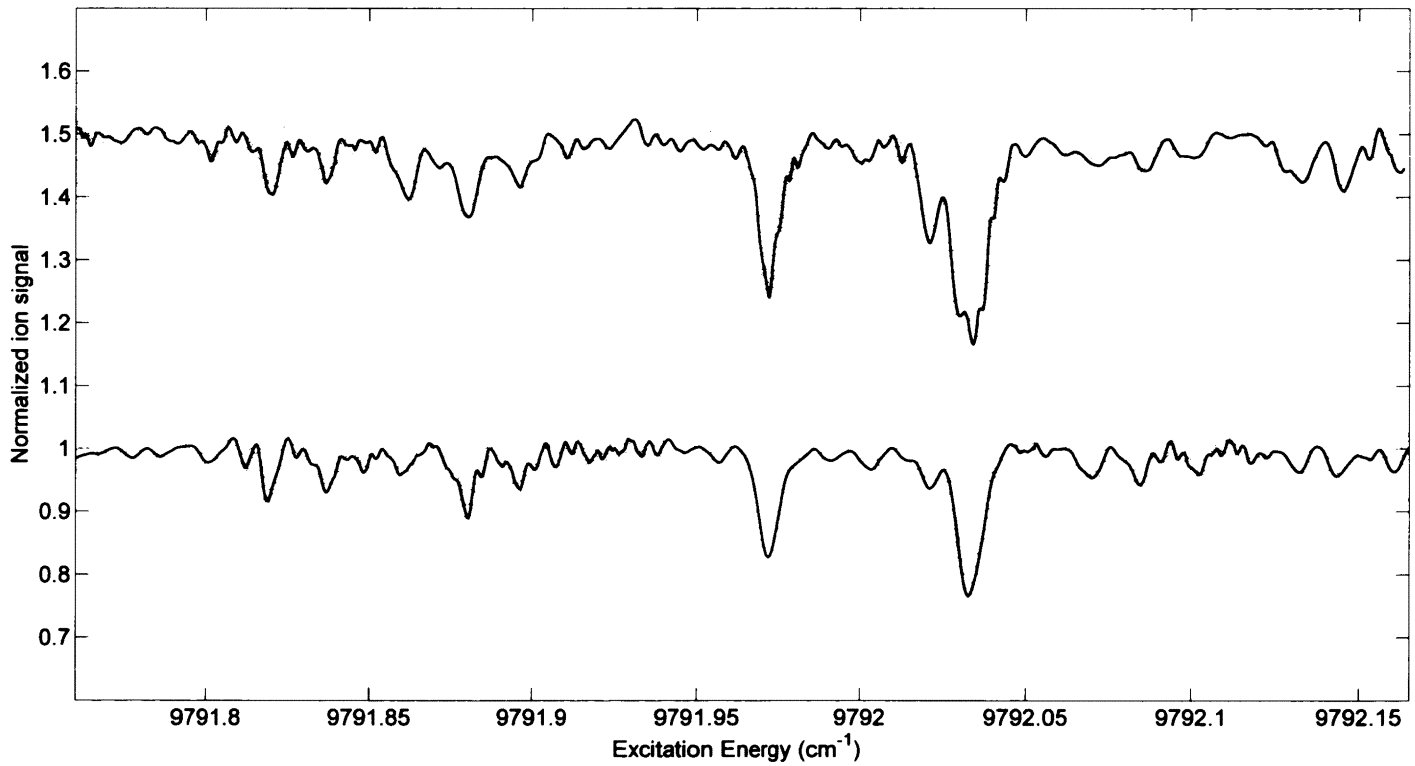


Figure 4.11: Depletion spectroscopy $a^3\Sigma^+(v{=}36) \rightarrow c^3\Sigma^+_{0^-}(v{=}34$ (lower), 36 (upper)) transitions. Gray dots are normalized depletion data averaged 100 shots per point. Fit lines are splines smoothed over 70 data points. The $v{=}36$ data is offset horizontally by 56.886 $cm^{-1}$ to show repeated patterns and offset vertically for clarity. Both traces use $J_{PA}{=}1$. Repeating patterns show the simple rotational progression of the $c^3\Sigma^+_{0^-}$ state.

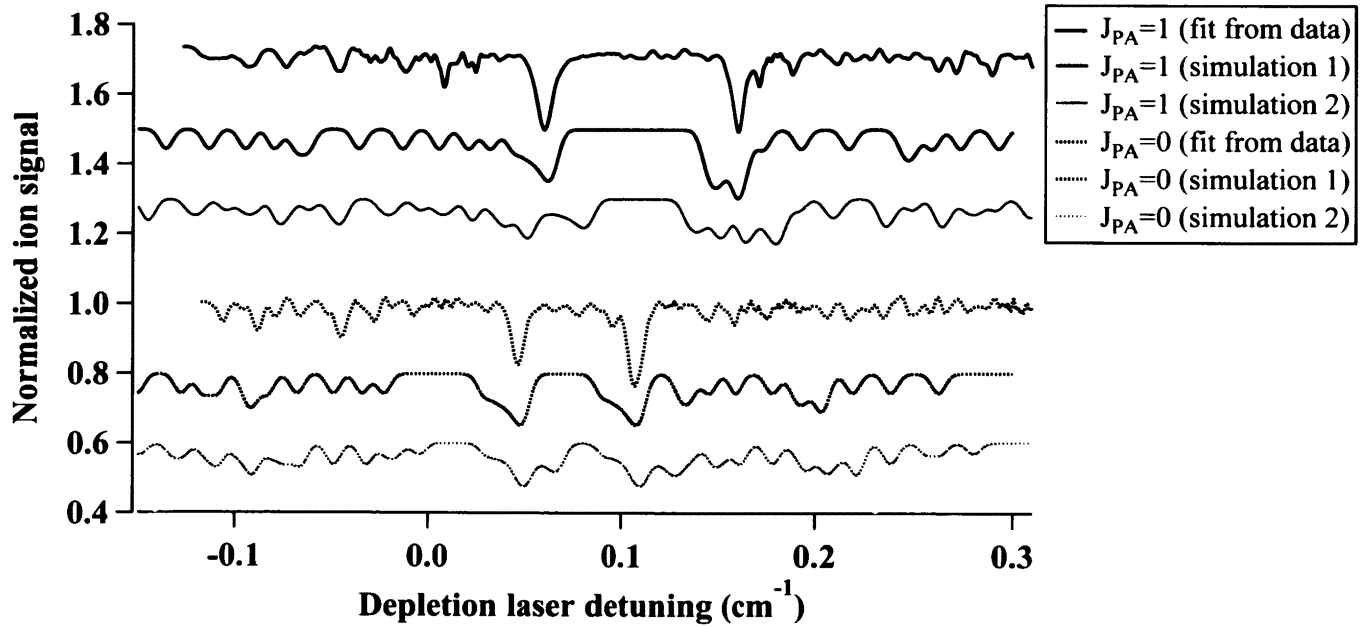


Figure 4.12: Simulated depletion spectrum of the $a^3\Sigma^+ \rightarrow c^3\Sigma^+_{0^-}$ transition. In simulation 1 (blue), all hyperfine states of the $\ell = J_{PA}$ rotational level in the $a^3\Sigma^+$ state are assumed to be equally populated with no population in the $\ell = J_{PA} + 2$ rotational level. In simulation 2 (red), all hyperfine states of the $\ell_a = J_{PA}, J_{PA} + 2$ rotational levels in the $a^3\Sigma^+$ state are assumed to be equally populated. The splined fits from the depletion measurements are shown in black. Each simulated spectroscopic feature is modeled as a Gaussian centered at the transition frequency with a characteristic width of 150 MHz, determined from the fit width of the measured spectroscopic features. Solid (dashed) lines correspond to $J_{PA}$=1 ($J_{PA}$=0). Lower (upper) traces comes from photoassociation to $J_{PA}$=0(1). Traces are offset vertically for clarity. The simulated values for the rotational constants are $B_a$=0.0028 $cm^{-1}$ and $B_c$=0.010 $cm^{-1}$.

levels.

As seen in Figure 4.13, the spectrum for depletion to the $\Omega = 1$ is much richer. Though the larger peaks appear to persist in this component, additional satellite features emerge, showing the additional hyperfine structure in the $c^3\Sigma^+$ state. Now that we more fully understand the structure of the $a^3\Sigma^+$ state, it is, in principle, possible to deconvolve it from depletion spectroscopy in order to analyze the $c^3\Sigma_1^+$ state.

## 4.4 Attempts to Simplify the Spectroscopy

At the time the depletion spectroscopy was done, we were largely unable to assign the observed transitions due to the very complex hyperfine structure in both the $a^3\Sigma^+$ and $c^3\Sigma^+$ states. We attempted to enlist possible collaborators who specialize in molecular spectroscopy but were ultimately unsuccessful. Instead, we tried to simplify the observed spectroscopy by refining our experimental techniques.

### 4.4.1 PA in the Optical Trap

During the previous generation of this experiment at Yale, vibrationally-excited RbCs molecules were trapped using a high-power $CO_2$ laser, but the molecules were always created in MOTs rather than from optically trapped atomic samples [89]. PA in the trap was long a goal of the previous experiment for a few reasons. First, following optical molasses, the precursor atoms are approximately an order of magnitude colder than in the MOTs ($\sim$10 $\mu$K, rather than $>$100 $\mu$K), resulting in translationally colder molecules. More importantly, the molecules are automatically loaded into the optical trap as soon as they are created. This greatly simplifies the alignment procedure of the trap relative to the MOTs and increases the signal size.

We determined that the previous failure to see PA in the optical trap was due to imperfect extinction of the repumping laser AOMs. Even when the RF switches controlling the AOMs are nominally off, a low level of light (tens of nW) is still diffracted and

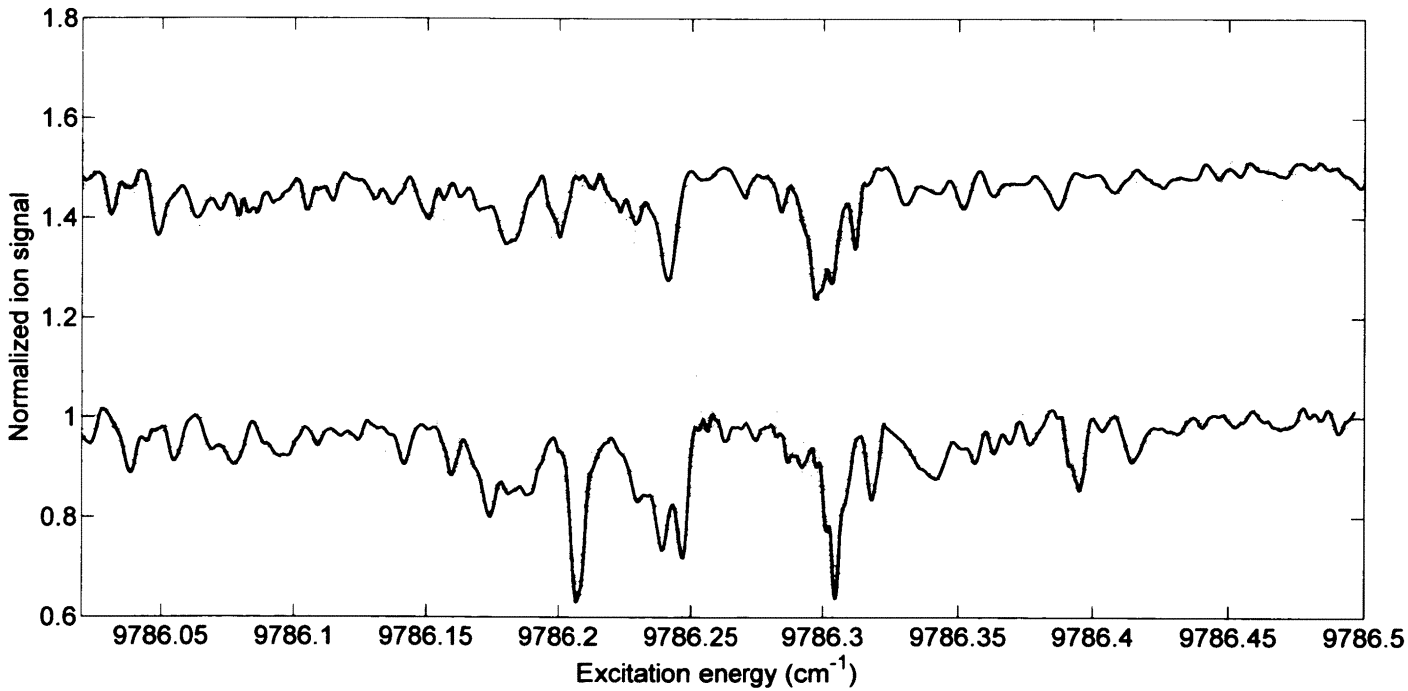


Figure 4.13: Depletion spectroscopy of the $a^3\Sigma^+(v{=}36) \rightarrow c^3\Sigma_1^+(v{=}34)$ transition. Gray dots are normalized depletion data averaged 100 shots per point. Curves are splines smoothed over 70 data points. Lower (upper) trace comes from photoassociation to $J_{PA}{=}0(1)$. Upper trace is offset vertically for clarity. Additional features come from hyperfine structure and $\Omega$-doubling in the $c^3\Sigma_1^+$ state.

reaches the experimental chamber. This low level of light is enough to optically pump the trapped atoms into their upper hyperfine states and therefore out of resonance with the PA laser. With the installation of mechanical laser shutters, the repumping laser can be completely blocked, leaving the atoms in the lower hyperfine states. PA in the trap was then immediately observed.

Using this technique, we were able to measure some population dynamics of molecular formation in the trap. As seen in Figure 4.14, the competing processes of molecular formation by PA and destruction due to inelastic collisions equalize after approximately 10 ms of PA. This behavior has been simulated by numerically solving the following rate equations, assuming the trap is not reloaded with atoms once PA begins:

$$\begin{aligned}\dot{n}_{\mathrm{RbCs}} = \; & bK_{\mathrm{PA}} n_{\mathrm{Rb}} n_{\mathrm{Cs}} - K_{(\mathrm{RbCs-Rb})} n_{\mathrm{RbCs}} n_{\mathrm{Rb}} - K_{(\mathrm{RbCs-Cs})} n_{\mathrm{RbCs}} n_{\mathrm{Cs}} \\ & - K_{(\mathrm{RbCs-RbCs^*})} n_{\mathrm{RbCs}} n_{\mathrm{RbCs^*}} - K_{(\mathrm{RbCs-RbCs})} n_{\mathrm{RbCs}}^2,\end{aligned} \tag{4.30}$$

$$\begin{aligned}\dot{n}_{\mathrm{RbCs^*}} = \; & (1-b) K_{\mathrm{PA}} n_{\mathrm{Rb}} n_{\mathrm{Cs}} - K_{(\mathrm{RbCs^*-Rb})} n_{\mathrm{RbCs^*}} n_{\mathrm{Rb}} \\ & - K_{(\mathrm{RbCs^*-Cs})} n_{\mathrm{RbCs^*}} n_{\mathrm{Cs}} - K_{(\mathrm{RbCs^*-RbCs})} n_{\mathrm{RbCs^*}} n_{\mathrm{RbCs}} \\ & - K_{(\mathrm{RbCs^*-RbCs^*})} n_{\mathrm{RbCs^*}}^2,\end{aligned} \tag{4.31}$$

where $b$ is the branching ratio to the $v$=36 level, $n_x$ is the density of species $x$, $K_{\mathrm{PA}}$ is the rate coefficient for photoassociation, and $K_{(x-y)}$ is the inelastic collision rate coefficient for species $x$ and $y$. Here $x$ = RbCs* refers to RbCs molecules in any state except $v$ = 36 state, and $x$ = RbCs refers only to $v$ = 36 molecules. We assume that all collisions at these temperatures ($T \approx 10\ \mu$K) proceed at the unitarity-limited rate for $s$-wave scattering ($K_{\mathrm{max}} = \langle v_{\mathrm{rel}} \frac{\pi}{k^2} \rangle \approx 9 \times 10^{-11}$ cm$^3$/s at 10 $\mu$K), as suggested by previous work in Refs. [108, 35, 89, 109]. Further, we set $K_{\mathrm{PA}}$ to the same value, as the PA rate should be at least mostly saturated for this weakly-bound state. The behavior is qualitatively reproduced in Figure 4.15.

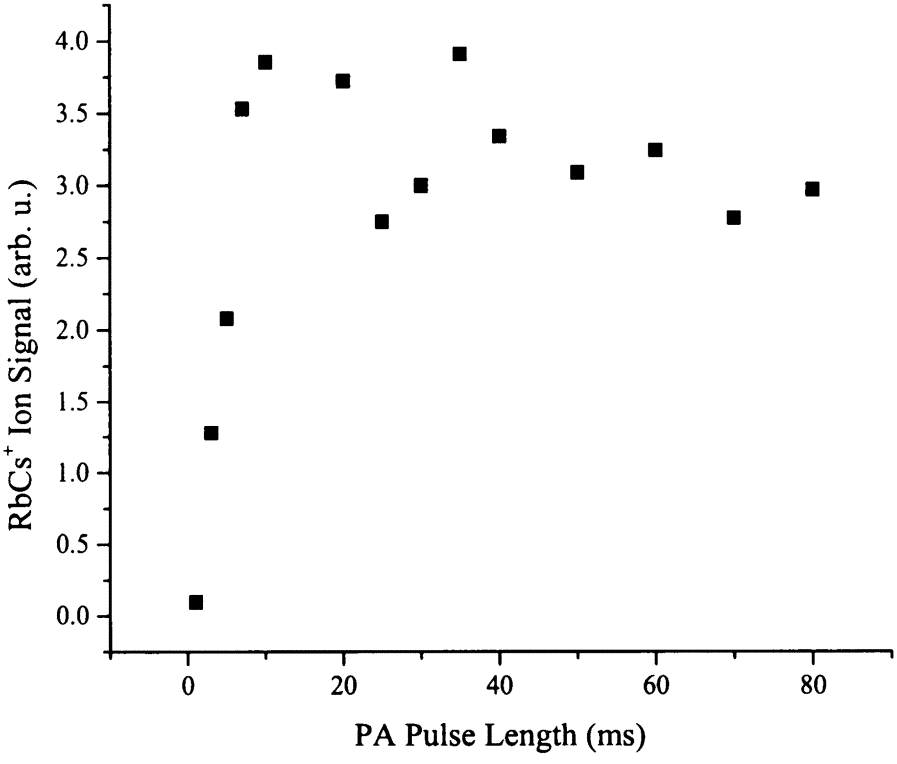


Figure 4.14: Molecular yield for varying PA exposure times in the optical trap. $CO_2$ optical trap was loaded with Rb and Cs atoms ($T \approx 10$ $\mu$K). The PA laser was on for the PA pulse length. Molecules were photoionized and detected immediately after the PA pulse ended.

### 4.4.2 Bright State PA

Photoassociation in the optical trap affords more control over the internal states of the precursor atoms relative to the dark SPOT MOTs. In order to increase atomic densities in the MOTs, the atoms are shelved in their lower hyperfine states to avoid light-assisted collisions. Thus, PA, which depends strongly on the atomic densities, is optimized to address the lower hyperfine state. In the atomic trap, however, the hyperfine state can be controlled trivially without loss of density by blocking or unblocking the repumping laser during the final milliseconds of the optical molasses phase of trap loading.

With this additional capability, we attempted PA to the $\Omega = 0^-$ state using atoms in their upper hyperfine states. Unexpectedly, we saw no indication of molecular formation.

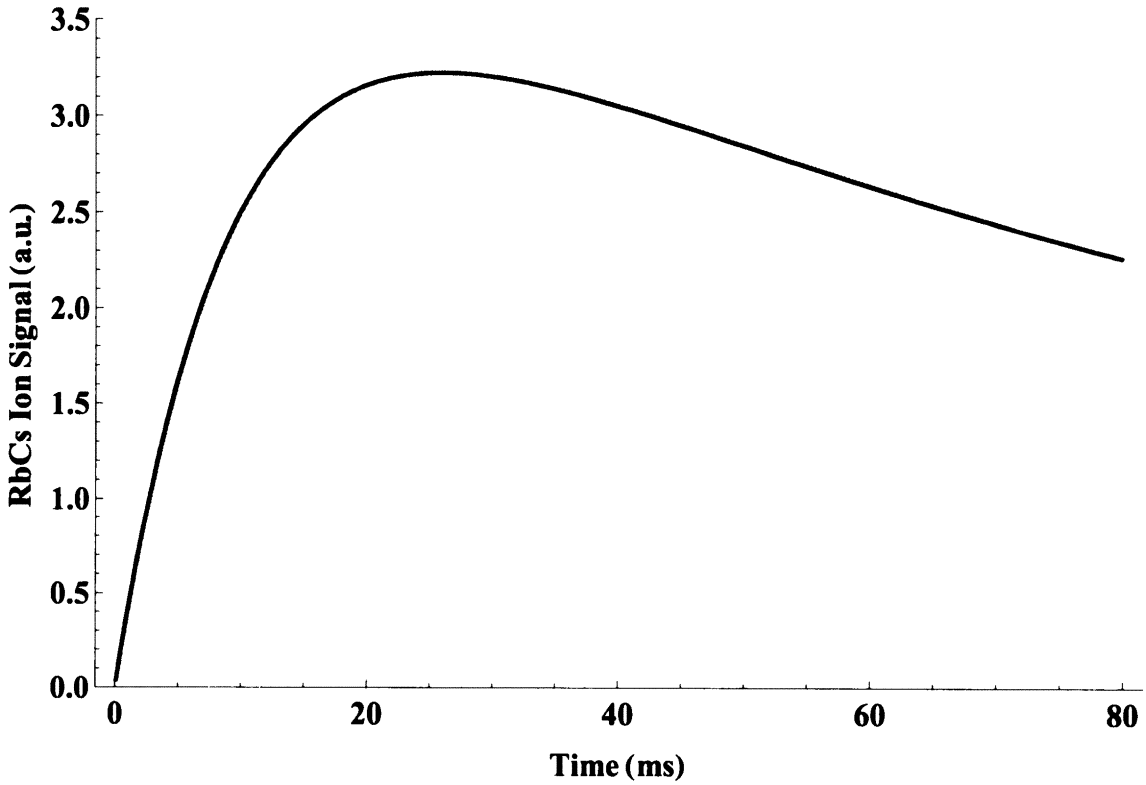


Figure 4.15: Simulated population dynamics for PA in an optical trap. All rate coefficients are taken to be $\approx 9\times10^{-11}$ cm$^3$/s. Initial atomic densities are taken as $n_{Rb}=n_{Cs}=5\times10^{11}$ cm$^{-3}$ and are assumed to not be reloaded during PA.

All combinations of hyperfine states for both atoms were used, with the PA laser tuned appropriately to account for the very precisely known ground state atomic hyperfine splittings, shown in Figure 4.16. This result has yet to be explained, and is quite surprising given that PA for different hyperfine levels has been observed in other experiments using both homonuclear and heteronuclear molecules [110, 111].

### 4.4.3 Limitations

For the narrowband spectroscopy of interest at the time, PA in the optical trap has both advantages and disadvantages. The most obvious advantage is a marked increase in the single-shot signal size due to the confinement of molecules as they are created. This increase comes, however, at a massive reduction in repetition rate. In the MOTs, detection rate is given by the pulsed dye laser rate (10 Hz). In the optical trap, the MOTs must be

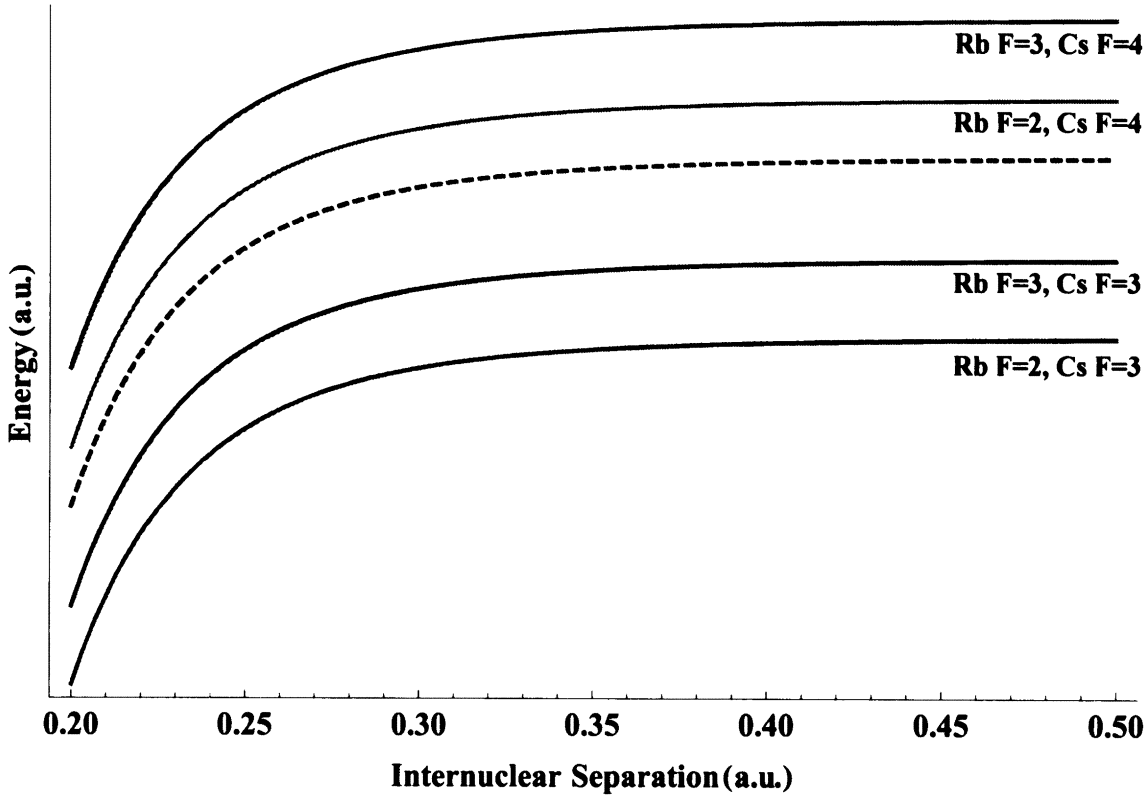


Figure 4.16: Splitting of the Rb $5s_{1/2}$ + Cs $6s_{1/2}$ atomic asymptote by the hyperfine interaction. Dashed line denotes potential in the absence of hyperfine splitting. The splitting between the highest and lowest asymptotes is given by the sum of the ground state Rb and Cs hyperfine structure, 12.23 GHz.

continually reloaded for 3-5 s, lowering the repetition rate to ~0.2 Hz.[5] Further, the optical molasses stage of trap loading was consistently prone to failure. During the so-called sample and hold process, the MOT trap laser frequencies were unlocked, red-detuned several linewidths, shifted back, and relocked. This was achieved by storing the laser lock control voltage, adding an offset voltage to detune the laser, and then relocking the laser using the previous stored control voltage. After several iterations, the laser would lock to the wrong saturated absorption feature, necessitating relocking of the trap laser by hand. This system was ultimately deemed untenable and inspired the construction of beat note

[5]The repetition rate when using the optical trap can, in principle, be increased if the atomic MOTs can be loaded more quickly. When using heated getters, the increase in loading rate afforded by using a higher getter current generally comes at the cost of a much shorter trapping lifetime. This is due to an increased background pressure. If an alternative loading scheme that increases the MOT rate without reducing the trap lifetime were implemented, such as loading from a Zeeman slowed beam, the repetition rate would be set by the sum of the MOT loading time and the 10 ms optical molasses stage used to load the optical trap.

laser locks like those in [112].

Although PA in the trap was not ultimately used for spectroscopic purposes at this stage in the experiment, this technique is expected to become very useful for future planned experiments that study collisions between molecules and atoms.

## 4.5 Summary

In this chapter, we have detailed efforts to increase the efficiency of molecular state transfer from the weakly-bound $a^3\Sigma^+(v{=}36)$ level that is heavily populated following spontaneous decay from the $\Omega = 0^-$ PA state at 897 nm. We have shown narrowband depletion spectroscopy of transitions from the $a^3\Sigma^+(v{=}36)$ state to the $\Omega = 0^-$ and $\Omega = 1$ components of different vibrational levels of the mixed $c^3\Sigma^+$ state. These spectra yield information on the hyperfine structure of the $a^3\Sigma^+$ state as well as the rotational splitting of the $c^3\Sigma^+$ state. These can be used in the future to assign the transitions observed in the measured $\Omega = 1$ spectra for possible use in STIRAP transfer to the $X^1\Sigma^+$ state.

# Chapter 5

# Deeply-Bound Photoassociation

## 5.1 Introduction

Much of the content of this chapter appears elsewhere in a slightly different form in [113].

Shortly after the depletion spectroscopy of the $a^3\Sigma^+ \rightarrow c^3\Sigma^+$ transitions presented in the previous chapter, Gabbanini and Dulieu reported short-range PA to a deeply-bound vibrational level of an excited electronic state in $^{85}$RbCs [114]. Historically, short-range PA, in the absence of an additional mechanism like resonant coupling or a shape resonance, was thought to be too inefficient to create large numbers of ground state molecules. The PA rates were thought to be vanishingly small due to very small Franck-Condon factors between the atomic scattering and molecular bound states. As a result, PA experiments, like those in the previous chapter, focused on transitions that used the larger amplitude, long-range portion of the scattering wavefunction. These weakly-bound PA states then spontaneously decay and populate similarly weakly-bound vibrational levels in the electronic ground states.

The tantalizing possibility of short-range PA is that spontaneous decay from the excited state may populate the rovibrational ground state in large numbers, eliminating the need for molecular state transfer, as illustrated in Figure 5.1. The molecular creation process can then be run continuously, possibly allowing for the accumulation of the molecules in

a trap as they are produced. This is in contrast to schemes that rely on molecular state transfer such as Stimulated Emission Pumping and Stimulated Raman Adiabatic Passage. These transfer schemes can only be run once per experimental realization, limiting the ultimate sample size.

Before the Gabbanini and Dulieu result, short-range heteronuclear PA had only been seen in LiCs [104], but has since been reported in NaCs and KRb as well [115, 116]. In each of these cases, unique molecular features, such as resonant coupling or shape resonances, were at least initially thought to be responsible for the high molecular production rates. In the case of resonant coupling, nearby excited states mix, altering the shape of the PA state wavefunction [117].[1] Shape resonances alter the shape of the scattering state wavefunction when the scattering energy becomes resonant with a molecular quasi-bound state [115]. Both of these phenomena can drastically change the free-to-bound Franck-Condon factor and the corresponding cross-section for PA. As we show, these additional mechanisms do not appear to be necessary for efficient $X^1\Sigma^+(v{=}0)$ molecular production.

## 5.2 Photoassociation at 11824 $cm^{-1}$

By scanning a PA laser only a few wavenumbers to the red of the atomic Cs D2 line near 852 nm, Gabbanini and Dulieu discovered a simple rotational progression associated with an excited molecular $\Omega{=}0$ state at 11824.06 $cm^{-1}$. The measured rotational constant of this PA state, $B_e$, corresponds to an internuclear separation, $\langle R\rangle \approx 4.8$ Å from $B_e{=}1/2\mu\langle R\rangle^2$, where $\mu$ is the reduced mass of RbCs. Examination of the potential energy curves in Figure 5.2 shows that this PA state may have the necessary Franck-Condon factors to decay to low-lying $X^1\Sigma^+$ state vibrational levels. It was unclear at the time, however, if the excited PA state has the correct symmetry to populate the $X^1\Sigma^+$ state via single-photon decay. Specifically, an $\Omega{=}0^-$ PA state should only decay to the $a^3\Sigma^+(\Omega = 0^-, 1)$ state, whereas

[1] For heavy atoms, such as Cs, spin-orbit coupling can mix molecular states with equal values of $\Omega$. If one state is long-range while the other is deeply-bound, the mixed state can possess large wavefunction amplitude at large and small internuclear separation.

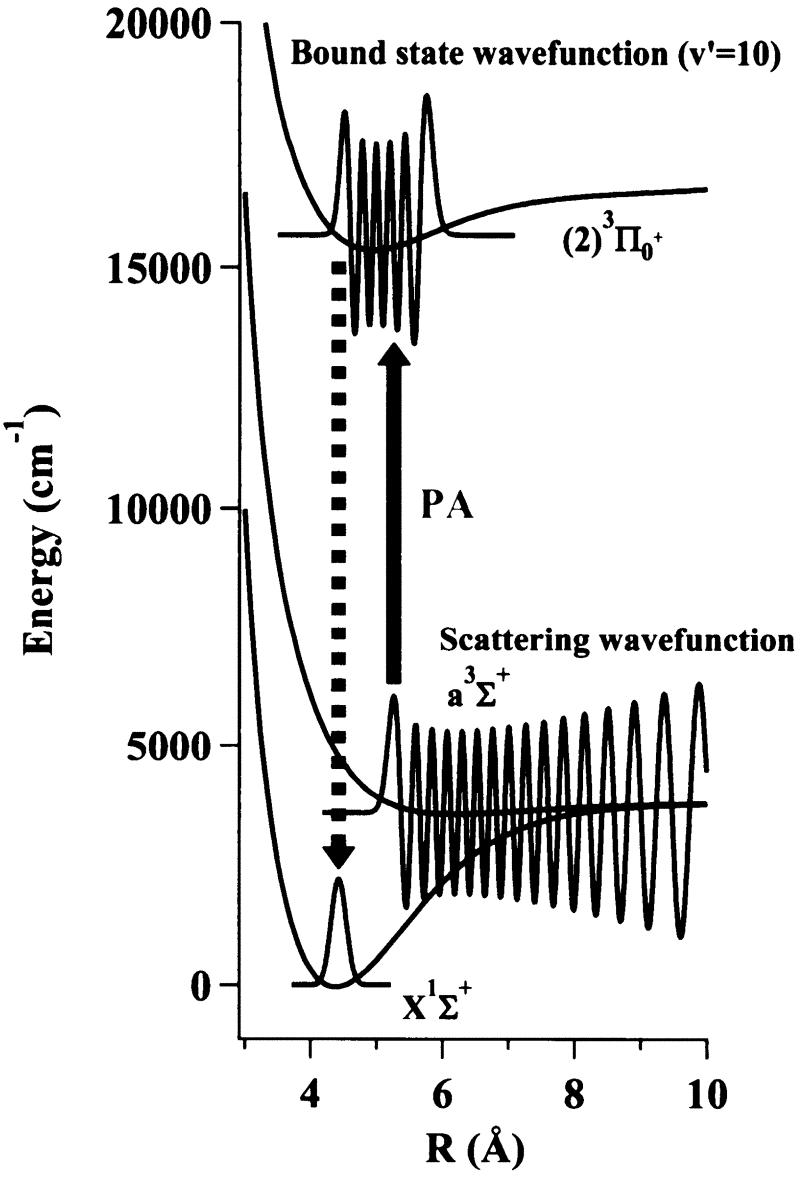


Figure 5.1: Calculated wavefunctions for free-to-bound photoassociation and bound-to-bound $(2)^3\Pi_{0^+}(v'=10) \rightarrow X^1\Sigma^+(v=0)$ spontaneous decay. Wavefunction amplitudes are not drawn to scale. Potential energy curves are from values in Ref. [118]. Figure reproduced from [113].

an $\Omega = 0^+$ PA state should populate both the $X^1\Sigma^+(\Omega = 0^+)$ and $a^3\Sigma^+$ states. In Refs. [114, 119, 120, 121], it was shown that vibrational levels in the shallow $a^3\Sigma^+$ state were being populated, but it was not determined if the $X^1\Sigma^+$ state was populated as well. This PA state was studied further in Ref. [119], where the state's electric dipole moment and the saturation intensity of PA were measured. Theoretical analysis of possible spontaneous decay pathways is given in Ref. [120].

### 5.2.1 REMPI Spectroscopy of the $X^1\Sigma^+ \rightarrow (4)^1\Sigma^+$ Transition

To determine which $X^1\Sigma^+$ vibrational levels, if any, were populated following spontaneous decay, we tuned our REMPI dye laser to drive transitions from low-lying vibrational levels in the $X^1\Sigma^+$ state to vibrational levels in the $(4)^1\Sigma^+$ state. We calculated the transition frequencies using the excited state spectroscopy in [122] and the $X^1\Sigma^+$ state potential in [19]. With the known transition frequencies, we simulated the REMPI spectra for population of different $X^1\Sigma^+$ vibrational levels. To reach these frequencies, Pyrromethene 597 dissolved in ethanol was used for the 16670→17450 $cm^{-1}$ range.

As seen in the ionization data in Figure 5.3, the resulting spectra are very complicated. Many additional lines, likely originating from very closely spaced $a^3\Sigma^+$ vibrational levels, dominate the signal. Definitive assignment of peaks to transitions from the $X^1\Sigma^+$ state by eye is essentially impossible. In order to systematically determine which levels are populated following spontaneous decay, we developed an additional technique to analyze our spectra.

### 5.2.2 Cross-Correlation Method

To quantify the extent to which our simulated spectra match the measured signal, we define a cross-correlation function given by

$$\mathrm{cor}(\Delta) = \int_{f_1}^{f_2} \mathrm{sim}(f + \Delta)\mathrm{sig}(f)df \tag{5.1}$$

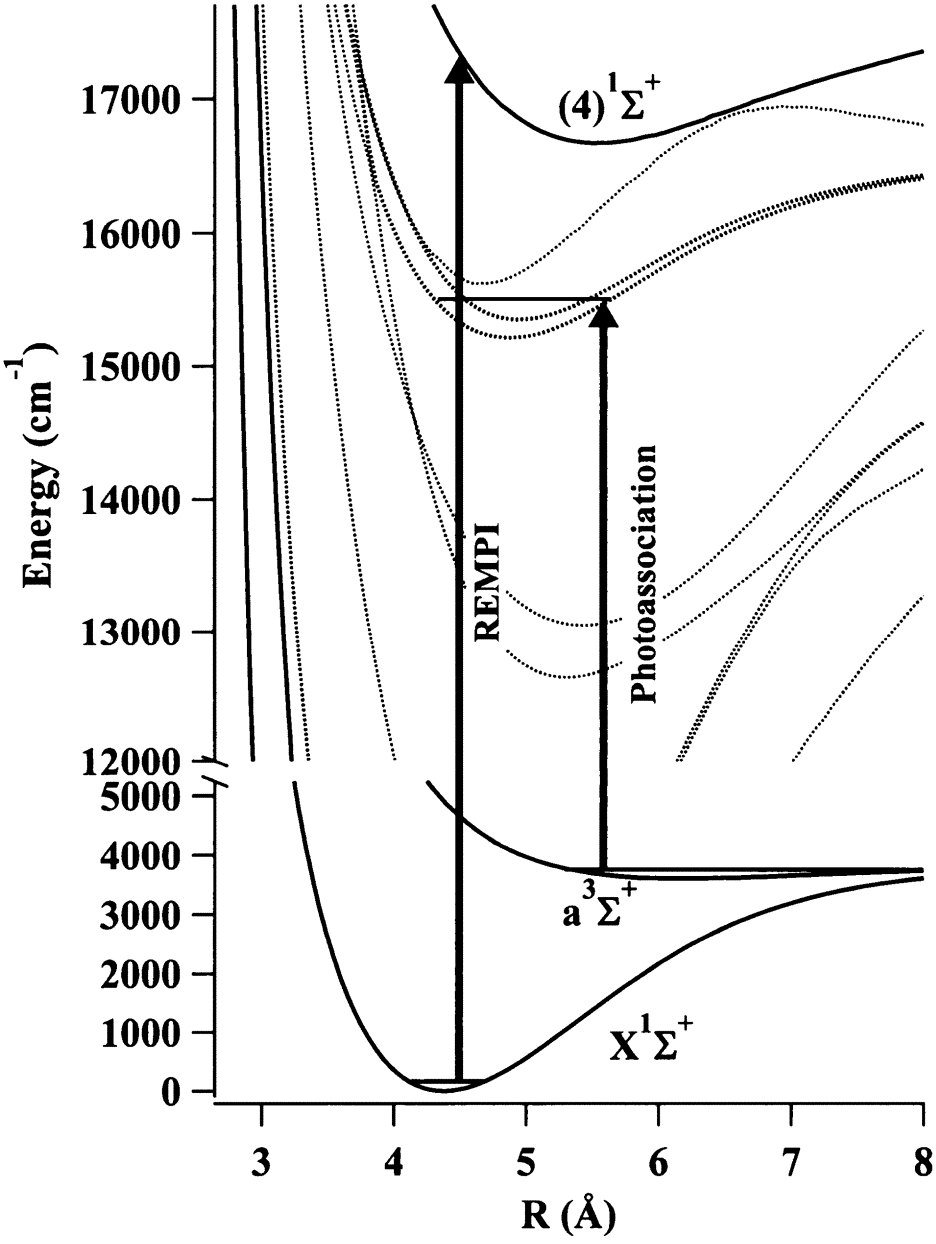


Figure 5.2: Relevant potential energies for deeply-bound PA near 11824 $cm^{-1}$ and REMPI spectroscopy of the $X^1\Sigma^+ \rightarrow (4)^1\Sigma^+$ transition. All $\Omega \neq 0$ states have been omitted. Potential energy curves are from values in Ref. [118].

where $f_1$ and $f_2$ are the lower and upper frequency bounds of the data set, sig($f$) is the measured spectroscopic signal, sim($f$) is the simulated spectrum, and $\Delta$ is a variable frequency offset. When the signal and simulation are well-matched, the cross-correlation value is sharply peaked at $\Delta$=0, while the largely uncorrelated offset spectrum and signal product is integrated to much smaller values for other values of $\Delta$.

To further understand the cross-correlation technique, it is useful to consider the identification of a single spectroscopic feature in the absence of noise or any additional structure. We model this feature as a Lorentzian with full-width at half-maximum (FWHM), $\Gamma$, centered at $f_0$. From the definition of the cross-correlation function with sig($f$) = sim($f$), we have

$$\mathrm{cor}(\Delta) = \int_{f_1}^{f_2} \left(\frac{1}{2\pi}\frac{\Gamma}{(f+\Delta-f_0)^2+(\frac{\Gamma}{2})^2}\right)\left(\frac{1}{2\pi}\frac{\Gamma}{(f-f_0)^2+(\frac{\Gamma}{2})^2}\right)df \qquad (5.2)$$

This is simply the convolution of the feature with itself, which yields a Lorentzian peak centered at $\Delta = 0$ with a FWHM of $2\Gamma$. Hence for $f_2 - f_1 \gg 2\Gamma$, cor($\Delta$) consists only of a sharp peak at $\Delta$=0.

Applying this technique to the specific case of the $(4)^1\Sigma^+$ REMPI spectroscopy, we find evidence that low-lying vibrational levels in the $X^1\Sigma^+$ state are populated following spontaneous decay from the PA line at 11824 $cm^{-1}$. As seen in Figure 5.3, there is a clear identification with $v_x$=1, among others. Although the vast majority of the observed features are unassigned, an $X^1\Sigma^+$ vibrational level identification only requires that ionization peaks be seen where predicted for the vibrational level in question.

Beyond the central peak at $\Delta = 0$, there are a few other recurring features in the cross-correlation function. First, we find additional peaks associated with the vibrational progression in the excited state. Second, we often see a broad triangular base underneath the peaks from vibrational transitions. This base comes from non-zero offsets in the ion signal and simulated spectrum. Specifically, the convolution of two constant functions results in a triangular lineshape. The familiar peaked structure of the cross-correlation

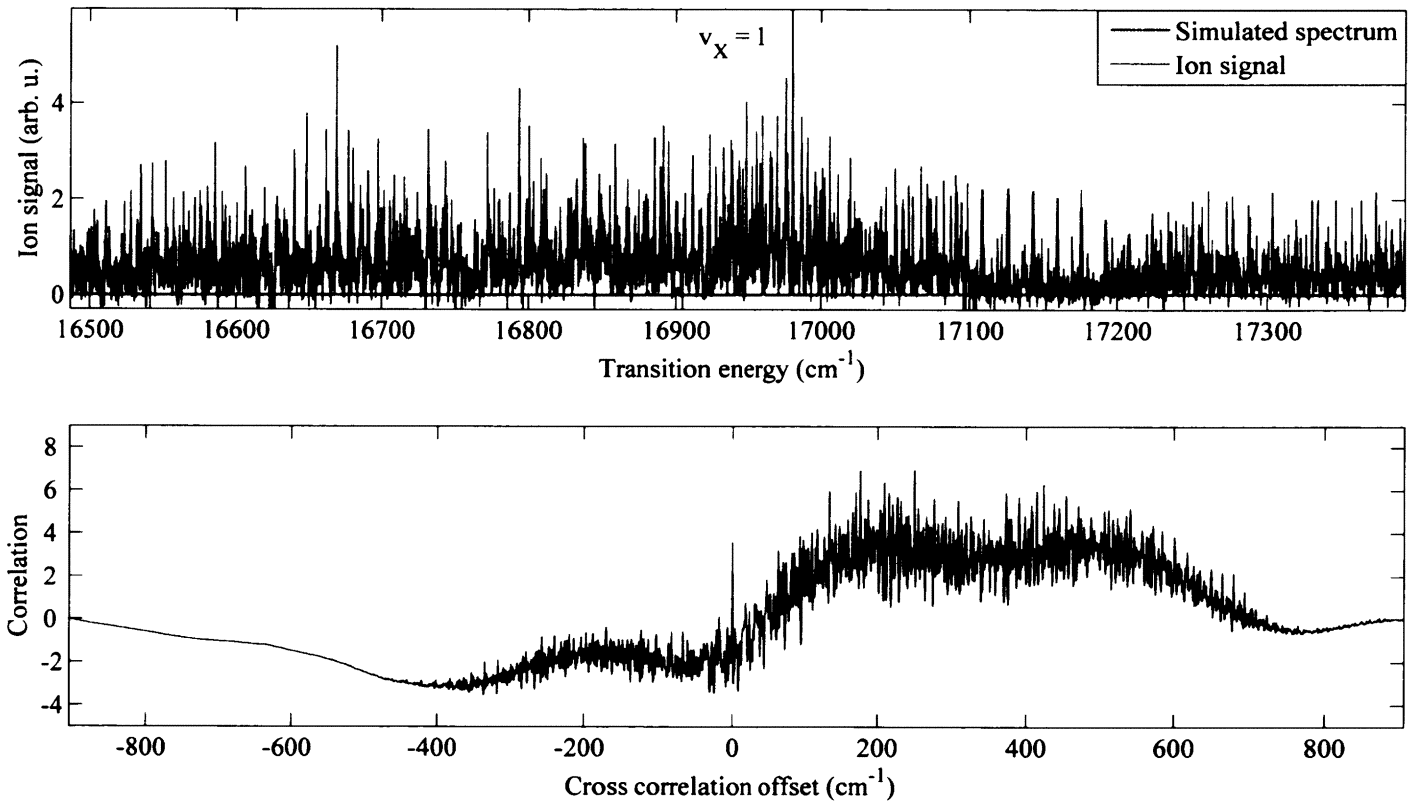


Figure 5.3: Ion signal, simulated spectrum, and cross-correlation of transitions from the $X^1\Sigma^+(v{=}1)$ level to vibrational levels in the $(4)^1\Sigma^+$ state. The large correlation at zero correlation offset denotes a good match between the ion signal and the simulated spectrum, suggesting population of the $X^1\Sigma^+(v{=}1)$ level. The asymmetry in the cross-correlation is due to the large number of unsimulated features, likely originating from $a^3\Sigma^+$ vibrational levels.

function then lies on top of this broad triangular lineshape. Third, the correlation function can be highly-asymmetric about $\Delta$=0 if there are large spectroscopic features that are not modeled in sim($f$). Generally, this asymmetry is a smoothly-varying function in $\Delta$, and the sharp peak at $\Delta$=0 can be easily discerned, as in Figure 5.3.

Although we can assign specific features in the ionization signal to transitions originating from the $X^1\Sigma^+$ state, we conducted additional spectroscopy to further corroborate our conclusion. This second round of spectroscopy, based on transitions to the $(2)^1\Pi$ state near 650 nm, turned out to afford an even more compelling method for identifying transitions from the $X^1\Sigma^+$ state.

### 5.2.3 REMPI Spectroscopy of the $X^1\Sigma^+ \rightarrow (2)^1\Pi$ Transition

The $(2)^1\Pi$ vibrational level positions are given in [123]. To reach the necessary transition frequencies, we switched our REMPI laser dye to DCM dissolved in DMSO. This combination gives wavelength coverage from 630-685 nm. As seen in Figures 5.4 and 5.5, the higher frequency portion of this spectroscopy looks much the same as in the previous measurements of the $X^1\Sigma^+ \rightarrow (4)^1\Sigma^+$ transition, but below 15500 $cm^{-1}$, the very dense features disappear. In their place, there is a much more regular, smaller set of peaks that is consistent with a well-resolved vibrational progression. We have fit these features, as seen in Figure 5.6, and made definitive assignment of numerous lines. Most interestingly, numerous transitions from the $X^1\Sigma^+(v$=0) ground state can be clearly identified, demonstrating that the vibrational ground state of $^{85}Rb^{133}Cs$ can be continuously populated via photoassociation.

This REMPI data can be used to measure the population, $p_{v_x}$, in a given $X^1\Sigma^+$ vibrational level, $v_x$. The spectra are fit to a sum of Lorentzian curves given by:

$$S(f) = \sum_{v_x v'_\Pi} \frac{(\Gamma + \beta \cdot F(v_x, v'_\Pi))^2 (1 - e^{-\alpha \cdot F(v_x, v'_\Pi)})}{(f - f_0(v_x, v'_\Pi))^2 + (\Gamma + \beta \cdot F(v_x, v'_\Pi))^2} p_{v_X}, \tag{5.3}$$

where $S(f)$ is the signal at laser frequency $f$, $v'_\Pi$ is the $(2)^1\Pi$ state vibrational level, $\Gamma$ is

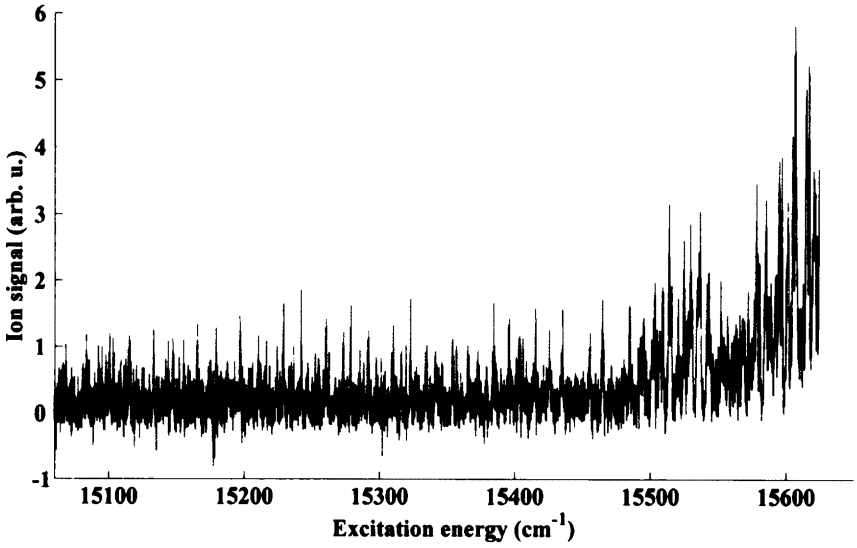


Figure 5.4: REMPI spectroscopy of the PA line at 11824 $cm^{-1}$ using the $X^1\Sigma^+ \rightarrow (2)^1\Pi$ transition. The smaller features at the lower end of the frequency range are due to transitions from the $X^1\Sigma^+$ state. The dense features at the high frequency end of the spectrum are likely due to transitions from the $a^3\Sigma^+$ state to another higher lying electronic state.

| $X^1\Sigma^+$ Vibrational Level ($v_x$) | Relative Population ($p_{v_x}/p_{v_0}$) |
|---|---|
| 0 | 1 |
| 1 | 1.25 |
| 2 | 1.25 |
| 3 | 0.75 |
| 4 | 0.5 |
| 5 | 0.25 |

Table 5.1: Relative $X^1\Sigma^+(v_x)$ vibrational level populations, $p_{v_x}/p_{v_0}$, following spontaneous decay from the PA line at 11824 $cm^{-1}$, extracted from REMPI spectroscopy data.

the spectral width of the pulsed dye laser, $f_0(v_x, v'_\Pi)$ is the transition frequency from $v_x$ to $v'_\Pi$, $\alpha, \beta$ are fit parameters that are constant for all transitions, $F$ is the known FCF (calculated from the data in Ref. [123]) for the transition at $f_0$, and $p_{v_x}$ is an adjustable $X^1\Sigma^+$ vibrational population fit parameter. $\alpha$ and $\beta$ describe the saturation and power broadening, respectively, of the transitions. The values of $p_{v_x}$ are adjusted by hand to fit the data, but are the same for all transitions originating from a single $X^1\Sigma^+$ vibrational level, $v_x$. These results are summarized in Table 5.1.

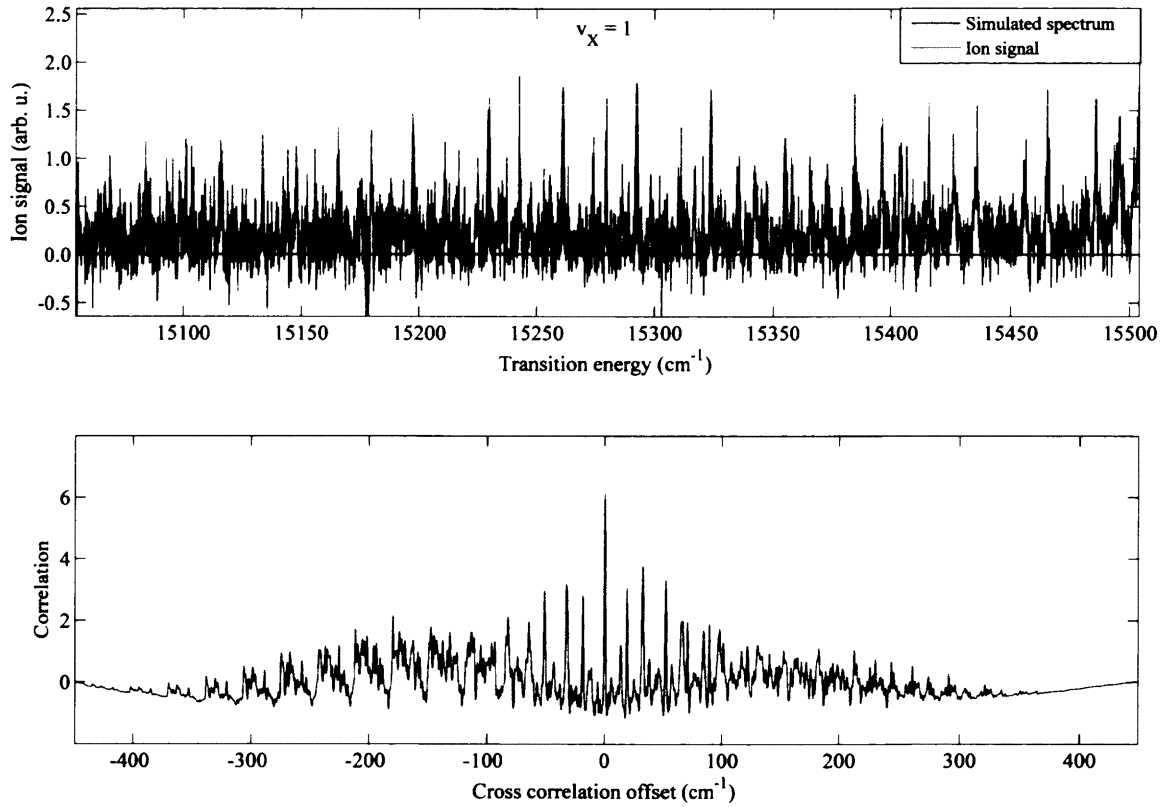


Figure 5.5: Cross-correlation of the PA line at 11824 cm$^{-1}$ to the $X^1\Sigma^+(v{=}1)$ state. The very large peak at zero offset is indicative of population of the $v$=1 state. Additional regular, sharply peaked features are consistent with the vibrational progressions of the $X^1\Sigma^+$ and $(2)^1\Pi$ states. REMPI is driven through the $(2)^1\Pi$ state.

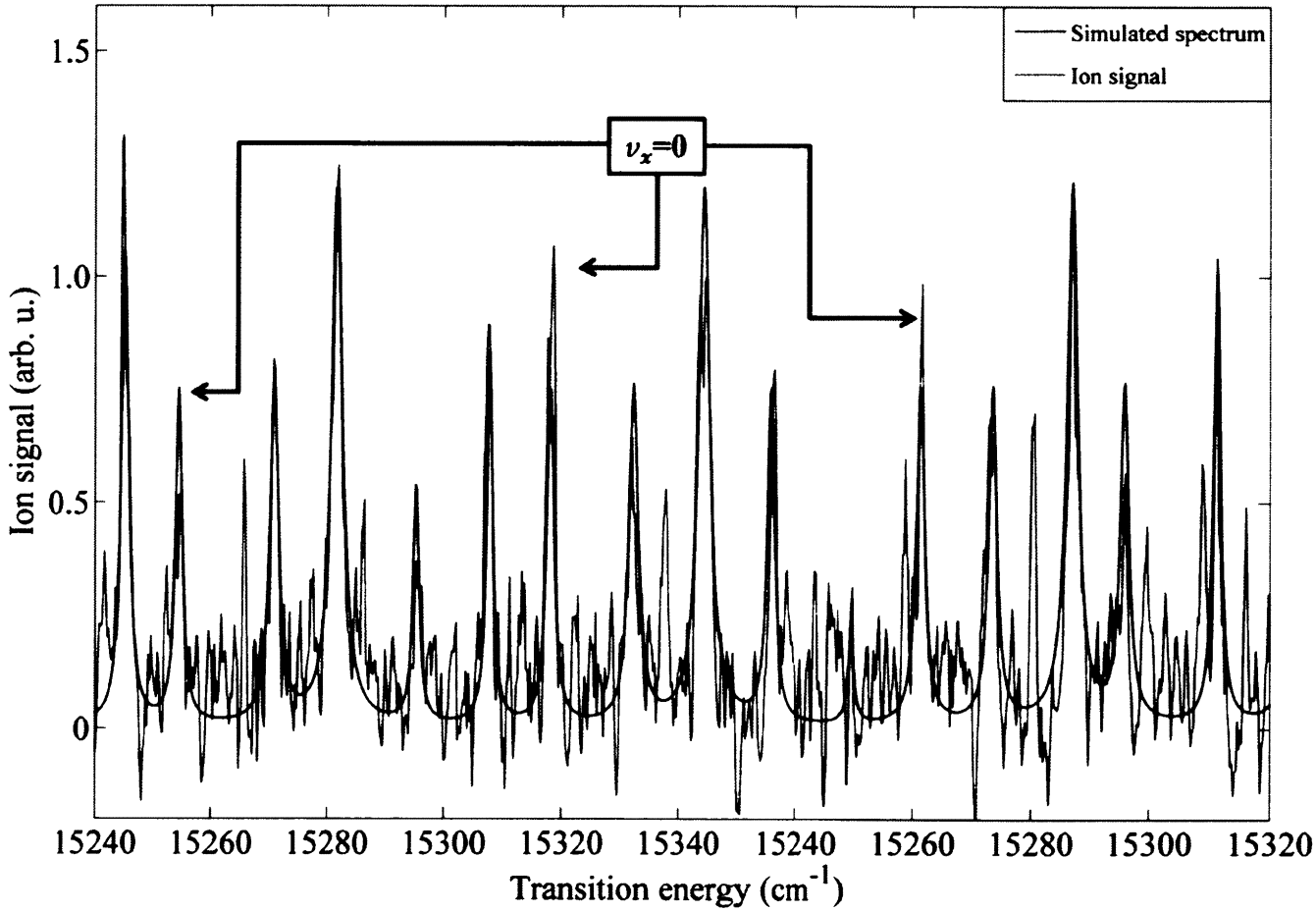


Figure 5.6: Ion signal and simulated spectrum from low-lying ($v_x$=0-4) vibrational levels in the $X^1\Sigma^+$ state to vibrational levels in the $(2)^1\Pi$ state. Transitions originating from the $X^1\Sigma^+(v_x=0)$ level are denoted with arrows.

## 5.3 Photoassociation to the $(2)^3\Pi_{0^+}$ State

Having shown that deeply-bound PA can create $X^1\Sigma^+$ state RbCs molecules in significant numbers, we sought out other nearby PA resonances that might make $X^1\Sigma^+(v{=}0)$ molecules more efficiently. The candidate state must have large free-to-bound and bound-to-bound FCFs as well as satisfy electric dipole transition selection rules between the atomic scattering ($a^3\Sigma^+$) and ground molecular ($X^1\Sigma^+$) states. This led us to analyze the $(2)^3\Pi_{0^+}$ state that had been partially characterized in [124].

### 5.3.1 Franck-Condon Factor Analysis

We calculated the bound-to-bound FCFs for transitions from low-lying vibrational levels in the $X^1\Sigma^+$ state to low-lying vibrational levels in the $(2)^3\Pi_{0^+}$ state using the RKR1 and LEVEL 8.0 programs [76, 77]. Free-to-bound FCF calculations were made using energy-normalized scattering state wavefunctions at 100 $\mu$K in the presence of the $a^3\Sigma^+$ potential and bound state wavefunctions of the $(2)^3\Pi_{0^+}$ state. To determine which $(2)^3\Pi_{0^+}$ vibrational level should create $X(v{=}0)$ molecules most efficiently, we calculated the products of the free-to-bound and bound-to-bound FCFs for each candidate PA state. These results are shown in Figure 5.7, and led us to investigate PA to the $v'{=}10$ vibrational level.

### 5.3.2 Rotational PA Spectroscopy

To calculate the PA resonance frequencies from the cold beam spectroscopy in [124], we subtract the energy difference between the bottom of the $X^1\Sigma^+$ potential well and the Rb $5s_{1/2}$ ($F{=}2$) + Cs $6s_{1/2}$ ($F{=}3$) atomic asymptote (3836.141 cm$^{-1}$) [19] from the $(2)^3\Pi_{0^+}$ term energies given in Ref. [124]. The measured PA frequencies and their deviations from the calculated values are given in Table 5.2. These discrepancies ($\sim$0.007 cm$^{-1}$) are consistent with the absolute accuracy of our wavemeter. Failure to observe PA to the $v'{=}3{,}6$ levels is consistent with the very small calculated free-to-bound FCFs. The absence of PA to $v'{=}7$ is discussed in Section 5.3.3. By scanning the frequency of the PA laser, we

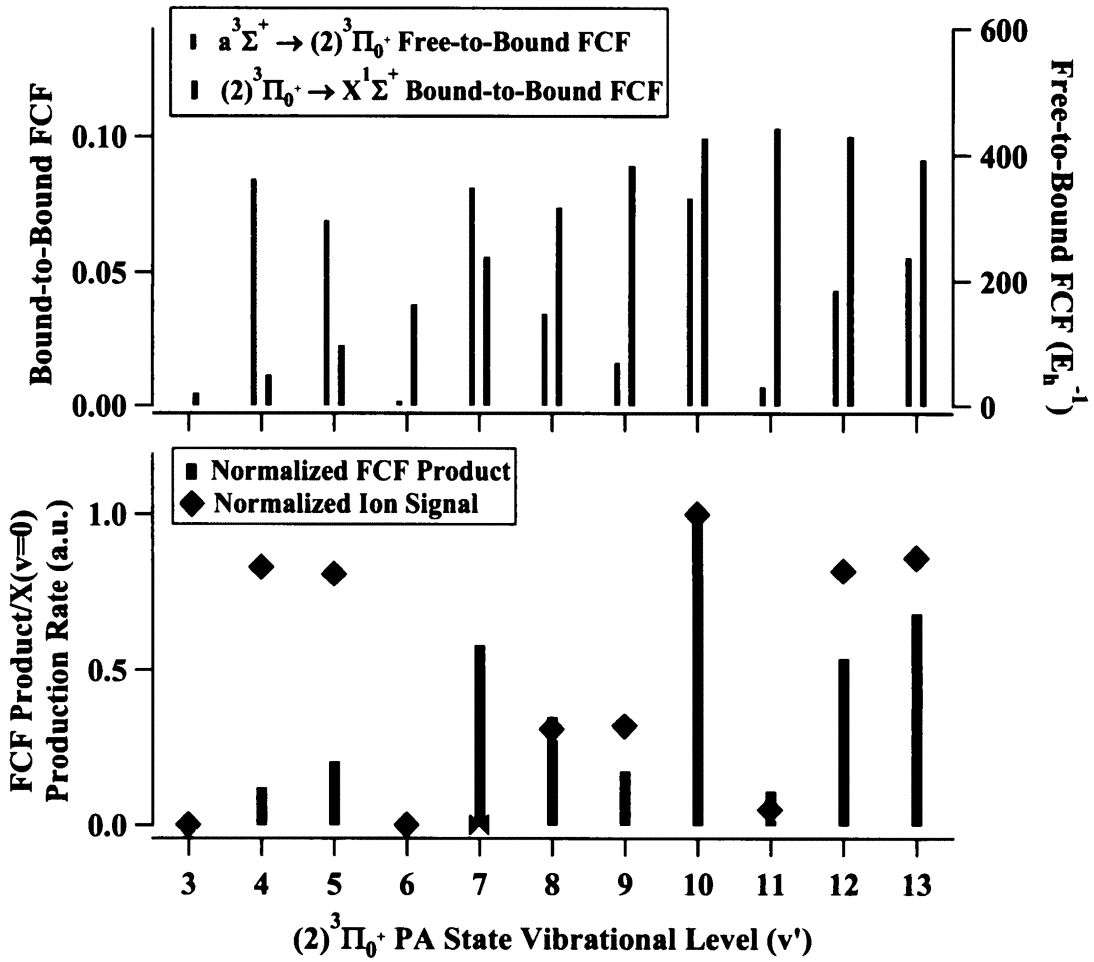


Figure 5.7: Top: Calculated Franck-Condon factors for different vibrational levels, $v'$, in the $(2)^3\Pi_{0+}$ state. The bound-to-bound FCFs (blue) are evaluated for transitions to the $X^1\Sigma^+(v=0)$ state. Free-to-bound FCFs (red) are calculated for an atomic scattering wavefunction at an energy corresponding to a temperature of 100 $\mu$K. Bottom: Calculated products of free-to-bound and bound-to-bound FCFs are shown in black. Measured $X^1\Sigma^+(v=0)$ ion signals are shown as points. Both are scaled such that the height of $v'=10$ is 1. Blue point indicates a level ($v'=7$) for which the PA laser itself strongly affects the Cs density. Figure reproduced from [113].

| $(2)^3\Pi_{0+}$ Vibrational Level | PA Frequency ($cm^{-1}$) | Difference from Prediction ($cm^{-1}$) |
|---|---|---|
| 13 | 11898.087 | -0.005 |
| 12 | 11871.452 | -0.002 |
| 11 | 11844.481 | -0.002 |
| 10 | 11817.183 | 0.002 |
| 9 | 11789.560 | 0.003 |
| 8 | 11761.620 | -0.004 |
| 5 | 11675.953 | -0.003 |
| 4 | 11646.798 | -0.007 |

Table 5.2: Resonance frequencies for PA to different vibrational levels in the $(2)^3\Pi_{0+}$ state. All frequency positions are for the $J'$=1 rotational level of the PA state.

verified the rotational constant of the excited $(2)^3\Pi_{0+}(v'=10)$ molecular state, and found the extracted rotational constant ($B_e$=0.0124(2) $cm^{-1}$) matched the value in [124] to within experimental precision. The rotational spectroscopy of the $(2)^3\Pi_{0+}(v'=10)$ state is shown in Figure 5.8.

### 5.3.3 REMPI Analysis of Populations of Decay from $(2)^3\Pi_{0+}$ ($v'$=10)

To determine the vibrational level population of the $X^1\Sigma^+$ state following spontaneous decay, we conducted REMPI analysis analogous to that done for the PA line at 11824 $cm^{-1}$ through the $(2)^1\Pi$ state, illustrated in Figure 5.9. The resulting spectroscopy and simulation, shown in Figure 5.10 and summarized in Table 5.3, show excellent agreement. The ($v'$=10) PA level makes $X^1\Sigma^+(v=0)$ molecules in greater proportion than other low-lying vibrational levels in the $X^1\Sigma^+$ state, supporting our Franck-Condon factor analysis.

Additionally, we determined relative values for $X^1\Sigma^+(v=0)$ molecular production rates for PA through various nearby vibrational levels, $v'$, of the $(2)^3\Pi_{0+}$ state, summarized in Figure 5.7. Qualitative agreement with our FCF analysis is generally good. The primary discrepancies come from an apparent over-production for PA through $v'$=4,5 and no production for $v'$=7. This may be due to perturbations of the Cs MOT by the PA laser

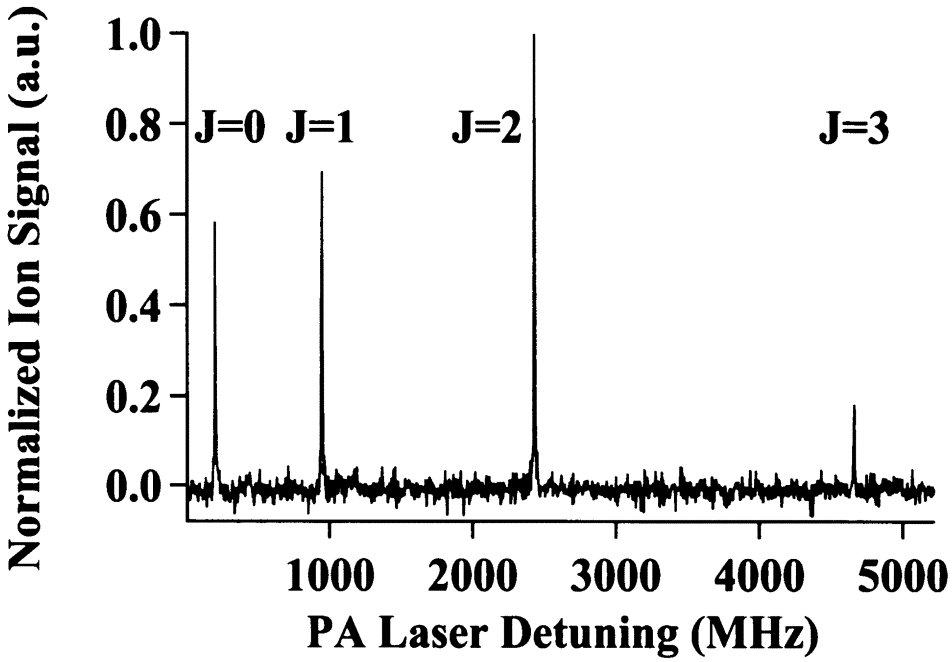


Figure 5.8: Rotational PA spectrum of the $(2)^3\Pi_{0^+}(v'=10)$ level. The measured rotational constant, $(B_{(v'=10)}=0.0124(2)\ cm^{-1}$, is consistent with the value given in Ref. [124] for this level $(B_{(v'=10)}=0.0123\ cm^{-1})$. Relative peak areas are consistent with calculated results using the formalism in Section 5.3.7. We use the peak areas (rather than heights) to account for observed broadening due to the Stark effect from the applied electric field used to accelerate the molecular ions. Failure to observe the $J$=4 rotational level at the predicted location is consistent with excitation of $\ell \leq 2$ scattering states to an $\Omega = 0^+$ PA state. Figure reproduced from [113].

| $X^1\Sigma^+$ Vibrational Level $(v_x)$ | Relative Population $(p_{v_x}/p_{v_0})$ |
|---|---|
| 0 | 1 |
| 1 | 0.7 |
| 2 | 0.5 |
| 3 | 0.3 |
| 4 | 0.3 |
| 5 | 0.2 |
| 6-10 | 0.3 |

Table 5.3: Relative $X^1\Sigma^+(v_x)$ vibrational level populations, $p_{v_x}/p_{v_0}$, following spontaneous decay from $(2)^3\Pi_{0^+}(v'=10)$, extracted from REMPI spectroscopy data. Table reproduced from [113].

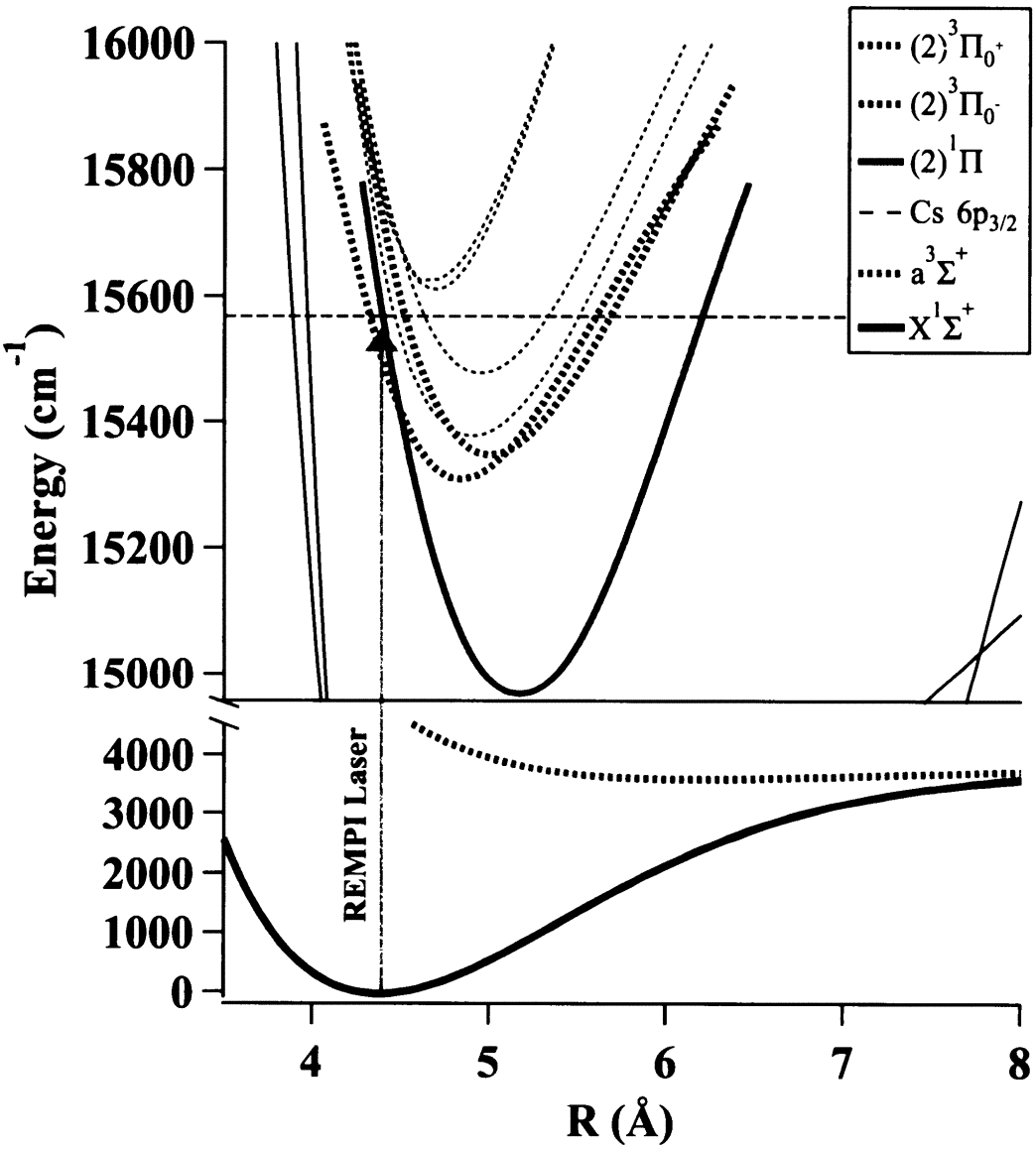


Figure 5.9: Relevant potential energy curves for RbCs from values in Refs. [121, 118, 124, 19, 123]. Photoassociation proceeds through deeply-bound levels of the $(2)^3\Pi_{0+}$ state. These levels spontaneously decay to the $X^1\Sigma^+$ and $a^3\Sigma^+$ states. The resulting $X^1\Sigma^+$ state vibrational population measured through REMPI analysis of $X^1\Sigma^+ \rightarrow (2)^1\Pi$ transitions. Single-photon transitions to the nearby $(2)^3\Pi_{0-}$ state are forbidden and do not contribute to the REMPI signal. Thick (thin) lines denote potentials extracted from experimental data (*ab initio* calculations). Solid (dotted) lines denote singlet (triplet) states. The $6p_{3/2}$ atomic Cs asymptote is given by the dashed horizontal line. Figure reproduced from [113].

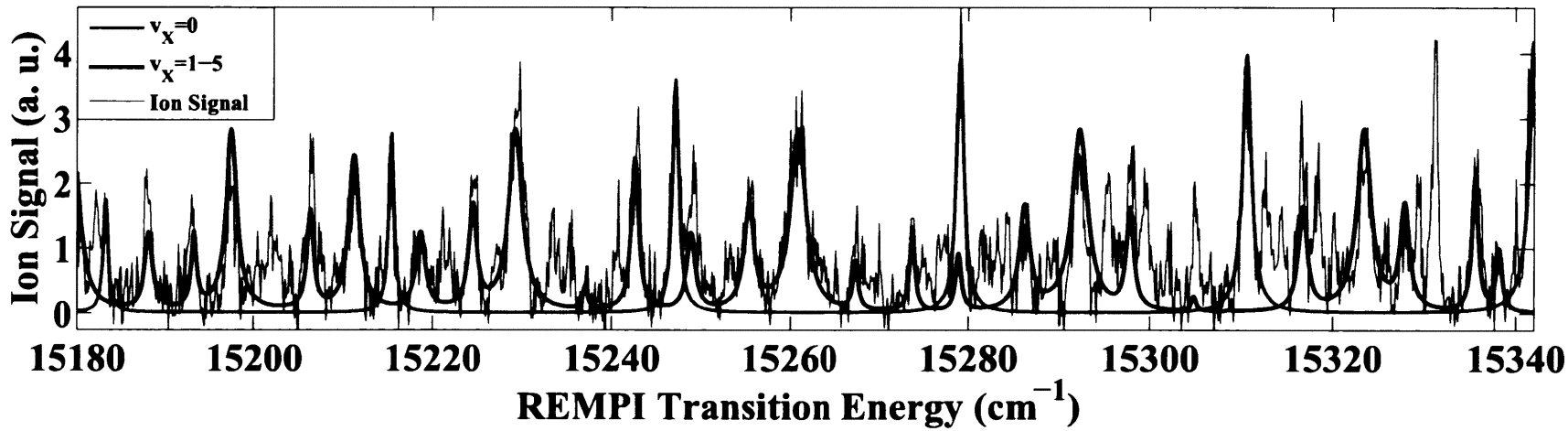


Figure 5.10: REMPI scan of vibrational progression of the $X^1\Sigma^+(v_x) \rightarrow (2)^1\Pi\ (v'_\Pi)$ transitions. For this data, the PA laser frequency is locked to the $J$=1 rotational line of the $(2)^3\Pi_{0^+}$ state (near 11817.18 $cm^{-1}$) while the frequency of the pulsed dye laser is scanned. Red (black) fit line shows the predicted spectra arising from population in $X^1\Sigma^+(v_x$=0) (sum of $v_x$=1-5). Line positions for the fit are based on spectroscopic data in Ref. [124]; peak heights and widths are set by calculated FCFs and fit vibrational populations, $p_{v_x}$. Figure reproduced from [113].

beam. For $v'$=4,5, the intense PA laser is approximately 75-100 $cm^{-1}$ red-detuned relative to the Cs D2 line, creating a potential well a few tens of $\mu$K deep for Cs atoms under our conditions, possibly increasing the Cs density and increasing the PA rate.[2] For $v'$=7, the PA resonance is very close to the D2 line and strongly perturbs the Cs MOT, precluding efficient molecular formation. Lastly, for the laser intensity ($I_{PA} \approx$550 W/$cm^2$) used here, modest saturation of PA was seen for $(2)^3\Pi_{0+}(v'=10)$, and is also likely for vibrational levels with similarly high free-to-bound FCFs ($v'$=4,5). The observed X($v$=0) production rate would therefore be reduced, relative to the expectation from the calculated FCF product.

The next two sections (5.3.4 and 5.3.5) are taken directly from [113] with minor typographical changes.

### 5.3.4 Saturation of Photoassociation Rate

We also measured the dependence of the molecular creation rate on PA laser intensity. This dependence is given in [80] as

$$K \propto \frac{I_{PA}}{(I_{PA} + I_{sat})^2}, \tag{5.4}$$

where $I_{sat}$ is the PA laser intensity that maximizes ground state molecular formation. By measuring the molecular production as a function of laser intensity, we can extract an approximate value for $I_{sat}$, as shown in Figure 5.11. We extract a fit value for $I_{sat}$ = 4(2) kW/$cm^2$, where the uncertainty is dominated by imprecise knowledge of the effective PA laser beam size at the position of the atoms. We can compare this fit value to one estimated using our free-to-bound FCF and a crudely approximated value for the product of angular factors and the electronic matrix element (taken here as $\langle d \rangle \sim 2ea_0$, where $e$ is the electron charge and $a_0$ is the Bohr radius). With this assumption, we estimate a saturation intensity for PA to the $(2)^3\Pi_{0+}(v'=10)$ state of $I_{sat}$ ~13 kW/$cm^2$, in crude qualitative agreement

[2]The trap depth is calculated as in [58], $U = -\frac{3\pi c^2}{2\omega_0^3}\frac{\Gamma}{\Delta}I$, where $\omega_0$ is the Cs D2 resonance frequency (11732 $cm^{-1}$), $\Gamma$ is the D2 excited state linewidth ($2\pi \cdot 5.2$ MHz), $\Delta$ is the laser detuning from resonance, $I$ is the laser intensity, and $c$ is the speed of light. Atomic Cs values come from Ref. [125].

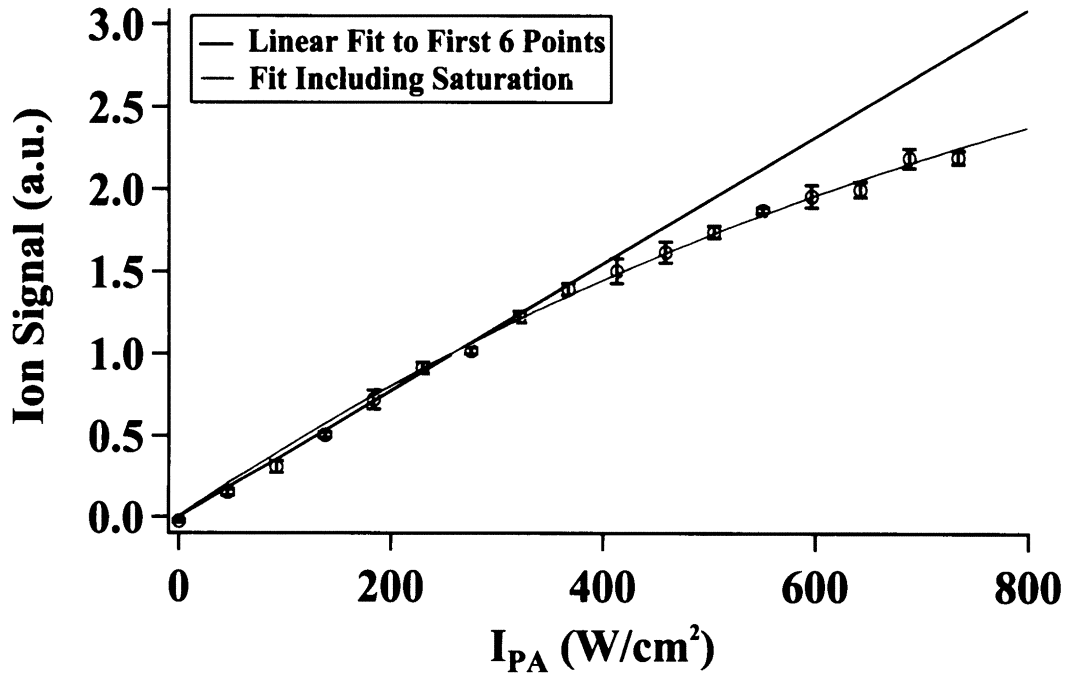


Figure 5.11: Onset of saturation in molecular production with increased laser intensity. Here the PA laser is locked to the $J$=1 line of the $(2)^3\Pi_{0^+}(v'=10)$ level. Fit to saturation behavior of Equation (2) (red) allows for extraction of the saturation intensity, $I_{sat}$. Figure reproduced from [113].

with our fit value.

### 5.3.5 Molecular $X^1\Sigma^+(v=0)$ Production Rate

Based on our experimental parameters (average atomic densities: $n_{Rb} \approx 6\times10^{10}$ cm$^{-3}$, $n_{Cs} \approx 8\times10^{10}$ cm$^{-3}$), the calculated FCF (330 $E_h^{-1}$, where $E_h$ is the Hartree energy), and a crudely approximate value for the electric dipole matrix element including all angular factors ($\langle d \rangle \sim 2ea_0$), we expect a total PA rate of approximately $R \sim 10^6$ molecules/s. This value takes into account that the PA laser beam is smaller than the atomic clouds in the MOTs. The interaction volume can be approximated as a cylinder with a radius defined by the beam waist ($\approx 100$ $\mu$m) and length given by the atom cloud diameter ($d \approx 400$ $\mu$m).

The ground state formation rate, $R_{X_0}$, is scaled by the branching fraction for decay from the PA state to the X($v$=0) state, and is given by $R_{X_0} = bR$. The value of $b$ is determined

by a combination of two factors: the electronic branching fraction and the bound-to-bound FCF. We crudely estimate the electronic state branching fraction as follows. The $(2)^3\Pi_{0+} \rightarrow X^1\Sigma^+$ electric dipole transition is nominally forbidden, due to the change in total spin $S$. However, mixing of singlet and triplet states due to the spin-orbit interaction is a significant effect in heavy molecules like RbCs, and such mixing leads to a non-zero transition amplitude. To calculate the mixing coefficient, we use a perturbative approach analogous to that described in Ref. [126]. The $(2)^3\Pi_{0+}$ state connects to the Rb $5p$ + Cs $6s$ asymptote and should mix most strongly with the nearby $(3)^1\Sigma^+$ state that connects to the same asymptote. In a simple approximation where we ignore the contribution of other atomic orbitals to these molecular states, the spin-orbit coupling matrix element between the states can be simply related to the spin-orbit splitting in the atomic Rb $5p$ state.[3] Expressing the atomic Rb spin-orbit Hamiltonian as $H_{SO} = V_{SO}(\vec{\ell}_a \cdot \vec{s}_a)$ (where $\vec{\ell}_a$ and $\vec{s}_a$ are the atomic electron's orbital and spin angular momenta, respectively), we calculate $V_{SO} \approx 110$ cm$^{-1}$, from the Rb $5p$ values in Ref. [127]. Then the approximate mixing coefficient, $c_{SO}$, between the $(2)^3\Pi_{0+}$ and $(3)^1\Sigma^+$ states is given by

$$c_{SO} \approx \frac{\sqrt{2}V_{SO}}{E_{(2)^3\Pi_{0+}} - E_{(3)^1\Sigma^+}}, \tag{5.5}$$

where the energy difference in the denominator has a value of $\approx 1700$ cm$^{-1}$ [126]. Hence, the transition probability is reduced by a factor of $|c_{SO}|^2 \approx 0.009$ compared to a fully allowed electric dipole transition. To calculate the electronic state branching fraction, we must also take into account the scaling of the spontaneous decay rate with $\omega^3$, where $\omega$ is the frequency of the decay radiation. The frequency for the $(2)^3\Pi_{0+} \rightarrow$ X decay ($\sim$15700 cm$^{-1}$) is a factor of 1.3 larger than that for the fully allowed decay to the $a^3\Sigma^+$ state ($\sim$12000 cm$^{-1}$). Hence the electronic state branching fraction for $(2)^3\Pi_{0+} \rightarrow$X decay should be $\sim (1.3)^3|c_{SO}|^2 \approx 0.02$. As shown in Figure 5.7, the ($v'$=10$\rightarrow v$=0) bound-to-bound FCF has the value $F \approx 0.1$. Hence we finally estimate a vibronic state branching ratio, $b \sim$

[3] A more detailed derivation of the relationship between the atomic and molecular spin-orbit mixing can be found in Appendix 1.

0.002. Putting this together with the calculated photoassociation rate, $R$, we therefore predict an approximate total X($v$=0) production rate of $R_{X_0}$ ~$2\times10^3$ molecules/s under our particular experimental conditions.

This calculated result can be compared to the approximately calibrated signal in our experiment. Based on our signal size ($3\times10^{-9}$ V·s terminated at 50 Ω), detector gain ($G_{\text{Channeltron}} \approx 10^7$, $G_{\text{Preamp}} \approx 5$), crudely estimated ionization efficiency (~ 5%) [128], and molecule fraction in the detection region for a given REMPI pulse (≈0.025, due to molecular motion at a temperature $T$ ≈100 μK), we estimate the observed X($v$=0) production rate to be $R_{X_0}$ ~$6\times10^3$ molecules/s, where the primary uncertainties come from the Channeltron detector gain and the ionization efficiency. This is in qualitative agreement with our theoretical estimate.

### 5.3.6 Nature of the Photoassociation State at 11824 cm$^{-1}$

Ji *et al.* [119] and Fioretti and Gabbanini [121] observed different, nearby short-range PA lines (including the line at 11824 cm$^{-1}$) that they assigned to the $(2)^3\Pi_{0+}$ state. Based on our results, however, the levels they observed must belong to the $\Omega$=$0^-$ component of the $(2)^3\Pi_0$ state. Our conclusion is based primarily on the very precise agreement of our observations with the data in Ref. [124]. The assignment in Refs. [119, 121] relied on much less precise comparison to *ab initio* calculations to distinguish between assignment to $\Omega=0^+$ versus $\Omega=0^-$ states. Further justifications of this assignment are given in Section 5.3.7.

Although single-photon decay to the $X^1\Sigma^+$ state is prohibited for $\Omega = 0^-$ states, we observed the formation of $X^1\Sigma^+$ molecules at rates comparable to those seen following PA to the $(2)^3\Pi_{0+}(v'=10)$ state. This unexpected formation could be due to a two-photon decay that proceeds through an $\Omega=1$ intermediate state. Compared to the case of direct, single-photon decay, this two-photon process should be suppressed by the $\omega^3$ dependence of the spontaneous decay rate to the higher-lying intermediate levels, where $\omega$ is the frequency of the decay photon. However, the intermediate states may have strong singlet/triplet mixing

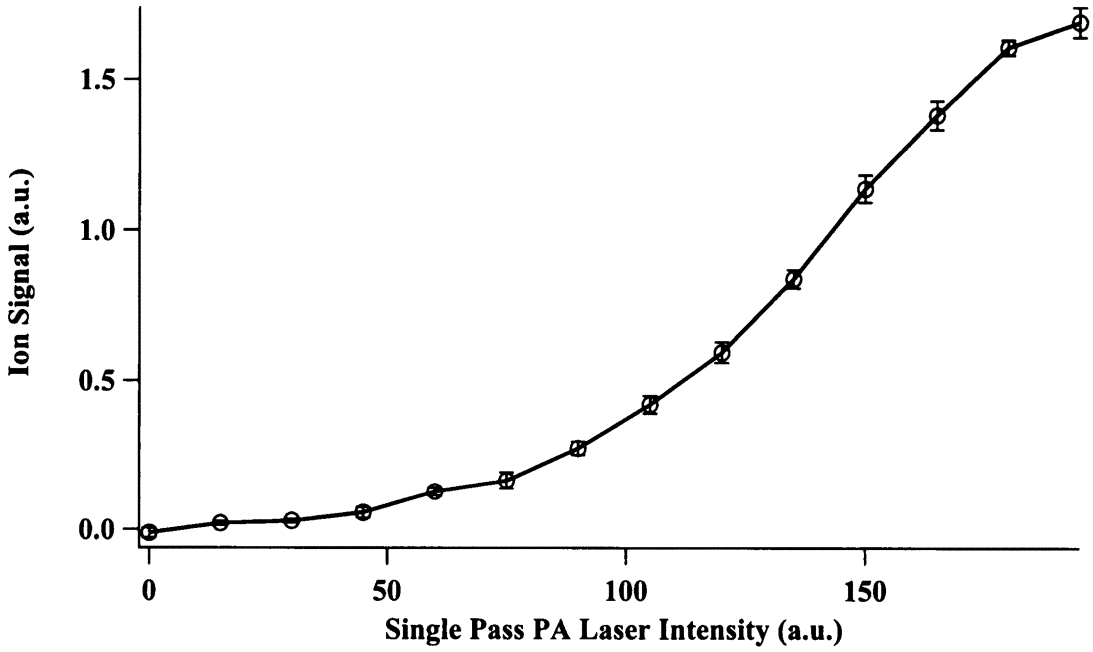


Figure 5.12: Saturation behavior of the $(2)^3\Pi_{0-}$ state. The positive concavity for the large majority of the data is opposite that seen in photoassociative saturation, which suggests an additional mechanism affecting the molecular production rate. Solid line is only to guide the eye.

that would enhance the relative formation rate of $X^1\Sigma^+(v{=}0)$ molecules for this process, compared to the direct, nominally forbidden decay from the $(2)^3\Pi_{0+}$ state. Further, the PA laser creates a potential well that is a few hundreds of $\mu$K deep for Cs atoms for this resonance ($\approx$8 cm$^{-1}$ red-detuned relative to the Cs D2 line) under our conditions. This may lead to an enhancement in the observed $X^1\Sigma^+(v{=}0)$ formation rate, beyond that expected simply from the PA rate and decay branching ratio. To investigate this possibility, we measured the $X^1\Sigma^+(v{=}0)$ formation rate following PA to the 11824 cm$^{-1}$ line as a function of PA laser intensity. As seen in Figures 5.12 and 5.13, the intensity dependence of molecular detection exhibits a qualitatively different behavior than that in Figure 5.11. The increasing slope is the opposite trend one would expect in the presence of photoassociative saturation from Eq. 5.4. At higher PA intensities, this mechanical effect visibly perturbed the MOT, reducing PA efficiency, as seen in Figure 5.13.

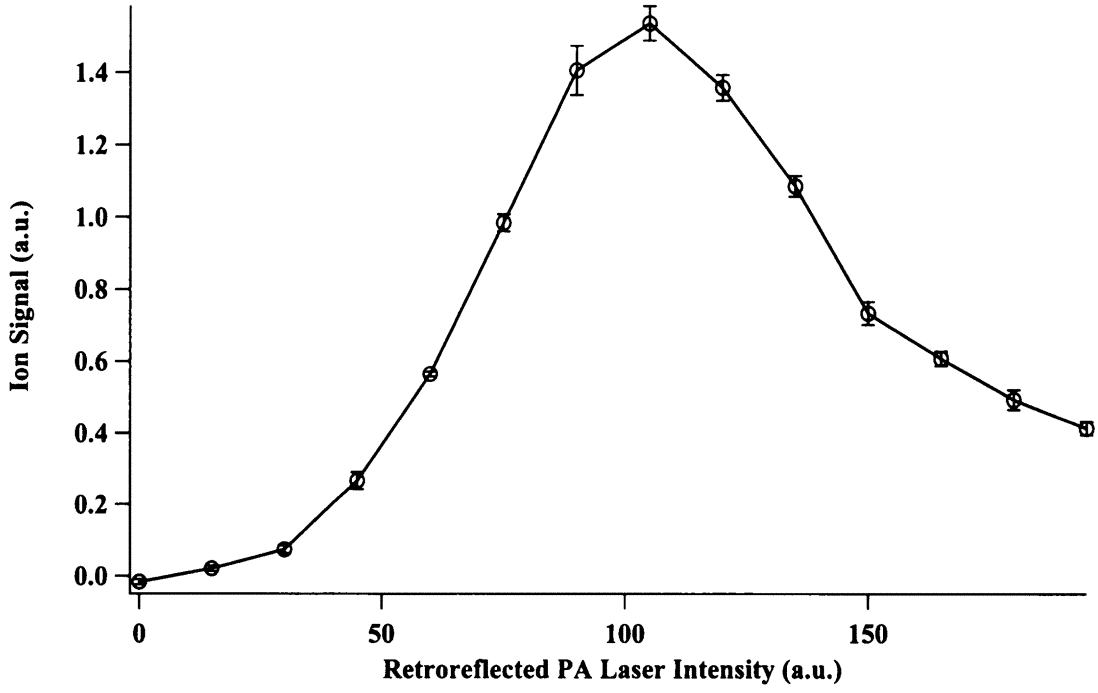


Figure 5.13: Saturation behavior of the $(2)^3\Pi_{0^-}$ state (retroreflected). The beam size of the first PA laser pass and retroreflection are not the same. Hence, the laser intensity of the single-pass and retroreflected saturation data should not be quantitatively compared. The retroreflected intensity can, however, be bounded as less than twice the single-pass intensity. For the highest PA laser intensities, the Cs MOT was visibly perturbed. Solid line is only to guide the eye.

### 5.3.7 Verifying Assignments

To further justify our assignment of the 11824 $cm^{-1}$ line to the $(2)^3\Pi_{0^-}$ state, we applied the rotational line strength formalism developed earlier in this thesis. We can convert the calculated line strength for given rotational level, $J'$, into an expected signal size by summing over scattering partial waves, $\ell$, and weighting the contributions from $W(J',\ell)$ (reproduced in Table 5.4) to account for the centrifugal barrier. This total signal size, $S(J',T)$, is given by

$$S(J',T) = \sum_{\ell} W(J',\ell) f(\ell,T), \tag{5.6}$$

where $T$ is the temperature and $f(\ell, T)$ is a temperature-dependent weighting function. In the simplest model, $f(\ell, T)$ is a partition function of the form:

$$f(\ell, T) = \frac{e^{-E(\ell)/k_B T}}{\sum_{\ell'}(2\ell'+1)e^{-E(\ell')/k_B T}}, \tag{5.7}$$

where the centrifugal barrier height, $E(\ell)$, is calculated as in Ref. [40] using the $C_6$ coefficient found in Ref. [129] and $k_B$ is Boltzmann's constant. In the case of $^{85}$RbCs, this gives $p$, $d$, and $f$-wave barrier heights of 56 $\mu$K$\cdot k_B$, 290 $\mu$K$\cdot k_B$, and 820 $\mu$K$\cdot k_B$, respectively.

For the temperatures of our atomic samples ($T \sim$100 $\mu$K), we expect the contributions from $\ell \geq 3$ to be negligible. Then, by considering the ratio of the signal sizes of $J'=2/J'=0$ for $\Omega=0^+$ and $J'=3/J'=1$ for $\Omega=0^-$, the ratios should depend only on the calculated angular factors encoded in $W(J', \ell)$, independent of the details of the atomic samples. Specifically, we find

$$\Omega = 0^+ \quad : \frac{S(2,T)}{S(0,T)} = \frac{\sum_\ell W(\ell,2) f(\ell,T)}{\sum_\ell W(\ell,0) f(\ell,T)} = \frac{W(1,2)}{W(1,0)} = 2 \tag{5.8}$$

$$\Omega = 0^- \quad : \frac{S(3,T)}{S(1,T)} = \frac{\sum_\ell W(\ell,3) f(\ell,T)}{\sum_\ell W(\ell,1) f(\ell,T)} = \frac{W(1,3)}{W(1,1)} = \frac{1}{4} \tag{5.9}$$

Comparing this result to our rotational spectroscopy in Figure 5.8, we find good agreement between the measured $J'=2$ to $J'=0$ ratio of 1.8 and the calculated value of 2. Using the data from Figure 3 in Ref. [119], we find similarly good agreement between the calculated $J'=3$ to $J'=1$ ratio of 1/4 and the measured value.[4] The excellent agreement between our calculation and the measured signal size ratios, coupled with the previous analysis based on level locations and intensity dependence of PA rate, gives us very high confidence in our molecular state assignment.

[4]Extensions of this rotational line strength formalism to include PA to other molecular states are given in Appendix 3.

| $^3\Pi_{0+}$ | $J'$=0 | $J'$=1 | $J'$=2 | $J'$=3 | $J'$=4 | $J'$=5 |
|---|---|---|---|---|---|---|
| $\ell$=0 | 0 | 1 | 0 | 0 | 0 | 0 |
| $\ell$=1 | 1 | 0 | 2 | 0 | 0 | 0 |
| $\ell$=2 | 0 | 2 | 0 | 3 | 0 | 0 |
| $\ell$=3 | 0 | 0 | 3 | 0 | 4 | 0 |
| $^3\Pi_{0-}$ | $J'$=0 | $J'$=1 | $J'$=2 | $J'$=3 | $J'$=4 | $J'$=5 |
| $\ell$=0 | 1.1 | 0 | 0.56 | 0 | 0 | 0 |
| $\ell$=1 | 0 | 4 | 0 | 1 | 0 | 0 |
| $\ell$=2 | 0.56 | 0 | 6.3 | 0 | 1.4 | 0 |
| $\ell$=3 | 0 | 1 | 0 | 8.8 | 0 | 1.9 |

Table 5.4: Calculated partial wave contributions, $\tilde{W}(J', \ell)$, from all $M_{F(\mathrm{Rb})}, M_{F(\mathrm{Cs})}$ combinations to purely Hund's case (a) $^3\Pi_0(|\Lambda'|=1,\ S'=1)$ state, deeply-bound PA levels. Tilde denotes that all calculated values of $W(J', \ell)$ within a given electronic state were normalized by the same value.

## 5.4 Summary

In this chapter, we have demonstrated the continuous formation of $X^1\Sigma^+(v=0)$ state RbCs molecules following spontaneous decay from deeply-bound PA levels. We have analyzed the formation rates for different vibrational levels, $v'$, of the $(2)^3\Pi_{0+}$ state and measured the saturation intensity of the $v'=10$ state that efficiently produces $X^1\Sigma^+(v=0)$ molecules. We have also determined the molecular symmetry of a deeply-bound PA level found in [114] based on the line strengths of PA to different rotational levels.

Deeply-bound PA of RbCs presents an interesting method of possibly creating large samples of trapped polar molecules. Given that the vibrational ground state is populated by spontaneous decay, no population transfer scheme is necessary, and molecules can be created continuously. Further, the energetics of RbCs are such that ground state molecules are predicted to be stable against two-body collisions [41]. In the next chapter, we discuss recent calculations on predicted molecular sample sizes based on this deeply-bound PA scheme as well as possible techniques for sample purification and further cooling.

# Chapter 6

# Future Directions

## 6.1 Introduction

In the previous chapter, we demonstrated numerous pathways to continuously produce ultracold vibronic ground state polar molecules. In order to probe much of the desired physics associated with this system, it will next be necessary to confine a large sample of these molecules with a long trap lifetime. The rotationally and vibrationally excited molecules that are also created during PA are predicted to lead to rapid trap loss through inelastic scattering with the desired $X^1\Sigma^+(v{=}0,\ J{=}0)$ molecules. Here we discuss a proposed method to purify the sample and include detailed calculations of the expected molecular densities and numbers. Much of the discussion of molecular trapping and sample purification appears in a slightly different form in Ref. [113].

## 6.2 Depletion Spectroscopy of the $X^1\Sigma^+(v{=}0)$ State

Electric dipole selection rules constrain the rotational levels of the $X^1\Sigma^+(v{=}0)$ state populated following spontaneous decay from the $(2)^3\Pi_{0^+}$ PA state. Further, the relative line strengths in emission and corresponding population fractions are set by the appropriate Hönl-London factors. For PA to the $(2)^3\Pi_{0^+}$ state with $J_{\mathrm{PA}}{=}1$, $S_{J=2}/S_{J=0}{=}2$ for the $X^1\Sigma^+$

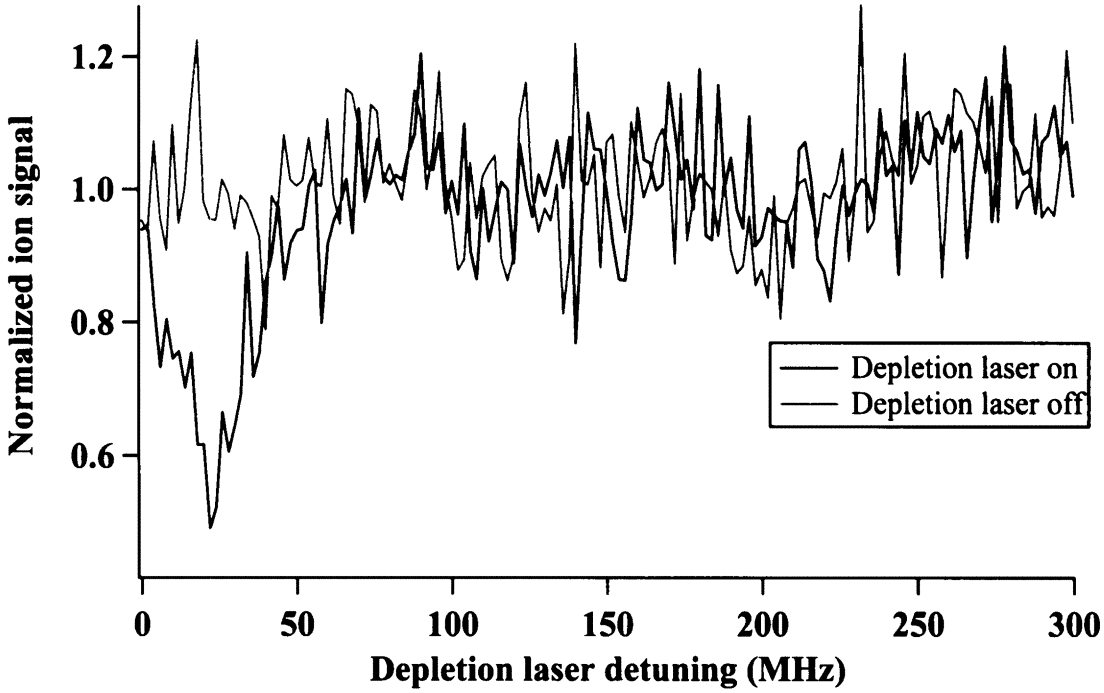


Figure 6.1: Depletion of $X^1\Sigma^+(v{=}0)$ molecules. Molecules are photoassociated through the $(2)^3\Pi_{0+}(v'{=}10,\ J_{PA}{=}0)$ level. Selection rules dictate that all $X^1\Sigma^+(v{=}0)$ molecules are in the $J_X{=}1$ rotational level. The target depletion state is $(2)^3\Pi_{0+}(v''_\Pi{=}7,\ J_\Pi{=}2)$ near 15544.55 $cm^{-1}$.

state. Hence, we expect 1/3 of the molecules created in the vibronic ground state to be in the $J{=}0$ state.

In order to verify the expected rotational populations, we have begun depletion spectroscopy of the vibronic ground state molecular sample. Initially, we intended to take advantage of the fully-allowed transitions to the $(2)^1\Pi$ state that we had used so successfully in our REMPI spectroscopy. Unfortunately, the additional spectroscopic features associated with this $\Omega = 1$ state complicated the analysis, leading us to find another target excitation state. Now, we are using the very well-characterized $(2)^3\Pi_{0+}$ state that we studied previously in the context of PA. These state locations are known to very high precision, and we have already seen indications of molecular depletion, shown in Figure 6.1.

## 6.3 Molecular Trapping and Sample Purification

Long trapping times require that the sample be purified of all species that might lead to inelastic scattering. The spontaneous decay of the photoassociation state populates numerous vibrational and rotational levels associated with the $X^1\Sigma^+$ and $a^3\Sigma^+$ electronic ground states. Any collision between a rotationally or vibrationally excited molecule with an absolute ground state molecule is likely to result in an inelastic scattering event that will convert the internal energy associated with the molecular excitation into kinetic energy shared between the two collision partners. Even the relatively small rotational energies ($\sim$0.5 K) are many times greater than the depth of any optical trap we can create ($<$1 mK). Thus any inelastic scattering event will lead to trap loss and rapid depletion of our sample.

In order to reduce this molecular trap loss, we intend to purify the sample by selectively removing the excited molecules from the trap. This process, first proposed in [89], exploits the chemical stability of RbCs to collisions with Cs atoms. In the absolute ground state, the RbCs + Cs $\rightarrow$ Rb + $Cs_2$ replacement reaction is endothermic by $\sim$190 $cm^{-1}$ and should not proceed at our ultracold temperatures [130]. Excited RbCs, however, is still subject to inelastic scattering processes with Cs atoms and should be rapidly ejected from the trap. Remaining Cs atoms after purification can then easily be removed with a weak resonant push laser beam. Hence, by intentionally loading a high density of Cs atoms into the trap, we may be able to selectively remove the excited molecules with only a modest reduction in the ground state molecular sample.

### 6.3.1 Photoassociation in the Optical Trap

The first tests of the atomic "scrubbing" technique will likely occur as follows. The optical trap will be loaded with both Rb and Cs atoms, as was done previously in our weakly-bound photoassociation work in Chapter 4. The PA laser will then be turned on for some period of time to create a mixed sample of excited and ground state molecules. Next, a resonant

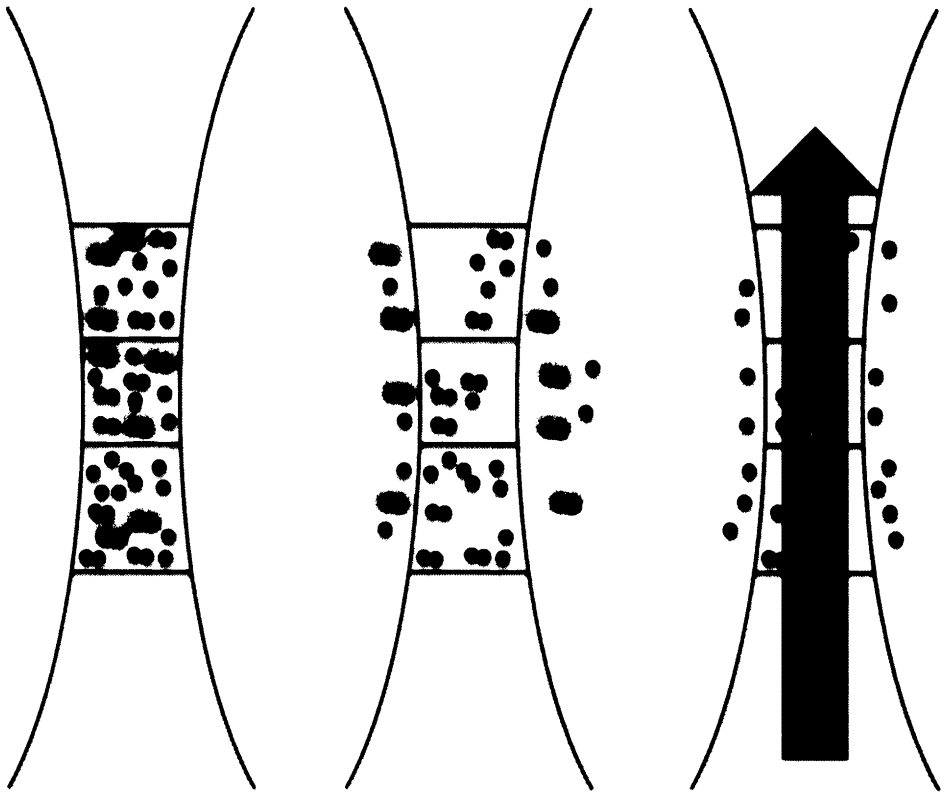

Figure 6.2: Schematic of trap purification through atomic scrubbing. Left: Optical trap initially contains excited (shaded) and ground state (unshaded) RbCs as well as Cs atoms. Middle: Atoms inelastically scatter with excited molecules, and both are ejected from the trap. Ground state molecular collisions are purely elastic and do not lead to trap loss. Right: A resonant push beam (arrow) ejects remaining Cs atoms, leaving a pure ground state molecular sample.

push beam will remove all of the Rb atoms, which would otherwise chemically react with ground state RbCs. All of the molecules will then be free to collide with the remaining Cs atoms. The ground state molecules should scatter elastically with atoms, remaining in the trap, while the excited state molecules should inelastically scatter and be ejected. This process is shown schematically in Figure 6.2. We can then measure the ground state molecular population for different trap hold times. If the scrubbing is successful, the molecular lifetime should shed the rapid loss associated with inelastic scattering and become more consistent with the chamber vacuum-limited loss seen in atoms.

### 6.3.2 Steady-State Molecular Accumulation

Although photoassociation in the optical trap will be useful for measuring the efficacy of the scrubbing technique, the pulsed nature of optical trap loading precludes continuous molecular production. Instead, we intend to photoassociate molecules directly from the MOTs and allow them to fall into the optical trap as was done previously in [89]. After some equilibration time, the ground state molecular density should approach a value where the competing processes of molecular creation via PA and destruction via inelastic scattering are balanced. We should then be able to remove the Rb atoms, load the optical trap with Cs atoms, and allow the purification to proceed.

The population analysis in the next two sections (6.3.3 and 6.3.4) can be found in [113].

### 6.3.3 Simple Population Models

To predict the expected molecular sample sizes using this scheme, we have modeled the population dynamics. The excited and ground state molecular populations during PA in the presence of inelastic scattering can be modeled using the following rate equations:

$$\dot{n}_{\mathrm{RbCs}} = \tilde{b} K_{\mathrm{PA}} n_{\mathrm{Rb}} n_{\mathrm{Cs}} - K_{(\mathrm{RbCs-Rb})} n_{\mathrm{RbCs}} n_{\mathrm{Rb}} - K_{(\mathrm{RbCs-RbCs^*})} n_{\mathrm{RbCs}} n_{\mathrm{RbCs^*}}, \quad (6.1)$$

$$\dot{n}_{\mathrm{RbCs^*}} = (1-\tilde{b}) K_{\mathrm{PA}} n_{\mathrm{Rb}} n_{\mathrm{Cs}} - K_{(\mathrm{RbCs^*-Rb})} n_{\mathrm{RbCs^*}} n_{\mathrm{Rb}} - K_{(\mathrm{RbCs^*-Cs})} n_{\mathrm{RbCs^*}} n_{\mathrm{Cs}} \quad (6.2)$$
$$- K_{(\mathrm{RbCs^*-RbCs})} n_{\mathrm{RbCs^*}} n_{\mathrm{RbCs}} - K_{(\mathrm{RbCs^*-RbCs^*})} n^2_{\mathrm{RbCs^*}},$$

where $\tilde{b}$=$b/3$ is the branching ratio to the $v$=$J$=0 level, $n_x$ is the density of species $x$, $K_{\mathrm{PA}}$ is the rate coefficient for photoassociation, and $K_{(x-y)}$ is the inelastic collision rate coefficient for species $x$ and $y$. Here $x$=RbCs* refers to RbCs molecules in any state except the X($v$=$J$=0) state, and $x$=RbCs refers only to rovibronic ground state molecules.

To calculate the approximate rate coefficients for inelastic scattering, we note that both $s$ and $p$-waves contribute at our temperatures. Further, we assume that each scattering wave component yields the maximum unitarity-limited contribution ($K_{\mathrm{UL}} = \langle v_{\mathrm{rel}} \frac{\pi}{k^2} \rangle$), as

suggested by previous work in Refs. [108, 35, 89, 109]. Given that $p$-wave scattering has 3 $(2\ell+1)$ components, the total rate coefficient for combined $s$ and $p$-wave scattering is given by $K_{\rm tot} = 4K_{\rm UL} \approx 1.2 \times 10^{-10}$ cm$^3$/s at 100 $\mu$K.

We set $K_{\rm PA}$ to the $s$-wave unitarity-limited value ($K_{\rm PA} \approx 3\times10^{-11}$ cm$^{-3}$), as it should be possible to saturate the PA rate with sufficient laser power [131].[1] Then in the limit of small branching, $\tilde{b} \ll 1$ ($\tilde{b} \sim 0.07\%$ for X($v$=$J$=0), and constant and equal Rb and Cs density ($n_{\rm Rb}$=$n_{\rm Cs}$), the steady-state density of rovibronic ground state molecules is given approximately by

$$n_{\rm RbCs} \approx \frac{\tilde{b}}{2\sqrt{5}} n_{\rm Cs}. \tag{6.3}$$

For improved atomic densities of $n_{\rm Rb}$=$n_{\rm Cs}$=$5\times10^{11}$ cm$^{-3}$, as achieved in Ref. [89], and including the effects of atomic loss from the MOTs due to PA, the ground state molecular density maximizes at $n_{\rm RbCs} \approx 5\times10^7$ cm$^{-3}$ after $\approx$40 ms for $\tilde{b}$=0.0007.

### 6.3.4 Simulated Scrubbing

We have also carried out simulations of the expected steady-state molecular densities following the scrubbing process using a simple model. Again, we estimate the inelastic scattering cross-sections using the combined $s$ and $p$-wave unitarity-limited rate of $1.2\times10^{-10}$ cm$^3$/s. The rate equations during the purification process are given by:

$$\dot{n}_{\rm RbCs} = -K_{\rm (RbCs-RbCs^*)} n_{\rm RbCs} n_{\rm RbCs^*}, \tag{6.4}$$

$$\dot{n}_{\rm RbCs^*} = -K_{\rm (RbCs^*-Cs)} n_{\rm RbCs^*} \tilde{n}_{\rm Cs} - K_{\rm (RbCs^*-RbCs)} n_{\rm RbCs^*} n_{\rm RbCs} - K_{\rm (RbCs^*-RbCs^*)} n^2_{\rm RbCs^*}, \tag{6.5}$$

where $\tilde{n}_{\rm Cs}$ is the density of Cs atoms in the trap. Using the calculated molecular densities after PA as the initial conditions, these rate equations can be solved numerically. As shown in Figure 6.3, for even modest co-trapped atomic Cs densities, excited molecules can be

[1] For PA to $J$=1 of the $(2)^3\Pi_{0^+}$ state, only $\ell$=0 contributes at our temperatures. Hence, we only include the $s$-wave contribution to $K_{\rm PA}$.

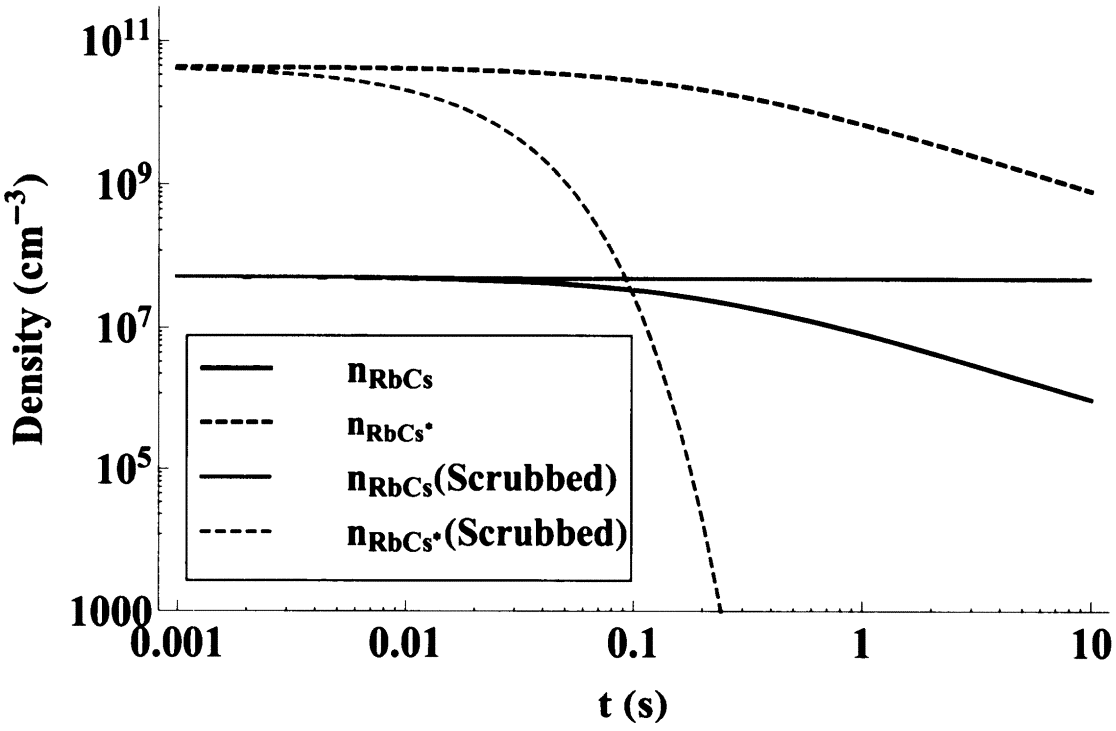


Figure 6.3: Simulated molecular density evolution in the presence of inelastic scattering. Black lines show the molecular population evolution in the absence of co-trapped Cs atoms. Red lines show evolution in the presence of a co-trapped Cs density, $n_{Cs}$=6×10$^{11}$ cm$^{-3}$. All inelastic rate coefficients are set to $K_{max}$ = 1.2 × 10$^{-10}$ cm$^3$. Figure reproduced from [113].

removed quickly with only a small reduction of the ground state molecular density. For a co-trapped Cs density of $\tilde{n}_{Cs}$=6×10$^{11}$ cm$^{-3}$ (as in e.g. Ref. [89]) and $\tilde{b}$=0.0007, $n_{RbCs}$ stabilizes at 5×10$^7$ cm$^{-3}$ after ≈200 ms with only a 7% reduction from the initial ground state molecular density (just before removal of the Rb atoms).

Now we consider realistic experimental conditions and the potential for this approach to create a sample of trapped X($v$=$J$=0) molecules. For a trap radius of 200 $\mu$m (as in e.g. Ref. [89]), reaching saturation of the PA transition using our experimental fit (calculated) value requires a laser power of approximately 5(16) W. Although it is difficult to achieve this power with a single laser beam pass, a relatively low finesse ($\mathcal{F}$∼5–20) power build-up cavity, as in [45], can be used to increase the intensity to the desired level over the trap

volume. We assume this saturation intensity can be achieved over the entire volume. The final results of this discussion can be summarized as follows, using what we consider to be realistic experimental parameters: for initial MOT densities of $n_{Rb}$=$n_{Cs}$=5×10$^{11}$ cm$^{-3}$, an X($v$=$J$=0) branching ratio of $\tilde{b}$=0.0007, a co-trapped Cs density of $\tilde{n}_{Cs}$=6×10$^{11}$ cm$^{-3}$, and a trap volume of $\pi$(200 $\mu$m)$^2$×1 mm, we calculate a X($v$=$J$=0) molecular density (number) $n_{RbCs}$=5×10$^7$ cm$^{-3}$ ($N_{RbCs}$=6×10$^3$) after approximately 240 ms (40 ms for loading, and 200 ms for "scrubbing" of unwanted states). This seems quite promising as a simple method for producing a sample of ultracold, polar RbCs molecules in their rovibronic ground state.

## 6.4 Further Cooling

The molecules that are created using the techniques described here are relatively hot ($T\sim$ 100-200 $\mu$K) compared to those created using techniques like Feshbach association ($T$ <1 $\mu$K) [33]. In order to probe certain physical regimes, it will be necessary to lower the sample temperature. Further, we expect that the molecules will be spread over many hyperfine levels in the rovibronic ground state. Here we discuss possible methods to cool the hyperfine population as well as to lower the translational temperature.

### 6.4.1 Hyperfine Cooling in the Rovibronic Ground State

Given that the hyperfine structure of the PA and rovibronic ground states is unresolved by our PA and depletion lasers, we expect that all possible hyperfine levels of the X($v$=0, $J$=0) state will be populated following spontaneous decay. In the rovibronic ground state, the expected splitting has been calculated to span approximately 100 kHz in [130]. This energy ($h$·100 kHz ≈ 5 $\mu$K·$k_B$) is much less than the optical trap depth ($U_0$ ≈ 200 $\mu$K·$k_B$), but is greater than the temperatures achievable in ultracold Cs ($T_{Cs}$ <1 $\mu$K). In this regime, rovibronic ground state molecules can undergo hyperfine state-changing collisions that lower the internal energy, heating the molecules translationally. This liberated energy is not enough, however, to eject them from the trap. Subsequent rethermalization through

collisions with the ultracold atoms may then prevent re-excitation of the hyperfine state, resulting in a sample of absolute ground state molecules. It is not yet clear that the cross-sections or rate coefficients for hyperfine state-changing collisions will be sufficient to permit rethermalization on an experimentally feasible time scale. Recent unpublished results from the KRb experiment at JILA, however, suggest that the rates may be fast enough [132].

### 6.4.2 Sympathetic Cooling with Cs Atoms

Given the necessity of atomic laser cooling in this experiment and the very low temperatures that can be achieved with atoms, one may consider using a much colder sample of Cs atoms to sympathetically cool the molecules through repeated elastic collisions. Cs atoms have been successfully implemented as a sympathetic coolant for Li atoms [133] and other schemes based on interactions with ultracold Rydberg atoms have been proposed [134]. For sufficiently rapid thermalization, the ultimate molecular temperature is given by the ultracold atomic temperature.

### 6.4.3 Evaporative Molecular Cooling

If a large stable molecular sample can be achieved, it may then be possible to use the evaporative cooling techniques successfully demonstrated in atoms to cool the sample further, perhaps even to quantum degeneracy. In this process, the hottest molecules are preferentially removed by gradually lowering the depth of the trap [135, 136, 137, 138]. Elastic collisions then rethermalize the sample to a lower temperature, increasing the overall phase space density at the cost of irreversibly ejecting a portion of the sample from the trap.

This scheme may, however, be more complicated for molecular systems. A recent paper by Mayle *et al.* [139] has suggested that at relatively high densities, samples of chemically non-reactive molecules like RbCs may undergo inelastic trap loss at high rates, comparable to those seen in reactive species like KRb. The enhanced loss rate comes from the very high density of states found in molecules. Specifically, the large number of states effectively

guarantees resonant-enhancement of three-body recombination reactions, which eject all of the reaction products. Although verification of this process with the non-reactive RbCs molecule would represent an important result, this trap-loss mechanism would present a barrier to achieving very high density molecular samples.

Despite the prediction of rapid sample depletion due to collisional Feshbach resonance induced trap loss, evaporative molecular cooling has been reported by Stuhl *et al.* in OH [28]. The stability of this molecule has been attributed to the unique ground state structure whereby colliding molecules are repelled from each other before reaching the short-range necessary to create the unstable two-body molecular complex. This permits the energy exchange necessary for rethermalization in evaporative cooling without corresponding rapid trap loss. Although the ground state of RbCs does not have this same structure, a similar scheme based on finding a level that prevents short-range interaction may circumvent this loss mechanism.

### 6.4.4 Temperature Measurement

In order to gauge the efficacy of any further translational cooling of the molecules, it will be necessary to measure the sample's temperature. The time-of-flight based absorption images that are so effective in atomic systems cannot be used here due to the absence of closed optical cycling transitions. An alternate scheme hearkens back to methods used in the early days of atomic laser cooling. In [140], an atomic sample was probed using resonant light for optical molasses, and the resultant fluorescence was measured as a function of different parameters. Based on the center-to-center distance of the probe beam and the sample, they were able to calculate the temperature from the fluorescence measurement. Although we lack the closed cycling transitions necessary to get reliable fluorescence measurements, we may be able to exploit the depletion techniques used previously to get similar information.

In Figure 6.4, we schematically show a thin depletion beam sampling an expanding molecular cloud. As the molecules absorb the light, they are excited and subsequently decay to non-resonant states, reducing the measured ion signal size. In the limit of a short

interaction time, the laser depletes the population defined by the cloud column density integrated over the beam area. The beam can then be rastered and the measurement repeated in order to sample the entire density profile. The depletion beam can then be rotated 90 degrees and rastered in the orthogonal direction to measure the other axis. Gaussian fits based on these density profiles can then be used to determine the cloud size for different expansion times. The temperature can then be extracted from the expansion rate, as we have done previously for atoms.

## 6.5 Conclusion

This thesis has sought to create a large sample of ground state polar molecules. Initially, we built on the successes of previous generations of the RbCs experiment at Yale by photoassociating weakly-bound molecules from pre-cooled samples of ultracold atoms. To implement a more sophisticated transfer mechanism to reach the rovibrational ground state, we conducted hyperfine and rotationally-resolved narrowband spectroscopy of candidate intermediate transfer states. Although this scheme was ultimately deemed untenable for our purposes, numerous experimental techniques were developed to measure and characterize the large number of molecular states addressed in our experiment.

The experiment then changed direction and demonstrated numerous direct pathways to the vibronic ground state through photoassociation to deeply-bound vibrational levels of the $(2)^3\Pi_{0^+}$ state, obviating the need for molecular state transfer. Through detailed analysis of the free-to-bound and bound-to-bound Franck-Condon factors associated with molecular formation and spontaneous decay, we predicted and verified a particular photoassociation resonance that efficiently populates the $X^1\Sigma^+(v{=}0)$ state. Given that the $X^1\Sigma^+(v{=}0)$ state is populated spontaneously, this production process can be run continuously, possibly allowing for the accumulation of the molecules as they are formed.

In the course of this study, we also developed a formalism for calculating rotational line strengths in PA and have used it to assign molecular states based on rotational spec-

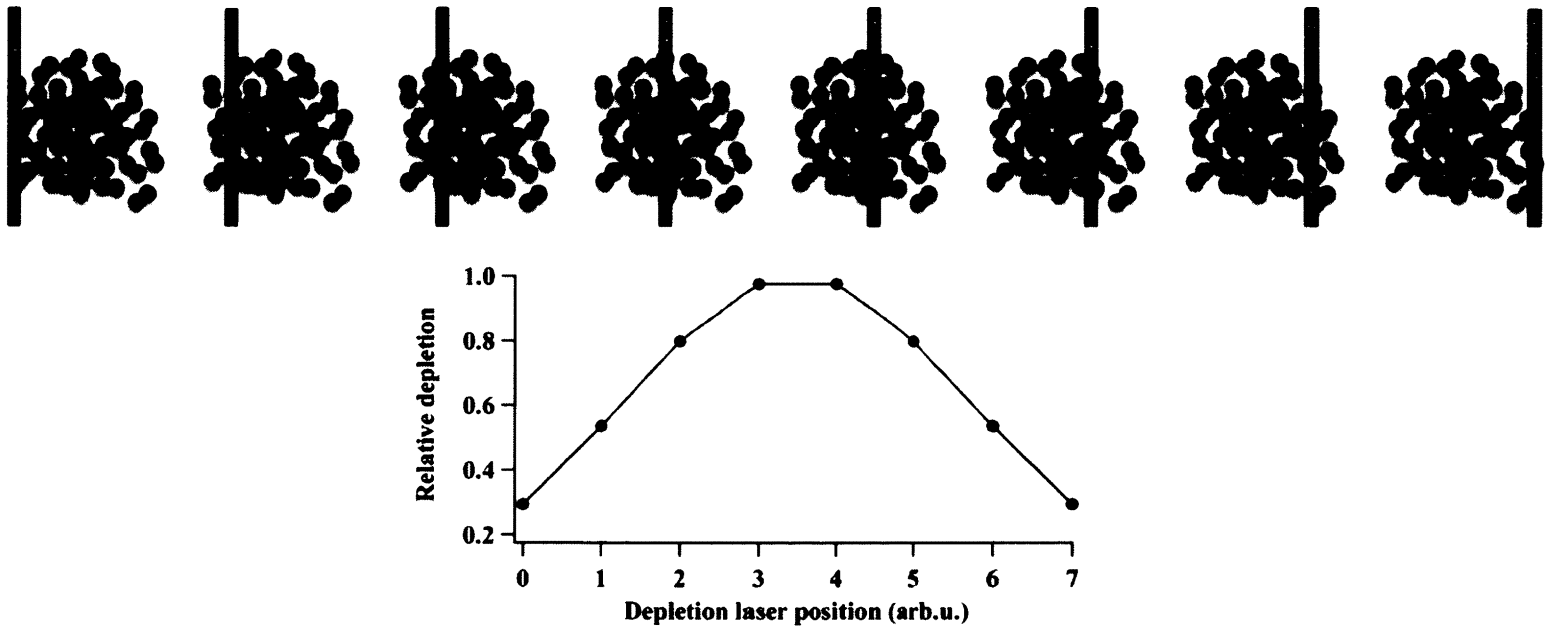


Figure 6.4: Schematic representation of depletion temperature measurement. A thin depletion beam (red) is rastered horizontally and samples different portions of the expanding molecular cloud. As the depletion beam samples denser portions of the molecular cloud, the depletion signal grows, giving geometric information of the expanded cloud's size. By repeating the measurement for different expansion times, the temperature can be extracted based on the ballistic expansion rate.

troscopy. Lastly, we have calculated expected population dynamics in an optical trap based on this deeply-bound PA scheme. Using the relevant rate equations for the competing processes of molecular formation and inelastic scattering, we find that PA and subsequent trap purification using ultracold Cs atoms may present a simple scheme for generating large, pure samples of polar molecules.

This comparatively simple method for producing ground state molecules may permit study of a host of ultracold phenomena. Beginning with relatively hot molecules ($T \sim$100 $\mu$K), one can investigate possible cooling mechanisms, such as sympathetic cooling through collisions with free Cs atoms or evaporative cooling through selective molecular ejection and subsequent rethermalization. An ultracold sample of RbCs can also be examined in the context of its chemical reactions with Rb atoms as well as possible three-body molecular recombination processes. Further, due to its heteronuclear nature, ground state RbCs acquires a dipole moment in the presence of an applied electric field. This gives rise to a dipole-dipole interaction between molecules that is predicted to drive the formation of novel many-body states. Most importantly, this wide array of molecular phenomena can be studied with a level of experimental control comparable to that available in the atomic systems whose techniques have made the work presented here possible.

# Microchannel Plate Readout

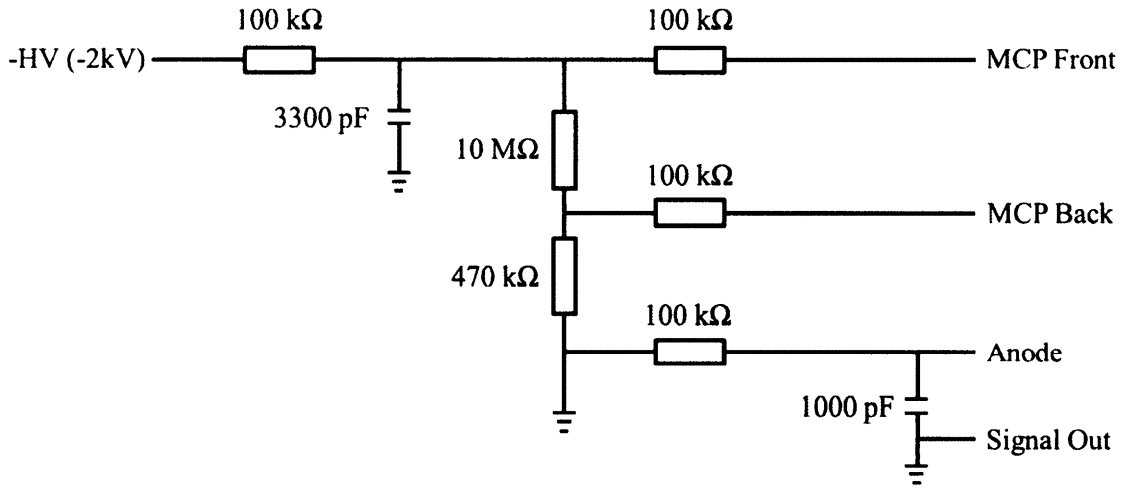


Figure A.1: Schematic of microchannel plate readout circuit. Circuit design comes from Ref. [102].

# Spin-Orbit Mixing

To relate the molecular and atomic spin-orbit coupling, we first calculate the mixing between the Hund's case (a) $(2)^3\Pi_{0+}$ and $(3)^1\Sigma^+$ states. In the $|\Lambda, S, \Sigma\rangle$ basis, we have

$$|(2)^3\Pi_{0+}\rangle = \frac{1}{\sqrt{2}}(|-1,1,1\rangle - |1,1,-1\rangle) \quad (6)$$

$$|(3)^1\Sigma^+\rangle = |0,0,0\rangle \quad (7)$$

Next, we transform these states into the decoupled atomic $|l_{\mathrm{Cs}}, m_{l(\mathrm{Cs})}, l_{\mathrm{Rb}}, m_{l(\mathrm{Rb})}\rangle$ $|s_{\mathrm{Cs}}, m_{s(\mathrm{Cs})}, s_{\mathrm{Rb}}, m_{s(\mathrm{Rb})}\rangle$ basis, where projections are relative to the internuclear axis. For Rb $5p$ + Cs $6s$ asymptote for the $(2)^3\Pi_{0+}$ state and Rb $5s$ + Cs $6s$ for the $(3)^1\Sigma^+$ state, this yields

$$|(2)^3\Pi_{0+}\rangle = \frac{1}{\sqrt{2}}(|0,0,1,1\rangle\,|\tfrac{1}{2},-\tfrac{1}{2},\tfrac{1}{2},-\tfrac{1}{2}\rangle - |0,0,1,-1\rangle\,|\tfrac{1}{2},\tfrac{1}{2},\tfrac{1}{2},\tfrac{1}{2}\rangle) \quad (8)$$

$$|(3)^1\Sigma^+\rangle = \frac{1}{\sqrt{2}}|0,0,1,0\rangle\,(|\tfrac{1}{2},\tfrac{1}{2},\tfrac{1}{2},-\tfrac{1}{2}\rangle - |\tfrac{1}{2},-\tfrac{1}{2},\tfrac{1}{2},\tfrac{1}{2}\rangle) \quad (9)$$

The spin-orbit Hamiltonian here is given by

$$H_{\mathrm{SO}} = b_{\mathrm{Rb}}(\vec{l}_{\mathrm{Rb}} \cdot \vec{s}_{\mathrm{Rb}}) + b_{\mathrm{Cs}}(\vec{l}_{\mathrm{Cs}} \cdot \vec{s}_{\mathrm{Cs}}) \quad (10)$$

where $b_{\mathrm{Rb}}$ and $b_{\mathrm{Cs}}$ are atomic spin-orbit coupling parameters. For the Rb $5p$ + Cs $6s$ asymptote of the $(2)^3\Pi_{0+}$ state, we can take $b_{\mathrm{Cs}}$=0, as $\vec{l}_{\mathrm{Cs}}$=0. Then dropping the atomic subscripts, we rewrite the dot product as $\vec{l} \cdot \vec{s} = l_x s_x + l_y s_y + l_z s_z$. By inspection, the $l_z s_z$

term does not contribute, and by symmetry, the contributions of the $l_x s_x$ and $l_y s_y$ terms must be equal. We can rewrite the $l_x s_x$ term as

$$l_x s_x = \left(\frac{l_+ + l_-}{2}\right)\left(\frac{s_+ + s_-}{2}\right) \tag{11}$$

where the subscripts denote the standard angular momentum raising and lowering operators. By conservation of the projection on the internuclear axis, only the $(l_+ s_- + l_- s_+)/4$ term can contribute.

Hence, we evaluate the following:

$$\langle (3)^1\Sigma^+ | H_{\mathrm{SO}} | (2)^3\Pi_{0^+} \rangle = 2\langle (3)^1\Sigma^+ | b_{\mathrm{Rb}} l_x s_x | (2)^3\Pi_{0^+} \rangle = \frac{-a_{\mathrm{Rb}}}{\sqrt{2}} \tag{12}$$

We can relate this to the fine structure splitting of atomic Rb by noting

$$E_{5p_{3/2}} - E_{5p_{1/2}} = \frac{b_{\mathrm{Rb}}}{2}\Big((j'(j'+1) - l(l+1) - s(s+1)\Big) - \frac{b_{\mathrm{Rb}}}{2}\Big((j(j+1) - l(l+1) - s(s+1)\Big) \tag{13}$$

where $j'$=3/2 and $j$=1/2. Thus, the fine structure splitting of Rb, $\Delta E_{\mathrm{FS}}$, is given by $\frac{3}{2} b_{\mathrm{Rb}}$. Putting this together with the molecular spin-orbit coupling matrix element, we have

$$\langle (3)^1\Sigma^+ | H_{\mathrm{SO}} | (2)^3\Pi_{0^+} \rangle = -\frac{\sqrt{2}}{3}\Delta E_{\mathrm{FS}} \tag{14}$$

# Extensions of Line Strength Calculation

The rotational line strength calculations presented here have focused on purely Hund's case (a) molecules, but many straightforward extensions can be made. Specifically, we consider Hund's case (c) molecules that are of great interest to weakly-bound PA of RbCs. We also use the rotational line strengths in PA to extract the collision temperature of the constituent atoms using a simple model.

### Hund's Case (c)

At long-range in RbCs, molecular states are generally no longer well-described in the Hund's case (a) basis. For many of the $\Omega' = 0$ states studied in [82], the spin-orbit interaction mixes states with different values of $S'$ but equal values of $\Omega'$. Hence we must write the body-fixed frame PA states as

$$|\Omega' = 0^+\rangle_{\mathrm{BF}} = a_\Sigma\,|1,0,0,0,0\rangle_{\mathrm{BF}} + \frac{a_\Pi}{\sqrt{2}}\big(\,|1,-1,1,1,0\rangle_{\mathrm{BF}} - |1,1,1,-1,0\rangle_{\mathrm{BF}}\,\big), \quad (15)$$

$$|\Omega' = 0^-\rangle_{\mathrm{BF}} = b_\Sigma\,|1,0,1,0,0\rangle_{\mathrm{BF}} + \frac{b_\Pi}{\sqrt{2}}\big(\,|1,-1,1,1,0\rangle_{\mathrm{BF}} + |1,1,1,-1,0\rangle_{\mathrm{BF}}\,\big), \quad (16)$$

where $a_\Sigma, a_\Pi, b_\Sigma, b_\Pi$ are mixing coefficients that describe the amount of $\Sigma(\Lambda'{=}0)$, $\Pi(|\Lambda'|{=}1)$ character of the state. The transformation of each component to the space-fixed frame is then done just as before in Chapter 3. The matrix elements are calculated analogously,

though with the inclusion of $S$=0 components of the atomic scattering state for the $\Omega'=0^+$ state.

### Results

In order to calculate the $W(J',\ell)$ matrices for long-range $\Omega'$=0 states, we need to know the values of the molecular mixing coefficients. $a_\Sigma, a_\Pi, b_\Sigma, b_\Pi$. For select special cases, these can be calculated analytically. At very long-range, we assume that in the excited molecular PA state that the electronic angular momentum is described purely by atomic $jj$-coupling, such that for an $\Omega' = 0$ state, $m'_{j(\mathrm{Rb})}+m'_{j(\mathrm{Cs})}=\Omega'=0$, where $m'_j$ is the projection of the total electronic angular momentum, $j$, of each constituent atom in the PA state.

For the spectra in Ref. [82], PA was done to long-range states associated with the Rb $5s_{1/2}$ and Cs $6p_{1/2}$ or $6p_{3/2}$ asymptotes. To calculate the mixing coefficients, we take the following normalized linear combinations of products of atomic basis states where $m'_{j(\mathrm{Rb})}+m'_{j(\mathrm{Cs})}=\Omega'=0$:

$$\begin{aligned}
&\frac{1}{\sqrt{2}}\left(|\tfrac{1}{2},\tfrac{1}{2}\rangle_{\mathrm{Rb}}|\tfrac{1}{2},-\tfrac{1}{2}\rangle_{\mathrm{Cs}}+|\tfrac{1}{2},-\tfrac{1}{2}\rangle_{\mathrm{Rb}}|\tfrac{1}{2},\tfrac{1}{2}\rangle_{\mathrm{Cs}}\right)\\
&\frac{1}{\sqrt{2}}\left(|\tfrac{1}{2},\tfrac{1}{2}\rangle_{\mathrm{Rb}}|\tfrac{1}{2},-\tfrac{1}{2}\rangle_{\mathrm{Cs}}-|\tfrac{1}{2},-\tfrac{1}{2}\rangle_{\mathrm{Rb}}|\tfrac{1}{2},\tfrac{1}{2}\rangle_{\mathrm{Cs}}\right)\\
&\frac{1}{\sqrt{2}}\left(|\tfrac{1}{2},\tfrac{1}{2}\rangle_{\mathrm{Rb}}|\tfrac{3}{2},-\tfrac{1}{2}\rangle_{\mathrm{Cs}}-|\tfrac{1}{2},-\tfrac{1}{2}\rangle_{\mathrm{Rb}}|\tfrac{3}{2},\tfrac{1}{2}\rangle_{\mathrm{Cs}}\right)\\
&\frac{1}{\sqrt{2}}\left(|\tfrac{1}{2},\tfrac{1}{2}\rangle_{\mathrm{Rb}}|\tfrac{3}{2},-\tfrac{1}{2}\rangle_{\mathrm{Cs}}+|\tfrac{1}{2},-\tfrac{1}{2}\rangle_{\mathrm{Rb}}|\tfrac{3}{2},\tfrac{1}{2}\rangle_{\mathrm{Cs}}\right)
\end{aligned} \tag{17}$$

where each atomic state is written in the $|j',m'_j\rangle$ basis. Next, we decompose the total electronic angular momenta of each atom into the constituent angular momenta, the atomic orbital angular momentum ($l'$) and electronic spin ($s'$). Hence we transform into the

$|l', m'_l, s', m'_s\rangle$ basis as

$$|\frac{1}{2}, m'_{j(\mathrm{Rb})}\rangle = \sum_{m'_{s(\mathrm{Rb})}} \langle 0,0,\frac{1}{2}, m'_{s(\mathrm{Rb})}|\frac{1}{2}, m'_{j(\mathrm{Rb})}\rangle \, |0,0,\frac{1}{2}, m'_{s(\mathrm{Rb})}\rangle \,, \tag{18}$$

$$|j'_{(\mathrm{Cs})}, m'_{j(\mathrm{Cs})}\rangle = \sum_{\substack{m'_{l(\mathrm{Cs})} \\ m'_{s(\mathrm{Cs})}}} \langle 1, m'_{l(\mathrm{Cs})}, \frac{1}{2}, m'_{s(\mathrm{Cs})}|j'_{\mathrm{Cs}}, m'_{j(\mathrm{Cs})}\rangle \, |1, m'_{l(\mathrm{Cs})}, \frac{1}{2}, m'_{s(\mathrm{Cs})}\rangle \,, \tag{19}$$

where the terms in brackets are Clebsch-Gordan coefficients. These expressions are then substituted back into Eq. 17. Finally, we couple $l'_{(\mathrm{Rb})}$ to $l'_{(\mathrm{Cs})}$ and $s'_{(\mathrm{Rb})}$ to $s'_{(\mathrm{Cs})}$ to form $L', \Lambda', S', \Sigma'$. This transformation to the $|L', \Lambda', S', \Sigma', \Omega'\rangle$ basis yields

$5s_{1/2} + 6p_{1/2}$ :

$$|\Omega' = 0^+\rangle_{\mathrm{BF}} = \sqrt{\frac{1}{3}}\,|1,0,0,0,0\rangle_{\mathrm{BF}} + \sqrt{\frac{1}{3}}\big(\,|1,-1,1,1,0\rangle_{\mathrm{BF}} - |1,1,1,-1,0\rangle_{\mathrm{BF}}\,\big) \tag{20}$$

$$|\Omega' = 0^-\rangle_{\mathrm{BF}} = \sqrt{\frac{1}{3}}\,|1,0,1,0,0\rangle_{\mathrm{BF}} - \sqrt{\frac{1}{3}}\big(\,|1,-1,1,1,0\rangle_{\mathrm{BF}} + |1,1,1,-1,0\rangle_{\mathrm{BF}}\,\big) \tag{21}$$

$5s_{1/2} + 6p_{3/2}$ :

$$|\Omega' = 0^+\rangle_{\mathrm{BF}} = \sqrt{\frac{2}{3}}\,|1,0,0,0,0\rangle_{\mathrm{BF}} - \sqrt{\frac{1}{6}}\big(\,|1,-1,1,1,0\rangle_{\mathrm{BF}} - |1,1,1,-1,0\rangle_{\mathrm{BF}}\,\big) \tag{22}$$

$$|\Omega' = 0^-\rangle_{\mathrm{BF}} = \sqrt{\frac{2}{3}}\,|1,0,1,0,0\rangle_{\mathrm{BF}} + \sqrt{\frac{1}{6}}\big(\,|1,-1,1,1,0\rangle_{\mathrm{BF}} + |1,1,1,-1,0\rangle_{\mathrm{BF}}\,\big) \tag{23}$$

With these values for the mixing coefficients, calculating the $W(\ell, J')$ matrices is straightforward, and the results are given in Table C.1. As before, we can take ratios of certain rotational level signals that are independent of properties of the atomic sample and depend only on the angular factors. In particular, we find that the $J'$=2 to $J'$=0 signal ratio for the purely long-range $\Omega'$=$0^+$ state is 2, just as in the deeply-bound, purely Hund's case (a) example. This is in contrast to the $\Omega'$=$0^-$ example, as the $J'$=3 level disappears for $\ell$=1 scattering for purely long-range PA. Hence instead of a $J'$=1 to $J'$=3 signal ratio of 4, the ratio diverges at long-range.

We have calculated these ratios for many different values for $a_\Sigma, a_\Pi, b_\Sigma, b_\Pi$ with the constraints $a_\Sigma^2 + a_\Pi^2 = b_\Sigma^2 + b_\Pi^2 = 1$ . For $\Omega'$=$0^+$ states, the $J'$=2 to $J'$=0 ratio is 2 for all

| $\Omega'=0^-(6p_{1/2})$ | $J'=0$ | $J'=1$ | $J'=2$ | $J'=3$ | $J'=4$ | $J'=5$ |
|---|---|---|---|---|---|---|
| $\ell=0$ | 1 | 0 | 0 | 0 | 0 | 0 |
| $\ell=1$ | 0 | 3 | 0 | 0 | 0 | 0 |
| $\ell=2$ | 0 | 0 | 5 | 0 | 0 | 0 |
| $\ell=3$ | 0 | 0 | 0 | 7 | 0 | 0 |
| $\Omega'=0^-(6p_{3/2})$ | $J'=0$ | $J'=1$ | $J'=2$ | $J'=3$ | $J'=4$ | $J'=5$ |
| $\ell=0$ | 0 | 0 | 0.83 | 0 | 0 | 0 |
| $\ell=1$ | 0 | 1 | 0 | 1.5 | 0 | 0 |
| $\ell=2$ | 0.83 | 0 | 1.19 | 0 | 2.1 | 0 |
| $\ell=3$ | 0 | 1.5 | 0 | 1.55 | 0 | 2.8 |

Table C.1: Calculated partial wave contributions, $\tilde{W}(J',\ell)$, from all $M_{F(\mathrm{Rb})}, M_{F(\mathrm{Cs})}$ combinations to purely long-range PA levels correlated to the $6p_{1/2}$ and $6p_{3/2}$ atomic Cs asymptotes. Tilde denotes that all calculated values of $W(J',\ell)$ within a given asymptote were normalized by the same value.

values of $a_\Sigma$ and $a_\Pi$. Hence, the $J'$=2 to $J'$=0 ratio is 2, independent of the extent of $\Lambda/\Pi$ and singlet/triplet mixing. This is consistent with our observations in both short-range PA in Ref. [113] and weakly-bound PA in Ref. [82]. For $\Omega'=0^-$ states, we have considered $b_\Sigma$ and $b_\Pi$ that have the same sign, which corresponds to states correlated to the Cs $6p_{3/2}$ asymptote, and opposite sign, which corresponds to states asymptotic to Cs $6p_{1/2}$. The ratios of the $J'$=1 to $J'$=3 line strengths for both are shown in Figure C.1. Although there is not an unambiguous determination of $b_\Sigma$ and $b_\Pi$ from the $J'$=1 to $J'$=3 line strength ratio, this calculation does give insight into the approximate $\Sigma$ and $\Pi$ content of $\Omega'=0^-$ states.

We can apply this analysis to recent long-range PA in RbCs in Ref. [141]. The rotational progressions in Figure 5 of this paper are consistent with multiple predictions based on our formalism. First, the $J'$=2 to $J'$=0 signal size is close to the expected value of 2 for the $\Omega'=0^+$. Second, the very long-range $(2)\Omega'=0^-$ state correlated to the Rb $5s$ + $6p_{1/2}$ asymptote has a vanishingly small $J'$=3 rotational level, as predicted in Figure C.1. Third, the $(3)\Omega'=0^-$ state correlated to the Rb $5s$ + $6p_{3/2}$ asymptote has a $J'$=1 to $J'$=3 signal size ratio within the predicted values of 0.5 and 4.

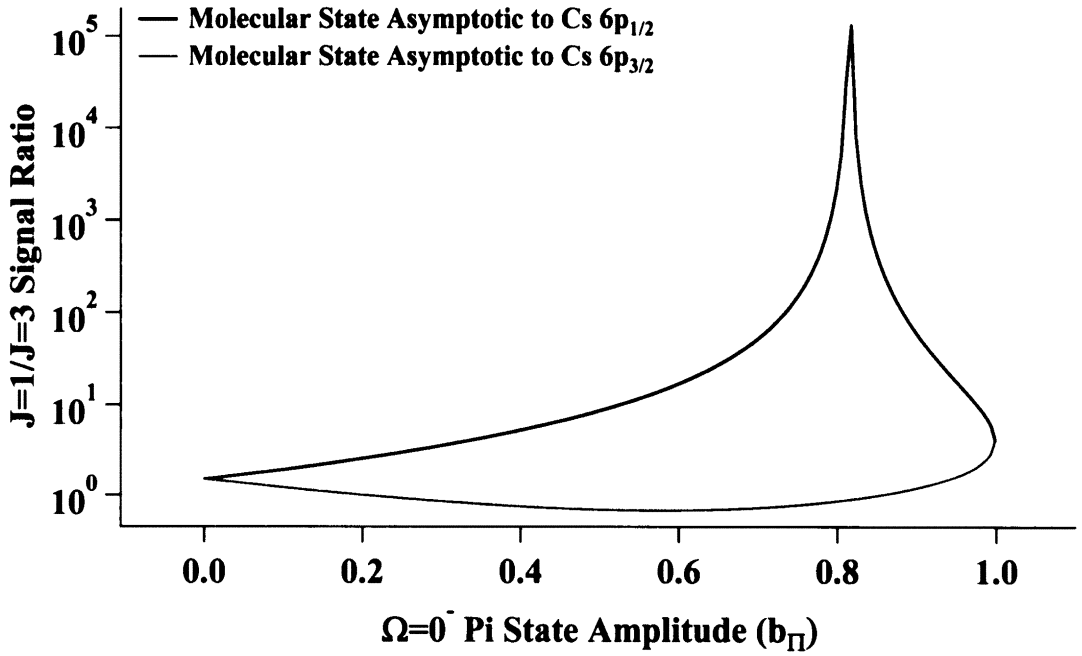


Figure C.1: $J$=1/$J$=3 signal ratio for different values of the $\Pi$ state amplitude, $b_\Pi$, in $\Omega'$=$0^-$ states correlated to the $6p_{1/2}$ (blue) and $6p_{3/2}$ (red) Cs asymptotes. $6p_{1/2}$ curve diverges at $b_\Pi = \sqrt{2/3} \approx 0.82$.

### Extracting Temperature Information from PA Spectra

For $\Omega$=$0^+$ states, where the $W(J', \ell)$ matrix values do not depend on the exact $\Sigma$ and $\Pi$ content of the state, we can use a partition function model to extract the collision temperature from the relative rotational level signal sizes. The total signal size, $S(J', T)$, is given by

$$S(J', T) = \sum_{\ell} W(J', \ell) f(\ell, T), \tag{24}$$

where $T$ is the temperature and $f(\ell, T)$ is a temperature-dependent weighting function. We use a simple model that accounts for suppression of higher partial waves, $\ell$, due to the centrifugal barrier of the form:

$$f(\ell, T) = \frac{e^{-E(\ell)/k_B T}}{\sum_{\ell'} (2\ell' + 1) e^{-E(\ell')/k_B T}}, \tag{25}$$

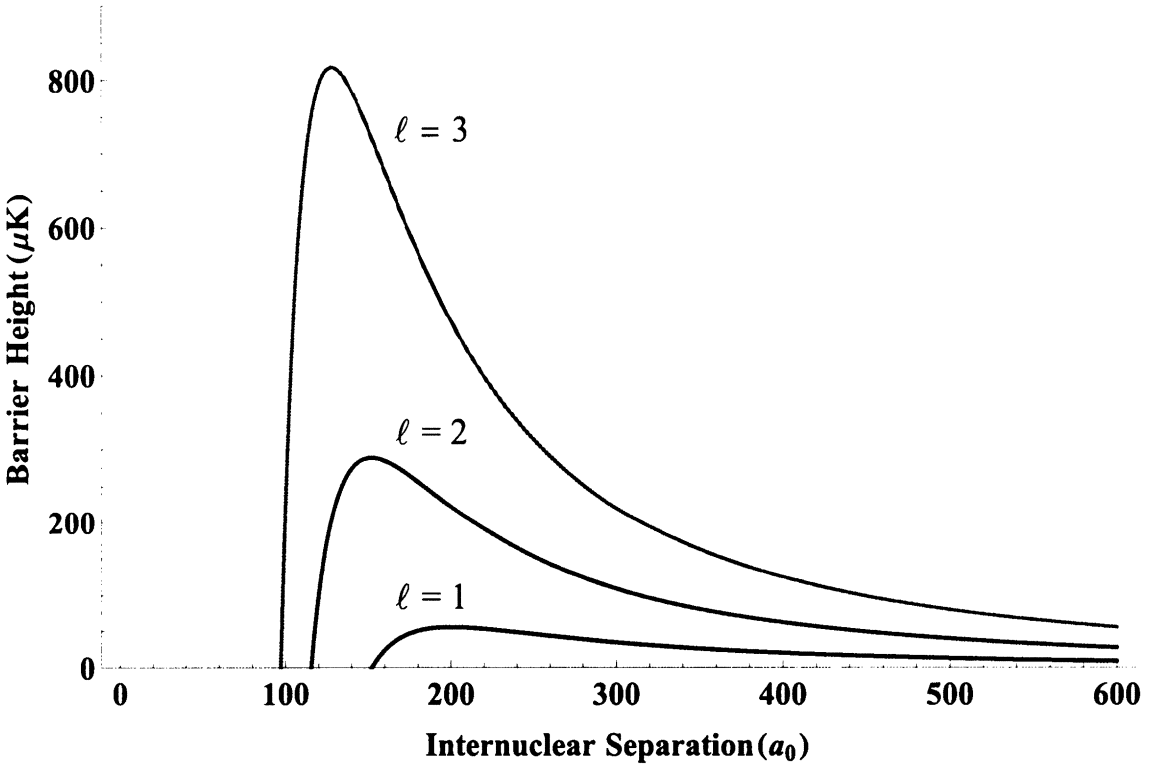


Figure C.2: Centrifugal barrier heights for $\ell$=1-3 partial waves in RbCs. The long-range potential is given here by $U_{LR} = -C_6/R^6 + \hbar^2\ell(\ell+1)/2\mu R^2$, where $\mu$ is the reduced mass for RbCs and $R$ is the internuclear separation. $C_6$ coefficient value comes from [129].

where $E(\ell)$ is the centrifugal barrier height. The fractional contribution to the spectrum for a single partial wave, $p_\ell(T)$, is then given by

$$p_\ell(T) = (2\ell+1)f(\ell,T). \tag{26}$$

For the calculated centrifugal barrier heights, shown in Figure C.2, $E_p$=56 $\mu$K$\cdot k_B$, $E_d$=290 $\mu$K$\cdot k_B$, and $E_f$=820 $\mu$K$\cdot k_B$, we find a best fit temperature of $T$=120 $\mu$K with fractional partial wave contributions, $p_s$=0.31, $p_p$=0.57, $p_d$=0.12, and $p_f$=1.5$\times 10^{-3}$. From the data in Ref. [113], we extract experimental values $p_s$=0.28, $p_p$=0.62, $p_d$=0.10, and $p_f \approx$ 0. These partial wave contributions are in approximate agreement with the simple partition function model, and the best fit temperature is consistent with atomic measurements from time-of-flight expansion.

# Bibliography


[1] S. Chu, C. Cohen-Tannoudji, and W.D. Phillips. Nobel lectures in physics 1997. *Reviews of Modern Physics*, 70(3):685–741, 1998.

[2] E. A. Cornell and C. E. Wieman. Nobel lecture: Bose-Einstein condensation in a dilute gas, the first 70 years and some recent experiments. *Reviews of Modern Physics*, 74:875–893, 2002.

[3] Wolfgang Ketterle. Nobel lecture: When atoms behave as waves: Bose-Einstein condensation and the atom laser. *Reviews of Modern Physics*, 74(4):1131–1151, 2002.

[4] Serge Haroche. Nobel lecture: Controlling photons in a box and exploring the quantum to classical boundary. *Reviews of Modern Physics*, 85(3):1083, 2013.

[5] David J. Wineland. Nobel lecture: Superposition, entanglement, and raising Schrödinger's cat. *Reviews of Modern Physics*, 85:1103, 2013.

[6] T. L. Nicholson, M. J. Martin, J. R. Williams, B. J. Bloom, M. Bishof, M. D. Swallows, S. L. Campbell, and J. Ye. Comparison of two independent Sr optical clocks with $1\times10^{-17}$ stability at $10^3$ s. *Physical Review Letters*, 109:230801, 2012.

[7] Ferdinand Schmidt-Kaler, Hartmut Häffner, Mark Riebe, Stephan Gulde, Gavin P.T. Lancaster, Thomas Deuschle, Christoph Becher, Christian F. Roos, Jürgen Eschner, and Rainer Blatt. Realization of the Cirac-Zoller controlled-NOT quantum gate. *Nature*, 422(6930):408–411, 2003.

[8] C.Y. Chen, Y.M. Li, K. Bailey, T.P. O'Connor, L. Young, and Z.-T. Lu. Ultrasensitive isotope trace analyses with a magneto-optical trap. *Science*, 286(5442):1139–1141, 1999.

[9] Till Rosenband, D.B. Hume, P.O. Schmidt, C.W. Chou, A. Brusch, L. Lorini, W.H. Oskay, R.E. Drullinger, T.M. Fortier, J.E. Stalnaker, et al. Frequency ratio of $Al^+$ and $Hg^+$ single-ion optical clocks; metrology at the 17th decimal place. *Science*, 319(5871):1808–1812, 2008.

[10] Gail Overton. Bose-Einstein condensate experiments to be conducted in space, July 2013. http://www.laserfocusworld.com/articles/2013/07/bose-einstein-condensate-experiments-to-be-conducted-in-space.html.

[11] Lincoln D. Carr, David DeMille, Roman V. Krems, and Jun Ye. Cold and ultracold molecules: science, technology and applications. *New Journal of Physics*, 11(5):055049, 2009.

[12] Goulven Quemener and Paul S. Julienne. Ultracold molecules under control! *Chemical Reviews*, 112(9):4949–5011, 2012.

[13] D. DeMille, S. Sainis, J. Sage, T. Bergeman, S. Kotochigova, and E. Tiesinga. Enhanced sensitivity to variation of $m_e/m_p$ in molecular spectra. *Physical Review Letters*, 100:043202, 2008.

[14] J. Stuhler, A. Griesmaier, T. Koch, M. Fattori, T. Pfau, S. Giovanazzi, P. Pedri, and L. Santos. Observation of dipole-dipole interaction in a degenerate quantum gas. *Physical Review Letters*, 95:150406, 2005.

[15] Mingwu Lu, Nathaniel Q. Burdick, Seo Ho Youn, and Benjamin L. Lev. Strongly dipolar Bose-Einstein condensate of dysprosium. *Physical Review Letters*, 107:190401, 2011.

[16] A. Micheli, G.K. Brennen, and P. Zoller. A toolbox for lattice-spin models with polar molecules. *Nature Physics*, 2(5):341–347, 2006.

[17] D. DeMille. Quantum computation with trapped polar molecules. *Physical Review Letters*, 88(6):067901–4, 2002.

[18] H.J. Metcalf and P. van der Straten. *Laser Cooling and Trapping.* Springer-Verlag New York, Inc., 1999.

[19] O. Docenko, M. Tamanis, R. Ferber, H. Knöckel, and E. Tiemann. Singlet and triplet potentials of the ground-state atom pair Rb + Cs studied by Fourier-transform spectroscopy. *Physical Review A*, 83:052519, 2011.

[20] Jonathan D. Weinstein et al. Magnetic trapping of calcium monohydride molecules at millikelvin temperatures. *Nature*, 395(6698):148–150, 1998.

[21] S. E. Maxwell, N. Brahms, R. deCarvalho, D. R. Glenn, J. S. Helton, S. V. Nguyen, D. Patterson, J. Petricka, D. DeMille, and J. M. Doyle. High-flux beam source for cold, slow atoms or molecules. *Physical Review Letters*, 95:173201, 2005.

[22] Wesley C. Campbell, Edem Tsikata, Hsin-I Lu, Laurens D. van Buuren, and John M. Doyle. Magnetic trapping and Zeeman relaxation of NH ($X^3\Sigma^-$). *Physical Review Letters*, 98:213001, 2007.

[23] ACME Collaboration. Order of magnitude smaller limit on the electric dipole moment of the electron, 2013. http://arxiv.org/abs/1310.7534v2.

[24] Hendrick L. Bethlem, Giel Berden, and Gerard Meijer. Decelerating neutral dipolar molecules. *Physical Review Letters*, 83:1558–1561, 1999.

[25] Sebastiaan Y. T. van de Meerakker, Paul H. M. Smeets, Nicolas Vanhaecke, Rienk T. Jongma, and Gerard Meijer. Deceleration and electrostatic trapping of OH radicals. *Physical Review Letters*, 94:023004, 2005.

[26] Brian C. Sawyer, Benjamin L. Lev, Eric R. Hudson, Benjamin K. Stuhl, Manuel Lara, John L. Bohn, and Jun Ye. Magnetoelectrostatic trapping of ground state OH molecules. *Physical Review Letters*, 98(25):253002, 2007.

[27] Brian C. Sawyer, Benjamin K. Stuhl, Dajun Wang, Mark Yeo, and Jun Ye. Molecular beam collisions with a magnetically trapped target. *Physical Review Letters*, 101:203203, 2008.

[28] Benjamin K. Stuhl, Matthew T. Hummon, Mark Yeo, Goulven Quéméner, John L. Bohn, and Jun Ye. Evaporative cooling of the dipolar hydroxyl radical. *Nature*, 492(7429):396–400, 2012.

[29] E.S. Shuman, J.F. Barry, and D. DeMille. Laser cooling of a diatomic molecule. *Nature*, 467(7317):820–823, 2010.

[30] Matthew T. Hummon, Mark Yeo, Benjamin K. Stuhl, Alejandra L. Collopy, Yong Xia, and Jun Ye. 2D magneto-optical trapping of diatomic molecules. *Physical Review Letters*, 110:143001, 2013.

[31] V. Zhelyazkova, A. Cournol, T.E. Wall, A. Matsushima, J.J. Hudson, E.A. Hinds, M.R. Tarbutt, and B.E Sauer. Laser cooling and slowing of CaF molecules, 2013. http://arxiv.org/abs/1308.0421v1.

[32] E. L. Raab, M. Prentiss, Alex Cable, Steven Chu, and D. E. Pritchard. Trapping of neutral sodium atoms with radiation pressure. *Physical Review Letters*, 59:2631–2634, 1987.

[33] K.-K. Ni, S. Ospelkaus, M. H. G. de Miranda, A. Pe'er, B. Neyenhuis, J. J. Zirbel, S. Kotochigova, P. S. Julienne, D. S. Jin, and J. Ye. A high phase-space-density gas of polar molecules. *Science*, 322(5899):231–235, 2008.

[34] S. Ospelkaus, A.A. Pe'er, K.-K. Ni, J.J. Zirbel, B. Neyenhuis, S. Kotochigova, P.S. Julienne, J. Ye, and D.S. Jin. Efficient state transfer in an ultracold dense gas of heteronuclear molecules. *Nature Physics*, 4(8):622–626, 2008.

[35] S. Ospelkaus, K.-K. Ni, D. Wang, M. H. G. de Miranda, B. Neyenhuis, G. Quemener, P. S. Julienne, J. L. Bohn, D. S. Jin, and J. Ye. Quantum-state controlled chemical reactions of ultracold potassium-rubidium molecules. *Science*, 327(5967):853–857, 2010.

[36] M.H.G. De Miranda, A. Chotia, B. Neyenhuis, D. Wang, G. Quéméner, S. Ospelkaus, J.L. Bohn, J Ye, and D.S. Jin. Controlling the quantum stereodynamics of ultracold bimolecular reactions. *Nature Physics*, 7(6):502–507, 2011.

[37] Tetsu Takekoshi, Markus Debatin, Raffael Rameshan, Francesca Ferlaino, Rudolf Grimm, Hanns-Christoph Nägerl, C Ruth Le Sueur, Jeremy M Hutson, Paul S Julienne, Svetlana Kotochigova, et al. Towards the production of ultracold ground-state RbCs molecules: Feshbach resonances, weakly bound states, and the coupled-channel model. *Physical Review A*, 85(3):032506, 2012.

[38] Cheng-Hsun Wu, Jee Woo Park, Peyman Ahmadi, Sebastian Will, and Martin W. Zwierlein. Ultracold fermionic Feshbach molecules of $^{23}Na^{40}K$. *Physical Review Letters*, 109:085301, 2012.

[39] Hung-Wen Cho, Daniel J. McCarron, Michael P. Köppinger, Daniel L. Jenkin, Kirsteen L. Butler, Paul S. Julienne, Caroline L. Blackley, C. Ruth Le Sueur, Jeremy M. Hutson, and Simon L. Cornish. Feshbach spectroscopy of an ultracold mixture of $^{85}Rb$ and $^{133}Cs$. *Physical Review A*, 87:010703, 2013.

[40] Kevin M. Jones, Eite Tiesinga, Paul D. Lett, and Paul S. Julienne. Ultracold photoassociation spectroscopy: Long-range molecules and atomic scattering. *Reviews of Modern Physics*, 78(2):483–53, 2006.

[41] Piotr S. Żuchowski and Jeremy M. Hutson. Reactions of ultracold alkali-metal dimers. *Physical Review A*, 81:060703, 2010.

[42] M. Aymar and O. Dulieu. Calculation of accurate permanent dipole moments of the lowest states of heteronuclear alkali dimers using extended basis sets. *Journal of Chemical Physics*, 122(20):204302, 2005.

[43] S. L. Cornish, N. R. Claussen, J. L. Roberts, E. A. Cornell, and C. E. Wieman. Stable $^{85}$Rb Bose-Einstein condensates with widely tunable interactions. *Physical Review Letters*, 85:1795–1798, 2000.

[44] Alfred O. Nier. A redetermination of the relative abundances of the isotopes of neon, krypton, rubidium, xenon, and mercury. *Physical Review*, 79:450–454, 1950.

[45] Andrew J. Kerman, Jeremy M. Sage, Sunil Sainis, Thomas Bergeman, and David DeMille. Production of ultracold, polar RbCs* molecules via photoassociation. *Physical Review Letters*, 92(3):033004–4, 2004.

[46] Wolfgang Ketterle, Kendall B. Davis, Michael A. Joffe, Alex Martin, and David E. Pritchard. High densities of cold atoms in a dark spontaneous-force optical trap. *Physical Review Letters*, 70(15):2253, 1993.

[47] M. H. Anderson, W. Petrich, J. R. Ensher, and E. A. Cornell. Reduction of light-assisted collisional loss rate from a low-pressure vapor-cell trap. *Physical Review A*, 50:R3597–R3600, 1994.

[48] Michael G. Littman and Harold J. Metcalf. Spectrally narrow pulsed dye laser without beam expander. *Applied Optics*, 17(14):2224–2227, 1978.

[49] E.R. Hudson. Private communication.

[50] C.J. Hawthorn, K.P. Weber, and R.E. Scholten. Littrow configuration tunable external cavity diode laser with fixed direction output beam. *Review of Scientific Instruments*, 72(12):4477–4479, 2001.

[51] N.B. Gilfoy. *Optical Production of Ultracold Polar Molecules.* PhD thesis, Yale University, 2011.

[52] M. Gustavsson. Private communication.

[53] Aviv Keshet and Wolfgang Ketterle. A distributed, graphical user interface based, computer control system for atomic physics experiments. *Review of Scientific Instruments*, 84(1):015105–015105, 2013.

[54] W. Ketterle, D.S. Durfee, and D.M. Stamper-Kurn. Making, probing, and understanding Bose-Einstein condensates. *Proceedings of the International School of Physics-Enrico Fermi. Volume 140:Bose-Einstein Condensation in Atomic Gases*, pages 67–176, 1999.

[55] T.P. Meyrath. *Experiments with Bose-Einstein Condensation in a Box.* PhD thesis, University of Texas at Austin, 2005.

[56] A. Ashkin. Acceleration and trapping of particles by radiation pressure. *Physical Review Letters*, 24:156–159, 1970.

[57] A. Ashkin. Trapping of atoms by resonance radiation pressure. *Physical Review Letters*, 40:729–733, 1978.

[58] Rudolf Grimm, Matthias Weidemüller, and Yurii B. Ovchinnikov. Optical dipole traps for neutral atoms. *Advances In Atomic, Molecular, and Optical Physics*, 42:95 – 170, 2000.

[59] T. Takekoshi and R.J. Knize. $CO_2$ laser trap for cesium atoms. *Optics letters*, 21(1):77–79, 1996.

[60] Roger M. Wood. *Laser-Induced Damage of Optical Materials.* Institute of Physics Publishing, 2003.

[61] B. Frohlich, T. Lahaye, B. Kaltenhauser, H. Kubler, S. Muller, T. Koch, M. Fattori, and T. Pfau. Two-frequency acousto-optic modulator driver to improve the beam pointing stability during intensity ramps. *Review of Scientific Instruments*, 78(4):043101 –043101–4, 2007.

[62] Joseph T. Verdeyen. *Laser Electronics*. Prentice Hall, 1989.

[63] A. Derevianko, W. R. Johnson, M. S. Safronova, and J. F. Babb. High-precision calculations of dispersion coefficients, static dipole polarizabilities, and atom-wall interaction constants for alkali-metal atoms. *Physical Review Letters*, 82:3589–3592, 1999.

[64] K. M. O'Hara, M. E. Gehm, S. R. Granade, and J. E. Thomas. Scaling laws for evaporative cooling in time-dependent optical traps. *Physical Review A*, 64:051403, 2001.

[65] Gerhard Herzberg. *Molecular Spectra and Molecular Structure. Vol. 1: Spectra of Diatomic Molecules*. Van Nostrand Reinhold, New York, 2nd edition, 1950.

[66] H. Lefebvre-Brion and R.W. Field. *The Spectra and Dynamics of Diatomic Molecules*. Elsevier, 2004.

[67] J.M. Brown and A. Carrington. *Rotational Spectroscopy of Diatomic Molecules*. Cambridge University Press, Cambridge, 2003.

[68] F. Hund. *Handbuch der Physik*, 24(561), 1933.

[69] James K.G. Watson. Hönl–london factors for multiplet transitions in Hund's case (a) or (b). *Journal of Molecular Spectroscopy*, 252(1):5–8, 2008.

[70] M. Born and R. Oppenheimer. Zur quantentheorie der molekeln. *Ann. Phys.*, 84(475), 1927.

[71] J. E. Jones. On the determination of molecular fields. II. From the equation of state of a gas. *Proceedings of the Royal Society of London. Series A*, 106(738):463–477, 1924.

[72] Philip M. Morse. Diatomic molecules according to the wave mechanics. II. Vibrational levels. *Physical Review*, 34:57–64, 1929.

[73] J. L. Dunham. The energy levels of a rotating vibrator. *Physical Review*, 41:721–731, 1932.

[74] I. Birzniece, O. Docenko, O. Nikolayeva, M. Tamanis, and R. Ferber. Fourier-transform spectroscopy and description of low-lying energy levels in the $b(1)^1\Pi$ state of RbCs. *The Journal of Chemical Physics*, 138:154304, 2013.

[75] O. Docenko, M. Tamanis, R. Ferber, T. Bergeman, S. Kotochigova, A.V. Stolyarov, Andreia de Faria Nogueira, and C.E. Fellows. Spectroscopic data, spin-orbit functions, and revised analysis of strong perturbative interactions for the $A^1\Sigma^+$ and $b^3\Pi$ states of RbCs. *Physical Review A*, 81(4):042511, 2010.

[76] R.J. Le Roy. RKR1 2.0: A computer program implementing the first-order RKR method for determining diatomic molecule potential energy curves. *University of Waterloo Chemical Physics Research Report CP-663*, 2004.

[77] R.J. Le Roy. Level 8.0: A computer program for solving the radial Schrödinger equation for bound and quasibound levels. *University of Waterloo Chemical Physics Research Report CP-663*, 2007.

[78] E. Merzbacher. *Quantum Mechanics*. Wiley, 1998.

[79] F.H. Mies. *Theoretical Chemistry: Advances and Perspectives*, volume 6B, pages 127–198. Academic, New York, 1981.

[80] John L. Bohn and P. S. Julienne. Semianalytic theory of laser-assisted resonant cold collisions. *Physical Review A*, 60(1):414–425, 1999.

[81] H. R. Thorsheim, J. Weiner, and P. S. Julienne. Laser-induced photoassociation of ultracold sodium atoms. *Physical Review Letters*, 58:2420–2423, 1987.

[82] J.M Sage. *Optical Production of Ultracold Polar Molecules.* PhD thesis, Yale University, 2006.

[83] Eite Tiesinga, Carl J. Williams, Paul S. Julienne, Kevin M. Jones. Paul D. Lett. and William D. Phillips. A spectroscopic determination of scattering lengths for sodium atom collisions. *National Institute of Standards and Technology, Journal of Research*, 101(4):505–520, 1996.

[84] D. Comparat, C. Drag, B. Laburthe Tolra, A. Fioretti, P. Pillet, A. Crubellier, O. Dulieu, and F. Masnou-Seeuws. Formation of cold Cs ground state molecules through photoassociation in the pure long-range state. *The European Physical Journal D*, 11(1):59–71, 2000.

[85] R.N. Zare. *Angular Momentum: Understanding Spatial Aspects in Chemistry and Physics.* Wiley, New York, 1988.

[86] G.B. Arfken, H.J. Weber, and F.E. Harris. *Mathematical Methods for Physicists: A Comprehensive Guide.* Elsevier, 2012.

[87] Jeremy M. Sage, Sunil Sainis, Thomas Bergeman, and David DeMille. Optical production of ultracold polar molecules. *Physical Review Letters*, 94(20):203001–4, 2005.

[88] Andrew J. Kerman, Jeremy M. Sage, Sunil Sainis, Thomas Bergeman, and David DeMille. Production and state-selective detection of ultracold RbCs molecules. *Physical Review Letters*, 92:153001, 2004.

[89] Eric R. Hudson, Nathan B. Gilfoy, S. Kotochigova, Jeremy M. Sage, and D. DeMille. Inelastic collisions of ultracold heteronuclear molecules in an optical trap. *Physical Review Letters*, 100(20):203201–4, 2008.

[90] C.E. Hamilton, J.L. Kinsey, and R.W. Field. Stimulated emission pumping: New methods in spectroscopy and molecular dynamics. *Annual Review of Physical Chemistry*, 37:493, 1986.

[91] W.C. Stwalley. Efficient conversion of ultracold Feshbach-resonance-related polar molecules into ultracold ground state ($X^1\Sigma^+ v$=0, $J$=0) molecules. *The European Physical Journal D*, 31(2), 2004.

[92] K. Bergmann, H. Theuer, and B. W. Shore. Coherent population transfer among quantum states of atoms and molecules. *Reviews of Modern Physics*, 70(3):1003–1025, 1998.

[93] K. Winkler, F. Lang, G. Thalhammer, P. v. d. Straten, R. Grimm, and J. Hecker-Denschlag. Coherent optical transfer of Feshbach molecules to a lower vibrational state. *Physical Review Letters*, 98(4):043201–4, 2007.

[94] K. Aikawa, D. Akamatsu, M. Hayashi, K. Oasa, J. Kobayashi, P. Naidon, T. Kishimoto, M. Ueda, and S. Inouye. Coherent transfer of photoassociated molecules into the rovibrational ground state. *Physical Review Letters*, 105:203001, 2010.

[95] T. Bergeman, A. Kerman, J. Sage, S. Sainis, and D. DeMille. Prospects for production of ultracold RbCs molecules. *The European Physical Journal D*, 31(2):179–188, 2004.

[96] D. DeMille. Private communication.

[97] K.K. Ni. *A Quantum Gas of Polar Molecules.* PhD thesis, University of Colorado, 2009.

[98] P. A. Ivanov, N. V. Vitanov, and K. Bergmann. Effect of dephasing on stimulated raman adiabatic passage. *Physical Review A*, 70:063409, 2004.

[99] T. Okoshi, K. Kikuchi, and A. Nakayama. Novel method for high resolution measurement of laser output spectrum. *Electronics Letters*, 16(16):630–631, 1980.

[100] John L. Hall and Miao Zhu. An introduction to phase-stable optical sources. *Laser Manipulation of Atoms and Ions, E. Arimondo, WD Phillips, and F. Strumia, eds.(North Holland, 1992)*, 671, 1992.

[101] R.W.P. Drever, J.L. Hall, F.V. Kowalski, J. Hough, G.M. Ford, A.J. Munley, and H. Ward. Laser phase and frequency stabilization using an optical resonator. *Applied Physics B*, 31(2):97–105, 1983.

[102] Stephan Kraft. *Formation, Trapping, and Interaction of Ultracold Molecules.* PhD thesis, Albert-Ludwigs-Universität Freiburg, 2006.

[103] Dajun Wang, Jin-Tae Kim, C. Ashbaugh, E.E. Eyler, P.L. Gould, and W.C. Stwalley. Rotationally resolved depletion spectroscopy of ultracold KRb molecules. *Physical Review A*, 75(3):032511, 2007.

[104] J. Deiglmayr, A. Grochola, M. Repp, K. Mortlbauer, C. Gluck, J. Lange, O. Dulieu, R. Wester, and M. Weidemuller. Formation of ultracold polar molecules in the rovibrational ground state. *Physical Review Letters*, 101(13):133004–4, 2008.

[105] D. Budker, D.F. Kimball, and D.P. DeMille. *Atomic Physics: An Exploration Through Problems and Solutions.* Oxford University Press, 2004.

[106] G. Grynberg, A. Aspect, and C. Fabre. *Introduction to Quantum Optics: From the Semi-classical Approach to Quantized Light.* Cambridge University Press, 2010.

[107] E. Arimondo, M. Inguscio, and P. Violino. Experimental determinations of the hyperfine structure in the alkali atoms. *Reviews of Modern Physics*, 49:31–75, 1977.

[108] N. Zahzam, T. Vogt, M. Mudrich, D. Comparat, and P. Pillet. Atom-molecule collisions in an optically trapped gas. *Physical Review Letters*, 96:023202, 2006.

[109] Johannes Deiglmayr, Marc Repp, Roland Wester, Olivier Dulieu, and Matthias Weidemüller. Inelastic collisions of ultracold polar LiCs molecules with caesium atoms

in an optical dipole trap. *Physical Chemistry Chemical Physics*, 13(42):19101–19105, 2011.

[110] Fredrik K. Fatemi, Kevin M. Jones, Paul D. Lett, and Eite Tiesinga. Ultracold ground-state molecule production in sodium. *Physical Review A*, 66:053401, 2002.

[111] Sourav Dutta. D.D. Elliott, and Yong P. Chen. Formation of ultracold LiRb molecules photoassociation near the Li ($2s^2S_{1/2}$) + Rb($ps^2P_{1/2}$ asymptote), 2013. http://arxiv.org/abs/1311.6361.

[112] U. Schunemann, H. Engler, R. Grimm, M. Weidemuller, and M. Zielonkowski. Simple scheme for tunable frequency offset locking of two lasers. *Review of Scientific Instruments*, 70(1):242–243, 1999.

[113] C.D. Bruzewicz, M. Gustavsson, Toshihiko Shimasaki, and D DeMille. Continuous formation of vibronic ground state RbCs molecules via photoassociation. *New Journal of Physics*, In press.

[114] C. Gabbanini and O. Dulieu. Formation of ultracold metastable RbCs molecules by short-range photoassociation. *Physical Chemistry Chemical Physics*, 13:18905–18909, 2011.

[115] P. Zabawa, A. Wakim, M. Haruza, and N. P. Bigelow. Formation of ultracold $X^1\Sigma^+(v{=}0)$ NaCs molecules via coupled photoassociation channels. *Physical Review A*, 84:061401, 2011.

[116] Jayita Banerjee, David Rahmlow, Ryan Carollo, Michael Bellos, Edward E. Eyler, Phillip L. Gould, and William C. Stwalley. Direct photoassociative formation of ultracold KRb molecules in the lowest vibrational levels of the electronic ground state. *Physical Review A*, 86:053428, 2012.

[117] C. M. Dion, C. Drag, O. Dulieu, B. Laburthe Tolra, F. Masnou-Seeuws, and P. Pillet. Resonant coupling in the formation of ultracold ground state molecules via photoassociation. *Physical Review Letters*, 86(11):2253, 2001.

[118] H. Fahs, A.R. Allouche, M. Korek, and M. Aubert-Frécon. The theoretical spin-orbit structure of the RbCs molecule. *Journal of Physics B: Atomic, Molecular and Optical Physics*, 35(6):1501, 2002.

[119] Zhonghua Ji, Hongshan Zhang, Jizhou Wu, Jinpeng Yuan, Yonggang Yang, Yanting Zhao, Jie Ma, Lirong Wang, Liantuan Xiao, and Suotang Jia. Photoassociative formation of ultracold RbCs molecules in the $(2)^3\Pi$ state. *Physical Review A*, 85:013401, 2012.

[120] N. Bouloufa-Maafa, M. Aymar, O. Dulieu, and C. Gabbanini. Formation of ultracold RbCs molecules by photoassociation. *Laser Physics*, 22(10):1502–1512, 2012.

[121] A. Fioretti and C. Gabbanini. Experimental study of the formation of ultracold RbCs molecules by short-range photoassociation. *Physical Review A*, 87:054701, 2013.

[122] Andreia F. Nogueira, C.E. Fellows, and T. Bergeman. Additional data on the $(4)^1\Sigma$ state of RbCs and potential determination. *The Journal of Chemical Physics*, 129:136101, 2008.

[123] T. Gustavsson, C. Amiot, and J. Verges. Spectroscopic investigations of the diatomic molecule RbCs by means of laser-induced fluorescence: II. Rotational analysis of five excited electronic states. *Molecular Physics*, 64(2):293–313, 1988.

[124] Yonghoon Lee, Youngjee Yoon, Sungyul Lee, Jin-Tae Kim, and Bongsoo Kim. Parallel and coupled perpendicular transitions of RbCs 640 nm system: Mass-resolved resonance enhanced two-photon ionization in a cold molecular beam. *The Journal of Physical Chemistry A*, 112(31):7214–7221, 2008. PMID: 18636697.

[125] Daniel A. Steck. Cesium d line data, 2010. http://steck.us/alkalidata.

[126] V. Zuters, O. Docenko, M. Tamanis, R. Ferber, V. V. Meshkov, E. A. Pazyuk, and A. V. Stolyarov. Spectroscopic studies of the $(4)^1\Sigma^+$ state of RbCs and modeling of the optical cycle for ultracold $X^1\Sigma^+(v{=}0,\ J{=}0)$ molecule production. *Physical Review A*, 87:022504, 2013.

[127] A. Banerjee, D. Das, and V. Natarajan. Absolute frequency measurements of the D1 lines in $^{39}$K, $^{85}$Rb, and $^{87}$Rb with $\sim$0.1 ppb uncertainty. *Europhysics Letters*, 65(2):172, 2004.

[128] C. Drag, B.L. Tolra, O. Dulieu, D. Comparat, M. Vatasescu, S. Boussen, S. Guibal, A. Crubellier, and P. Pillet. Experimental versus theoretical rates for photoassociation and for formation of ultracold molecules. *IEEE Journal of Quantum Electronics*, 36(12):1378–1388, 2000.

[129] A. Derevianko, J. F. Babb, and A. Dalgarno. High-precision calculations of van der Waals coefficients for heteronuclear alkali-metal dimers. *Physical Review A*, 63:052704, 2001.

[130] J. Aldegunde, Ben A. Rivington, Piotr S. Żuchowski, and Jeremy M. Hutson. Hyperfine energy levels of alkali-metal dimers: Ground-state polar molecules in electric and magnetic fields. *Physical Review A*, 78:033434, 2008.

[131] Ionut D. Prodan, Marin Pichler, Mark Junker, Randall G. Hulet, and John L. Bohn. Intensity dependence of photoassociation in a quantum degenerate atomic gas. *Physical Review Letters*, 91:080402, 2003.

[132] J. Ye. Private communication.

[133] M. Mudrich, S. Kraft, K. Singer, R. Grimm, A. Mosk, and M. Weidemüller. Sympathetic cooling with two atomic species in an optical trap. *Physical Review Letters*, 88:253001, 2002.

[134] B. Zhao, A. W. Glaetzle, G. Pupillo, and P. Zoller. Atomic rydberg reservoirs for polar molecules. *Physical Review Letters*, 108:193007, 2012.

[135] Naoto Masuhara, John M. Doyle, Jon C. Sandberg, Daniel Kleppner, Thomas J. Greytak, Harald F. Hess, and Greg P. Kochanski. Evaporative cooling of spin-polarized atomic hydrogen. *Physical Review Letters*, 61(8):935, 1988.

[136] Wolfgang Petrich, Michael H. Anderson, Jason R. Ensher, and Eric A. Cornell. Stable, tightly confining magnetic trap for evaporative cooling of neutral atoms. *Physical Review Letters*, 74:3352–3355, 1995.

[137] Kendall B. Davis, Marc-Oliver Mewes, Michael A. Joffe, Michael R. Andrews, and Wolfgang Ketterle. Evaporative cooling of sodium atoms. *Physical Review Letters*, 74:5202–5205, 1995.

[138] Charles S. Adams, Heun Jin Lee, Nir Davidson, Mark Kasevich, and Steven Chu. Evaporative cooling in a crossed dipole trap. *Physical Review Letters*, 74(18):3577, 1995.

[139] Michael Mayle, Goulven Quéméner, Brandon P. Ruzic, and John L. Bohn. Scattering of ultracold molecules in the highly resonant regime. *Physical Review A*, 87:012709, 2013.

[140] Paul D. Lett, Richard N. Watts, Christoph I. Westbrook, William D. Phillips, Phillip L. Gould, and Harold J. Metcalf. Observation of atoms laser cooled below the Doppler limit. *Physical Review Letters*, 61:169–172, 1988.

[141] Yang Yan, Ji Zhong-Hua, Yuan Jin-Peng, Wang Li-Rong, Zhao Yan-Ting, Ma Jie, Xiao Lian-Tuan, and Jia Suo-Tang. Experimental study of rovibrational spectrum of ultracold polar RbCs molecules. *Acta Phys. Sin.*, 61(21), 2012.

**Abstract**

# The Welfare Effects of Policy Interventions in the US Health Care Industry: Evidence from the Nursing Home Industry and Health Insurance Markets

Martin Benjamin Hackmann

2014

How should governments regulate health care markets? In my dissertation, I study the positive and the normative implications of policy changes in two important US health care markets: the nursing home industry and the health insurance market. The dissertation is organized into three chapters.

In the first chapter, I study the welfare effects of Medicaid provider rate changes in the US nursing home industry. To disentangle the effects on Medicaid spending, consumer welfare, and provider profits, I estimate a model of demand and supply. Applying the model to provider and consumer micro data from Pennsylvania delivers two main results. First, I find that nursing homes increase the number of skilled nurses per resident by 2-3% in response to a universal 1% increase in the Medicaid reimbursement rates. Second, I find that staffing levels are on average inefficiently low. The demand estimates suggest that the total willingness to pay of all residents in a given nursing home equals $109,000 per year for an additional skilled nurse. On the other hand, detailed information on wages and fringe benefits from cost reports indicate that it costs providers only $82,000 per year to employ another skilled nurse. Combining the demand and cost estimates with the evidence on provider responses suggests that an increase in Medicaid rates can enhance social welfare. Specifically, I find that a universal increase in Medicaid reimbursement rates of 5% would lead to an annual welfare gain of $27 million in Pennsylvania, about 24% of the underlying increase in Medicaid spending, ignoring the deadweight loss from raising the additional Medicaid dollars.

In the second chapter, I present joint work with Amanda Kowalski, Yale University, and Jonathan Kolstad, The Wharton School of the University of Pennsylvania, on the role

of selection in Massachusetts health insurance market. This paper was published in the *American Economic Review, Papers & Proceedings* under the title "Health Reform, Health Insurance, and Selection: Estimating Selection into Health Insurance Using Massachusetts Health Reform". In this study, we implement an empirical test for selection into health insurance using changes in coverage induced by the introduction of mandated health insurance in Massachusetts. Our test examines changes in the cost of the newly insured relative to those who were insured prior to the reform. We find that counties with larger increases in insurance coverage over the reform period face the smallest increase in average hospital costs for the insured population, consistent with adverse selection into insurance before the reform. Additional results, incorporating cross-state variation and data on health measures, provide further evidence for adverse selection.

In the third chapter, I present joint work with Amanda Kowalski and Jonathan Kolstad, which builds onto the analysis presented in the second chapter. The working title of this paper is "Adverse Selection and an Individual Mandate: When Theory Meets Practice". In this paper, we develop a model of selection that incorporates a key element of recent health reforms: an individual mandate. We identify a set of key parameters for welfare analysis, allowing us to model the welfare impact of the actual policy as well as to estimate the socially optimal penalty level. Using data from Massachusetts, we estimate the key parameters of the model. We compare health insurance coverage, premiums, and insurer average health claim expenditures between Massachusetts and other states in the periods before and after the passage of Massachusetts health reform. In the individual market for health insurance, we find that premiums and average costs decreased significantly in response to the individual mandate; consistent with an initially adversely selected insurance market. We are also able to recover an estimated willingness-to-pay for health insurance. Combining demand and cost estimates as sufficient statistics for welfare analysis, we find an annual welfare gain of $335 per person or $71 million annually in Massachusetts as a result of the reduction in adverse selection. We also find evidence for smaller post-reform markups in the individual market, which increased welfare by another $107 per person per year and about $23 million per year overall. To put this in perspective, the total welfare gains were 8.4% of medical expenditures paid by insurers. Our model and empirical esti-

mates suggest an optimal mandate penalty of $2,190. A penalty of this magnitude would increase health insurance to near universal levels. Our estimated optimal penalty is higher than the individual mandate penalty adopted in Massachusetts but close to the penalty implemented under the ACA.